

**The interaction between silicate minerals
and C-O-H bearing melts
in the Earth's mantle**

Der Bayreuther Graduiertenschule für Mathematik und Naturwissenschaften

zur Erlangung der Würde eines
Doktors der Naturwissenschaften

- Dr. rer. nat. -

Dissertation

vorgelegt von

Davide Novella

aus Schio (Italien)

Bayreuth, 2013

Die vorliegende Arbeit wurde von April 2010 bis September 2013 am Bayerisches Geoinstitut, Universität Bayreuth unter Leitung von Prof. Dr. D.J. Frost angefertigt.

Vollständiger Abdruck der von der Bayreuther Graduiertenschule für Mathematik und Naturwissenschaften (BayNAT) der Universität Bayreuth genehmigten Dissertation zur Erlangung des akademischen Grades eines Doktors der Naturwissenschaften (Dr. rer. nat.).

Datum der Einreichung der Dissertation: 25 September 2013
Datum des wissenschaftlichen Kolloquiums: 17 Dezember 2013

Amtierender Direktor: Prof. Dr. Franz Xaver Schmid

Prüfungsausschuss:
Prof. Dr. D.C. Rubie, Bayerisches Geoinstitut, Universität Bayreuth (Vorsitzender)
Prof. Dr. D.J. Frost, Bayerisches Geoinstitut, Universität Bayreuth (1. Gutachter)
Prof. Dr. H. Keppler, Bayerisches Geoinstitut, Universität Bayreuth (2. Gutachter)
Prof. Dr. J. Senker, Anorganische Chemie, Universität Bayreuth

*Dicen que C.S.
tiene una mata de almendra,
con un letrero que dice:
el que no sabe, que aprenda!
P.L.*

Table of contents

Summary	1
Zusammenfassung.....	3
1. Introduction.....	7
1.1 A small blue dot.....	7
1.2 The volatile content of the Earth's mantle	10
1.3 Earth's deep water cycle	12
1.4 The speciation of H ₂ O in the Earth's mantle.....	14
1.5 Carbon in the Earth's mantle.....	19
1.6 Evidence for melts/fluids in the deep mantle	19
1.7 H ₂ O effect on melting processes	22
1.7.1 The effects of H ₂ O on peridotite melting temperatures.....	22
1.7.2 The effects of H ₂ O on melting in simple systems.....	24
1.8 Geophysical effects of H ₂ O in the mantle.....	27
1.9 Aims of the thesis	29
2. Methods	31
2.1 Sample synthesis at high pressure and temperature	31
2.2 Sample characterization	33
2.2.1 Scanning electron microscopy	33
2.2.2 Electron microprobe analyses	35
2.2.3 Raman spectroscopy.....	36
2.2.4 Laser ablation inductively coupled plasma mass spectrometry.....	37
2.2.5 Secondary ion mass spectrometry	39
2.2.6 Elastic recoil detection analyses.....	43
3. The composition of hydrous partial melts of garnet peridotite at 6 GPa: implications for the origin of group II kimberlites.....	47
3.1 Introduction	47
3.2 Methods.....	50
3.2.1 Experimental procedure.....	50
3.2.2 Starting materials	52

3.2.3 High pressure and high temperature experiments	53
3.2.4 Analytical techniques	55
3.3 Results.....	55
3.3.1 Subsolidus experiment.....	55
3.3.2 Hydrous melt experiments	56
3.3.3 Attainment of mineral-mineral and mineral melt chemical equilibrium	61
3.3.4 Oxygen fugacity in the experimental capsules	62
3.3.5 Loss of H ₂ or H ₂ O during experiments.....	63
3.4 Discussion	63
3.4.1 Phase relations.....	63
3.4.2 Mineral and melt compositions.....	66
3.4.3 Melt H ₂ O concentrations and the depression of melting	70
3.4.4 Low degree hydrous melts and the origin of group II kimberlites.....	73
4. The distribution of H₂O between silicate melt and nominally anhydrous peridotite and the onset of hydrous melting in the deep upper mantle.....	81
4.1 Introduction	81
4.2 Methods.....	84
4.2.1 Sample synthesis and selection	84
4.2.2 NanoSIMS	88
4.2.2 ERDA	89
4.3 Results.....	90
4.3.1 H ₂ O concentrations in NAMs	90
4.3.1.1 Olivine	92
4.3.1.2 Clinopyroxene	93
4.3.1.3 Orthopyroxene	93
4.3.1.4 Garnet	94
4.3.2 Distribution of H ₂ O	94
4.4 Discussion	95
4.4.1 The pressure dependence of $D_{H_2O}^{\min/melt}$ for peridotite assemblages	95
4.4.2 The production of low degree hydrous melts in the upper mantle.....	99
4.4.3 The variation in inter-mineral partitioning of H ₂ O with depth and the effect on seismic anisotropy in the upper mantleí í í í í í í í ..	103

5. Melting phase relations in the systems Mg₂SiO₄-H₂O and MgSiO₃-H₂O at upper mantle conditions.....	107
5.1 Introduction	107
5.2 Experimental and analytical details	109
5.3 Results.....	111
5.3.1 Results of experiments performed at 6 GPa	113
5.3.2 Results of experiments performed at 13 GPa	115
5.4 Discussion	117
5.4.1 Models for the effect of H ₂ O on the melting of Mg ₂ SiO ₄ and MgSiO ₃	117
5.4.1.1 Results at 6 GPa.....	119
5.4.1.2 Results at 13 GPa.....	124
5.4.2 The effect of pressure on melting point depression due to H ₂ O in simple and complex silicate systems.....	127
6. Effect of temperature and CO₂ on mineral-melt H₂O partitioning in the upper mantle and the production of volatile-bearing melts atop the transition zone.....	133
6.1 Introduction	133
6.2 Experimental and analytical methods	134
6.3 Results.....	138
6.4 Discussion	141
6.4.1 The distribution of water in the MSH system at upper mantle conditions	141
6.4.2 The distribution of H ₂ O at 13 GPa in the MSCH system	146
6.4.3 The production of melts atop the transition zone.....	149
7. General conclusions.....	153
7.1 Further work.....	159
Acknowledgments	161
References.....	163
Appendix	177
Erklärung	181

Summary

The experiments in this study were performed to examine the effect of volatile components on the melting of mantle rocks at conditions of the deep upper mantle (~180-400 km).

Chemical compositions, including H₂O contents, of hydrous melts, compatible with those that would form by small degree melting of an upper mantle peridotite at 180 km depth and near adiabatic temperatures, were determined using a series of iterative crystallization experiments. Experiments were performed in a multianvil apparatus at 6 GPa and 1400 °C employing a hydrous, natural mantle peridotite, which was equilibrated with a large volume of hydrous melt. The melt composition was iterated in a series of experiments until it was in equilibrium with a complete peridotite assemblage with mineral compositions close to those encountered in a sub solidus experiment at the same conditions. The H₂O content of the melt could be accurately determined through a mass balance calculation as a result of the large volume of melt employed. The hydrous melt compositions, when compared on a volatile free basis, are found to be similar to group II kimberlites. A model is proposed, whereby group II kimberlites form from cratonic lithosphere that has been previously melted but then metasomatised resulting in the addition of ~1.7 wt % phlogopite to the rock. Parameters in the model are constrained through the mineral melt partition coefficients of both H₂O and K₂O, which imply melting at near adiabatic temperatures. The H₂O concentrations of mineral phases within the peridotite assemblages were also measured using an ion probe and elastic recoil detection analysis. Using the known melt H₂O contents mineral-melt partition coefficients for olivine, clinopyroxene, orthopyroxene and garnet were determined. Using these results the onset and extent of melting at conditions equivalent to 180 km below a mid ocean ridge was examined as a function of bulk mantle H₂O concentration. The results indicate that current estimates for the H₂O content of the depleted mantle (50-200 ppm H₂O) are insufficient to induce mantle melting at these conditions, which requires ~700 ppm wt H₂O to produce 0.1 % melting and 1600 ppm for 1 % melting. However, melting can occur at these conditions within the mantle source of ocean island basalts, which is estimated to contain up to 900 ppm wt H₂O. If adiabatic temperatures are 200 °C higher within such plume related sources, melt fractions of over 1 % can be reached at 180 km depth. In addition, based on inter-mineral H₂O partitioning a model that predicts the distribution of H₂O between peridotite mineral phases as a function of depth at H₂O undersaturated conditions is presented. The model indicates that for a fixed mantle H₂O content of 200 ppm wt, the olivine H₂O content will increase with depth solely due to changes in inter-

phase partitioning and mineral modes. The results of this model provide an explanation for the reduction in seismic anisotropy observed at depths >200 km.

Further experiments were conducted at 6 and 13 GPa in the simplified systems $\text{Mg}_2\text{SiO}_4\text{-H}_2\text{O}$ and $\text{MgSiO}_3\text{-H}_2\text{O}$ to determine the effect of H_2O on melting point depression. Melting phase relations were examined using a simple thermodynamic model that supports the almost complete dissociation of H_2O to OH^- bonded to melt silicate components at these conditions, although results for forsterite at 13 GPa are inconclusive due to uncertainties in the dry melting temperature. This simple model is unsuccessful in predicting the depression of melting temperature due to H_2O for peridotite melts, however, indicating that hydrous melting models in simple systems provide little guidance as to the behavior of H_2O in natural melt compositions. In addition, H_2O partition coefficients were determined as a function of temperature for end member forsterite and enstatite at 6 and 13 GPa. Very little temperature dependence to the partition coefficients was observed except for forsterite at 13 GPa.

Experiments performed in the $\text{MgO}\text{-SiO}_2\text{-H}_2\text{O}\text{-CO}_2$ system at 13 GPa were used to investigate the effect of CO_2 on the mineral-melt H_2O partition coefficient. It was found that a melt $\text{CO}_2/(\text{CO}_2+\text{H}_2\text{O})$ (weight) ratio of 0.3 causes the forsterite H_2O partition coefficient to decrease by 50 % compared to the CO_2 -free partition coefficient, due to a significant drop in the measured forsterite H_2O content. This effect decreases with increasing temperature and must be caused by strong interaction between CO_2 and H_2O in hydrous melts. The results imply that at the base of the upper mantle $\text{H}_2\text{O-CO}_2$ bearing melts can form at adiabatic conditions if as little as 250 ppm wt of H_2O is present in the bulk mantle. This dramatic effect of CO_2 on the mineral-melt partitioning of H_2O may explain seismic observations interpreted to be caused by the presence of melt at the base of the upper mantle.

Zusammenfassung

Die Experimente in dieser Arbeit wurden durchgeführt, um den Effekt von volatilen Komponenten auf das Schmelzen von Mantelgesteinen unter den Bedingungen des tiefen oberen Erdmantels (150-400 km Tiefe) zu untersuchen.

Mithilfe einer Reihe von iterativen Kristallisationsexperimenten wurde die chemische Zusammensetzung einschließlich des H₂O-Gehalts von solchen wässerigen Schmelzen bestimmt, die vergleichbar mit Schmelzen sind, welche sich bei geringem Aufschmelzungsgrad eines Peridotits im oberen Erdmantel bei ca. 180 km Tiefe und quasi adiabatischen Temperaturen bilden. Die Experimente wurden in einer Vielstempelpresse bei 6 GPa und 1400 °C mit einem wasserhaltigen, natürlichen Mantelperidotit durchgeführt, der sich im Gleichgewicht mit einem grossen Volumen von wässriger Schmelze befand. Die Schmelzzusammensetzung wurde in einer Serie von Experimenten iterativ verfeinert, bis sie sich im Gleichgewicht mit einem kompletten Peridotit-Mineralbestand befand, wobei der Mineralchemismus dem eines experimentell unter sub-solidus Bedingungen equilibrierten Peridotits entsprach. Der Wassergehalt der Schmelze konnte durch eine Massenbilanzierungsberechnung genau bestimmt werden, da sich das Gestein mit einem grossen Volumen von Schmelze im Gleichgewicht befand. Die Zusammensetzungen der wässerigen Schmelzen sind ähnlich zu denen von Kimberliten der Gruppe II, wenn man sie unter Nichtberücksichtigung der flüchtigen Elemente vergleicht. Es wird ein Modell vorgeschlagen, in dem sich Kimberlite der Gruppe II in kratonischer Lithosphäre bilden, die vorher teilweise aufgeschmolzen war, aber dann metasomatisch überprägt wurde, so dass als Resultat dem Gestein 1.7 Gew.% Phlogopit hinzugefügt wurden. Die Parameter des Modells sind durch die Verteilungskoeffizienten zwischen Mineralen und Schmelze von H₂O und K₂O bedingt, was auf ein Aufschmelzen unter adiabatischen Bedingungen schliessen lässt. Die H₂O-Gehalte der Mineralphasen innerhalb der Peridotite wurden mit der Ionensonde und elastische Rückstreu detektionsanalyse gemessen. Mithilfe der bekannten H₂O-Gehalte wurden die Verteilungskoeffizienten zwischen Schmelze und Olivin, Klinopyroxen, Orthopyroxen und Granat bestimmt. Mit diesen Ergebnissen wurde dann die Inizierung und das Ausmass der Schmelzbildung bei Bedingungen von 180 km Tiefe unter einem mittelozeanischen Rücken als Funktion des H₂O-Gehalts des Gesamtmantelgestein untersucht. Die Resultate deuten darauf hin, dass die gegenwärtigen Abschätzungen für den H₂O-Gehalt des verarmten Mantels (50-200 ppm Gew. H₂O) nicht ausreichend sind um Schmelzbildung unter diesen Bedingungen zu

induzieren, die ~700 ppm Gew. H₂O für 0.1 % Schmelze, bzw. 1600 ppm Gew. H₂O für 1 % Schmelze erfordert. Unter diesen Bedingungen kann jedoch Aufschmelzung in dem Mantel-Entstehungsbereich von Ozeaninsel-Basalten (OIB) induziert werden, für den Wassergehalte von ca. 900 ppm Gew. H₂O abgeschätzt werden. Falls die adiabatischen Temperaturen in diesen Bereichen 200 °C höher sind, können Aufschmelzungsgrade von 1 % in einer Tiefe von 180 km erreicht werden. Darüberhinaus wird auf Basis der Verteilung von H₂O zwischen den Mineralen ein Modell präsentiert, das die Verteilung von H₂O zwischen den Peridotit-Mineralphasen als Funktion der Tiefe bei H₂O-undersättigten Bedingungen vorhersagt. Das Modell sagt ausserdem voraus, dass bei einem konstanten H₂O-Gehalt des Mantels von 200 ppm Gew. der Anstieg des H₂O-Gehalts von Olivin mit der Tiefe nur durch die Änderungen der Verteilungskoeffizienten und der Mineralkomponenten bestimmt wird. Die Ergebnisse dieses Modells liefern daher auch eine mögliche Erklärung für die Reduzierung der seismischen Anisotropie des Erdmantels, die bei Tiefen >200 km beobachtet wird.

Weitere Experimente wurden bei 6 und 13 GPa in den vereinfachten Systemen Mg₂SiO₄-H₂O und MgSiO₃-H₂O durchgeführt, um den Einfluss von H₂O auf die Schmelzpunkterniedrigung zu bestimmen. Schmelzphasenbeziehungen wurden mithilfe eines einfachen thermodynamischen Modells untersucht, das die fast vollständige Dissoziation von H₂O zu dem bei diesen Bedingungen an Komponenten der Silikatschmelze gebundenem OH beinhaltet, wobei die Resultate für Forsterit bei 13 GPa aufgrund der Unsicherheiten bei der wasserfreien Schmelztemperatur nicht schlüssig sind. Dieses einfache Modell kann allerdings die Schmelzpunkterniedrigung durch H₂O für peridotitische Schmelzen nicht erklären, was darauf hindeutet, dass Modelle für Schmelzbildung unter Wassereinfluss in einfachen Systemen nur wenige Hinweise auf das Verhalten von H₂O in natürlichen Schmelzzusammensetzungen geben. Darüberhinaus wurden H₂O Verteilungskoeffizienten als Funktion der Temperatur für die Endgliedzusammensetzungen Forsterit und Enstatit bei 6 und 13 GPa bestimmt. Dabei war die Temperaturabhängigkeit der Verteilungskoeffizienten δ mit Ausnahme von Forsterit bei 13 GPa δ nur sehr gering.

Um den Einfluss von CO₂ auf den H₂O Verteilungskoeffizienten zwischen Mineralen und Schmelze zu bestimmen, wurden Experimente im System MgO-SiO₂-H₂O-CO₂ bei 13 GPa durchgeführt. Es wurde festgestellt, dass bei einem Gewichtsverhältnis CO₂/(CO₂+H₂O) von 0.3 der H₂O Verteilungskoeffizient von Forsterit um 50 % gegenüber dem CO₂-freien Verteilungskoeffizient reduziert ist, wie es durch einen signifikant geringeren H₂O-Gehalt von

Forsterit in diesem Fall dokumentiert wird. Dieser Effekt verringert sich mit ansteigender Temperatur und muss durch die starke Wechselwirkung von H₂O und CO₂ in wässrigen Schmelzen verursacht sein. Die Ergebnisse implizieren auch, dass sich an der Basis des oberen Erdmantels H₂O-CO₂-haltige Schmelzen unter adiabatischen Bedingungen bilden können, wenn so geringe Wassergehalte wie 250 ppm Gew. H₂O im Mantel vorhanden sind. Dieser dramatische Einfluss von CO₂ auf die Verteilungskoeffizienten von H₂O zwischen Mineralphasen und Schmelze könnte auch seismische Beobachtungen erklären, die als das Auftreten von Schmelzen an der Basis des oberen Erdmantels interpretiert werden.

1. Introduction

1.1 A small blue dot

Hydrogen is the most abundant element in the universe, comprising 73 % of the Sun and, based on the compositions of their atmospheres, between 80-90 % of the giant planets. Hydrogen and volatile elements in general are clearly not evenly distributed throughout the solar system, however. The most abundant element on Earth, for example, is Fe (32 % by mass), followed by oxygen (30 %), silicon (15 %) and magnesium (14 %), with the volatiles elements H and C having estimated concentrations of <1000 ppm (McDonough, 2001). The dichotomy in volatile distribution in the solar system is considered to arise from partial condensation from the solar nebula where temperatures decreased radially with distance from the Sun (Lewis, 2004). In the outer solar system complete condensation could occur, however, temperatures in the inner solar system were too high for highly volatile elements to condense (Fig. 1.1).

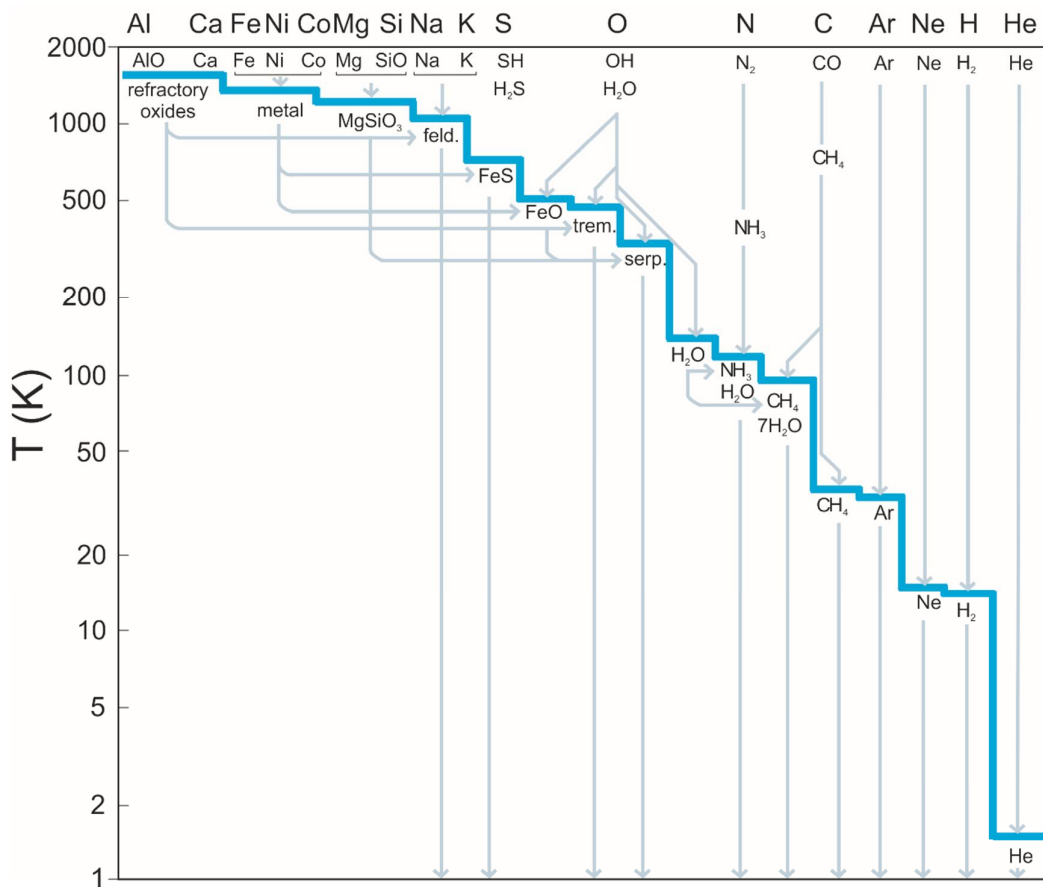


Fig. 1.1: Equilibrium condensation of elements from the solar nebula as a function of nebula temperature. (Modified after Lewis, 2004).

Solar winds eventually dispersed the remaining nebula leaving the inner solar system depleted in volatile elements, with the magnitude of the depletion increasing with decreasing condensation temperature. It is postulated that the so called snow line, where H₂O condensed to form ice was at the outer edge of what is now the asteroid belt at ~5 AU (Mumma et al., 2003). Most astrophysical models for terrestrial planet accretion indicate that initial accretion occurred from a local radial “feeding zone”, whereas later accretion involved material mixing from increasing radial distance due to an increase in orbital eccentricity caused by gravitational interactions (Rubie et al., 2010). The most likely origin for volatiles on Earth, therefore, would be as a result of this later mixing of more volatile-rich material from nearer to the asteroid belt (Marty, 2012).

Earth is the “blue planet” with approximately 71 % of its surface covered by liquid water. Surface water makes Earth unique among the terrestrial planets i.e. a habitable planet capable of supporting life. This unique habitat is underlined in one of the most distant photographs of the Earth, which was taken by the Cassini spacecraft on 19th July 2013 as it orbits Saturn 898 million miles away (Fig. 1.2). The Earth appears as a faint blue dot in an otherwise inhospitable solar system.



Fig. 1.2: The Blue dot Earth (above arrow) seen from Saturn by the Cassini spacecraft on 19th July 2013. (Modified photo from NASA/JPL-Caltech/Space Science Institute).

Even if liquid water covers almost three quarters of the surface, its mass is only a small portion of our planet. In fact, the Earth's surface water amounts to $\sim 1.4 \times 10^{21}$ kg, which is only 0.023 % of the mass of the Earth ($\sim 6 \times 10^{24}$ kg). Other surface water reservoirs, such as ground water, glaciers, permafrost, lakes etc., make up only a fraction of this total surface water (Shlkomanov, 1993). However, the Earth's hydrosphere and water cycle are essential to life and H₂O vapor also makes the most direct contribution to the Greenhouse effect. Similar arguments can be made for CO₂. Although they make up only tiny proportions of the bulk Earth, H₂O and CO₂ are by far the most important chemical components to life.

Gas giants possess primary atmospheres that formed directly from the gas of the accretion disc. Terrestrial planets, on the other hand, and particularly Earth are considered to have secondary atmospheres that degassed from the mantle via volcanic eruptions (e.g. Rubey, 1951). Models suggest that the atmosphere and hydrosphere out-gassed at a very early stage in Earth's history, however, this degassing has continued to the present day although at a considerably slower rate (e.g. Allègre et al., 1986-87). Table 1.1 shows typical gas compositions from volcanoes in different tectonic settings (Symonds et al., 1994).

Table 1.1. Volcanic gas compositions in vol %. (Source: Symonds et. al., 1994)

Volcano	Kilauea Summit	Ertaø Ale	Momotombo
Tectonic Setting	Hot Spot	Rift	Subduction Zone
H ₂ O	37.1	77.2	97.1
CO ₂	48.9	11.3	1.44
SO ₂	11.8	8.34	0.50
H ₂	0.49	1.39	0.70
CO	1.51	0.44	0.01
H ₂ S	0.04	0.68	0.23
HCl	0.08	0.42	2.89
HF	---	---	0.26

H₂O dominates in most volcanic gasses, followed by CO₂ and then SO₂ (Anderson, 1975). H₂O in particular dominates in subduction zone volcanoes, which is likely related to H₂O being subducted back into the mantle at these convergent plate boundaries. H₂O in subduction zone magmas contributes to the generally highly explosive nature of these volcanic eruptions.

The Earth's interior is, therefore, also a reservoir for volatile elements that have degassed to the surface over Earth's history. Although likely only present in small amounts, volatiles can have important influences on the physical and chemical properties of the Earth's interior. The Earth, for example, appears to be also unique in the solar system in respect of having plate tectonic processes. It has been suggested that the presence of H defects in minerals of the mantle may influence mantle rheology and the nature of plate tectonic processes (Hirth and Kohlstedt, 2003). In order to understand the role that volatiles play in the Earth's interior both currently and throughout Earth's history, it is essential to understand their geochemical behaviour and distribution inside the Earth.

1.2 The volatile content of the Earth's mantle

The Earth's bulk volatile inventory could potentially be estimated from evaluations of the volatile contents of chondritic meteorites, considered to be representative of the material from which terrestrial planets formed. While quite accurate estimates can likely be made in this way for the bulk Earth concentrations of refractory elements, such as rare earth elements, which condense at high temperatures, estimates are highly uncertain for volatile elements. This is because volatiles are strongly depleted relative to chondrites in the Earth. However the concentration of some volatile elements in the Earth such as Ar, that have radiogenically produced isotopes, can be approximated from their isotopic ratios. By assuming that the initial bulk Earth depletion in Ar was similar to other volatile elements, concentrations of volatiles in the Earth can be estimated. In this way Marty (2012) determined that the Earth's interior may host 1000–3000 ppm H₂O and up to 500 ppm C.

The most direct estimates for the H₂O content of the Earth's upper mantle come from estimates of the pre-eruptive volatile contents of mid ocean ridge basalts (MORBs). Volatile solubility in magmas decreases as magmas rise to the surface causing degassing. The initial pre-eruptive volatile content can only be determined from melts that preserve these volatiles, either because they are trapped as bubbles in the rapidly quenched glass, the so called popping rocks (e.g. Javoy and Pineau, 1991), or because the melts are trapped at higher pressures as inclusions in crystallizing minerals (Saal et al., 2002). The mantle concentration of volatile components is then normally determined by comparison with a trace element that is considered to behave similarly to the volatile during mantle melting. The concentrations of these non-volatile trace elements can be better constrained in the mantle because they can be considered to have near

chondritic ratios with other well determined mantle trace elements. In Fig 1.3, $\text{H}_2\text{O}/\text{Ce}$ and CO_2/Nb ratios for MORB melt inclusions were plotted by Saal et al. (2002) as a function of melt Na_2O content.

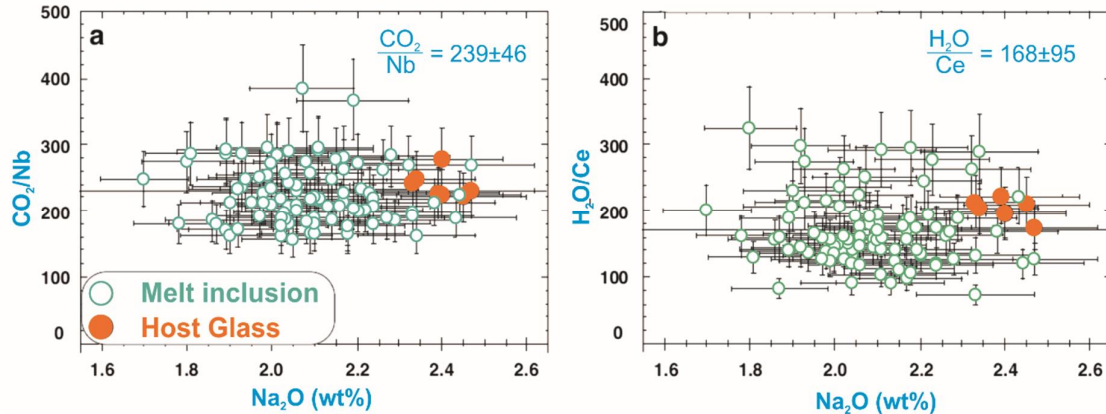


Fig. 1.3: Ratios of volatile components and trace elements in olivine melt inclusions as a function of Na_2O content of hosting lavas. As these ratios do not change over large concentrations of Na_2O , which is a proxy for the degree of fractionation or partial melting, they likely behave similarly during these processes. (Modified after Saal et al. (2002).

As Na_2O is varying between magmas as a result of the degree of melting and fractional crystallization, the fact that these ratios remain relatively constant must imply similar behaviour of each of the two components during melting and later evolution of the magma. From these ratios it is therefore possible to determine the mantle ratio of these components and from an estimate of the absolute concentration of the normalizing element in the mantle source, the mantle volatile content can be determined. Such determinations are given in Table 1.2 for H_2O and CO_2 .

Table 1.2: water content of MORBs and OIBs mantle source region

MORBs				
source	sample	H_2O (ppm wt)	CO_2 (ppm wt)	
Michael (1988)	basalt glasses	140-350		
Dixon et al., (2002)	basalt glasses	100-400		
Saal et al., (2002)	melt inclusions in olivine	142±85	72±19	
Simons et al., (2002)	basalt glasses	54-120		
Workman and Hart (2005)	basalt glasses	70-160	36±12	

OIBs				
source	sample	H_2O (ppm wt)	CO_2 (ppm wt)	
Dixon et al., (1997)	basalt glasses	525±75	1300±800	
Dixon et al., (2002)	basalt glasses	750		
Nichols et al., (2002)	basalt glasses	620-920		
Simons et al., (2002)	basalt glasses	750		

For the depleted MORB source most estimates range up to 150 ppm of H₂O and 70 ppm CO₂. Higher H₂O values reported by Michael (1998) and Dixon et al., (2002) in Table 1.2 are from enriched MORB sources. Ocean island basalts (OIB) are considered to be formed by melting of mantle plumes that originate from an enriched source that resides at greater depth within the mantle than the MORB source. OIBs are richer in volatiles with estimated H₂O contents as high as 750 ppm wt i.e. ~ 4 times typical depleted MORB values.

1.3 Earth's deep water cycle

At divergent plate boundaries asthenospheric mantle up wells to fill space left by the separating lithospheric plates. As the asthenosphere rises decompression causes it to melt and produce MORBs that pave the oceans floor and are volumetrically the most important igneous rock on the planet. During this process volatiles from the mantle degas to fill surface reservoirs such as the hydrosphere and atmosphere. These surface reservoirs were most likely originally formed in a similar fashion although early degassing would have been more rapid due to the higher temperature of the Earth's interior.

During cooling of the oceanic crust circulation of sea water into the lithosphere occurs as implied by the formation of secondary minerals such as serpentine and talc. One manifestation of this hydrothermal circulation process is the hydrothermal chimneys known as "black smokers" that are present along mid ocean ridges. They emit clouds of precipitating metals and sulphides that were initially dissolved in hydrothermal fluids at higher temperatures within the crust. Long residence of the oceanic lithosphere under the ocean causes significant amounts of hydrous alteration of the crust, and carbonate minerals can also be precipitated in these alteration processes. Alteration can penetrate deep into the lithosphere as a result of deep faults formed particularly at the so called outer rise in front of a subduction zone, where the slab starts to bend before subducting. In addition, sediments rich in clay minerals and carbonate are deposited on the sea floor. Ultimately the oceanic lithosphere cools with time, becoming denser than the underlying asthenosphere. At this point it dips back into the interior at a subduction zones. As a consequence of this process, volatile components in the lithosphere are recycled into the mantle (Fig. 1.4).

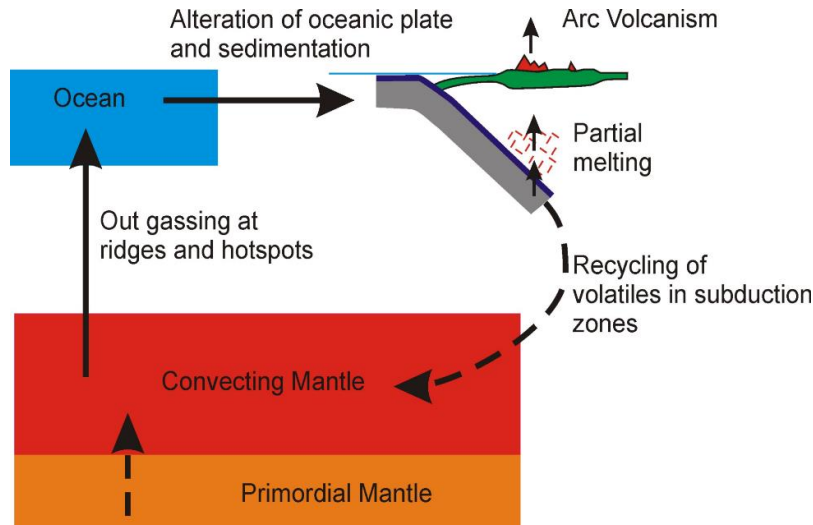


Fig. 1.4: Earth's deep water cycle. At subduction zones, the oceanic lithosphere is recycled into the Earth's interior. The oceanic sediments, crust and underlying peridotite forming the subducting slab contain H₂O which is in part released to the above mantle wedge triggering melting processes and in part transported to depth. Out gassing processes mainly at spreading centers return H₂O to the hydrosphere. (Modified after Rüpke et al., 2006)

The subducting slab comprises portions of mantle peridotite, oceanic basaltic crust and sediments all of which can contain volatile elements emplaced at the surface. As the slab undergoes prograde metamorphism, hydrous and carbonate minerals breakdown and release fluids into the overlying mantle (Peacock, 1990). H₂O present in the porous sediments escapes at shallow depths while with increasing depths it is released by the breakdown of minerals such as serpentine (see e.g. Rüpke et al., 2004). These fluids rise into the overlying mantle wedge and are responsible for the high degrees of melting that occur beneath island arc volcanoes and for the metasomatic component obvious in island arc magmas (Tatsumi et al., 1986; Kushiro, 1987). However, it is likely that not all volatiles in the slab are released into the overlying mantle and recycled back to the surface on a short timescale. As shown in Fig 1.5, models for old extensively hydrated slabs, which are initially cold and subduct quickly, imply that temperatures are low enough for significant amounts of H₂O to be subducted into the deep mantle (Hacker, 2008), therefore replenishing a certain proportion of the H₂O lost due to volcanism at mid ocean ridges. Volatiles within the mantle are therefore likely to be circulated by plate tectonic processes with recycled volatiles from the surface possibly mixing in the interior with primordial volatiles still present in the Earth since its formation. The mobility of these volatiles in the interior will be controlled by the forms in which volatiles are present in the mantle under different conditions.

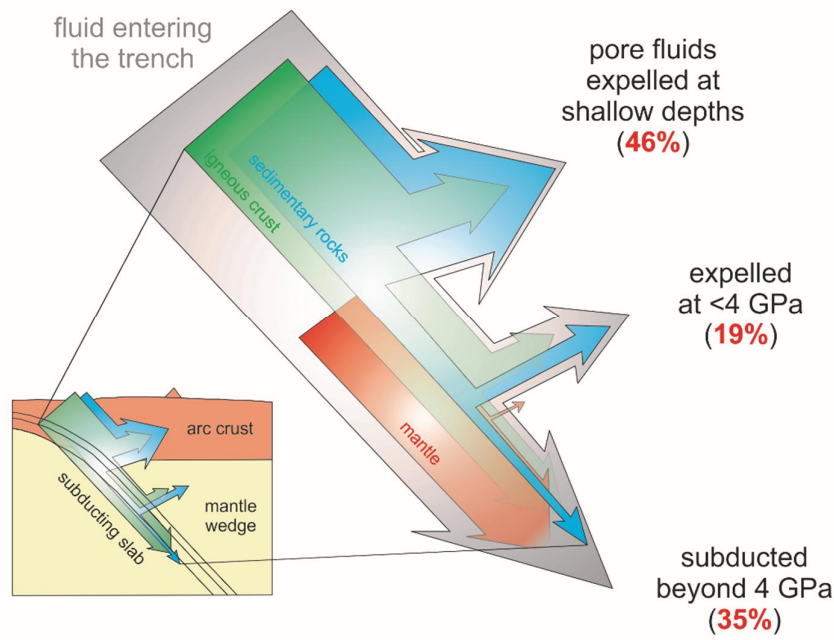


Fig. 1.5: Estimates for losses in H₂O from the subducting lithosphere for a cold rapidly subducting slab. The slab is considered to comprise 3 components: sediments, basaltic crust and underlying mantle. Each portion has an initial estimated H₂O content based on deep sea drilling samples. Using a thermal model for the subduction zone and phase equilibrium estimates for the dehydration of minerals, the proportion of H₂O lost from the slab is determined. Most H₂O is lost as pore fluid expelled at shallow depths (46 %). 19 % H₂O is then lost due to dehydration of minerals at pressures less than 4 GPa, however 35 % of the H₂O in the slab, mainly in the mantle component, is estimated to be subducted to greater depths. (Modified after Hacker, 2008).

1.4 The speciation of H₂O in the Earth's mantle

The speciation of H₂O in the mantle depends on the amounts of H₂O present and the pressure and temperature conditions considered. Volatiles are incompatible components and partition strongly into silicate melts at conditions where melts form in the shallow mantle (e.g. Michael, 1988). If sufficient volatiles are present in the mantle they can induce the existence of melts at conditions below the dry solidus (e.g. Asimow and Langmuir, 2003). At lower temperatures if large proportions of volatiles are present such as in subduction zones, volatiles can be present as supercritical fluids. At relatively low temperatures in subduction zones or in the lithospheric mantle H₂O can also be hosted within hydrous minerals such as serpentine, amphiboles and phlogopite. In subduction zones the thermal path followed by the slab will determine the depth of slab dehydration. Serpentine (antigorite) that forms for example in the mantle portions of hydrated slabs breaks down when temperatures increase above 700 °C (Bose and Ganguly, 1995). However, if subduction temperatures are low enough it has been predicted that serpentine in some slabs may avoid dehydration and transport H₂O into the deeper mantle (Bose and Ganguly, 1995; Hacker 2008). At pressures greater than 6 GPa further dense hydrous

magnesium silicate phases have been formed in experiments at temperatures generally less than 1000 °C (Fig 1.6).

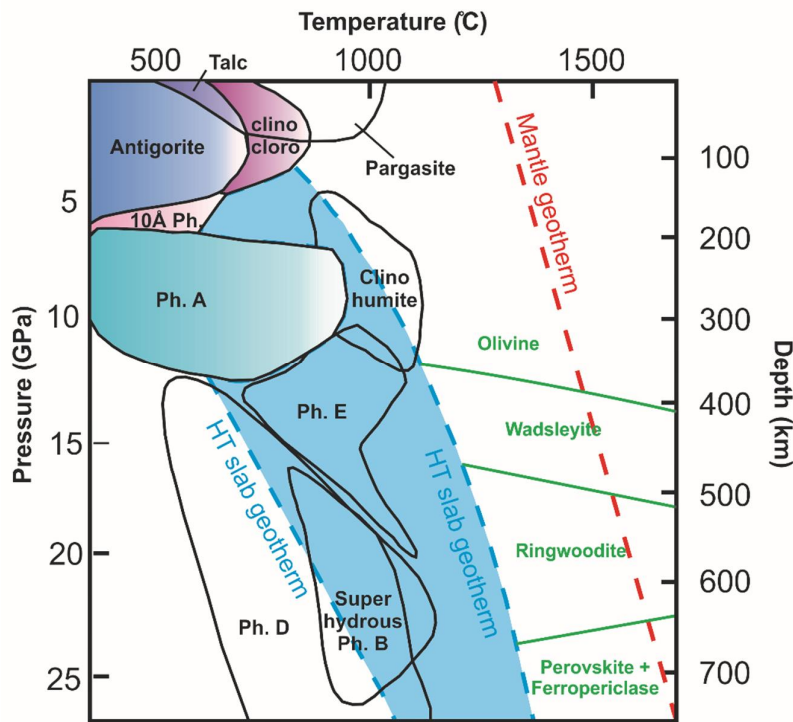


Fig. 1.6: Pressure-temperature diagram showing the principal hydrous and anhydrous phases in subduction zones. Thermal profiles of a hot and cold slab are shown. (Modified after Mainprice and Ildefonse, 2009).

These phases may transport H₂O within the slab to deeper conditions, however, their presence is still debated and these phases have never been found naturally (Othani, 2005; Frost, 2006). Fluid released due to dehydration or decarbonation of minerals in slabs will rise into the overlying mantle wedge. As temperatures are higher in the mantle wedge fluid saturated melting is predicted to ultimately occur due to this influx of fluid (Grove et al., 2006).

Water can also exist in Earth's mantle as hydroxyl defects, in so called nominally anhydrous minerals (NAMs), where the H⁺ cation is not a major structural component as in hydrous minerals. Fourier transform infra red spectroscopy (FTIR) is generally used to examine the H₂O contents of these minerals. Bell and Rossman (1992) analyzed more than 200 minerals from a worldwide collection of peridotite xenoliths and measured substantial amounts of H₂O. Olivine and garnet were found to contain up to 50 ppm wt H₂O with the most hydrous NAMs being pyroxenes that were found to often contain up to 200-500 ppm wt. Some of the highest H₂O contents have been measured in natural omphacite and clinopyroxene crystals found in

eclogitic xenoliths (Skogby et al., 1990; Bell and Rossman 1992) which contain up to 1000 ppm H₂O. Following these discoveries extensive experimental work was performed to understand the solubility of H₂O in these minerals. These early experiments were generally performed at low temperatures (<1200 °C) on single mineral phases in equilibrium with H₂O fluids (Keppler and Bolfan-Casanova, 2006). Figure 1.7 shows experimentally determined H₂O contents in olivine at 1100 °C measured in various studies.

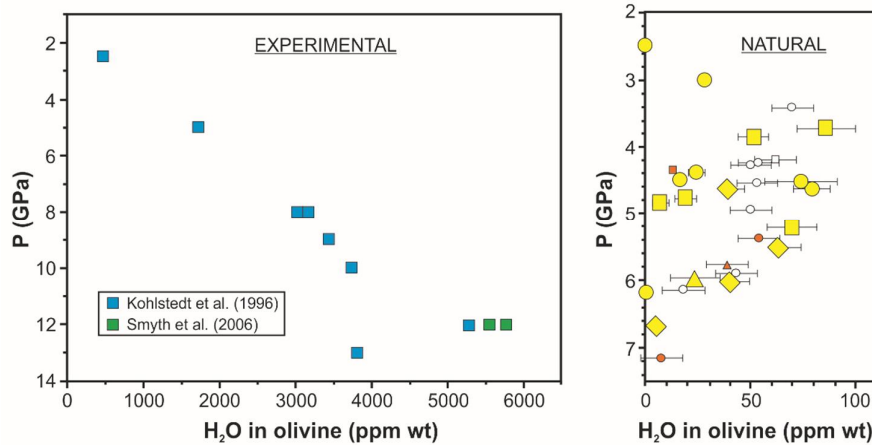
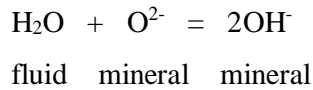


Fig. 1.7: (Left) The H₂O solubility in olivine measured as a function of pressure at 1100 °C. Values by Kohlstedt et al. (1996) have been corrected based on the FTIR calibration of Bell et al. (2003). (Right) Olivine H₂O contents measured in mantle xenoliths from the Kaapvaal craton and plotted as a function of equilibration depth, where 7 GPa is approximately 200 km (Modified after Peslier et al., 2010).

The H₂O content increases with pressure. In simple terms the dissolution of a pure H₂O fluid in mineral phases can be described as:



where O²⁻ is an initially un-protonated oxygen site in the mineral structure. Taking the standard state to be pure H₂O at 1 bar and the temperature of interest, the equilibrium constant for this reaction can be written as:

$$K = \frac{[a_{\text{OH}^-}]^2}{f_{\text{H}_2\text{O}} \cdot [a_{\text{O}^{2-}}]}$$

where a_{OH^-} is, for example, the activity of the OH⁻ in the mineral and $f_{\text{H}_2\text{O}}$ is the fugacity of

pure H₂O. Because the activity $a_{O^{2-}}$ should remain constant and $a_{OH^-} \propto X_{OH^-}$, then the mole fraction (X_{OH^-}) of dissolved H₂O in the mineral should be proportional to $\sqrt{f_{H_2O}}$. This is the case when OH defects in the mineral are isolated hydroxide groups. However, the solubility of H₂O in the minerals becomes proportional to f_{H_2O} and $f_{H_2O}^2$ if the defects correspond to OH-pairs or four protons [(OH)₄], respectively. The type of substitution depends on the mineral (for a review see Keppler and Bolfan-Casanova, 2006). The H₂O content of olivine therefore increases with pressure, as seen in Fig. 1.7 because f_{H_2O} increases. In Fig. 1.7 measurements of natural olivine samples from mantle xenoliths are also shown as a function of depth. Concentrations are generally below those determined experimentally and some of the lowest values are from the highest pressures, which is in contrast to experimental measurements. In the experiments, however, the equilibrium fluid phase is relatively pure H₂O (although even at 1100 °C there will be silicate material dissolved in the fluid). The main difference between natural and experimental samples is that in the mantle volatile bearing liquid phases, whose presence can be inferred from their metasomatic effects (Erlank et al. 1987; Peslier et al., 2010), are most likely not pure H₂O. There are two possible reasons for this. Either H₂O fluids in the mantle are diluted by other volatile components to make, for example, a mixed H₂O-CO₂ fluid phase, or temperatures at which the minerals equilibrated were such that silicate melting occurred. Figure 1.8 shows measurements by Férot and Bolfan-Casanova (2012) for olivine H₂O contents as a function of temperature at 7.5 GPa.

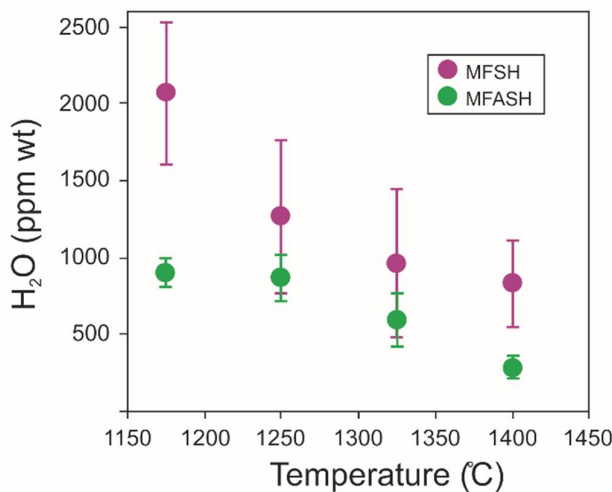
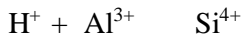


Fig. 1.8: Olivine H₂O concentrations as a function of temperature in two systems (MgO-FeO-SiO₂-H₂O±Al₂O₃) at 7.5 GPa. The formation of silicate melts at temperatures above 1200 °C leads to a lowering of the olivine H₂O content as H₂O is diluted by the silicate melt. (Modified after Férot and Bolfan-Casanova, 2012).

As temperatures increase melting occurs above 1200 °C. Although the H₂O content of the silicate melt is still relatively high, it is much lower than a fluid once temperatures rise above the eutectic and rather than the H₂O content being controlled only by f_{H_2O} it will depend on $a_{H_2O}^{melt}$ which will equate to $X_{H_2O}^{melt} \cdot \gamma_{H_2O}^{melt} \cdot f_{H_2O}$ if the standard state is pure H₂O at 1 bar and T. The concentration of H₂O in the mineral phase is therefore also a function of the amount of H₂O in the melt phase, i.e. $X_{H_2O}^{melt}$. In order to predict H₂O contents of mineral phases coexisting with melts it is important to also determine the amount, or activity, of H₂O in the melt phase. Rather than the solubility being the controlling factor as for fluids, when melts are the coexisting phase the partitioning of H₂O between minerals and melts ($D_{H_2O}^{\text{min/ melt}}$) becomes the determinant factor in mineral H₂O contents. This requires the ability to measure the H₂O content of the silicate melts and in order to construct models for the H₂O contents of phase in the mantle it is important to be able to describe melt H₂O contents as a function of P, T and bulk composition. As shown in Fig 1.8 different chemical systems, with or without Al, result in different equilibrium olivine H₂O contents. This could potentially arise from two effects. Either the presence of Al₂O₃ in the melt lowers $a_{H_2O}^{melt}$ or a small amount of Al in olivine influences the energetics of protonation. Although the second possibility is not necessarily the case, the mechanism by which minerals are protonated will have a strong influence on their H₂O contents. For most minerals the particular oxygen site protonated is unclear and multiple sites are probably involved (e.g. Smyth et al., 2006; Umemoto et al., 2011 for olivine). FTIR only provides some constraints and neutron diffraction, the only absolute method for determining H sites, cannot be performed on samples with such low total H contents. However, in most instances the protonation site is not as important as the substitution mechanism that charge balances the addition of H⁺. In garnet minerals it has been well recognized that a hydrogarnet mechanism can occur where Si is replaced by 4H⁺ cations (Ackermann et al., 1983). It has been proposed that in olivine, FTIR bands can be placed in two groups with one group corresponding to a Si defect mechanism, i.e. related to 4H⁺, and the other to the creation of a Mg²⁺ defect balancing 2H⁺. Smyth et al., (2006) performed single crystal X-ray diffraction on forsterite containing almost 1 wt % H₂O and found the structure to be consistent with Mg²⁺ vacancies. For pyroxenes a strong dependence of the H₂O content on Al implies the substitution mechanism:



(Rauch and Keppler, 2002). Due to the sensitivity of some minerals to the concentrations of such charge balancing components, significant changes in mineral H₂O contents can potentially occur with changes in mineral chemistry as a function of P, T or degree of melting (Mierdel et al., 2007).

1.5 Carbon in the Earth's mantle

While H₂O dissolves to appreciable amounts in peridotitic NAMs, C dissolves to a very limited extent in mantle minerals, reaching ~10 ppm wt at the bottom of the upper mantle (Shcheka et al., 2006). Graphite and diamond are observed in mantle-derived rocks, but C can also be present at depth in the oxidized state as carbonate minerals or melts or as a CO₂ component of a fluid phase. If CO₂ is present in mantle fluids the activity of H₂O will be lowered causing the H₂O contents of coexisting minerals to drop.

Whether C exists in oxidized, e.g. carbonate, or reduced, e.g. diamond, forms will depend on the oxygen fugacity (*f*_{O₂}) which was recently investigated by Stagno et al. (2010, 2012). These experiments indicate that with increasing pressure the *f*_{O₂} of the mantle will decrease and carbonates minerals and melts should be reduced to either graphite or diamond at depths >100 km. Oxygen fugacities of the cratonic lithospheric mantle indicate conditions mainly in the diamond or graphite stability field and consistent with coexisting fluids which have a low CO₂ concentration (Stagno et al. 2012).

Kimberlite magmas are, however, proposed to have high CO₂ concentrations (e.g. Wyllie, 1980) and their source which is at depths >180 km, must therefore be sufficiently oxidized for the particular CO₂ component to be stable.

1.6 Evidence for melts/fluids in the deep mantle

Magmas erupted at the surface provide evidence for the presence of volatiles in the mantle. Mantle xenoliths are proof of the presence of volatiles in the mantle as they contain minerals with dissolved H₂O contents, diamonds and carbonates. In addition, however, xenoliths contain evidence for the passage of melts or fluids deep within the mantle that causes mantle metasomatism, i.e. the addition of incompatible elements to a mineral assemblage often causing

the formation of new minerals. Metasomatism is caused by the passage of fluids and melts and is evident in the cratonic lithosphere even at depths >100 km (Erlank et al., 1987; Kopylova and Russel, 2000; van Achterbergh et al., 2001), conditions where it could not have been caused by the passage of dry melts. The chemical nature of metasomatism implies that the melts or fluids were able to concentrate large amounts of incompatible elements, which can only occur if melt or fluid fractions were small. Erlank et al. (1987) described a series of progressively metasomatised assemblages as a result of metasomatic interaction of a fluid/melt phase with garnet peridotite. The lowest grade of metasomatism added the hydrous mineral phlogopite ($KMg_3AlSi_3O_{10}(OH)_2$) to the rock, which then becomes a garnet phlogopite peridotite. The process adds H_2O and K_2O to the rock but lowers the amount of Al_2O_3 . The next state is the loss of garnet from the rock due to conversion to phlogopite and loss of Al, which then becomes a phlogopite peridotite. In the final stage the potassium rich amphibole K-richterite ($KCaNaMg_5Si_8O_{22}(OH)_2$) is also formed producing a phlogopite K-richterite peridotite. This metasomatic sequence underlines the frequently encountered relationship between both H_2O and K because both are likely incompatible during melting or the release of fluids. High pressure hydrous fluidmelts therefore crystallize K-rich hydrous minerals, which also have a higher thermal stability than other hydrous phases. This relationship between K and H_2O can be seen in mantle basaltic melt compositions (Michael, 1988), which implies that such metasomatism may have affected large portions of the mantle at some point. The presence of H_2O bearing melts in the upper mantle is also implied by the occurrence of xenoliths with olivine-free lithologies containing considerable amounts of H_2O , such as MARID rocks (Fig. 1.9).



Fig. 1.9: A MARID nodule from a kimberlite. MARID rocks are comprised of mica-amphibole-rutile-ilmenite-diopside and are thought to be cumulates crystallized from H_2O rich magmas (Konzett et al., 1997) at depths >100 km in the cratonic lithosphere. Black line is 1 cm long. (Modified photo from J. Konzett).

These exotic rocks are named from the phase assemblage mica-amphibole-rutile-ilmenite-diopside that forms them (Dawson and Smith, 1977). The origin of such rocks has been experimentally determined to be as deep as 100 km (Kushiro and Erlank, 1970; Konzett et al. 1997) and the occurrence of H₂O-bearing minerals in them suggests the presence of considerable amounts of H₂O in their source melt at depth. Further evidence for the presence of deep mantle melting comes from the existence of kimberlites, magmas which originate at depths >180 km. To form at such great depths kimberlites must have had an initial high volatile content. The pre-eruptive volatile content of these magmas is hard to assess, however, as they are almost totally degassed. The composition of kimberlitic magmas is also hard to determine as they are generally a mixture of xenoliths, xenocrysts and crystals that crystallized from the magmas (Mitchell, 1986). As shown in Fig. 1.10, the origin of the different crystals can often not be unambiguously identified.

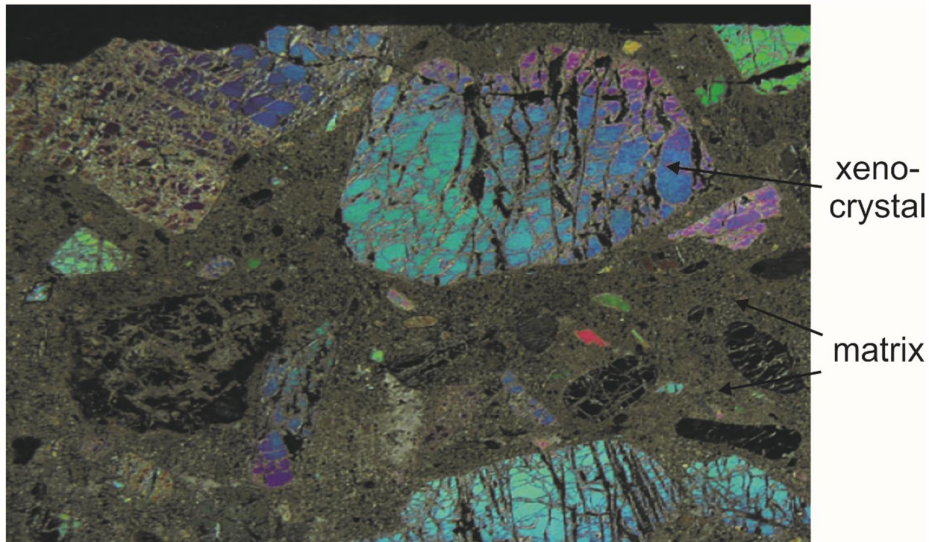


Fig. 1.10: A transmitted light microscope image of a kimberlite rock in crossed polars. The field of view is 2 cm across and dominated by phenocrysts of forsterite and smaller phlogopite and garnet. The fine matrix is composed of serpentine, calcite, phlogopite and opaques. (Modified photo from the Imperial College London Rock Library).

Kimberlites are also extensively altered by the circulation of gasses during cooling of the rocks, which results in the formation of secondary minerals such as serpentine and calcite, which also underlines the volatile nature of the original magma (Fig. 1.10). Estimates of primary kimberlite compositions including volatile contents are highly uncertain. Table 1.3 shows compositions recently estimated by Sparks et al., (2009).

Table 1.3: Estimated primary kimberlite compositions. (Source: Sparks et al., 2009)

	Untijiesberg (2003)	Le Roex et al. (2003)	Wesselton	Group II Orangeite
SiO ₂	29.56	36.28	36.28	36.3
TiO ₂	3.82	0.9	0.90	1
Al ₂ O ₃	2.74	0.92	0.92	3.2
Fe ₂ O ₃	11.24	1.15	1.15	NA
FeO	9.22	9.22	4.20	7.6
MnO	0.22	0.21	0.21	0.2
MgO	30.8	34.52	34.52	29.7
CaO	17.73	14.65	14.65	6.0
Na ₂ O	0.07	0.4	0.40	0.1
K ₂ O	1.35	0.34	0.34	3.2
P ₂ O ₅	2.21	1.4	1.40	1.1
CO ₂	8.63	12.12	4.13	3.6
H ₂ O	4.92	10.35	5.67	6.8

Kimberlites are generally divided into two groups. Group I kimberlites are characterized by higher TiO₂, CaO and CO₂ contents, while group II kimberlites, that are also called orangeites, have higher SiO₂ and K₂O contents. Group II kimberlites are mica rich and are considered to have been more H₂O rich magmas. Extremely enriched trace element signatures imply a previously metasomatised source (Becker and Le Roex, 2005). In order to understand the origin of kimberlites melting experiments have been performed on various compositions at pressures >6 GPa (Edgar et al., 1988; Edgar and Charbonneau, 1993; Girnis et al., 1995, 2011; Ulmer and Sweeney, 2002; Sokol et al., 2013). A major problem in the determination of the origin of such melts, however, is the poorly constrained initial volatile content and the difficulty in determining melt volatile contents at high pressures. Kimberlite melting attests to the existence of high volatile concentrations in the Earth's deep interior and their origin is a key issue in the understanding of volatile behavior in the mantle.

1.7 H₂O effect on melting processes

1.7.1 The effects of H₂O on peridotite melting temperatures

H₂O lowers the melting temperature of silicate rocks as does CO₂ and other volatiles (e.g. Kushiro et al., 1968; Mysen and Boettcher, 1975). The apparently large influence of H₂O on

silicate melting arises mainly from the low molecular mass, which means that a relatively small weight fraction equates to a large mole fraction, and from the relatively high incompatibility of H₂O during melting. Figure 1.11 shows estimates for the effect of H₂O on the melting of peridotite mantle by Hirschmann (2006).

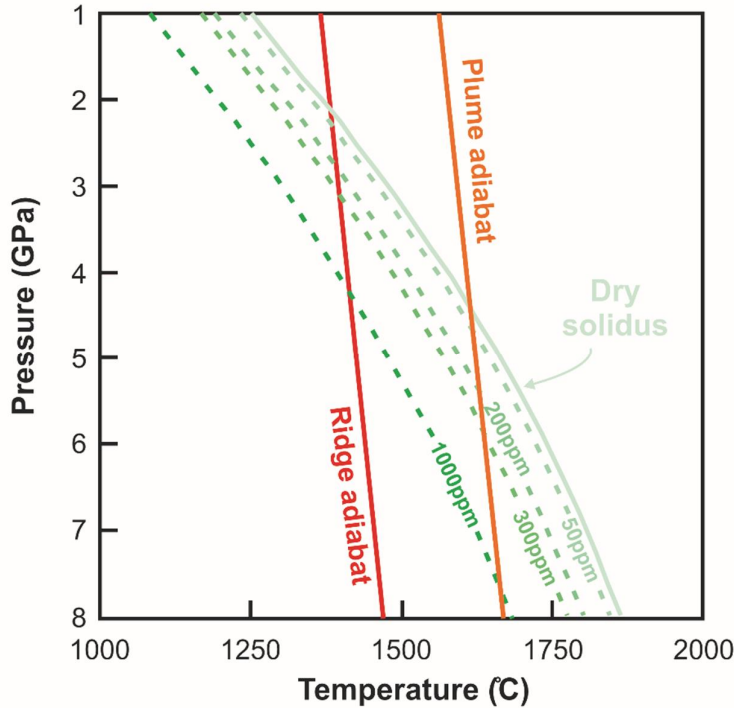


Fig. 1.11: The depression of the dry peridotite solidus as a function of bulk H₂O content. During decompression up welling asthenospheric mantle follows an adiabatic pressure-temperature path. If the mantle is dry the mantle will start to melt at 2 GPa, i.e. 60 km, whereas if it were to contain 1000 ppm H₂O it would melt at 4.3 GPa, that is 120 km. Plumes may be 200°C hotter and therefore a plume containing 1000 ppm H₂O would potentially start to melt around 8 GPa (= 240 km). (Modified after Hirschmann, 2006).

Dry mantle will commence melting at 60 km but if the mantle were to contain 1000 ppm of H₂O it would melt at 120 km. The onset of hydrous melting will be controlled by two factors. Firstly, the partition coefficients of H₂O between mineral and melt phases. In the case where H₂O exceeds the storage capacity of a mantle peridotite, the higher these coefficients are the more H₂O is required in the mantle before these phases are saturated at a given pressure along the adiabat and melting can commence. The onset of melting is aided by the fact that the main mineral in the mantle, olivine, has an H₂O partition coefficient that decreases with decreasing pressure. Secondly, the occurrence and proportion of melt at any pressure will depend on the H₂O content of the melt. Melt H₂O contents will vary as a function of pressure, temperature and degree of melting. As the dry solidus increases steeply with pressure more H₂O is required in the melt to depress the melting temperature to the adiabat. As the melt is only stable as a

result of the presence of H₂O, the amount of melt formed at a given P and T will be a function of the total H₂O in the system (Hirschmann et al., 2009). If the amount of H₂O increases, the melt fraction will increase at a given P and T but the melt H₂O content will remain relatively unchanged except in the concentration of other highly incompatible elements. With increasing temperature the amount of H₂O required to stabilize the melt will decrease. As a result the H₂O content of coexisting minerals will decrease assuming that the H₂O mineral melt partition coefficients remain approximately constant. In summary, it is clear that the ability to describe $D_{H_2O}^{\text{min/melt}}$ and melt H₂O contents as a function of P and T are integral to the understanding of mineral H₂O contents in the mantle. In addition, these parameters control the proportion of melt formed in the mantle with depth. Currently there are no constraints on the amount of H₂O required to stabilize melts at pressures above 3 GPa. This means, for example, that estimates for the pre-eruptive volatile content of H₂O rich magmas such as group II kimberlites is also unknown.

Fig. 1.11 demonstrates how the presence of H₂O in the mantle can extend the region of melting beneath mid ocean ridges, creating relatively small degree melts that can still have important implications for mantle geochemistry and geophysics. These melts can contribute to the heat transfer between mantle and surface, the redistribution of volatiles during melting can influence mantle properties such as rheology and electrical conductivity and they cause extraction of volatiles from larger volumes of the mantle compared to those from which the main phase of mantle melting occurs, at depths < 60 km. In addition, because small degree melts extract highly incompatible elements from the mantle they cause high levels of chemical fractionation (Wyllie, 1977; Eggler, 1978; Falloon and Green, 1989; Stolper and Newman, 1994; Gaetani and Grove, 1998; Wyllie and Ryabchikov, 2000; Asimow and Langmuir, 2003). In order to understand the cycling of volatiles in the Earth's interior, accurate investigations of the effects that water and other volatiles have on mineral phases and melting processes, at mantle conditions, are essential.

1.7.2 The effects of H₂O on melting in simple systems

H₂O depresses the silicate solidus but deriving thermodynamic relationships to describe this depression is extremely complex in natural chemical systems due to the high number of potentially influential components. H₂O rich melts of mantle peridotite do not quench to glasses above 3 GPa so the original H₂O content is very difficult to determine. Some idea of the effects

of H₂O on melting can be gained by studying simplified chemical systems (e.g. Inoue, 1994). Thermodynamic description of simplified systems can provide some insight into the microscopic behavior of H₂O in silicate melts (Silver and Stolper, 1985), which can potentially guide more complex models. In Fig 1.12 (left) the phase relations of Mg₂SiO₄ melting in the presence of H₂O are shown after the experiments of Hodges (1974).

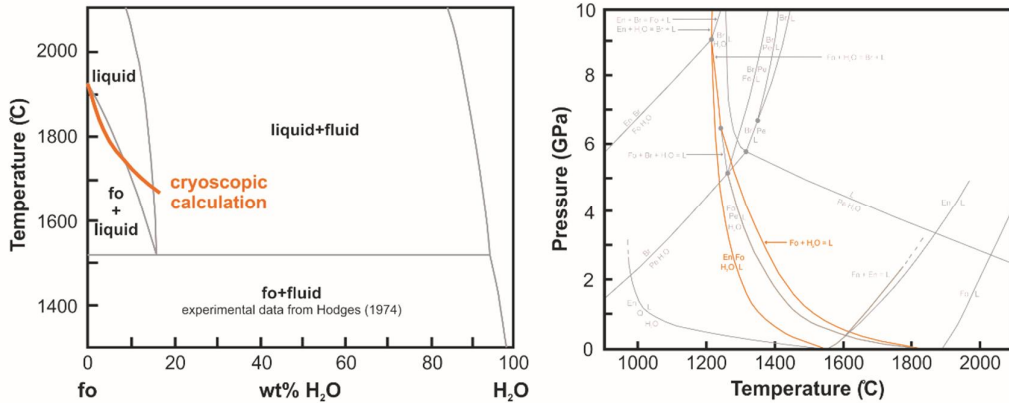


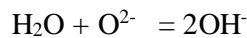
Fig. 1.12: (Left) Melting phase relations of Mg₂SiO₄ as a function of H₂O content at 1 GPa. (Modified after Hirschmann, 2006 and Hodges, 1974). (Right) Phase relations of H₂O saturated phases in the system MgO-SiO₂-H₂O. H₂O saturated melting curves for forsterite and enstatite are shown. (Modified after Ellis and Wyllie, 1979).

The liquidus temperature of forsterite is depressed as the proportion of H₂O in the melt increases. Ultimately a fluid saturated eutectic is reached where forsterite and melt coexist with fluid. The highest melt H₂O content is reached at this point of fluid saturation and it is ~17 wt % H₂O at 1 GPa. The fluid phase is also predicted to contain a proportion of dissolved silicate (<5 wt %). Fig. 1.12 (right) shows estimate for the temperature of the H₂O saturated melting point of Mg₂SiO₄ proposed by Ellis and Wyllie (1979). This is seen to decrease to 1250 °C with increasing pressure to 7 GPa as a result of the increasing solubility of H₂O in the melt. The cryoscopic melting equation can in principle be used to describe the melting depression due to the presence of H₂O, i.e.:

$$\ln X_{Fo}^{liq} = -\frac{\Delta_{fus}H}{R} \left(\frac{1}{T} - \frac{1}{T_m} \right)$$

where X_{Fo}^{liq} is the mole fraction of Mg₂SiO₄ in the melt, $\Delta_{fus}H$ is the enthalpy of fusion for end member Mg₂SiO₄ and T_m is the dry melting temperature of forsterite. $\Delta_{fus}H = Tm \cdot \Delta_{fus}S$

where the entropy of fusion $\Delta_{fus}S$ has been determined at 1 bar to be $\sim 52.7 \text{ JK}^{-1}\text{mol}^{-1}$ (Navrotsky et al. 1989). If the melt is considered to be a simple mixture of Mg_2SiO_4 molecules and H_2O , the cryoscopic approximation results in the red dashed curve in Fig. 1.12 (Hirschmann, 2006), which is a poor fit to the data. There are instead a number of variables that must be considered in developing a suitable melting model. Mixing may not involve Mg_2SiO_4 units, for example, but could be equally considered to arise from mixing of $\text{MgSi}_{0.5}\text{O}_2$ molecules with H_2O . However, as pointed out by Silver and Stolper (1984), H_2O in the melt will likely dissociate and react with oxygen from the silicate forming the equilibrium,



where the O^{2-} atoms are not associated with H and therefore describe the activity of the silicate component in the melt, which is an ideal mixture of all 3 components. The silicate activity will depend, therefore, on the number of oxygens in the silicate on which protonation can potentially occur and the degree of dissociation of H_2O , which can be described with an equilibrium constant K i.e.:

$$K = \frac{(X_{\text{OH}^-}^{\text{melt}})^2}{(X_{\text{H}_2\text{O}}^{\text{melt}})(X_{\text{O}^{2-}}^{\text{melt}})}.$$

The attraction of this treatment is that spectroscopic evidence for the magnitude of K , the equilibrium constant, can be potentially gained from analysis of silicate melt glasses through FTIR (Zotov and Keppler, 1998). In situ studies in the diamond anvil cell indicate that there are significant differences between H_2O speciation in glasses and melts (Shen and Keppler, 1995). These in situ analyses, however, provide independent justification and constraints for the model of Silver and Stolper (1984) such as a determination for the temperature dependence of K . Results from the studies of Zotov and Keppler (1998) and Shen and Keppler (1995) are displayed in Fig. 1.13.

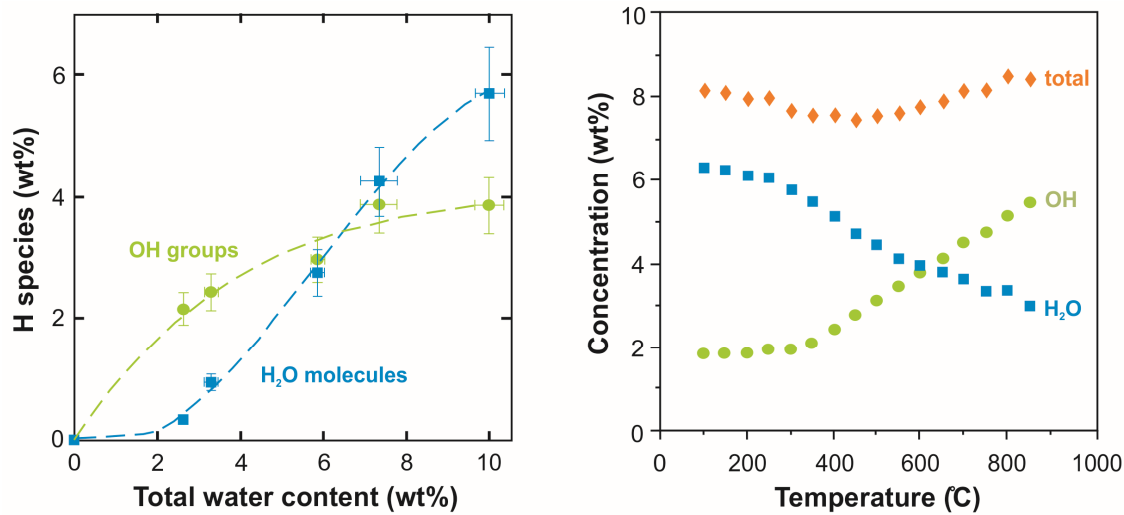


Fig. 1.13: (Left) The variation with total H₂O content of the concentrations of OH groups and H₂O molecules in hydrous Na₂Si₄O₉ glasses (Source: Zotov and Keppler, 1998). (Right) In situ measurements of the speciation of 8.1 wt % H₂O in hydrous sodium aluminosilicate glass (Modified after Shen and Keppler, 1995).

From studies of simplified silicate-H₂O systems at high pressure, general models for the effect of H₂O on silicate melting can be developed and potentially extended into more complex systems. By combining such models with mineral melt H₂O partition coefficients, a complete description of the distribution of H₂O between mantle phases could be obtained.

1.8 Geophysical effects of H₂O in the mantle

The presence of H₂O in minerals and melts in the mantle can influence a range of geophysical properties. H defects in minerals are thought to influence electrical conductivity of the mantle (for a review, see Yoshino and Katsura, 2013). H defects also influence elastic properties of minerals, lowering their seismic velocities (e.g. Jacobsen et al., 2008). This may explain regions of low seismic velocity detected in the mantle although these regions might also arise due to the formation of small degree volatile bearing melts (e.g. Tauzin et al., 2010). The presence of H defects in minerals also influences their rheological properties potentially lowering the viscosity of the mantle as the H₂O content increases (Hirth and Kohlstedt, 1996; Karato and Jung, 1998). This, for example, has been argued to explain the difference in viscosity between the lithosphere and asthenosphere, with the lithosphere being mainly dry due to melting. However, Mierdel et al. (2007) have also pointed out that changes in the solubility of H₂O in orthopyroxene as a result of a decrease in the Al content with depth might cause exsolution of H₂O and mechanical weakening of the asthenosphere due to partial melting.

Karato and Jung (2003) performed deformation experiments to determine the lattice preferred orientation fabric developed in olivine as a function of various parameters (Fig. 1.14).

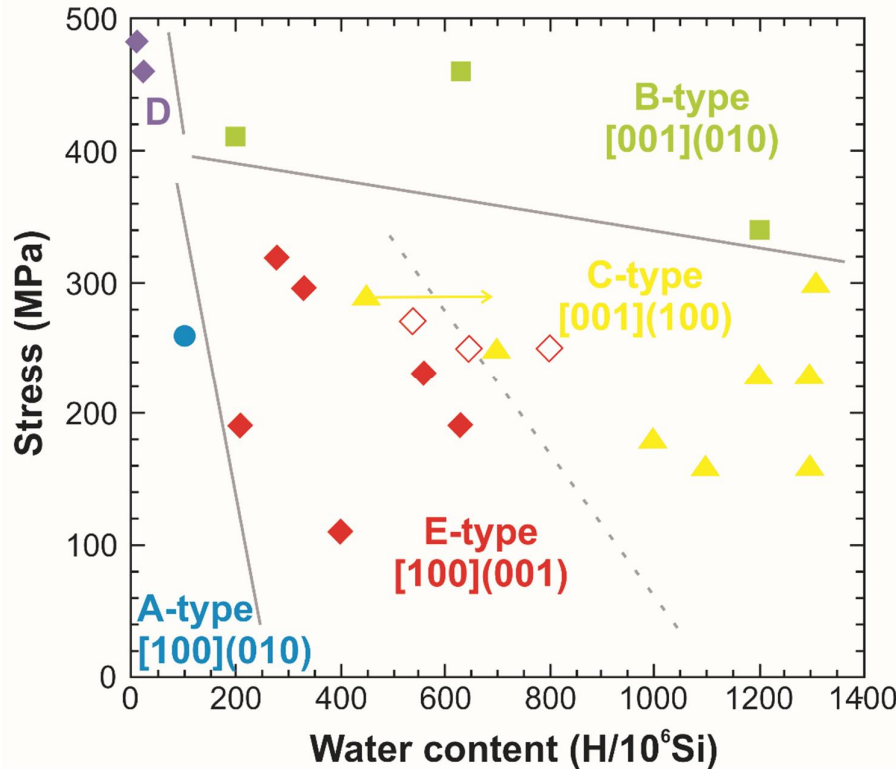


Fig. 1.14: Dominant olivine slip systems as a function of deviatoric stress and water content. (Modified after Karato et al., 2008).

When deformation occurs through dislocation creep, the alignment of olivine aggregates relative to an applied horizontal shear stress will depend on the dominate slip system of the active dislocations. Karato and Jung (2003) found that this dominant slip direction depends strongly on the concentration of dissolved H defects in olivine. For reasonable ranges of mantle H_2O contents the dominant fabric varies from A to E to C-type. For each fabric a different orientation of olivine mineral grains is expected relative to the shear direction. Because olivine elastic properties are anisotropic this will cause variations in the seismic anisotropy of the mantle due to the H_2O concentration. Karato and Jung (2003) used this experimental observation to explain differences in shear wave splitting of seismic waves in the mantle above subduction zones and were able to interpret the observations in terms of variations in stress, H_2O content and flow direction of the mantle. Because these variations in fabric depend so strongly on mantle H_2O content, they are perhaps one of the most sensitive remote indicators of the concentration of water in the mantle.

1.9 Aims of the thesis

Against the background outlined above this thesis is aimed at determining the interaction between silicate minerals and volatile-bearing melts at depths corresponding to the Earth's deep upper mantle (>100 km). The major aims of this thesis are focused on the role that H₂O, the major volatile in the Earth, has on melting processes at upper mantle conditions and a number of issues were explored following different approaches:

1. Firstly, the aim was to determine the chemical composition of hydrous melts in equilibrium with upper mantle peridotite at depths in the mantle where deep melts such as kimberlites originate ($\times 180$ km) and where incipient melting may occur beneath mid ocean ridges. The challenge in this investigation was to determine the H₂O content of melts that are in equilibrium with mantle peridotite assemblages, which is made difficult because melts do not quench to glasses that can be directly analyzed for H₂O at these conditions. Using this data models for the depression of melting due to H₂O can be tested or developed. An additional aim was to examine if there was an effect of H₂O on the composition of silicate melts in peridotitic systems.
2. A second aim was to determine the H₂O contents of upper mantle NAMs in peridotite assemblages in equilibrium with hydrous melts. Using these results the H₂O storage capacity in the mantle can be assessed and partition coefficients for H₂O between mantle peridotite minerals and small degree melts can be determined. With the data gathered in this study, hydrous melting proportions in the Earth's mantle can be quantitatively addressed as can the partitioning of H₂O between mantle minerals.
3. A third aim was to develop a predictive and quantitative model for the effect of pressure on the depression of melting in silicates systems due to H₂O. This was to be achieved by studying melting phase relations in simplified Mg₂SiO₄-H₂O and MgSiO₃-H₂O systems at conditions of the deeper upper mantle (6 and 13 GPa). Thermodynamic calculations based on such data allow models to be developed for the effect of water on melting processes through the entire upper mantle pressure range.
4. A final aim was to determine how CO₂ effects melting phase relations and mineral-melt H₂O partitioning in simplified chemical systems at deep upper mantle conditions.

In this study the variation of mineral/melt partition coefficients of H₂O with temperature is also addressed.

Details of how these 4 issues were addressed with regards to the specific scientific background, the adopted methodologies, results and implications are reported below in the individual Chapters 3 to 6.

2. Methods

Experimental and analytical techniques employed during the course of this thesis are described in this Chapter. Additional details regarding these techniques and the conditions of individual experiments relevant to each particular study are reported separately as part of the following Chapters.

2.1 Sample synthesis at high pressure and temperature

High pressure (HP) and high temperature (HT) experiments were performed using a multianvil apparatus in order to equilibrate samples at upper mantle conditions. A multianvil apparatus comprises a hydraulic press that is capable of generating pressures corresponding to those in the lower mantle, ~25 GPa and up to 3000 K. High pressures are generated by focusing the load from the hydraulic press onto a sample within a pressure medium via two-stages of anvils. First, a hydraulic piston compresses 2 sets of hardened tool steel anvils each comprised of 3 segments mounted into opposing guide blocks, as shown in Fig. 2.1.

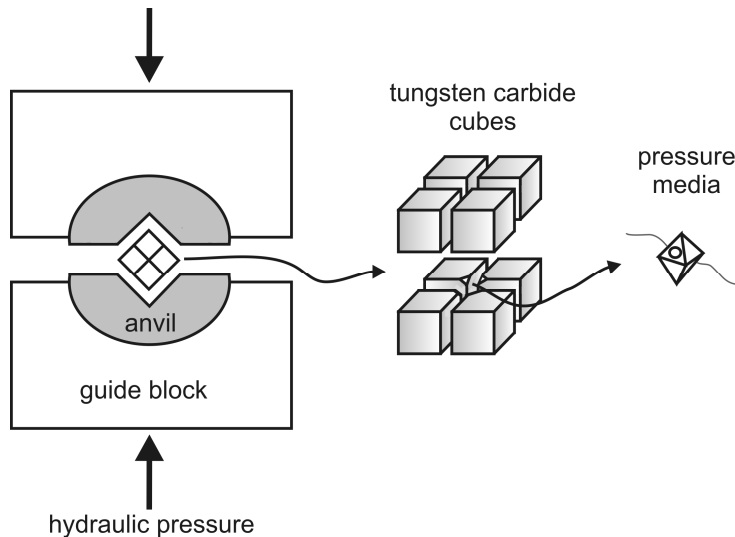


Fig. 2.1: Illustration of the multianvil apparatus with the 8 tungsten carbide cubes and the pressure media.

The steel anvils are shaped to compress a cubic chamber in which 8 cubes made of tungsten carbide are inserted, forming a second-stage system of anvils. Each of the 8 cubes has at least one corner truncation, such that when all 8 cubes are assembled an octahedral chamber is formed at the center of the anvils. An octahedral shaped pressure medium containing the sample inside a furnace is placed in this cavity. A schematic figure of a multianvil apparatus is

2. Methods

shown in Fig. 2.1 and further details regarding the history and development of the multianvil presses can be found in Keppler and Frost (2005) and Ito (2007).

The octahedral edge length (OEL) of the pressure medium and the truncation edge length (TEL) of the tungsten carbide cubes have different sizes depending on the pressure range under investigation. In the experiments described here tungsten carbide anvils with 15 and 11 mm TEL were used with pressure media with 25 and 18 mm OEL. The OEL/TEL ratio, i.e. 25/15 and 18/11, governs the size of the sample and the pressure that can be achieved in a particular experiment. The pressure media was a Cr₂O₃-doped (5 wt%), MgO octahedron which had a hole drilled through two opposing faces. In the hole, a ZrO₂ sleeve was inserted as a thermal insulator. In 18 mm assemblies used above 10 GPa the ZrO₂ sleeve was shortened and at the top and bottom two softer MgO rings were placed to compensate for the incompressibility of ZrO₂ within the MgO pressure media. Inside this sleeve, a stepped graphite or LaCrO₃ resistance heater, depending on the target P and T of the experiment, was placed. The sample, contained in a noble metal capsule (e.g. Pt or alloys such as Pt/Rh or Au/Pd) was enclosed in an MgO sleeve separating it from the heater. Noble metal capsules with 2 and 4 mm diameters were used in the 25/15 and 18/11 assemblies, respectively. Two MgO spacers were placed at the top and bottom of the MgO sleeve containing the capsule. The temperature during the experiment was controlled by a type D thermocouple (W_{3%}Re-W_{25%}Re) that was placed in a 4-hole, hard Al₂O₃ cylinder inserted in a hole drilled through one of the MgO spacers. The thermocouple junction was separated from the top of the capsule by a thin (0.25 mm thick) MgO disk or Re foil depending on the experiment (see next chapters). A cross section of an octahedral assembly is shown in Fig. 2.2.

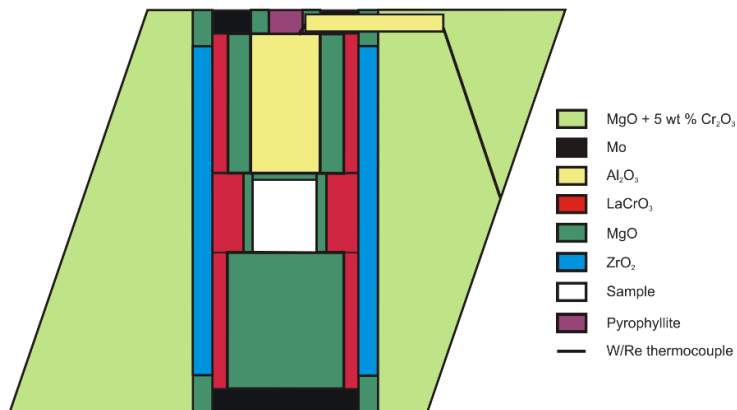


Fig. 2.2: Cross section of a 25/15 octahedron employed in the multianvil apparatus at 13 GPa.

Multianvil presses with maximum loads of 500, 1200 and 5000 tonnes installed at the Bayerisches Geoinstitut (BGI) were used to generate pressures up to 13 GPa, i.e. the depth corresponding to the base of the upper mantle. Pressure calibrations for these devices are described in Frost et al. (2004) and Keppler and Frost (2005). Pressure calibrations for both assemblies employed in this study are shown in Fig. 2.3.

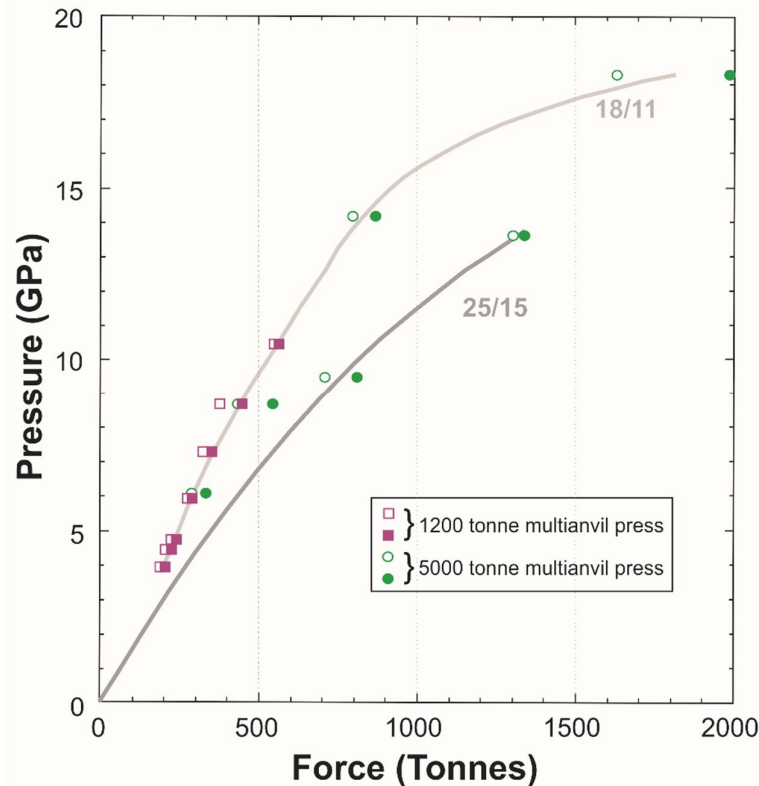


Fig. 2.3: Pressure calibration curves obtained at high temperature for 25/15 and 18/11 assemblies in the 1000 and 5000 t multianvil press. (Source: Frost et al., 2004).

The calibration of Frost et al. (2004) was confirmed by performing some further experiments at the temperature of interest (see e.g. Chapter 3 for details).

2.2 Sample characterization

2.2.1 Scanning electron microscopy

Scanning electron microscopy (SEM) measurements were performed on most of the experimental charges in order to identify mineral phases and to determine semi-quantitatively

the mineral compositions. Samples were mounted in epoxy and polished on one side to a surface finish of ~1 micron. Samples were then coated with ~10 nm of carbon. In a scanning electron microscope, electrons are generated from an electron gun and are focused and collimated on the sample using a number of magnetic lenses and apertures. Images are obtained by scanning an electron beam on the polished sample surface. When the electrons hit the sample surface they interact with the atoms of the target material producing different types of secondary emissions. Secondary electrons (SE), for example, have low energy and are emitted from a very thin layer at the sample surface. Their intensity consequently depends on the surface features of the sample and therefore they provide images with important topographic information. Backscattered electrons (BSE) have higher energy than SE and are produced by elastic interactions between the electrons and the atoms of the sample. BSE images are strongly dependent on the atomic number of the target sample and are, therefore, useful in that they provide a sample image with brightness that is a function of atomic mass. An example of a BSE image of a typical experiment taken at the SEM is shown in Fig. 2.4.

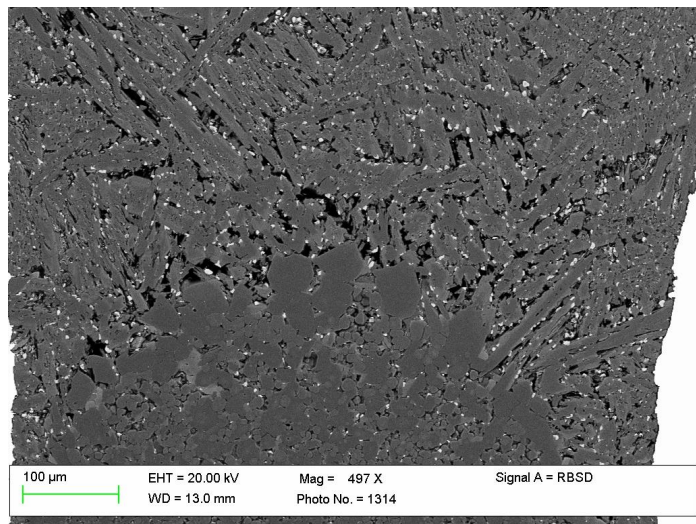


Fig. 2.4: BSE image taken at the SEM and showing crystals of orthopyroxene (dark), clinopyroxene (light) and garnet (grey with round shape and high relief) at the bottom of the capsule. These crystals segregated from the melt which quenched to form the fibrous crystals at the top of the image.

Even though the SEM is optimized for imaging analyses, it is also equipped with an x-ray spectrometer that can be used to determine qualitative chemical compositions of mineral phases. When the electrons of the focused beam hit the sample they can remove electrons from the inner shells. As a consequence, electrons from the outer shell fill the vacancy formed by the ejected electron in the inner shell and the energy difference is released as a characteristic

x-ray. X-rays of all energies, distinctive for each element present in the target sample, can be simultaneously collected in energy dispersive (ED) mode and provide qualitative, and semi-quantitative, chemical analyses. A thorough review of the SEM technique can be found in Reed (2005).

SEM analyses were performed in this study by means of a LEO Gemini 1530 SEM at the BGI, which is equipped with a Schottky type electron gun. In analyses performed in this study an accelerating voltage of 20 kV was generally employed allowing a spatial resolution of $\sim 1\text{nm}$.

2.2.2 Electron microprobe analyses

Electron microprobe analyses (EMPA) were conducted on all the experimental charges produced in the multianvil experiments in order to accurately determine the chemical composition of the product mineral phases. EMPA is very similar to SEM but is used to conduct precise quantitative analyses of major and minor components of solids instead of imaging analyses. An electron beam is produced by a tungsten filament and is accelerated toward the sample after being focused and collimated, similarly to the SEM (see section 2.2.1). The characteristic x-ray photons emitted by a particular element upon the interactions between the electron beam and the target material can be collected not only by an ED spectrometer (EDS) but also by wavelength dispersive spectrometers (WDS). For WDS analyses, characteristic x-rays from the sample are selected based on their wavelength using Bragg reflections from crystals with known interplanar spacings (d). Measurements of characteristic x-ray emissions with different wavelengths require the use of various crystals with different d spacings such as synthetic LiF, PET or TAP crystals (see e.g. Reed, 2005). Precise quantitative analyses are made possible by comparing the intensities of the characteristic x-rays emitted by the sample with those emitted by standards with known composition. Standards materials employed in this study were natural or synthetic crystals (e.g. of forsterite and enstatite) and metals (e.g. Fe). High accuracy is attained since the limit of detection of EMPA can be as low as tens-hundreds of ppm wt. The analyses are performed under vacuum conditions of $\sim 7 \times 10^{-6}$ Torr. A precise description of EMPA is reported in Reed (2005).

In this study the chemical composition of crystalline phases was determined by means of a JEOL JXA-8200 electron microprobe installed at the BGI which is equipped with 5 WDS. A focused spot mode was used in order to analyze small crystals (down to $20\text{ }\mu\text{m}$ across) present

on the surface of the polished sample and a beam of 1-2 μm diameter was used. Corrections were applied to the raw intensity values to account for electron energy loss and backscattering in the sample volume in addition to absorption and fluorescence corrections (e.g. ZAF) in order to reduce the analyses (see following Chapters for details).

2.2.3 Raman spectroscopy

Raman spectroscopy is a commonly used technique in chemistry and Earth Sciences since it allows quick identification of mineral phases. Raman spectroscopy is based on the Raman effect, which results in the inelastic scattering of light due to vibrations of molecules in an illuminated material. Monochromatic light, normally produced by a laser in the visible range, is focused on the area of interest. Some of the incident beam can interact with the fundamental vibrational frequencies typical of the investigated material, and when this happens molecules are excited from a ground state to a virtual energy state. The scattered light can therefore lose or gain energy upon interactions with the investigated material. If a minor increment of the vibrational energy of the molecule occurs, the incident light loses energy and this phenomenon is referred to as Stokes Raman scattering. At the same time, if a small loss of vibrational energy occurs, the scattered light will gain energy and this is called Anti-Stokes Raman scattering. The Stokes and Anti-Stokes vibrational frequencies are respectively shifted to lower and higher energies of the Rayleigh scattering i.e. light that is scattered without a change in energy. The light scattered from the sample is collected by lenses and passed into a spectrometer. A typical Raman spectrum plots intensity versus energy where each peak corresponds to a vibrational frequency in the particular sample.

Analyses in this study were conducted on a number of experimental charges in order to distinguish between different polymorphs of a characteristic mineral at a particular pressure (e.g. forsterite and wadsleyite, see Chapters 5 and 6). Raman spectra were collected at BGI by means of a LABRAM Raman spectrometer equipped with a microscope in order to investigate small areas of a particular sample (several μm in diameter). This Raman setup is equipped with a He-Ne laser with 632 nm red line wavelength. Measurements were conducted in air at room temperature, with a resolution of $1-2 \text{ cm}^{-1}$ and collecting 3 accumulations of 15 seconds each. In order to identify a particular phase, the obtained spectra were compared to those reported in the RUFF database (Downs, 2006).

2.2.4 Laser ablation inductively coupled plasma mass spectrometry

Laser ablation inductively coupled plasma mass spectrometry (LA-ICP-MS) was also performed on many multianvil experiments in order to obtain melt compositions from heterogeneous assemblages of quenched crystals. This widely used technique is extremely useful in order to determine the chemical concentration of elements and isotopes down to ppm wt, or even ppb wt, level. A LA-ICP-MS comprises an ablating laser, a plasma generator and a mass spectrometer. A 193 nm ArF laser beam is commonly employed, which is focused on the sample that is contained in an air tight chamber, causing material to be ablated from the targeted zone. The ablated material is transported by a carrier gas mixture of He with trace amounts of H₂ into the ICP torch that consists of 3 concentric quartz tubes. In the ICP torch, Ar gas is energized by inductive heating using an electromagnetic coil and extremely high temperatures (5000-7000 °C) are reached, causing the production of plasma. As a result the atoms of the sample aerosol are first converted into a gas and then into ions by the ICP discharge. The ions of the plasma are focused by a system of electrostatic lenses and passed into the mass spectrometer for element characterization. For this purpose a quadrupole mass spectrometer is normally employed, where ions are separated based on the ratio of their mass and charge by a quadrupole mass filter. This comprises 4 rods which create an oscillating electric field within a vacuum of approximately 1×10^{-5} Torr. The electric field is adjusted such that it allows only ions with a specific mass/charge ratio to travel to the detector at a specific time, with all other ions being deflected and lost through rods. The electric field can be changed at a very high rate allowing quasi simultaneous measurements of a high number of elements to be collected in a very short period of time. A more detailed overview of LA-ICP-MS applied to the Earth Sciences can be found for example in Sylvester (2008).

In this study, LA-ICP-MS was used to accurately determine the chemical composition of heterogeneously quenched melts produced in some of the high pressure experiments (see Fig. 2.4). LA-ICP-MS measurements were performed at the BGI by means of the LA-ICP-MS setup as described above. Hydrous melts from pressures above 3 GPa quench to a mass of crystals with different morphologies and sizes. Some of these quench crystals can be more than 100 microns in size, which means that large sample areas need to be analyzed in order to obtain representative averages. The electron microprobe beam can be opened or scanned over a wide area to average the composition of these regions; however the topography of the surface causes

2. Methods

large uncertainties and mass balance calculations, as described in Chapter 3, result in high residuals.

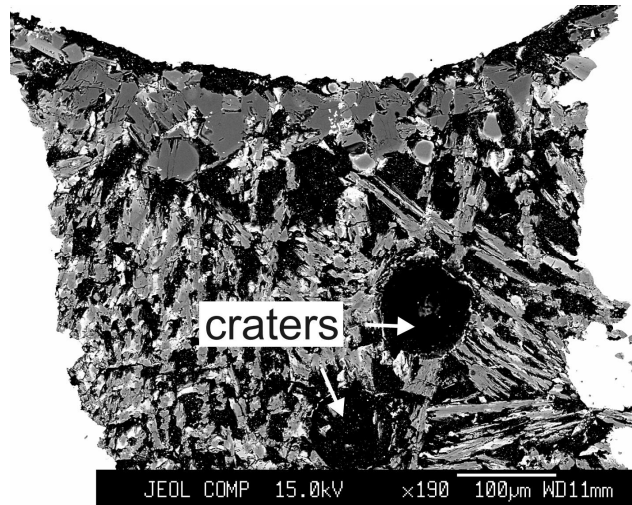


Fig. 2.4: BSE image of a polished charge containing mineral phases (at the very top) in equilibrium with a large pool of quenched material resembling a melt phase at HP-HT. It can be seen that the melt does not quench to a glass but instead crystallizes to form fibrous, heterogeneous crystals. The dark circles are the craters produced by the LA-ICP-MS analyses. The bright material surrounding the experimental charge is the noble metal (Au/Pd) capsule employed in this particular experiment.

A comparison of analyses performed on melt determined by LA-ICP-MS and EMPA from the same experimental run is reported in Table 2.1.

Table 2.1: comparison between EMPA and LA-ICP-MS analyses

	opx		melt			LA-ICP-MS (70 µm)
	EMPA	LA-ICP-MS	EMPA (10 µm)	EMPA (20 µm)	EMPA (30 µm)	
SiO ₂	56.68 (22)*	56.30	52.25 (2.97)	51.14 (1.80)	46.59 (46)	42.74
Al ₂ O ₃	2.35 (34)	2.68	6.38 (84)	7.18 (1.32)	7.52 (71)	8.38
CaO	1.27 (11)	1.40	5.51 (2.36)	6.10 (2.29)	8.70 (1.02)	9.21
FeO	4.36 (21)	4.32	6.26 (83)	6.90 (53)	8.97 (1.21)	9.74
NiO	0.08 (2)	0.08	0.09 (4)	0.09 (2)	0.06 (2)	0.05
MgO	34.67 (29)	34.62	27.85 (2.53)	26.83 (2.92)	25.40 (1.13)	26.20
Na ₂ O	0.25 (2)	0.29	0.92 (30)	0.98 (49)	1.50 (36)	2.29
Cr ₂ O ₃	0.22 (5)	0.19	0.31 (6)	0.25 (4)	0.21 (2)	0.14
TiO ₂	0.03 (2)	0.03	0.22 (16)	0.32 (16)	0.65 (15)	0.77
MnO	0.08 (3)	0.09	0.13 (5)	0.12 (5)	0.17 (3)	0.17
K ₂ O	0.01 (1)	0.00	0.08 (10)	0.09 (11)	0.23 (10)	0.30
Total	100.00	100.00	100.00	100.00	100.00	100.00

*: number in parentheses are 1 standard deviations based on 10-15 analyses, in reference to the last digit

In Table 2.1 analyses for both orthopyroxene crystals and heterogeneously quenched silicate melts using both EMPA and LA-ICP-MS are shown. All analyses are normalized to 100 % for comparison purposes. Very good agreement is observed between the 2 analytical techniques when crystals of orthopyroxene are measured. Orthopyroxene crystals were measured using a nominal 1 μm spot beam for EMPA but LA-ICP-MS analyses ablated the sample over a 20-30 μm diameter region. However, very poor agreement is observed between the 2 techniques when measurements are carried out on the heterogeneously quenched melt. Due to the large quench crystal size the EMPA beam diameter must be increased to provide a suitable average analysis of the melt. As the beam diameter is increased the EMPA analyses for most elements vary in the direction of the LA-ICP-MS analyses but elements remain significantly different even at an EMPA beam diameter of 30 μm . Although analyses have been normalised to 100 % the original microprobe totals remain around 99 % up to a beam diameter of 20 μm . However for larger beam diameters microprobe totals start to decrease and are only 94 % at 30 μm . The quality of the analyses, therefore, starts to degrade at very large beam diameters. Because the melt being analysed in Table 2.1 comprised over 90 % of the sample, mass balance residuals using the known bulk composition and compositions of melt and mineral phases can be used to assess the quality of the melt analyses. Mass balance residuals are large for most elements when EMPA melt analyses are employed. The smallest mass balance residuals were obtained for melts analysed using LA-ICP-MS and employing the largest possible laser pits of up to 80 μm .

In general EMPA seems to overestimate SiO_2 melt contents and underestimate the proportion of alkalis in the melt. This is likely due to the topography of the surface produced during polishing, which may preferentially pluck weaker smaller mineral phases from the surface. As the LA-ICP-MS measurements excavate down to >30 μm from the surface the analysis is more reflective of the bulk material. An example of such a measurement is displayed in Fig. 2.4. Quantitative LA-ICP-MS analyses were calibrated using an external NIST 610 glass standard, employing the concentrations reported by Spandler et al. (2011) and internal standardization was conducted by normalizing to 100 wt % the sum of the oxides.

2.2.5 Secondary ion mass spectrometry

Secondary ion mass spectrometry (SIMS) is one of the most sensitive surface analysis techniques. It is particularly powerful for the measurements of low contents of light elements

such as H and C in solids. A schematic representation of the ion probe employed in SIMS measurements described here is shown in Fig. 2.5.

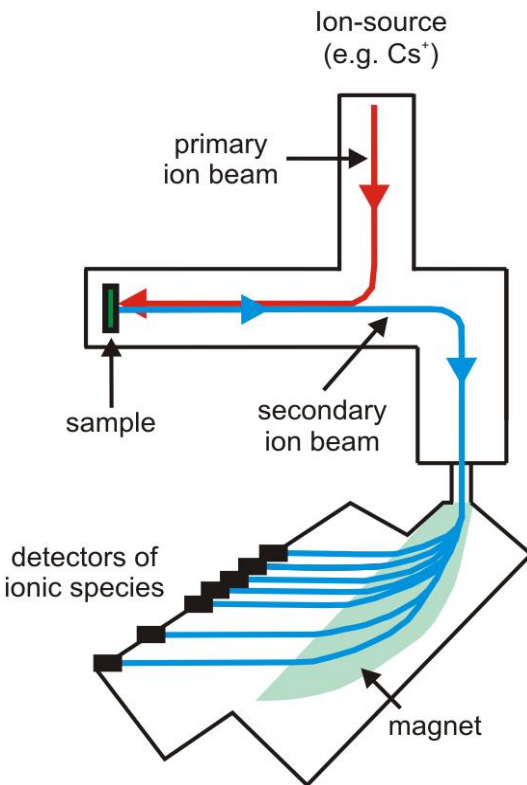


Fig. 2.5: Simplified diagram of a Cameca nanoSIMS 50L employed in this study.

In a SIMS ion probe, a primary ion beam is generated by an ion gun in the primary ion column. Different ion beams (e.g. Cs^+ , O^-) can be used depending mainly on the elements to be analyzed. In the primary ion column, the ion beam is accelerated and focused with a set of lenses onto the polished surface of the sample, which is mounted into the sample holder under an extremely high vacuum ($\sim 2 \times 10^{-10}$ Torr). All operations are conducted under high vacuum in order to limit the scatter of ions by residual gas, suppress the background of the instrument and decrease the contamination from gas species present on the sample surface. When the focused, primary ion beam hits the sample it sputters and partially ionizes material, forming a crater at the target area (Fig. 2.6).

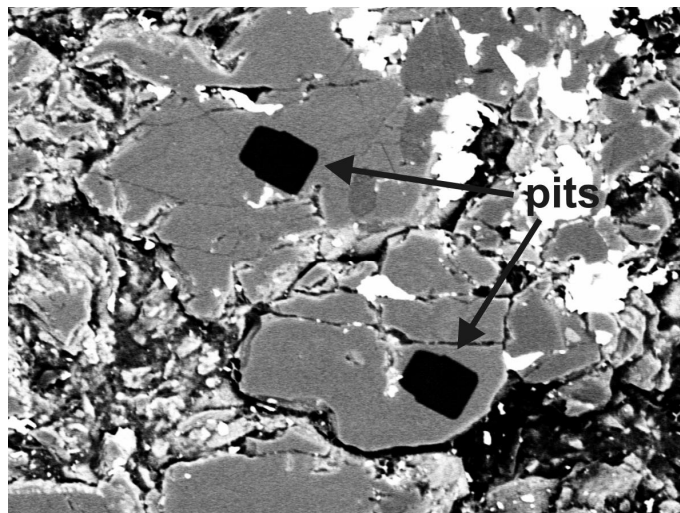


Fig. 2.6: BSE image of a polished experimental charge showing pits formed after nanoSIMS analyses on the minerals clinopyroxene (top-left) and garnet (bottom-right). The width of the picture is approximately 250 µm.

The depth of the forming pits depends on the properties of the analyzed sample and the conditions of current and beam size employed. In the analyses performed in this study the sputtered regions were approximately $25 \times 25 \mu\text{m}^2$ and reached a depth of few microns. A number of neutral and charged atoms and molecules are produced upon sputtering. Secondary ions are extracted by applying an accelerating voltage to a charged extraction plate. Depending on the analyses, positive or negatively charged ions can be extracted from the sputtered area and then focused by ion optics. The secondary ions are subsequently filtered according to their nominal mass (mass/charge ratio) by the electromagnet of a mass spectrometer, and are eventually counted by a detector (Faraday cup or by electron multipliers).

In this study, SIMS was used in order to determine the H contents of nominally anhydrous minerals produced in the multianvil experiments. Analyses were performed at the Department of Terrestrial Magnetism using a Cameca nanoSIMS 50L ion microprobe, optimized for high spatial resolution, sensitivity and mass resolution. Negative ions ($^{12}\text{C}^-$, $^{19}\text{F}^-$, $^{30}\text{Si}^-$ and $^{16}\text{OH}^-$) were collected in the analyses. $^{16}\text{OH}^-$ signals from olivines, pyroxenes and garnets produced in the multianvil experiments were measured, allowing the determination of their H_2O contents. SIMS is a comparative technique and reference materials are therefore needed in order to provide quantitative analyses. Reference minerals with known H contents described by Koga et al. (2003) were used in this regard. Individual standards of H-bearing olivine, clinopyroxene, orthopyroxene and garnet with known concentrations of H_2O (Koga et al., 2003) were

measured at the beginning and during each session, and calibration curves were obtained by linear fitting of the collected data (Fig. 2.7).

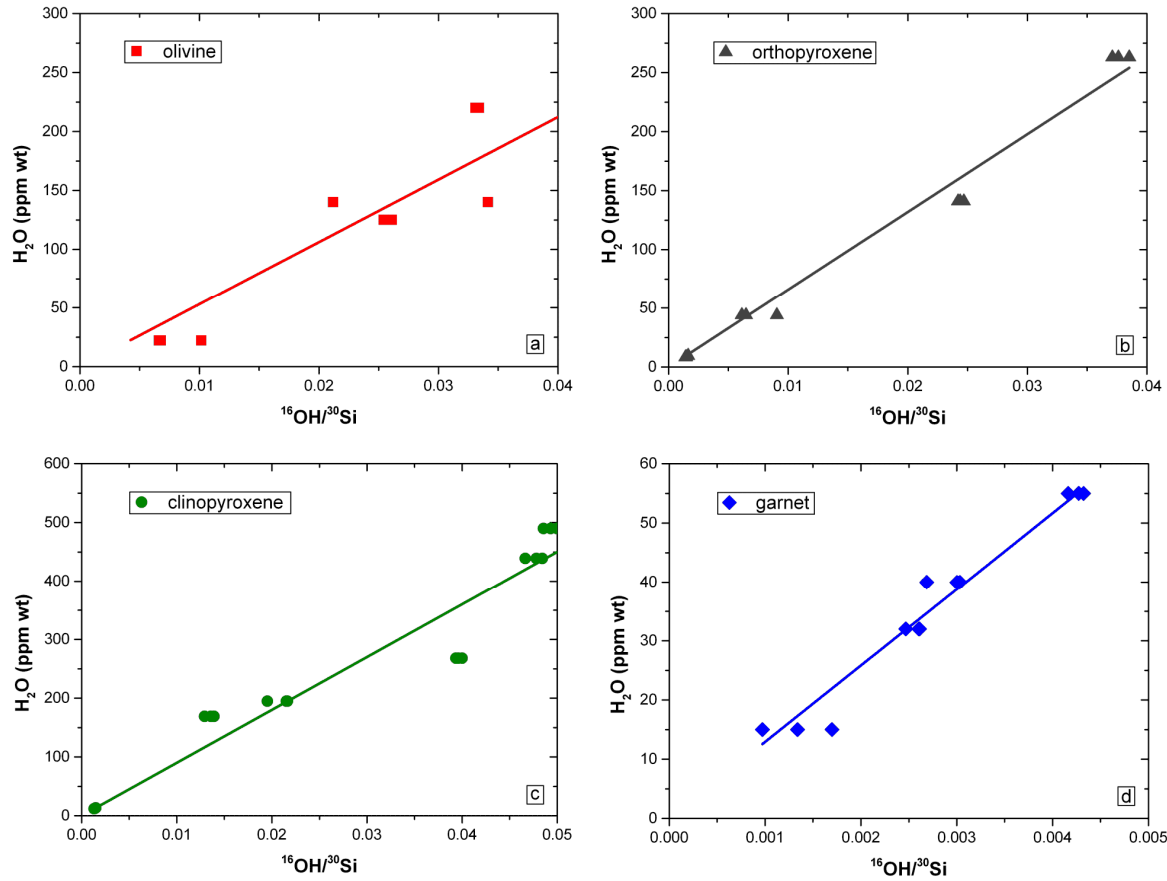


Fig. 2.7: NanoSIMS calibration curves for olivine (a), orthopyroxene (b), clinopyroxene (c) and garnet (d) from a single nanoSIMS session. Calibrations (lines) are obtained by linear regression of the $^{16}\text{OH}/^{30}\text{Si}$ signal obtained by the ion probe using the known water concentrations of the standard minerals.

Using the slope of the fitted calibration curves the H₂O contents of minerals were calculated based on the measured mineral $^{16}\text{OH}/^{30}\text{Si}^-$ ratios.

In order to conduct precise quantitative determination of low amounts of H in nominally anhydrous minerals (tens of ppm wt), paramount are the sample preparation and the standards. In particular, polished samples require a very fine preparation (e.g. roughness of the surface should be below $\pm 20\text{nm}$) in order to obtain a low detection limits. In this study the sample preparation procedure described by Koga et al. (2003) was adopted. To perform low-blank H measurements, the polished samples were removed from the epoxy holders after chemical characterization and mounted in a hole drilled on an aluminum disc filled with indium so that H-bearing epoxy was avoided in the preparation of the samples. A detailed description of the

sample preparation and analytical procedures adopted in this study can be found in (Koga et al., 2003). Further information regarding the investigated samples and the conditions of the analyses are reported in Chapters 4 and 6.

2.2.6 Elastic recoil detection analyses

Elastic recoil detection analyses (ERDA) were performed on some samples in order to provide an independent confirmation of mineral H contents. ERDA is an ion beam technique which in fact can provide absolute determinations of light element concentrations such as H in solids that are independent of calibrant materials. It is a relatively uncommon technique in Earth Sciences as it requires the use of a particle accelerator, i.e. a central large scale facility. ERDA is performed with a ${}^4\text{He}^+$ (3 MeV) beam, generated by a single stage Van de Graaf particle accelerator, which is focused down to $4 \times 4 \mu\text{m}^2$ on the polished surface of a sample using quadrupole magnetic lenses. Several types of secondary emissions occur due to the interaction of the ion beam with the sample matrix and different detectors positioned in the sample chamber allow simultaneous measurements of these emissions during the analyses. A simplified overview of the analyses chamber setup is displayed in Fig. 2.8.

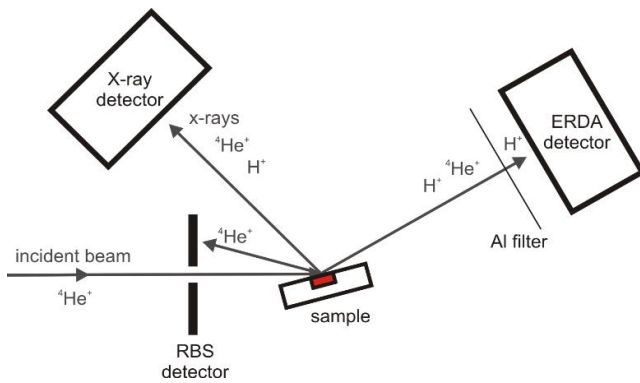


Fig. 2.8: Schematic representation of an ERDA analysis chamber setup with the different detectors employed.

Particle induced x-rays emission (PIXE) is a method employed for the analyses of trace elements. This technique provides information on the absolute trace element concentration ($14 < Z$) based on the analysis of the X-rays emitted by the target excited by the beam. The X-rays can be collected by a detector positioned at 45° from the incident beam as shown in Fig. 2.8 and are useful for distinguishing the area of interest within a particular sample. In addition, Rutherford backscattered spectrometry (RBS) is also performed by means of a charged particle annular detector. The RBS detector collects ions of the incident beam that are backscattered by

the sample surface and is positioned at 170° with respect to the incident beam (Fig. 2.8). RBS is used to determine the matrix composition of the analyzed area, and consequently the location of the crystal of interest in a specific sample. Furthermore, RBS is employed as a charge monitor of the incident beam. In fact, as a result of the tilted sample position during ERDA analysis (see later) the total electric charge deposited on the target cannot be directly measured. RBS is therefore employed to deduce the total number of incident particles on the target during acquisition, which is required to allow quantification of the H content. Additionally, when the focused beam collides with the sample surface, it interacts with H present in the sample and causes elastic recoil, ejecting the H⁺ from the sample matrix. These ejected particles are collected by an ERDA detector. An aluminium filter placed in front of the detector stops forward scattered ⁴He⁺ particles and allows only H⁺ from the sample to be counted (Fig. 2.8). Prior to the analysis of the sample H content using the ERDA configuration, the sample is positioned perpendicular to the incident beam. In this initial configuration a number of standards (e.g. Al₂O₃, CaCO₃, Kapton polyimide) are analyzed in order to determine the RBS solid angle. After this step, RBS, PIXE and ERDA are simultaneously performed with the sample tilted at a grazing angle of 15° with respect to the incident beam, as shown in Fig 2.8, in order to allow the ERDA detector to collect protons (H⁺) ejected from the sample. In this configuration, the ERDA solid angle was calibrated from the analysis of Kapton in the ERDA configuration. At these conditions, the incident beam size that is scanned over the sample becomes ~4x16 μm², and during the analyses only a small amount of H is removed from the surface of the sample (~ 2 μm depth). The acquisition is conducted by scanning the ion beam over a selected area of interest (a few tens of μm²) in order to preserve the sample from H loss by diffusion due to the incident beam.

Spectrometry on the forward recoil atoms allows quantitative analyses to be performed without the use of an external standard. Initially, the PIXE, RBS and ERDA data are processed with the RISMIN software (Daudin et al., 2003) where 2D elemental maps of the scanned area are produced. This allows the determination of homogeneous portion of the analyses which correspond to the crystal of interest. After the selection of the area of interest, the PIXE, RBS and ERDA spectra corresponding to the crystal are extracted. RBS and ERDA spectra are processed with the SIMNRA software (Mayer, 1999) in order to determine the H content of the analyzed minerals by simulating the ERDA spectra. The simulation is conducted by changing the concentration of H of the mineral until the produced fit matches the number of counts that are measured by the detector.

ERDA analyses presented here were carried out at the Pierre Sue Laboratory and a description of the setup is reported by Khodja et al. (2001). More thorough reports regarding this analytical technique and the determination of H in geological samples can be found for example in Bureau et al. (2003, 2009) and Raepsaet et al (2008). Further information regarding the analyses performed in this study can be found in Chapters 4 and 6.

3. The composition of hydrous partial melts of garnet peridotite at 6 GPa: implications for the origin of group II kimberlites

3.1 Introduction

Along an average mantle adiabat dry peridotite melts at depths shallower than approximately 50 km (e.g. Asimow et al., 2004). However, there are many clear examples in nature of melts being formed at significantly greater depths, such as kimberlites and lamproites (e.g. Moore and Gurney, 1989; Moore et al., 1991) and melts responsible for the metasomatism apparent in mantle xenoliths from cratonic lithosphere (Erlank et al., 1987). Evidence for deep melting is also apparent in diamond inclusions (Walter et al., 2008), and has in some instances been inferred from geophysical observations, both from seismic data (Song et al., 2004; Bagley and Revenaugh, 2008) and from measurements of electrical conductivity (Evans et al., 2005). It has, for example, been proposed that the seismic low velocity zone (LVZ) at the top of the asthenosphere may in part be explained by the presence of small degree volatile bearing partial melts (Lambert and Wyllie, 1968; Mierdel et al., 2007; Hirschmann, 2010; Ni et al., 2011).

H_2O and CO_2 have the potential to lower the peridotite solidus to stabilize partial melts at nominal mantle temperatures at great depths in the mantle (e.g. Kushiro et al., 1968; Mysen and Boettcher, 1975). Beneath mid ocean ridges such volatiles may extend the onset of partial melting to greater depths than expected for volatile free magma genesis (Plank and Langmuir, 1992; Asimow et al., 2004). Initial volatile-bearing small degree melts are particularly important as they may strip trace elements and volatiles from larger volumes of mantle compared to the region from which the majority of basaltic melt is extracted (Asimow et al., 2004). They will also influence estimates for the H_2O content of the mantle which are generally based on the H_2O contents of basalts coupled with an estimate for the degree of partial melting (e.g. Saal et al., 2002). To model the onset of melting in such a scenario and to investigate if melts could be responsible for the LVZ, requires specific information on several aspects of the effects of volatiles on melting. For CO_2 the redox relationship with silicate hosted ferric Fe may be a crucial factor affecting carbon participation in the initial production of melts. It has been proposed that at depths >100 km carbon may be

predominantly hosted as graphite and diamond and that oxidation to form carbonatite or a silicate melt CO₂ component is controlled by ferrous-ferric reduction which may occur only at quite shallow depths (Stagno et al., 2013). In order to model H₂O participation in deep melting requires information on the compositions of small degree partial melts in addition to the partition coefficient for H₂O ($D_{H_2O}^{\text{min/melt}}$) between the coexisting nominally anhydrous minerals and such melts (Hirschmann et al., 2009). Melt compositions, and in particular H₂O contents, are not only crucial for calculating $D_{H_2O}^{\text{min/melt}}$ but melt and residue compositions will likely also have a direct influence over $D_{H_2O}^{\text{min/melt}}$. For this reason it is important that $D_{H_2O}^{\text{min/melt}}$ is determined for realistic melt compositions, which for deep melting scenarios requires that the melts are in equilibrium with the nominally sub solidus peridotite assemblage. The likely low bulk H₂O content of the mantle (e.g. Palme and Ø Neill, 2003) means that the degree of melting caused by H₂O at pressures greater than the onset of dry melting will be insufficient to significantly perturb the major element concentration of the mantle residue. Realistic small degree melts are likely enriched in incompatible elements such as Na, K and Ti which may have an influence on $D_{H_2O}^{\text{min/melt}}$. Many determinations of $D_{H_2O}^{\text{min/melt}}$ have been made for melts that are not in equilibrium with a residual peridotite assemblage (e.g. Aubaud et al., 2004) and may therefore not be strictly applicable to modeling the onset of melting. Shifts in mineral compositions near the solidus, particularly for clinopyroxene, may also have an important influence on $D_{H_2O}^{\text{min/melt}}$.

Whereas many reliable methods exist for determining mineral H₂O (hydroxyl) contents, the determination of melt H₂O contents is experimentally more challenging. To date no studies exist through which to reasonably estimate the H₂O content of melts saturated by a peridotite assemblage at pressures above 3.5 GPa. This is a major barrier to our understanding of the effect of pressure on hydrous melting and it is mainly caused by the difficulties in performing such experiments. One of the main problems is that at pressures above 3 GPa, melts of the appropriate composition do not form glasses on quenching but instead form an assemblage of quench crystals (Walter, 1998; Tenner et al., 2011). These crystal mats are difficult to analyze in terms of major elements due to heterogeneity, large grain size and porosity but are totally impossible to analyze in terms of H₂O content using spectroscopic or ion probe techniques. Most of the H₂O from the original liquid is unlikely to be locked into the prepared surface of the quenched sample. Some studies have attempted to provide estimates of quenched

crystallized melt H₂O contents using the deficit in electron microprobe analysis totals (e.g. Ohtani et al., 2000) but any number of reasons might be cause for the resulting low analysis totals such that this cannot be considered an acceptable method. The only reliable technique for determining melt H₂O contents in the absence of quenched glasses is therefore to perform a mass balance based on analysis of major elements in the run products compared with the original starting material. However, such a treatment also raises further problems. The uncertainties on the concentrations determined through mass balance for a small degree melt would be extreme and variable loss of H₂O from the experimental capsules during heating would significantly bias the result. Further more, the infiltration of carbon through metal capsule walls that has been observed in many experiments (Brooker et al., 1998; Liu et al., 2006; Balta et al., 2011) would invalidate the entire mass balance methodology as it can produce an unquantifiable amount of CO₂ in the melt phase.

One approach to estimating melt H₂O contents at high pressures and temperatures is to develop a generalized model for the effect of H₂O on suppressing the peridotite solidus (Hirschmann et al., 2009; Hirschmann, 2010). While this is a very promising methodology it ignores likely effects that H₂O has on influencing the composition of silicate melts in equilibrium with mantle residues. In addition, very few reliable data exist through which to calibrate such models at pressures above 3 GPa. A large number of studies have been performed to examine the effect of H₂O on peridotite partial melting at pressures > 3 GPa (e.g. Hirose and Kawamoto, 1995; Hirose, 1997; Balta et al., 2011; Tenner et al., 2012). In the spinel-peridotite field the overriding effect of adding H₂O seems to be an apparent increase in the melt SiO₂/(MgO+FeO) ratio (Hirose and Kawamoto, 1995; Hirose, 1997; Gaetani and Grove, 1998). A similar effect was recently reported for small degree melts of garnet peridotite at 3 GPa (Balta et al., 2011) although at 3.5 GPa Tenner et al. (2012) report that melt SiO₂/(MgO+FeO) ratios are shifted to lower values in the presence of H₂O. At pressures of 5-11 GPa Kawamoto and Holloway (1997) reported hydrous garnet peridotite melts to be MgO-rich and low in SiO₂ and Al₂O₃.

In this study, we have placed constraints on the chemical composition of low degree hydrous melts in equilibrium with a garnet peridotite assemblage at 6 GPa and 1400 °C. The principal goal was to determine the H₂O content of a melt coexisting with a residual mineral assemblage compatible with that expected for the asthenospheric mantle at these conditions. We use an iterative crystallization technique to identify melt compositions that are in

equilibrium with peridotite but we employ large melt to crystal ratios to reduce mass balance uncertainties, because this is the only way to determine the melt H₂O content. To minimize H₂O loss from the experiments we employ double capsules but more importantly we employ heating times of <1 hour, which should also aid in the minimization of carbon contamination from the furnace. We employ a number of tests to examine the approach to equilibrium in these experiments. Ultimately, the data collected here are used to model the effect of H₂O on melting at depths corresponding to the LVZ and to address the origin of group II kimberlites.

3.2 Methods

3.2.1 Experimental procedure

The experimental determination of the composition of small degree melts (where F the melt fraction is < 0.1) in natural peridotite systems is a challenging task even in the absence of volatiles and quench crystallization. The volume of small degree melts makes them hard to chemically analyze and promotes melt modification through reaction with solid phases during quenching. Two main methods have in the past been used to overcome these problems. The first employs an initially porous diamond aggregate assemblage to extract and separate melts from the residue (Johnson and Kushiro, 1992, Hirose and Kushiro, 1993), while in the second so-called sandwich technique (Stolper 1980, Faloon and Green, 1987) large fractions of proposed small degree melt compositions are equilibrated with a peridotite residue in a series of iterative experiments (Robinson et al., 1998; Dasgupta and Hirschmann, 2007).

The first technique is not useful for H₂O-bearing experiments due to the risk of contaminating melts with CO₂ or CH₄. The sandwich technique is potentially more suitable, however, and was recently employed for this purpose at 3 GPa by Balta et al. (2011). A small degree hydrous melt would not significantly affect the major element composition of the solid assemblage; therefore, the correct melt composition should be multiply saturated with a peridotite mineral assemblage. The first step in a sandwich experiment study is to perform a sub solidus or dry experiment to determine the mineral compositions of a peridotite assemblage at a given pressure and temperature. Then an initial guess melt composition is equilibrated with the peridotite in sub-equal proportions. If the melt is not in equilibrium with the peridotite, solid-melt reactions will occur and the resulting melt, which should still comprise a large and easily analyzed portion of the experimental charge, should shift in

composition to be closer to equilibrium with the peridotite. By repeating this procedure and using the resulting melt as the initial melt in successive experiments a stage is ultimately reached where minimal reaction occurs between the peridotite and the multiply saturated melt. Such a methodology is potentially very suitable for experiments performed above 3 GPa where quench crystallization means that mass balance estimates of H₂O contents must be made. Melt H₂O contents are determined by assuming all H₂O from the bulk composition is in the melt and determining the melt fraction from a mass balance based on analyses of all other oxides in the melt and mineral phases. Such a determination, however, becomes highly inaccurate if the proportion of melt is small. Hirschmann and Dasgupta (2007) outlined a modification of the iterative sandwich technique where instead of using the product melt composition at the end of each experiment to determine the next melt composition, the partition coefficients between minerals and melts are used to derive a model for the next melt composition based on the chemical composition of the initial melt free assemblage. Such an approach has the advantage that the iterated melt compositions converge more rapidly on the final equilibrium melt. In the current study it was found that the accuracy of mass balance results improved if small peridotite assemblage fractions were employed, i.e. <20 %. Under these circumstances the method of Hirschmann and Dasgupta (2007) is particularly effective because melt compositions would otherwise shift only gradually upon each iteration.

To provide credible estimates of melt H₂O contents using mass balance requires that experiments do not lose significant H₂O during heating. Hall et al. (2004) demonstrated that over the course of 24 hours heating at 1300 °C approximately 32 % H₂O can be lost from a basaltic melt in Au₈₀Pd₂₀ capsules. Under such circumstances it would seem that only very short run durations can hope to preserve H₂O contents that are close to the original and in the current study run times were of the order of 30 minutes to ensure this. In addition, several studies have shown that carbon can diffuse into experimental capsules which should also be minimized by short run durations. In this study a double capsule arrangement was also employed with an outer Pt-Rh capsule and inner Au₈₀Pd₂₀, similar to that employed by Balta et al. (2011) for the same purpose. While peridotite and melt compositions were placed in the inner capsule, the outer capsule contained only the melt composition in the hope of minimizing H₂O loss in the inner capsule by maintaining a high external H₂O activity and similar *fO*₂. However, as will be shown, H₂O loss from both inner and outer capsules was minimal during the course of the experiments and assemblages observed in both inner and outer capsules could be used to determine multiply saturated melt compositions.

Initial experiments indicated that the necessary short run durations prevented suitable chemical equilibrium between sub equal proportions of melt and solid peridotite. Short run times also prevented the conventional use of a melt layer sandwiched between layers of peridotite because chemical equilibrium cannot be achieved upon the short run times. Instead it was found that equilibrium could only be obtained by using < 20% peridotite and by intimately mixing the melt and peridotite compositions. In addition the temperature of each experiment was initially raised by 50 °C above the set point. The run temperature was then approached by cooling over 5 minutes. In this way the entire assemblage was initially melted and all solid phases crystallized from the melt during the cooling phase. This is therefore a crystallization rather than a sandwich experiment. As will be seen, this also ensured the separation of melt from crystals required in order to allow melts to be suitably analyzed and to avoid quench modification of the solid assemblage.

The chemical analysis of the quenched silicate melt assemblage is also challenging using the electron microprobe. The formation of large quench crystals and chemical heterogeneity on a scale larger than 10 microns means that large microprobe beam diameters are required but the analyzed surface is generally uneven and contains voids. In initial experiments melt analyses performed with the electron microprobe resulted in high mass balance residuals. It was found that melt analyses made using laser ablation inductively-coupled plasma mass spectrometry (LA-ICP-MS) resulted in much smaller mass balance residuals. LA-ICP-MS also required large analyzable melt pools.

3.2.2 Starting materials

The peridotite bulk composition of Jagoutz et al. (1979) was selected for the near solidus assemblage in the experiments. This composition (PD-1, Table 3.1) is based on primitive ultramafic nodules and is similar to pyrolite (Ringwood, 1966, 1979). In Table 3.1, the compositions of melts that were equilibrated with this peridotite are reported. The initial melt composition (BASD-1, Table 3.1) was prepared by examining mineral melt partition coefficients from experiments performed between 2-3 GPa (Gaetani and Grove, 1998; Balta et al., 2011). The subsequent melts were prepared as a result of analyzing and mass balancing the resulting quenched melts.

Table 3.1: Chemical composition of starting mixtures (wt %)

	PD-1	BASD- 1	BASD- 7	BASD- 8	BASD- 9	BASD- 10	BASD- 11	BASD- 12	BASD- 13	BASD- 14
<chem>SiO2</chem>	45.88	44.00	39.96	37.86	39.78	39.97	40.77	40.77	40.16	39.88
<chem>Al2O3</chem>	3.91	15.17	5.67	5.21	4.84	5.45	4.60	5.13	5.40	5.64
<chem>CaO</chem>	3.39	9.93	8.01	7.57	5.36	8.18	7.78	7.90	7.95	7.80
<chem>FeO</chem>	8.12	7.81	8.28	12.30	13.60	11.66	11.31	9.80	9.04	8.67
<chem>NiO</chem>	0.26	0.03	0.02	0.02	0.08	0.08	0.08	0.05	0.04	0.04
<chem>MgO</chem>	37.27	12.82	23.30	21.77	19.43	20.64	21.58	22.44	22.87	23.42
<chem>Na2O</chem>	0.28	2.43	2.90	2.74	1.35	2.04	0.94	1.92	2.41	2.45
<chem>Cr2O3</chem>	0.44	0.07	0.10	0.14	0.22	0.17	0.33	0.21	0.16	0.15
<chem>TiO2</chem>	0.24	0.66	0.84	1.42	3.52	0.87	1.11	0.97	0.90	0.89
<chem>MnO</chem>	0.14	0.11	0.15	0.14	0.23	0.16	0.21	0.18	0.16	0.16
<chem>K2O</chem>	0.03	0.12	0.29	0.41	0.65	0.35	0.82	0.55	0.42	0.40
<chem>H2O</chem>	0.00	6.86	10.49	10.41	10.94	10.45	10.47	10.48	10.49	10.50
Sum	100.00	100.00	100.00	100.00	100.00	100.00	100.00	100.00	100.00	100.00

All the starting mixtures were prepared by grinding previously weighed proportions of oxides and carbonates for one hour under ethanol in an agate mortar. Mixtures were then dried, placed in a Fe-saturated Pt crucible, and decarbonated at 1000 °C for 4-6 hours. Mixtures were then glassed by melting in air at 1600 °C for twenty minutes and then rapidly quenching in icy water. This step was repeated four times, grinding the quenched glass for one hour under ethanol and drying it at every cycle to provide higher homogeneity of the mixture. The glass was recovered from the crucible and then reduced in a 1-atmosphere furnace, at 1024 °C and an oxygen fugacity (fO_2) of 2 logs units below the quartz-fayalite-magnetite oxygen buffer for approximately 12 hours. This process was performed twice in order to ensure a complete reduction of the mixture. Mg(OH)2 and Al(OH)3 were then added to the glasses to obtain the hydrous melt compositions that had been previously weighed with an intentional deficit of MgO and Al2O3.

3.2.3 High pressure and high temperature experiments

High pressure (HP) and high temperature (HT) experiments were performed at 6 GPa using a 1200 tonne Kawai type multianvil apparatus installed at the Bayerisches Geoinstitut (BGI). Tungsten carbide anvils of 15 mm truncation edge length were employed with a 25 mm edge length Cr2O3-doped octahedron. A stepped graphite furnace was employed for the

experiments, which was surrounded inside the pressure medium by a ZrO_2 sleeve. A 4 mm diameter outer Pt-Rh capsule was placed at the center of the assembly, separated by an MgO sleeve. MgO spacers were also placed above and below the capsule. The temperature was measured by means of $\text{W}_{97}\text{Re}_{3}\text{-W}_{75}\text{Re}_{25}$ (D type) thermocouple inserted within an alumina sleeve and the effect of pressure on the thermocouple emf was ignored. The pressure was calibrated using the CaGeO_3 garnet to perovskite phase transition (Ross et al., 1986). In a separate experiment the temperature variation inside the Pt/Rh capsules was determined to be within 40 °C of the thermocouple temperature using the two pyroxene thermometer calibration of Brey et al. (1990).

An initial dry subsolidus experiment was performed with the PD-1 peridotite composition in a graphite sleeve inserted in the Pt/Rh capsule. This experiment was equilibrated for 24 hours. Melt crystallization experiments employed double-capsules as described by Kagi et al. (2005) and Balta et al. (2011). An inner Au/Pd capsule containing known proportions of mantle peridotite and hydrous melt was enclosed by an outer Pt/Rh capsule containing just hydrous melt. The inner Au/Pd capsules were pre-soaked with Fe by equilibrating with an iron bearing silicate assemblage in a gas mixing furnace at 1100 °C and $2 \log f\text{O}_2$ below the FMQ buffer, for approximately 1 day. After being equilibrated in the gas mixing furnace, the capsules were recovered and cleaned with HF overnight at ~ 80 °C. After packing the peridotite/melt mixtures in the capsule, the top of the Au/Pd capsule was welded. H_2O loss during welding was checked by weighing the capsule before and after. Once prepared, the Au/Pd capsule was inserted in the Pt/Rh capsule along with the outer hydrous melt composition separating the two capsules. The Pt/Rh outer capsule was then welded closed, with the capsule weight being once again monitored for H_2O loss.

Crystallization experiments were performed at 6 GPa, equivalent to ~180 km depth in the mantle, and a nominal temperature of 1400 °C. This is the adiabatic temperature calculated by Katsura et al. (2010) corresponding to this depth. Target pressure was reached in 4 hours with the target temperature initially reached at a heating rate of 100 °C/min. Once at target temperature, the experiment was further heated by 50 °C over a period of 5 minutes, then kept at this temperature for 5 minutes, and then cooled down to target temperature over 5 minutes. Then each experiment was kept at temperature for 30 minutes. This technique was found to produce well equilibrated assemblages composed of large crystals (>100 μm) suitable for various mineral H_2O analysis techniques (Chapter 4). The overstep of 50 °C in the

temperature is of similar magnitude to the gradient in temperature over the capsule, which is, therefore, a similar magnitude to the temperature uncertainty.

3.2.4 Analytical techniques

After recovery to room pressure the capsules were removed from the ceramic assembly, mounted in epoxy resin, sectioned and polished in the absence of water. Chemical compositions of crystalline phases were determined using a JEOL JXA-8200 electron microprobe at the BGI. The operating conditions for chemical analyses were 15 kV acceleration voltage and a current of 15 nA, with a counting time of 20 s on the peak position and 10 s on each side for the background. Alkalies were measured first in the procedure, in order to limit potential losses during the analyses. Natural and synthetic minerals were used as standards for most elements, while metal standards were employed for Ni, Cr, Fe and Ir. A spot beam of 1 μm diameter was used in obtaining the chemical compositions of the mineral phases. Analyses were reduced using the PRZ correction routine.

Chemical compositions of quenched melts were obtained using LA-ICP-MS installed at the BGI, by means of a 193nm ArF Excimer laser combined with a quadrupole mass spectrometer. Since large pools of melt can be produced with the crystallization approach described here, up to 10 pits of $\sim 80 \mu\text{m}$ diameter could be ablated on a single charge, providing accurate analyses of the dendritic quenched melt. The NIST SRM 610 glass (Spandler et al., 2011) was used as external standard. Internal standardization was performed by normalizing the sum of the oxides to 100 wt %.

3.3 Results

3.3.1 Subsolidus experiment

The mineral phase analyses from the subsolidus experiment performed on the peridotite composition (PD-1, Table 3.1) are reported in Table 3.2.

Table 3.2: Chemical composition (in wt %) and modal abundances of mineral phases in the subsolidus run

	ol	cpx	gt
SiO ₂	40.48 (33) ¹	54.24 (93)	42.91 (75)
Al ₂ O ₃	0.12 (5)	2.68 (65)	21.33 (1.05)
CaO	0.17 (2)	9.63 (48)	4.77 (37)
FeO	9.60 (15)	5.18 (11)	6.56 (15)
NiO	0.37 (6)	0.16 (7)	0.02 (2)
MgO	48.84 (24)	24.80 (63)	22.19 (24)
Na ₂ O	0.03 (2)	1.03 (7)	0.06 (4)
Cr ₂ O ₃	0.10 (2)	0.44 (3)	1.53 (10)
TiO ₂	0.05 (3)	0.31 (4)	0.90 (5)
MnO	0.13 (4)	0.19 (5)	0.26 (4)
K ₂ O	0.004 (3)	0.08 (2)	0.001 (1)
Total	99.99 (48)	99.33 (1.00)	100.59 (23)
Mode	0.54	0.32	0.14

¹: standard deviation. Analyses on approximately 20 crystals were used for each phase.

The assemblage comprised 14 wt % garnet, 32 wt % clinopyroxene (cpx) and 54 wt % olivine. The absence of orthopyroxene (opx) is in agreement with the results of Walter (1998) for a similar bulk composition at 6 GPa and 1670 °C. The mineral modes are also in very good agreement with this previous study. Balta et al. (2011) also found an orthopyroxene free assemblage at 3 GPa and 1375 °C although Davis et al. (2011) produced an opx bearing assemblage by equilibrating a dry peridotite at 3 GPa and 1440 °C for 1 week. Although garnet 3+ cations sum to slightly less than 2 per 12 oxygen formula units (1.9) this is not matched by any Si or 2+ cation excess to imply that the sample contains a significant majorite component. The olivine Mg-number (=molar Mg/(Mg+Fe)x100) is 89.6 but as discussed later the application of several thermometers implies imperfect Fe-Mg equilibration in the experiment. Clinopyroxene and garnet compositions are identical within error to those determined by Walter (1998) at 1670 °C.

3.3.2 Hydrous melt experiments

Typical hydrous melt experiments are shown in Fig. 3.1.

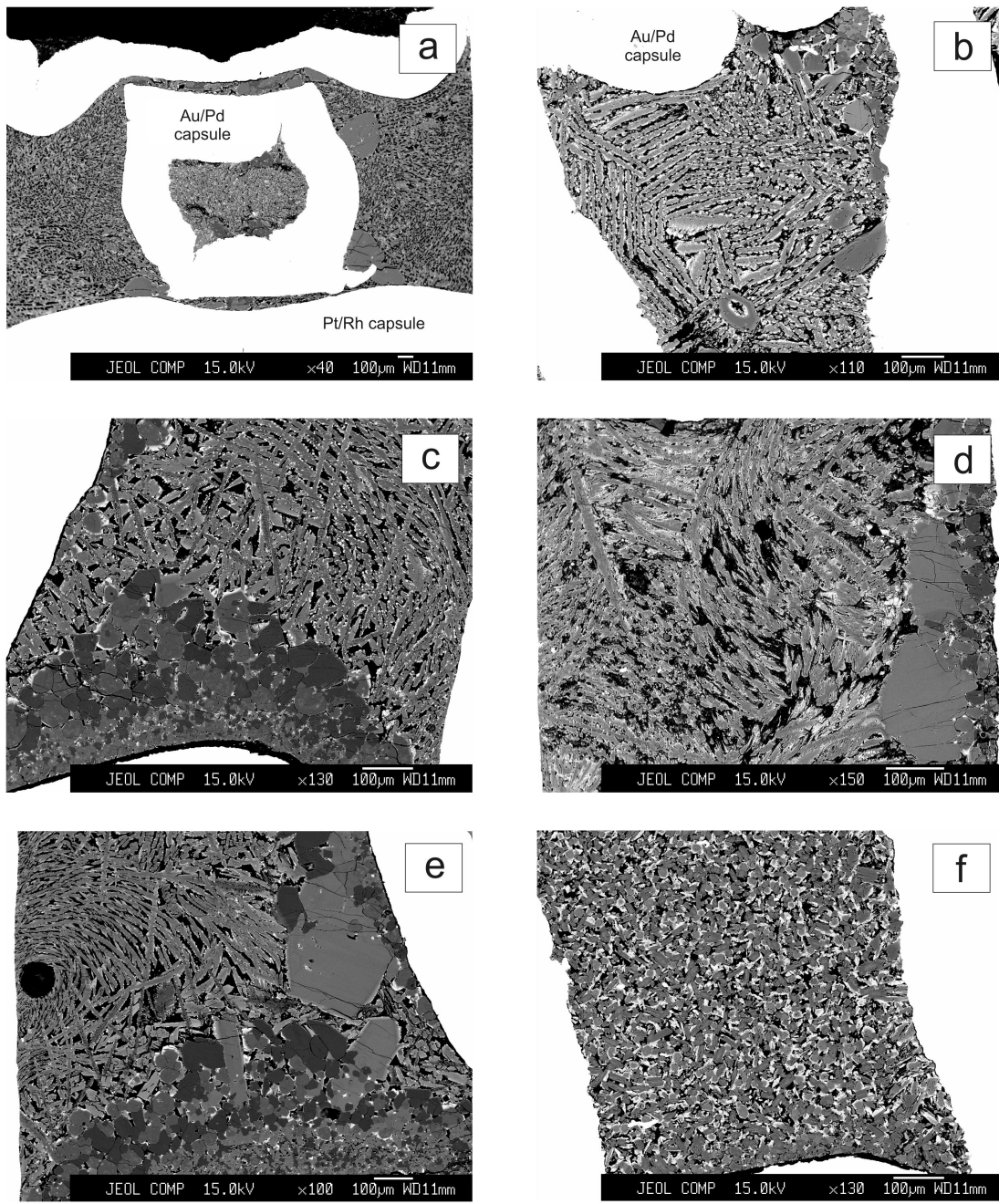


Fig. 3.1: Backscattered electrons images from selected experimental runs. Fig. 3.1a (exp. S5252, Table 3) is an overview of the double capsule used in this study, where an outer Pt/Rh capsule contained an inner Au/Pd capsule surrounded by melt. Crystals and large pools of quenched melt with dendritic structure can be recognized in both inner and outer capsule. Fig. 3.1b shows the phase assemblage of the inner capsule of experiment S5213 (Table 3) where opx (medium grey crystals) and garnet (grey crystals) formed in equilibrium with a large amount of melt. Figures 3.1c to 3.1e present phase assemblages from experiments S5200, S5581 and S5129, respectively. In these experiments, large crystals of olivine (dark), clinopyroxene (light grey), and garnet (medium grey) up to 200 μm across were found in equilibrium with quenched crystals resembling the melt produced at high pressure and high temperature. The black circle in Fig. 3.1e indicates a typical pit produced after LA-ICP-MS analyses. Fig. 3.1f displays a phase assemblage of an experiment where the melt failed to segregate from the crystalline matrix. Fig. 3.1f is an example of an experiment where incomplete melt segregation meant it was impossible to identify quench melt from equilibrium crystals.

In general, crystals were formed in both inner and outer capsules coexisting with large regions of finer fibrous quenched melt crystals. In some experiments where the peridotite portion of the initial starting mixture was > 20 wt % or the bulk H₂O content was < 9 wt %, incomplete separation of melt and minerals occurred (Fig. 3.1f). The interstitial melt creates an extremely difficult texture to interpret on quenching because the melt crystals are impossible to discriminate from those of the solid assemblage. Significant quench modification of crystals also occurs. In these experiments the interstitial melts were impossible to meaningfully analyze and the experiments were generally discarded. Only when significantly large pools of melt separated from the solid assemblage, was the quenched texture easy to discriminate (Fig. 3.1b-e). Such separation only occurred when melt fractions were large but the only way found to ensure the separation always occurred was to initially overstep the set point temperature by 50 °C. LA-ICP-MS analyses of separated melt pools showed small standard deviations in melt analyses and the melts appear well homogenized at the 80 micron scale of the analyses (Fig. 3.1e). In at least 6 experiments assemblages of olivine, clinopyroxene and garnet were found in equilibrium with large pools of hydrous melt. One experiment (S5281) was also saturated in orthopyroxene in addition to these three phases. In a number of further experiments, however, orthopyroxene was found to replace olivine in the assemblage and in several experiments clinopyroxene was absent. The compositions of quenched melt and mineral phases produced in the experiments are reported in Table 3.3. Mass balance was performed using mineral and melt analyses of 11 elements. An additional phase composed of 100 % FeO was added to account for Fe loss (Tenner et al., 2012). The system of equations was minimized to obtain the phase modes and the melt H₂O content. The melt was assumed to be the only H₂O bearing phase. The melt composition was normalized to 100% during the minimization. The sum of the squared residuals was generally in the range 0.1-0.6 with Na₂O being by far the main contributor to the residual. Melts with residuals above 1 were discarded. In the majority of experiments the melt mode was above 80% such that the difference between the starting composition and the resulting melt composition was relatively small. Fe loss in inner capsules was in the range 2-3 % of the initial Fe content, while in the outer capsules it was up to 7 %. Similar losses of Ni were noted, which may have also alloyed with the capsule. Large losses of K occurred in all hydrous experiments and Na losses were observed in most of the experiments.

3. The composition of hydrous partial melts of garnet peridotite at 6 GPa

Table 3.3: Experimental run products and chemical composition, in wt %, of mineral phases (microprobe analyses) and melts (LA -ICP-MS analyses)

Run (start. mix)	SiO ₂	Al ₂ O ₃	CaO	FeO	NiO	MgO	Na ₂ O	Cr ₂ O ₃	TiO ₂	MnO	K ₂ O	H ₂ O	Total
S5129 (BASD-7)													
ol	41.39(15) ¹	0.07(2)	0.13(1)	6.13(15)	0.05(2)	53.22(19)	0.08(8)	0.03(2)	0.01(4)	0.08(4)	0.03(2)	100.21(29)	
cpx	55.63(23)	3.06(36)	14.48(51)	2.91(13)	0.01(2)	22.05(6)	1.67(13)	0.16(2)	0.08(4)	0.08(4)	0.06(3)	99.76(28)	
gt	43.34(29)	22.56(23)	5.27(35)	4.70(23)	0.01(2)	23.78(33)	0.10(4)	0.62(9)	0.24(6)	0.19(6)	0.03(2)	100.00(32)	
melt	40.12(10) ²	6.00(0)	8.72(31)	8.51(15)	0.01(2,06)	21.42(1)	2.32(24.12)	0.05(4,11)	1.05(2,28)	0.18(35)	0.28(15)	11.34(12)	
S5200 (BASD-8)													
ol	40.99(15)	0.07(1)	0.14(1)	9.03(28)	0.05(3)	50.78(35)	0.04(1)	0.02(1)	0.03(2)	0.08(4)	0.00(1)	101.21(33)	
cpx	55.33(21)	2.97(31)	14.85(1.10)	4.03(27)	0.02(2)	20.95(96)	1.55(14)	0.20(5)	0.10(1)	0.09(3)	0.02(3)	100.13(22)	
gt	43.03(31)	22.05(70)	5.54(49)	6.94(56)	0.02(3)	21.89(70)	0.07(3)	0.73(10)	0.42(0)	0.16(4)	0.01(1)	100.87(32)	
melt	38.39(1.78)	4.96(8)	8.62(1.75)	11.62(6)	0.01(83)	19.90(15)	2.45(15.5)	0.09(1.25)	1.54(4)	0.15(1)	0.20(27.0)	12.09(1.68)	
S5213 (BASD-9)													
opx	55.80(73)	1.61(14)	0.85(6)	5.97(8)	0.04(2)	34.16(37)	0.19(2)	0.25(3)	0.11(3)	0.13(4)	0.01(1)	99.23(58)	
melt	40.79(1.97)	5.14(60)	5.74(81)	11.23(51)	0.03(9.31)	18.00(2.94)	1.70(1.75)	0.19(40)	3.60(3.44)	0.24(1)	0.66(67)	12.7(63)	
S5213-1* (BASD-9 + PD-1)													
opx	56.35(26)	1.55(12)	0.71(7)	6.13(37)	0.05(3)	34.09(48)	0.19(2)	0.25(2)	0.12(3)	0.12(3)	0.01(1)	99.89(50)	
gt	42.48(25)	20.96(32)	2.82(12)	7.96(16)	0.01(2)	22.82(12)	0.04(1)	1.69(12)	0.74(4)	0.26(3)	0.01(1)	100.00	
melt	39.25(3.91)	4.85(1.75)	6.30(1.93)	11.85(1.04)	0.03(21.46)	18.44(5.68)	1.37(2.89)	0.18(2)	3.25(15.46)	0.23(8)	0.74(12)	13.51(1.46)	
S5218-O ¹ (BASD-9)													
opx	56.41(44)	1.63(17)	0.96(4)	6.50(25)	0.05(4)	33.95(34)	0.20(2)	0.23(4)	0.11(2)	0.16(3)	0.01(1)	100.05(65)	
gt	42.07(42)	20.77(68)	3.77(39)	8.23(26)	0.03(4)	22.69(35)	0.04(1)	1.27(14)	0.98(24)	0.33(6)	0.00(1)	100.19(58)	
melt	39.93(1.86)	4.95(1.92)	6.34(5)	11.54(75)	0.03(8.53)	17.09(1.69)	1.03(32.1)	0.18(11)	3.80(7.06)	0.25(0)	0.57(8.92)	14.30(93)	
S5252 (BASD-10)													
opx	57.09(61)	1.66(12)	1.80(13)	4.37(12)	0.03(2)	35.18(75)	0.29(3)	0.15(2)	0.03(2)	0.08(5)	0.01(1)	100.68(26)	
cpx	55.82(23)	2.71(8)	11.73(59)	3.74(15)	0.03(3)	24.52(37)	1.22(4)	0.30(3)	0.04(1)	0.11(2)	0.02(1)	100.24(30)	
gt	43.10(36)	21.21(19)	5.57(12)	5.93(14)	0.02(3)	23.25(20)	1.15(6)	0.04(2)	0.33(4)	0.20(2)	0.01(1)	100.81(48)	
melt	38.23(20)	5.49(22)	8.24(1.05)	8.57(5)	0.02(1.2.6)	19.61(3)	3.42(11.1)	0.12(65)	0.77(17.14)	0.15(5)	0.20(29.3)	15.17(5)	
S5270 (BASD-11)													

3. The composition of hydrous partial melts of garnet peridotite at 6 GPa

Table 3.3: continued

Run (start, mix)	SiO ₂	Al ₂ O ₃	CaO	FeO	NaO	MgO	Na ₂ O	Cr ₂ O ₃	TiO ₂	MnO	K ₂ O	H ₂ O	Total	
opx	56.37(85)	1.17(14)	1.84(24)	5.46(36)	0.06(3)	34.17(31)	0.17(4)	0.18(5)	0.04(2)	0.14(3)	0.01(2)	99.63(98)		
cpx	54.98(36)	1.81(15)	14.44(44)	4.25(13)	0.04(3)	22.86(26)	0.75(3)	0.37(8)	0.08(2)	0.14(4)	0.03(1)	99.73(23)		
gt	42.52(41)	21.16(40)	5.35(23)	6.84(24)	0.02(3)	22.19(21)	0.02(1)	1.70(21)	0.36(4)	0.28(5)	0.00(0)	100.43(38)		
melt	38.43(1)	4.49(13)	9.08(16)	10.57(5)	0.03(5.28)	19.92(3)	0.51(57.9)	0.18(1.85)	1.50(25)	0.22(0)	1.17(6)	13.88(5)	100.00	
S5278 (BASD-11)														
opx	57.23(46)	1.47(18)	2.24(16)	5.12(15)	0.07(3)	33.70(33)	0.17(2)	0.26(4)	0.03(3)	0.14(3)	0.01(1)	100.45(51)		
cpx	55.10(65)	1.85(17)	13.53(1.10)	4.23(21)	0.03(3)	23.58(92)	0.67(6)	0.37(6)	0.06(2)	0.15(32)	0.03(2)	99.60(59)		
gt	41.89(1.35)	20.57(53)	5.29(8)	6.30(10)	0.02(3)	23.00(83)	0.02(0)	1.94(24)	0.30(3)	0.28(5)	0.00(0)	99.59(1.42)		
melt	37.41(0)	4.55(7)	9.14(14)	10.26(2)	0.04(4.24)	19.68(8)	1.63(6.06)	0.21(4)	1.24(5.31)	0.22(5)	0.63(32.1)	15.01(2)	100.00	
S5281 (BASD-12)														
ol	40.43(31)	0.07(5)	0.24(30)	7.23(15)	0.12(5)	52.17(68)	0.03(3)	0.03(2)	0.03(2)	0.10(5)	0.01(1)	100.47(44)		
cpx	56.46(23)	1.46(15)	2.03(23)	4.33(11)	0.04(3)	34.88(41)	0.28(3)	0.14(4)	0.03(2)	0.09(4)	0.01(1)	99.75(58)		
gt	54.62(93)	2.14(19)	13.20(1.17)	3.75(25)	0.03(3)	24.10(1.82)	1.09(10)	0.22(6)	0.06(4)	0.14(3)	0.03(3)	99.37(47)		
melt	42.71(46)	21.63(39)	4.80(32)	5.64(70)	0.02(2)	23.22(58)	0.04(2)	1.13(19)	0.31(8)	0.21(5)	0.00(1)	99.71(43)		
S5291 (BASD-13)														
ol	40.63(33)	0.07(2)	0.17(3)	7.27(13)	0.08(3)	51.79(80)	0.04(2)	0.02(2)	0.02(2)	0.10(4)	0.00(0)	100.18(1.00)		
cpx	55.04(59)	2.38(11)	14.25(77)	3.64(11)	0.02(3)	23.02(1.65)	1.35(9)	0.16(3)	0.08(2)	0.10(4)	0.02(1)	100.05(67)		
gt	43.03(54)	22.13(22)	4.50(35)	5.26(1.07)	0.02(3)	23.97(96)	0.06(2)	0.75(12)	0.25(12)	0.19(8)	0.01(0)	100.47(28)		
melt	40.50(29)	4.72(46)	8.83(1.02)	9.29(69)	0.02(2.03)	21.96(15)	1.21(158.81)	0.08(2.15)	1.23(4.49)	0.19(43)	0.07(187.27)	11.91(60)	100.00	
S5577 (BASD-14)														
ol	40.86(33)	0.06(2)	0.15(2)	6.79(14)	0.08(5)	52.15(47)	0.03(2)	0.02(1)	0.02(1)	0.03(3)	0.09(4)	0.01(1)	100.26(33)	
cpx	55.14(62)	2.29(5)	14.13(86)	3.22(9)	0.02(2)	23.55(90)	1.32(7)	0.16(2)	0.06(3)	0.11(4)	0.02(1)	99.01(82)		
gt	43.24(20)	22.27(26)	4.35(19)	5.40(44)	0.03(5)	23.35(47)	0.06(3)	0.65(7)	0.28(6)	0.19(4)	0.01(1)	99.90(62)		
melt	41.06(1.34)	4.90(50)	8.74(0)	8.06(1.93)	0.01(2.38)	22.05(13)	1.08(251.25)	0.08(99)	0.99(3)	0.17(4)	0.09(138.7)	12.78(1.61)	100.00	
S5581 (BASD-14)														
ol	41.11(22)	0.06(2)	0.13(1)	6.20(15)	0.07(4)	52.88(33)	0.05(7)	0.02(0)	0.01(0)	0.09(2)	0.01(1)	100.63(37)		
cpx	55.18(54)	2.49(24)	12.97(92)	3.10(16)	0.03(3)	23.78(88)	1.24(10)	0.17(3)	0.06(2)	0.10(5)	0.01(1)	99.13(39)		
gt	43.25(19)	21.87(31)	4.76(43)	4.80(33)	0.02(3)	23.70(42)	0.05(2)	0.69(7)	0.32(6)	0.16(4)	0.01(1)	99.62(39)		
melt	40.63(13)	5.06(0)	8.37(31)	7.43(11)	0.01(2.03)	22.28(0)	2.76(1)	0.08(24)	0.98(0)	0.16(1)	0.21(23.78)	12.02(9)	100.00	

[†] the number in parentheses close to the mineral components is one standard deviation ; the number in parentheses close to the melt components is the percent residual given by the mass balance calculations

[‡] experiment from outer capsule where the starting composition was melt mixture

* experiment from inner capsule where the starting composition was 80% in weight of the melt mixture plus 20% in weight of the peridotite mixture

3.3.3 Attainment of mineral-mineral and mineral melt chemical equilibrium

The experimental run times were short to limit the loss of H₂O and it is particularly important to test that equilibrium between phases was still achieved. The crystalline phases that could be unambiguously identified as solid before quenching were in general homogeneous in composition (Table 3.3) and displayed no significant chemical zoning (Fig. 3.1), except within 5 µm of the edges where some quench modification occurred in some instances. Many crystals formed, particularly in the outer capsules, had sizes up to 200 microns (Fig. 3.1d-e). A number of thermometers can be used to test whether equilibrium between mineral phases was likely achieved. The Fe-Mg exchange thermometers between olivine and garnet (O'Neill and Wood, 1979) and garnet and clinopyroxene (Ellis and Green, 1979) were employed for this purpose in addition to the enstatite-in-clinopyroxene thermometer of Nimis and Taylor (2000). In experiments containing orthopyroxene the thermometers of Harley (1984) and Brey and Köhler (1990) were also applied. In the best instances temperatures using these thermometers showed maximum differences of <40 °C. In experiments where thermometers indicated small ranges of temperature the average temperature was 30 °C higher than the set point of 1400 °C, which possibly reflects the crystallization temperature during cooling from the 50 °C initial overstep or a difference from the thermocouple temperature due to the thermal gradient. The consistency of many experiments is a good indication that equilibrium was reached as the O'Neill and Wood (1979) thermometer is particularly sensitive. These tests also indicate that the thermometers operate extremely well at these conditions, which are close to the limit in pressure for which they are generally employed on natural samples. Ulmer and Sweeney (2002) found similar evidence for equilibrium being reached in experiments with large volatile bearing melt fractions run for even shorter periods of time at similar conditions.

Experiments where differences between temperatures determined using the three main thermometers exceeded 100 °C were discarded. In many instances these were experiments where the melt fraction was relatively small (<70 wt %) and it is likely that the entire assemblage was not completely molten during the overstep in heating by 50 °C. This implies that on the time scale of the experiments it is not possible to equilibrate the hydrous melt with a solid residue, but instead equilibrium is achieved as a result of almost simultaneous crystallization of phases from a single homogeneous melt composition. It has been postulated

that when sufficient melting occurs in multianvil experiments, the thermal gradient generally leads to rapid dissolution and recrystallization of mineral grains even without an initial overstep of the temperature (Lesher and Walker, 1988). Crystallization is probably the only way of approaching chemical equilibrium in short experiments because extremely long run times are likely required for equilibrium to be achieved through mineral cation diffusion. Long run times would lead to gradual H₂O loss from the capsule. Fe-Mg equilibrium was apparently not reached, for example, in the sub solidus experiment (Table 3.2), for which the O'Neill and Wood (1979) thermometer, the most sensitive of the three, predicts a temperature 230 °C above the run temperature. Under dry conditions even run times of one day are therefore insufficient to yield equilibrium.

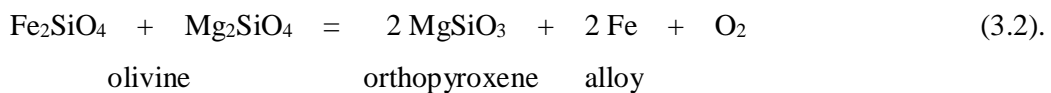
The olivine/melt Fe-Mg exchange coefficient,

$$K_D = \frac{[X_{Fe}^{ol}][X_{Mg}^{melt}]}{[X_{Fe}^{melt}][X_{Mg}^{ol}]} \quad (3.1)$$

can be used to assess equilibrium mineral - melt equilibrium in the experiments. For experiments in which the solid assemblage was deemed to be in equilibrium, melt K_D values vary from 0.29 to 0.35 with the higher values corresponding to charges with greater Fe loss. The range is shifted to slightly lower values compared to that observed by Walter (1998) at 6 GPa (0.34-0.36) at the dry solidus, with the small shift being in excellent agreement with the effect of temperature predicted by the model of Toplis (2004). Several experiments were excluded on the grounds that melt K_D values were significantly above 0.4.

3.3.4 Oxygen fugacity in the experimental capsules

In two experiments, 3 wt % of Ir metal powder was added to the inner capsule in order to estimate the oxygen fugacity based on the equilibrium



Fe from the silicates alloys with the Ir to produce a Fe-Ir alloy, the composition of which is sensitive to the fO₂ (Woodland and O'Neill, 1997; Stagno and Frost, 2010). The fO₂ can be

measured using chemical analyses of the silicate and alloy phases. In the experiments in question olivine failed to crystallize, however, a reasonable estimate can be made of the fictive olivine composition based on orthopyroxene and garnet compositions. The resulting oxygen fugacities are -1.8 and -2.2 log units relative to the QFM oxygen buffer, which is within error (~0.5 log units) identical to the fO_2 at which the experiment starting powders were initially reduced at 1 atmosphere. This range of fO_2 is quite consistent with that expected for the mantle at 6 GPa (Frost and McCammon, 2008; Stagno et al., 2013) and also indicates that little oxidation of silicates has occurred during the experiment. Significant oxidation of silicates by H₂O would likely lead to H₂ being lost from the capsule.

3.3.5 Loss of H₂ or H₂O during experiments

An important question is whether it is likely that H₂O was lost from the capsules during the experiments either as H₂O or H₂. This can be assessed by examining the extent of crystallization for a given initial bulk H₂O content. Whether melt successfully separates to form a pool depends on the melt fraction, which in turn depends on the proportion of H₂O in the experimental charge. The formation of interstitial melts, where the melt did not separate from the residue (Fig. 3.1f), occurs quite reproducibly when initial bulk H₂O contents were below 8 wt % and the melt fraction falls below 70 wt %. Whereas bulk water contents of 10.5 wt % resulted in refined melt fractions that were between 86 and 90 wt % for six individual experiments, i.e. a reproducible and narrow range. If significant loss of H₂O occurred during the experiments we would expect to see variable amounts of crystallization and the formation of interstitial melts.

3.4 Discussion

3.4.1 Phase relations

Starting from the initial ‘best guess’ hydrous melt composition further melt compositions were determined following the procedure of Hirschmann and Dasgupta (2007), whereby the determined mineral melt partition coefficients are used to estimate successive melt compositions. Using this procedure it was possible to arrive at melt compositions that crystallized olivine, clinopyroxene and garnet, i.e. the assemblage observed in the subsolidus peridotite experiment at the same conditions (Table 3.2), after only 2 further melt iterations. Fe loss to the capsule, however, meant that in most instances the solid residues contained less

Fe than expected from the subsolidus peridotite. The most successful, well equilibrated experiments to crystallize the 3 phases were those where only the melt composition was employed and approximately 10 % crystallization occurred from this melt.

Further melt compositions were then fabricated from the successful melt analyses, in order to check that the achieved melt composition was indeed in equilibrium with peridotite (BASD-9 to 14). This resulted, however, in a number of problems. One problem, as related previously, arose because equilibrium between melt and a solid residue could not be obtained in the short run times, as indicated through the application of various thermometers. However, in several experiments where either small portions of peridotite were mixed with the proposed melt composition or the melt composition alone was crystallized, orthopyroxene replaced olivine in the crystallizing assemblage. As shown in Fig. 3.2, melts coexisting with ol, cpx and gt were found to have almost identical ranges of composition compared to those coexisting with opx, cpx and gt. There appears to be no chemical component in the melt that can discriminate between these two assemblages. Loss of H₂O from the capsule does not seem to provide a suitable explanation as the observation is consistently reproducible i.e. all melt compositions fabricated from melts originally coexisting with the ol-bearing assemblage crystallize opx. The only difference between melts that crystallized olivine and those crystallizing opx appears to be the initial starting melt compositions. As shown in Fig. 3.2a, starting compositions from which olivine bearing assemblages formed have higher (Mg+Fe)/Si ratios than the final melts, reflecting the olivine crystallization, whereas melts where opx forms change very little during crystallization. It is the ~ 10% crystallization of the ol-bearing assemblage which causes a shift in the melt (Mg+Fe)/Si ratio to lower values. A plausible explanation, therefore, is that the melts produced by crystallization of olivine during cooling over the 50 °C interval have moved towards the opx stability field. But once the run temperature of 1400 °C is reached there is insufficient driving force or time for olivine to react with the melt and transform to opx. When the melt compositions are reproduced and equilibrated at the same conditions, however, they crystallize opx. Experiment S5281 indicates that the melts are very close to compositions where all 4 minerals phases crystallize. As a result it can be concluded that the melt composition that is saturated in the 3 mineral phases lies somewhere between the starting compositions and the final mass balanced melt compositions. In addition, the temperature at which the melt is multiply saturated is also bracketed between 1400 and 1450 °C, over which the crystallization occurs.

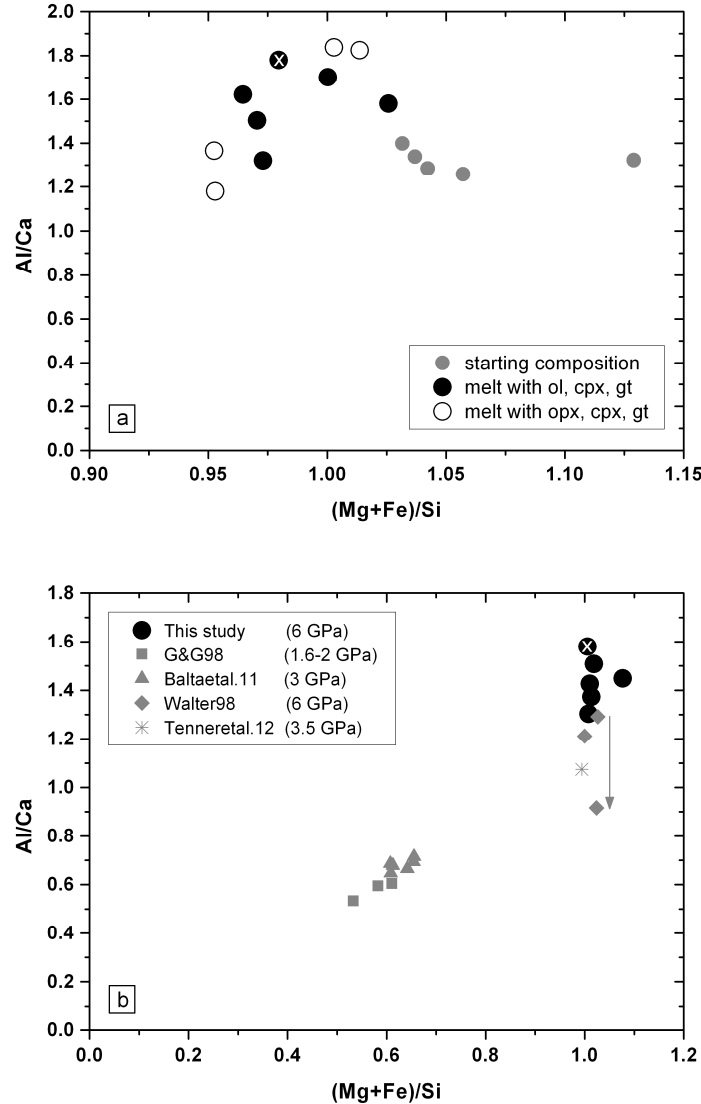


Fig. 3.2: Major element ratios, Al/Ca versus $(\text{Mg}+\text{Fe})/\text{Si}$, of hydrous melts produced at 6 GPa and 1400°C. **(a)** melts and starting compositions from this study. The grey filled circles show the starting compositions BASD-7, -8, -12, -13 and -14 (see Table 3.1). Black filled circles are melts produced in equilibrium with olivine, cpx and gt while black, empty circles are melts that were found in equilibrium with opx, cpx and gt (Table 3.3). The black circle with the white cross indicates run S5281, where ol, opx, cpx and gt were produced in equilibrium with melt. **(b)** Averaged initial and final melt compositions from olivine+cpx+gt (+ opx in S5281-white cross) saturated experiments are shown by black filled circles, and are compared to data from the literature, in grey. Grey squares are hydrous melts from Gaetani and Grove (1998) produced at 1.6-2 GPa; grey triangles are low degree hydrous melts produced by Balta et al. (2011) at 3 GPa; the grey asterisk is a hydrous melt produced by Tenner et al. (2012) at 3.5 GPa; grey diamonds are melts produced near the dry peridotite solidus at 6 GPa by Walter (1998). The grey arrow indicates the evolution of the melt composition of Walter (1998) with increasing temperature from 1710 to 1755 °C.

The differences in melt composition between the initial starting melt and the residual melt, in equilibrium with olivine, are small. The main shifts are a decrease in MgO content by 0.8-1.8 wt % coupled with a similar magnitude increase in H₂O content, while CaO also increases by 0.5-1.2 wt %. As such the bracket on the 3 phases saturated composition is relatively narrow.

In fact the saturating melt composition must be close to the average of the initial and final melts, which is plotted in Fig. 3.2b. Due to thermal gradients and the necessity for short run times it is probably difficult to achieve a greater level of precision in the composition of multiply saturated melt compositions in the multianvil.

3.4.2 Mineral and melt compositions

As shown in Fig. 3.2b the determined hydrous melt compositions coexisting with ol, cpx and gt have very similar $(\text{Mg}+\text{Fe})/\text{Si}$ ratios to those reported by Walter (1998) close to the dry peridotite solidus at 1700 °C, and have only slightly higher Al/Ca ratios. Na_2O concentrations are also higher in the hydrous melts but this reflects differences in the effective melt fraction between experiments. It would seem, therefore, that other than lowering the peridotite solidus temperature, H_2O has very little discernable effect on the major element melt chemistry.

If data are compared at various pressures, then hydrous melts at 6 GPa are more Mg-rich and have higher Al/Ca ratios than those at 1.6 and 3 GPa (Fig. 3.2b). There are, however, only small differences with the 4 phase saturated melt reported by Tenner et al. (2012) from experiments at 3.5 GPa and 1350 °C. This seems slightly surprising that melts shift so dramatically in MgO content between 3 and 3.5 GPa and that melts at 3.5 GPa have much stronger affinities with those at 6 GPa compared to 3 GPa.

The melts produced in this study are nepheline normative based on the CIPW scheme. In Fig. 3.3, however, the melt compositions are plotted on a volatile free basis in two projections using the garnet lherzolite normative scheme described by Kelemen et al. (1992). The first is a projection from cpx onto olivine-opx-garnet, while the second is from opx onto olivine-cpx-garnet. The near solidus melts of dry mantle peridotite between 3 to 7 GPa reported by Walter (1998) are shown in addition to hydrous near solidus melts reported between 1.6 and 3.5 GPa by Gaetani and Grove (1998), Balta et al. (2011) and Tenner et al. (2012). Hydrous melts from this study are dominantly olivine and cpx normative. Again it can be seen that there is very little difference between where olivine and opx bearing melts from this study plot, although results from 3 of the 5 opx bearing samples are opx normative. The hydrous melts from this study plot close to the anhydrous near solidus melts of Walter (1998) at 6-7 GPa.

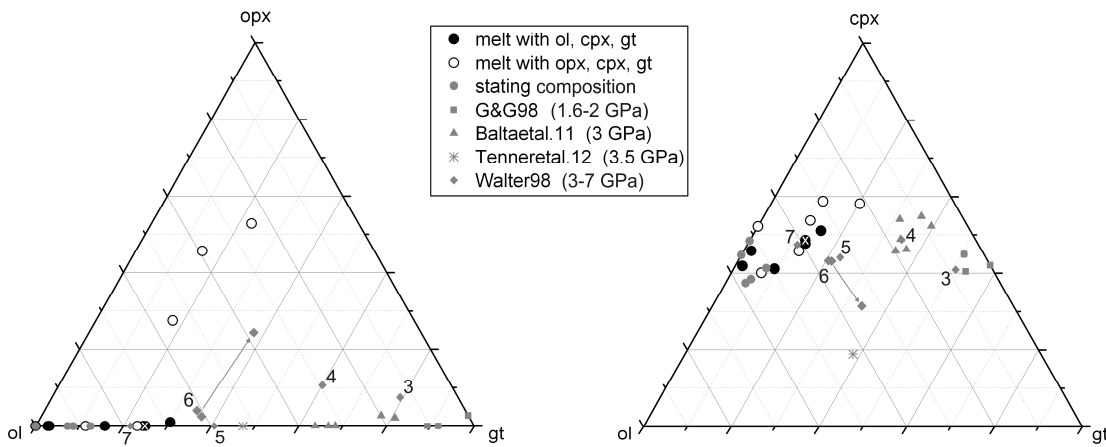


Fig. 3.3: Normative diagram projected from cpx onto the olivine-opx-garnet surface (left) and from opx onto the olivine-cpx-garnet surface (right), following the method of Kelemen et al. (1992). Symbols are as in Fig. 3.2. Figures indicate the pressure in GPa of near solidus melts from the study of Walter (1998). The arrow indicates the melt composition change from near to the solidus at 6 GPa from Walter (1998).

It can be seen that there is a consistent evolution with pressure for both hydrous and anhydrous melts from cpx and garnet normative melts at low pressure, to dominantly olivine and cpx normative melts at high pressure. If we consider melts crystallizing at depth in the lithospheric mantle, for example, this would imply a shift from eclogitic vein rocks at low pressure (<3 GPa) to wehrlite assemblages at high pressure (~6 GPa). Wehrlite xenoliths that have been reported with equilibration pressures of approximately 6 GPa (Kopylova and Caro, 2004) could therefore have formed from the crystallization of small degree hydrous melts.

Walter (1998) provides a series of regressions in terms of melt fraction (F) for major elements in melts produced in his nominally dry peridotite melting experiments, which can be extrapolated to zero F . There is good agreement between these estimated zero melt fraction values at 6 GPa compared with the compositions of hydrous melts in equilibrium with olivine, cpx and garnet from this study when compared on a volatile free basis. In Walter (1998) melt contents of 10 wt % CaO are predicted at zero F , whereas hydrous melts from this study are in the range 9.4–10.5 wt % on a volatile free basis. The range of MgO and Al₂O₃ contents of the hydrous melts are similarly within 1 wt % of the zero F values of Walter (1998) of approximately 6 and 24 wt % respectively. SiO₂ melt contents from this study cover a relatively wide range from 44–47 wt % but the values are correlated with FeO, which varies due to Fe loss to the metal capsule. The melt with the least Fe loss, however, contains 13.2 wt % FeO and 43.7 wt % SiO₂, which is in excellent agreement with the zero F values of 13.4 and 44.1 wt % respectively of Walter (1998). Major element hydrous melt

compositions are, therefore, in excellent agreement with estimates for small degree anhydrous melt compositions.

The hydrous melt TiO_2 contents vary from 1-1.5 wt %. The PD-1 bulk peridotite composition employed in this study (Jagoutz et al., 1979) contains 0.24 wt % TiO_2 . Using mineral-melt partition coefficients from this study we can estimate from the melt TiO_2 content the effective melt fraction relative to the proposed bulk composition, which is between 7 and 16 %. This range is quite high but it is extremely sensitive to the TiO_2 content in the assumed bulk composition. If we were to assume the depleted MORB mantle composition of Workman and Hart (2005) that contains only 0.13 wt % TiO_2 then the melt compositions would be equivalent to melt fractions between 0 and 4 %.

There is a wide variation in the Na_2O and K_2O contents of the hydrous melts, which vary between 1-2.7 and 0.07-0.29 wt % respectively. These variations couple strongly with the mass balance residuals for these elements, implying that alkalis were variably lost from the melts. If the missing alkalis inferred from the mass balance are added back to the melt then the Na_2O melt compositions fall in the range 2.1-3.7 wt % and K_2O values are in the range 0.2-0.4 wt %. The alkalis were certainly not lost during chemical analyses because very similar concentrations can be obtained using both LA-ICP-MS and electron microprobe. The standard deviations of melt analyses within each sample are also relatively small. A plausible explanation is that Na_2O and K_2O dissolved into an H_2O -rich fluid which exsolves from the melt during quench crystallization. There is no evidence for hydrous minerals in the quench crystal assemblage, so as crystallization occurred free water, which cannot all partition into the structure of quenched crystals, must have exsolved and separated. In experiments where the outer capsule was pierced on recovery, water was observed to bubble out of the capsules. This was not done to all experiments so as not to damage the crystalline assemblage in the charge. Loss of alkalis to H_2O -rich fluids that separate on quenching likely explains the variable depletion of melts in these elements.

Fig. 3.4 shows clinopyroxene-melt partition coefficients for hydrous melts compared with dry melts from Walter (1998) at the same pressure and hydrous melts from Balta et al. (2011) and Tenner et al. (2012) at lower pressures.

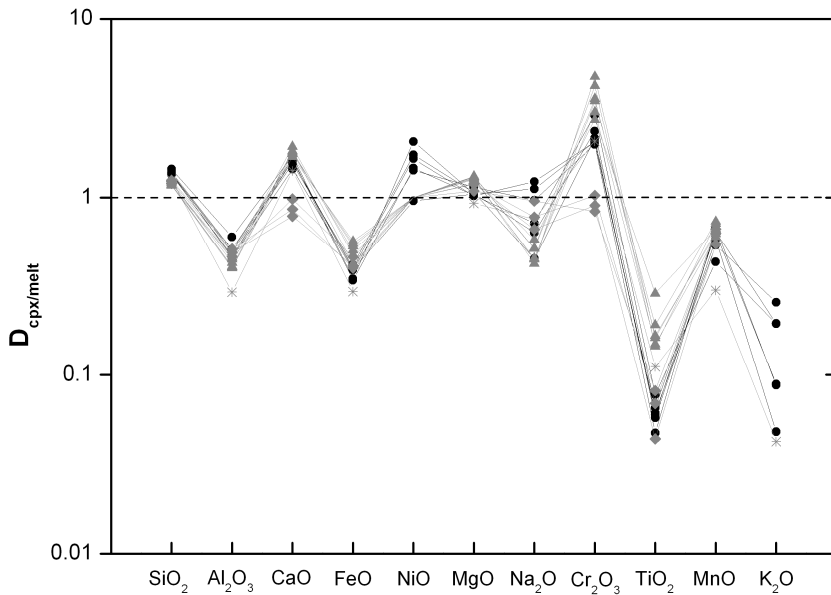


Fig. 3.4: Clinopyroxene-melt partition coefficients for multiply saturated hydrous melts at 6 GPa (black circles) compared with the dry-near solidus melt of Walter (1998), and hydrous melts of Balta et al. (2011) from 3 GPa and Tenner et al. (2012) from 3.5 GPa. Symbols for the literature data are as in Fig. 3.2.

The wide variation of Na, K and Ni partition coefficients from this study are coupled to losses apparent in the mass balance calculations. As explained above, for Na and K a plausible explanation is that they were mobilized in the charge in a hydrous fluid, which exsolved and separated from the melt during quench crystallization. Ni was likely lost with Fe due to alloying with the capsule. The partition coefficient of Ti seems to vary as a function of pressure, as consistent values are found between this study and the dry melting study of Walter (1998), which are higher than values for hydrous melts at lower pressures. On the other hand partition coefficients for Ca and Cr seem to be higher in the dry study of Walter (1998) compared to all wet melting studies regardless of pressure. For Ca this arises as a result of higher Ca contents in cpx in wet compared to dry experiments, which is quite a well reproduced phenomenon. The dry near solidus melt of Walter (1998) contain 9 wt % CaO which is near identical to the hydrous melts of this study. The near solidus cpx of Walter (1998), however, contains 7.8 wt % CaO compared to 13-15 wt % in this study. Although this difference could be reasonably attributed to temperature differences, as can Cr partitioning differences, the dry sub solidus cpx from this study also contained only 9.6 wt % CaO. An identical observation was made by Balta et al. (2011) at 3 GPa when comparing wet and dry cpxs produced at identical temperatures, which contained 17-18 wt % and 12.8 wt % CaO respectively. Balta et al. (2011) attribute this to a contraction of the cpx stability field in the presence of H₂O, however, we note that in experiments containing opx applying the Ca-Mg

exchange thermometer (Brey and Köhler, 1990) gives reasonable estimates for the wet samples, implying that the wet cpx stability field is unchanged with respect to opx. We suspect that this difference between wet and dry cpx compositions arises from the difficulty in equilibrating Ca contents of cpx and gt in dry samples and that dry cpx Ca contents are not in equilibrium. This is probably also the case in the study of Balta et al. (2011).

Garnet-melt partition coefficients are shown in Fig. 3.5, compared to the same literature data as described above for cpx.

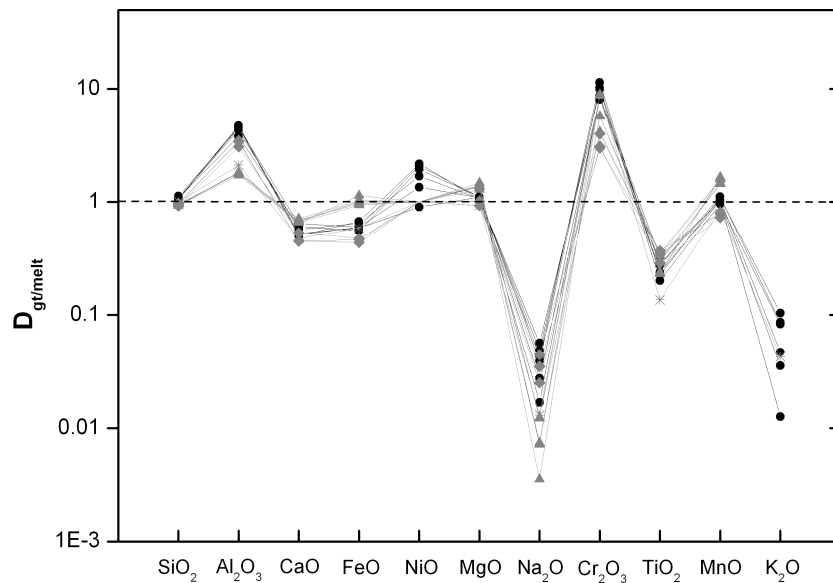


Fig. 3.5: Garnet-melt partition coefficients of eleven chemical components determined for multiply saturated hydrous melts at 6 GPa (black circles) compared with the same data as in Fig 3.4.

The partition coefficient for Al increases with increasing pressure from 3 to 6 GPa as a consequence of the lower melt alumina concentration at 6 GPa [5-6 wt % Al₂O₃ in our experiments and 6-7 in low degree dry melts from Walter (1998)] compared to 3 GPa (~13 wt %, Balta et al., 2011). Partition coefficients for Cr are higher than those reported close to the dry solidus at the same pressure by Walter (1998) but similar to the wet melting values of Balta et al. (2011) at 3 GPa, implying a reduction of the Cr partition coefficient with increasing temperature.

3.4.3 Melt H₂O concentrations and the depression of melting

In order to estimate the proportion of hydrous melt that may exist in the mantle at a given set of conditions, information on the depression of the silicate solidus as a function of melt H₂O

content is required. Such a relationship is necessary, for example, to determine the H₂O contents required for melts to form along a mantle adiabat at a specific depth. A particularly important aspect in this respect is that the effect of H₂O on melting point depression is likely to also be a function of silicate melt composition, and the compositions of specific importance at depths greater than 90 km are those in equilibrium with a residual 3 phases peridotite assemblage because the degree of melting will be small.

The chemical compositions of the melts produced in this study are very similar, when normalized to H₂O free conditions, to those analyzed close to the dry solidus at 1700 °C by Walter (1998). The depression of melting due to H₂O in the experiments from the current study can, therefore, be estimated to be 300 °C. The corresponding melt H₂O content is bracketed between the H₂O content of the 3 phase saturated starting melts, 10.5 wt%, and the resulting mass balanced melt H₂O contents 11.3-12.8 wt%. The resulting melting point depression as a function of melt H₂O content is shown in Fig. 3.6 along with data at 3.5 GPa from the previous study of Tenner et al. (2012).

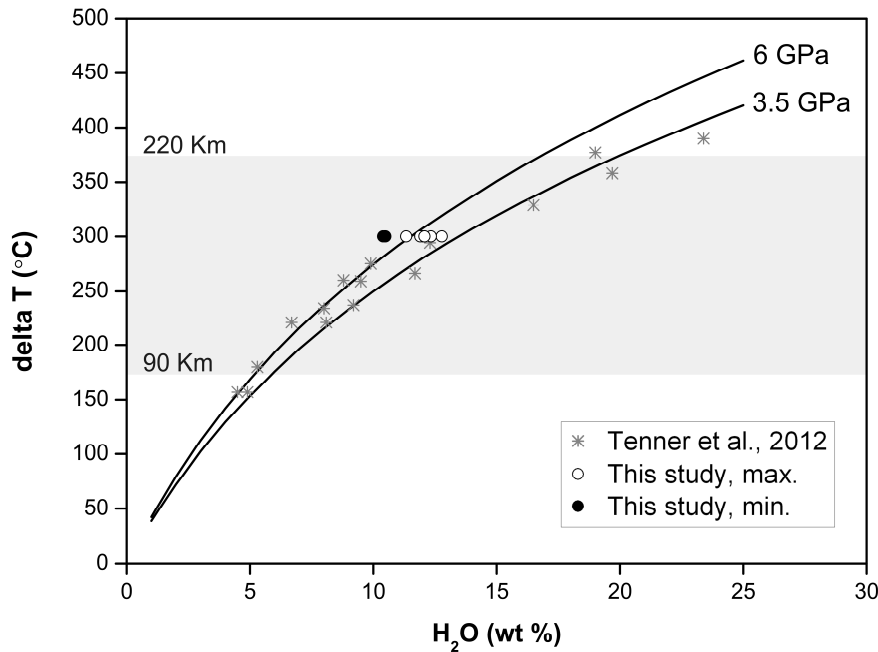


Fig. 3.6: The melting temperature depression plotted as a function of melt H₂O content for low degree hydrous peridotite melts. Data at 3.5 GPa are from Tenner et al. (2012). Data at 6 GPa are from this study: black filled circles indicate the H₂O content of the melt starting mixtures (Table 3.1), while the black empty circles indicate the water content of the multiply saturated (olivine bearing) melts given by mass balance calculations. The actual melt H₂O content should be bracketed by the open and filled symbols. Curves calculated from the cryoscopic equation (eq. 3.3) are shown calculated at 3.5 and 6 GPa. The grey area indicates the temperature depression required for hydrous peridotite melts to form over the depth interval of the seismically observed low velocity zone, as demarcated by Hirschmann et al. (2009).

Tenner et al. (2012) propose a simple model to describe the depression of melting due to H₂O. The model is based on the cryoscopic equation:

$$T_P^{hyd} = \frac{T_P^{dry}}{\left[1 - \frac{R}{\Delta S^{fus}} \ln(1 - X_{OH^-}^{melt}) \right]} \quad (3.3)$$

where R is the gas constant, T_P^{hyd} and T_P^{dry} are the hydrous and dry silicate melting temperatures at a given pressures, $\hat{e}S^{fus}$ is the molar entropy of fusion of the silicate and $X_{OH^-}^{melt}$ is the mole fraction of dissolved OH⁻ in the melt. Such a model is similar to that proposed by Silver and Stolper (1985) where dissolved H₂O reacts with oxygen in the melt to establish the equilibrium,



Tenner et al. (2012) assume, however, that full dissociation occurs to produce 2OH. The mole fraction of OH in the melt is then calculated from the melt H₂O content (H₂O wt %) as

$$X_{OH^-}^{melt} = \frac{(2H_2\text{Owt\%}/18.015)}{(2H_2\text{Owt\%}/18.015) + (100 - H_2\text{Owt\%})/\text{mol.wt}_{(\text{Silicate})}} \quad (3.5)$$

The molecular weight selected for the silicate phase is potentially an adjustable term in the model. Silver and Stolper (1985) assumed a molecular weight of the melt on a one oxygen basis. Where as Tenner et al. (2012) fit their experimental data assuming a 3 oxygen melt formula which gives a molar weight of 111 g/mol. Combining this value with literature data they determine a $\hat{e}S^{fus}$ of 44.4 J/K/mol.

Fig. 3.6 shows a comparison between this model calculated at 3.5 GPa and at 6 GPa. The model at 6 GPa is calculated by assuming the dry melting temperature determined by Walter (1998) and is shown to be quite consistent with the experimental bracket provided by this study. The shaded area indicates the melting point depression required for hydrous melts to exist along a mantle adiabat in the region of the seismic LVZ. The deepest extend of the LVZ

is estimate at 220 km which is approximately 7.5 GPa and data in this study are therefore consistent with melts at this depth containing 15-16 wt % H₂O.

3.4.4 Low degree hydrous melts and the origin of group II kimberlites

Kimberlites are volatile rich, ultrabasic silicate magmas that as a result of their highly enriched incompatible element contents must be produced by low degree partial melting of sources that have most likely been previously metasomatised (e.g. Eggler, 1978, 1989; Wyllie, 1980; Tainton and Mckenzie, 1994; Mitchell, 2004; Becker and Le Roex, 2006). The presence in kimberlites of diamonds and xenoliths that record high equilibration pressures implies that these magmas must originate from depths greater than 150 km and are therefore the deepest sourced magmas (e.g. Boyd, 1973; Carswell and Gibb, 1987; Yaxley et al., 2012). Kimberlites are subdivided into two types of rocks. Group I kimberlites appear to be more CO₂-rich and have been argued to have sub lithospheric sources (Smith, 1983). Group II rocks, referred to as orangeites after Mitchell (1995), generally contain mica i.e. are more H₂O-rich, and have been argued to originate within the subcontinental lithosphere (Smith, 1983). In Fig. 3.7 proposed ranges in composition of these two kimberlite groups are plotted on a volatile free basis from the compilation assembled by Becker and le Roex (2006).

Experimental studies conducted to investigate the genesis of both types of kimberlites can be divided into two types. The first have been performed to determine conditions where kimberlite melt compositions become multiply saturated in mantle phases (e.g. Edgar et al., 1988; Edgar and Charbonneau, 1993; Girnis et al., 1995; Ulmer and Sweeney, 2002; Girnis et al., 2011; Sokol et al., 2013). Such experiments must make assumptions on the likely pre-eruptive volatile contents of kimberlites, however, and quite often come to the conclusion that kimberlites were not saturated in all garnet-lherzolite phases. The melts produced are naturally close to those of the kimberlite melt starting compositions because they are near liquidus. The second type of experiments are those performed to assess if kimberlite melts can be produced from typical mantle garnet-lherzolite rocks in the presence of different proportions of volatiles (e.g. Canil and Scarfe, 1990; Ringwood et al., 1992; Kawamoto and Holloway, 1997; Dalton and Presnall, 1998; Brey et al., 2008; Gudfinnsson and Presnall, 2005).

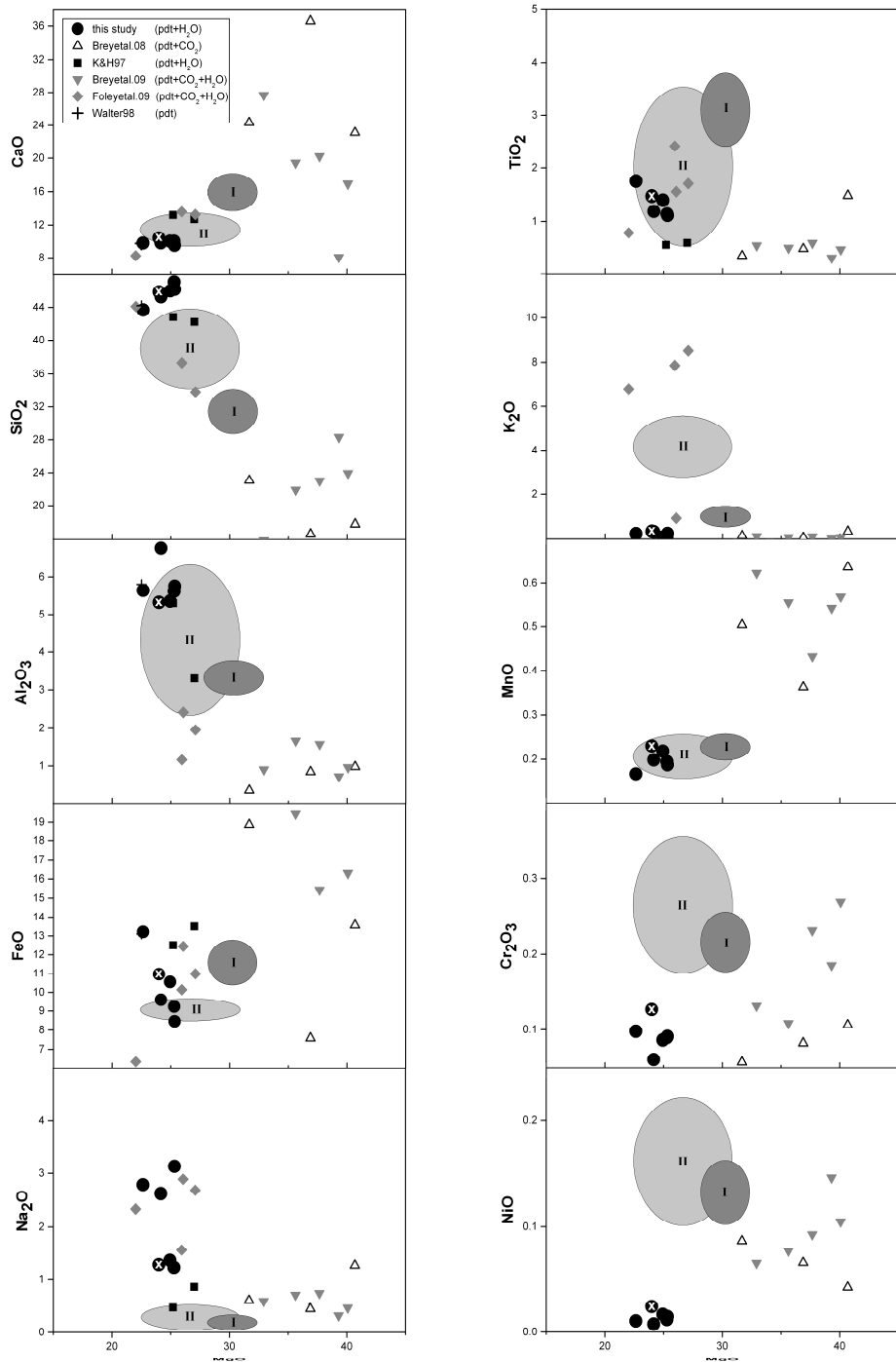


Fig. 3.7: Chemical compositions of hydrous multiply saturated melts are compared with melt compositions produced in previous volatile-bearing melting studies and the range of compositions estimated for natural group I and II kimberlites. Melts produced in this study in equilibrium with ol+cpx+garnet are indicated by filled circles with the white cross indicating an experiment that was in addition saturated in opx. Black squares indicate the H_2O -saturated near solidus melts of Kawamoto and Holloway (1997). Black, empty triangles indicate multiply saturated, CO_2 -rich melts from Brey et al. (2008). Inverse, grey triangles and grey diamonds are composition of CO_2 and H_2O bearing melts from Brey et al. (2009) and Foley et al. (2009), respectively. The cross indicates estimated dry peridotite zero melt fraction compositions at 6 GPa ~1700°C from the study of Walter (1998). Natural kimberlite data are from the ranges reported by Becker and le Roex (2006). The darker grey areas are for group I kimberlites, while the lighter grey areas are group II. All compositions are plotted on a volatile free basis.

The melt compositions from our study can be used to make the same type of assessment because, as outlined below, their similarity with group II orangeites implies a possible origin for these kimberlites from H₂O induced partial melting of garnet lherzolite or garnet wehrlite at approximately 6 GPa.

Kawamoto and Holloway (1997) performed experiments on H₂O-saturated garnet-lherzolite between 5 and 11 GPa and proposed that group II kimberlites might originate from partial melting of hydrated peridotite mantle at relatively low temperatures, approximately 1000 °C. The 4-phase saturated melt compositions from 5 and 7.5 GPa and from ~1000 °C are shown in Fig. 3.7, on a volatile free basis, and are remarkably similar to those of group II kimberlites, although FeO contents are too high and K₂O and other minor components were not considered. Compositions of hydrous melts produced by Kawamoto and Holloway (1997) at higher pressures, 10-11 GPa, are too high in MgO (>35 wt %) and FeO (~15-17 wt %) and low in Al₂O₃ and SiO₂ compared to natural kimberlites and are not shown. In Fig. 3.7 melts produced in studies where peridotite has been melted in the presence of CO₂ and CO₂-H₂O are also shown, normalized to volatile free compositions, in order to assess how melt compositions are likely to shift in the presence of CO₂ in this pressure range. Brey et al. (2008) investigated carbonated garnet lherzolite melting between 6-10 GPa. The 4-phase saturated CO₂-rich melts of Brey et al. (2008) produced between 1400-1700 °C, (Fig. 3.7), are SiO₂ and Al₂O₃ poor and CaO rich compared to all natural kimberlites. Brey et al. (2008) noted that higher temperature melts approach group I kimberlites in SiO₂ and CaO contents but these melts are still too low in Al₂O₃ and are no longer in equilibrium with cpx. Brey et al. (2009) performed similar experiments on melting of peridotite in the presence of H₂O and CO₂ in a 3:2 molar ratio. The multiply saturated melt compositions produced between 6-10 GPa and 1300-1400 °C (Fig. 3.7) are slightly less CaO rich but have slightly more Al₂O₃ and SiO₂ than melts produced from CO₂-peridotite systems at similar conditions. Multiply saturated melts produced by Foley et al. (2009) from K₂O enriched peridotite in the presence of a 3:7 ratio H₂O-CO₂ mixture between 5-6 GPa and 1180-1240 °C, however, show the same general trend but in addition have lower MgO average contents. These melts plot very close and in some cases within the field of group II kimberlites for the major elements. The effect of H₂O on carbonated peridotite melts can be rationalized because H₂O lowers the silicate solidus and therefore increases the proportion of silicate melt components, i.e. SiO₂ and Al₂O₃, in the carbonate melts, which are otherwise dominated by CaO and MgO. Adding

H_2O , therefore, has a similar effect as increasing temperature for a carbonate melt in equilibrium with peridotite. In respect of these 4 components, much of the field of group II magmas can be produced by melting of garnet wehrlite or garnet lherzolite at approximately 6 GPa and near adiabatic temperatures in the presence of $\text{H}_2\text{O}-\text{CO}_2$. Group I kimberlites can most likely also be produced from peridotites fluxed by an even narrower range of H_2O and CO_2 compositions, as proposed by Sokol et al. (2013).

Although the compositions of group II kimberlites are consistent with H_2O -rich $\pm\text{CO}_2$ fluxed melting of garnet-lherzolite or wehrlite, FeO , alkalis and several other minor elements are in poor agreement. The hydrous melt FeO contents from this study vary between 8.5 and 13.5 wt % as a result of losses of Fe due to alloying with noble metal capsules during the experiments. Ni was similarly affected. However, it is the FeO poor melts, in equilibrium with $\sim\text{Fo93}$ olivine compositions, which show the best agreement with the natural samples. This is consistent with an origin of group II kimberlites in cratonic lithosphere, where such olivine compositions are quite typical (e.g. Boyd, 1989). Low FeO contents are attributed to an early phase of extensive melting that created the cratonic lithosphere and also raised Cr_2O_3 contents in the residue. Group I kimberlite FeO contents, on the other hand, are more consistent with an origin in the asthenospheric mantle, where Fo89 olivine likely dominates (e.g. Boyd, 1989).

Hydrous melt Na_2O contents range from 1.5 to 4 wt %, and do not match group II values, which are <0.4 wt %. This most likely implies a melt depleted source, which was not re-enriched in Na_2O . High K_2O contents, on the other hand, are a prominent characteristic of group II kimberlites, which average ~ 4 wt % on a volatile free basis (Becker and le Roex, 2006) but K_2O concentrations in experimental melts are significantly lower, apart from in the study of Foley et al. (2009) where a K_2O enriched (1.74 wt %) starting material was employed. The high K_2O concentration of group II kimberlites is a source characteristic (Mitchell, 1995; Becker and le Roex, 2006). Using partition coefficients for K_2O it is not possible to obtain these high concentrations from typical garnet lherzolite compositions (i.e. Jagoutz et al., 1979), regardless of the melting fraction, as shown in Fig. 3.8.

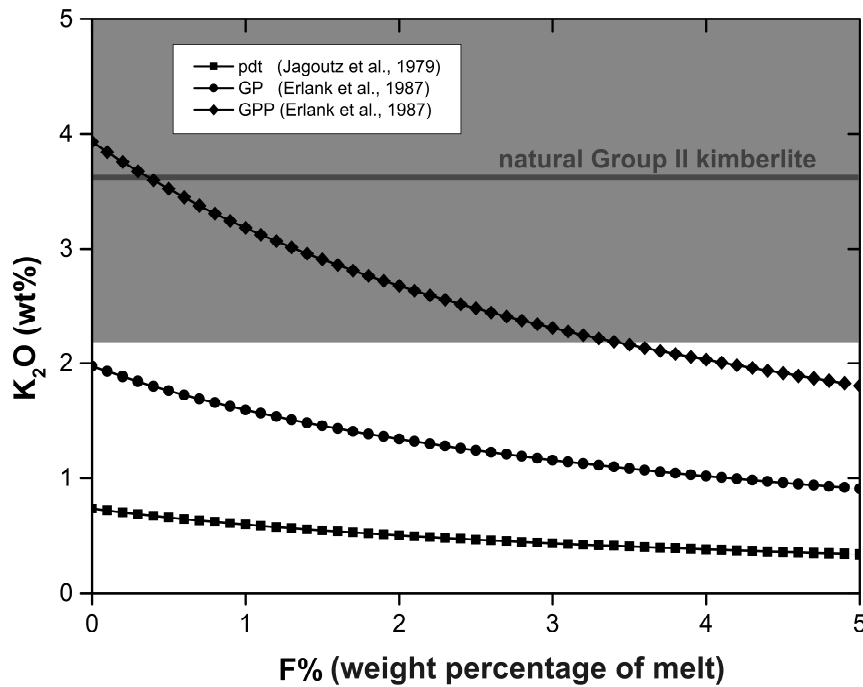


Fig. 3.8: Melt K₂O contents as a function of the percentage of partial melting (F %) calculated for melts produced from a natural peridotite (Jagoutz et al., 1979), a garnet peridotite (GP) and a garnet, phlogopite peridotite (GPP) reported by Erlank et al. (1987). Values for natural group II kimberlites proposed by Becker and le Roex (2006) are also displayed for comparison (horizontal, grey line with shaded area representing standard deviation). The calculations were performed for batch melting and using K partition coefficients determined from this study.

For this calculation K partition coefficients were determined from our experiments but corrected for the previously discussed K₂O-loss from the melt using the mass balance residuals. The resulting coefficients are in good agreement with previous studies (Chamorro et al., 2002; Tenner et al., 2012; Suzuki et al., 2012). Metasomatic processes that lead to K₂O enrichments have been documented in peridotitic xenoliths from the sub continental lithosphere, both from South Africa (Erlank et al., 1987) and for other cratons (Kopylova and Russel, 2000; van Achterbergh et al., 2001). Erlank et al. (1987) identified a sequence of progressively metasomatised assemblages from garnet peridotite (GP), progressing to garnet phlogopite peridotite (GPP), phlogopite peridotite (PP) and finally phlogopite K-richterite peridotite (PKP). This sequence introduces K₂O and H₂O into the rock and leads to a decrease in the Al₂O₃ content. As shown in Fig. 3.8, melting of a GPP composition, which contains initially 0.16 % K₂O, can produce K₂O rich melts that match group II kimberlite magmas, if melt fractions are <3.5 % (Becker and le Roex, 2006) and average K₂O values are approached at a 0.5 % melting. GPP metasomatism can be considered as the addition of ~1.5

wt % phlogopite ($\text{KMg}_3\text{AlSi}_3\text{O}_{10}\{\text{OH}\}_2$) to a peridotite assemblage (Erlank et al., 1987) and as shown in Fig. 3.9 low degree melting of such a rock produces group II type K_2O contents.

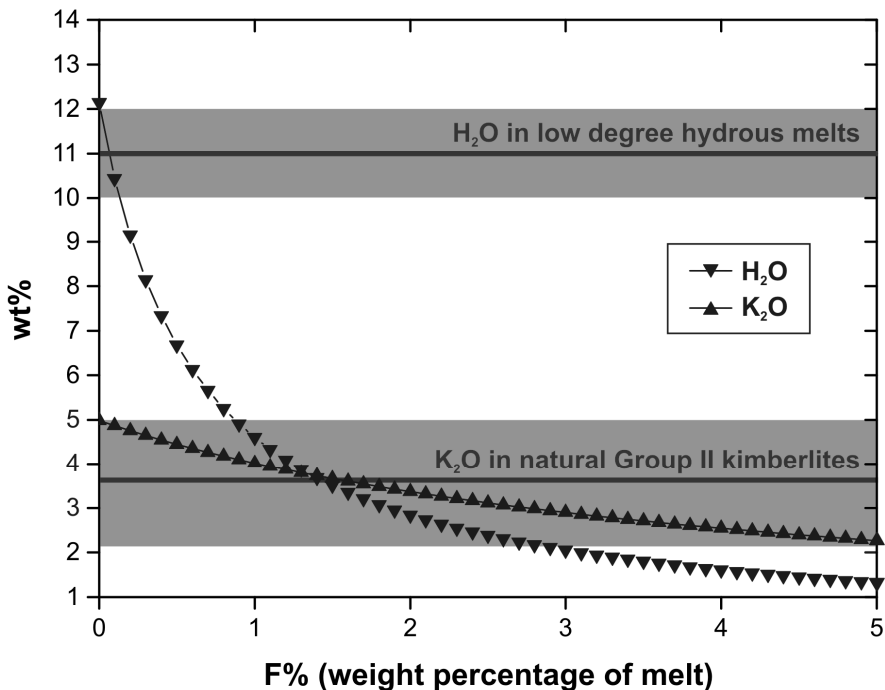


Fig. 3.9: Melt H_2O and K_2O contents calculated as a function of the percentage of partial melting for a mantle peridotite (Jagoutz et al., 1979) composition enriched by adding 1.7 wt % $\text{KMg}_3\text{AlSi}_3\text{O}_{10}\{\text{OH}\}_2$ phlogopite- i.e. similar to GPP. The calculations were performed for batch melting and using partition coefficients for K from this study and for H_2O as described in the text. The range of K_2O contents for natural group II kimberlites reported by Becker and le Roex (2006) is indicated (horizontal line), in addition to the H_2O content required to stabilize these melts at 1400 °C and 6 GPa (horizontal line), as determined in this study. Shaded areas indicate standard deviations of the K_2O (Becker and le Roex, 2006) content and a melt H_2O content uncertainty of 1 wt %.

However, we can obtain additional constraints on the melting process by also considering the partitioning of H_2O , and by determining the melt fraction required to produce sufficient H_2O to stabilize melting at 1400 °C if the peridotite rock initially contained 1.7 % phlogopite. We have calculated the partition coefficient for H_2O between a mantle peridotite and low degree melts based on melt H_2O contents from this study and coexisting mineral H_2O contents measured in Chapter 4. Multiply saturated hydrous melts at 6 GPa and adiabatic temperatures contain approximately 10-12 wt % H_2O . To achieve the H_2O and K_2O contents of group II kimberlites, melt fractions of ~0.2 % are required at these conditions. In this analysis it is assumed that phlogopite is consumed in the melting process and in fact experimental studies indicate that phlogopite breaks down below 1300 °C at 6 GPa (Konzett and Ulmer, 1999). Kimberlite melts produced in this way could still have equilibrated with the mantle at higher

temperatures if the very low degree melts produced upon phlogopite breakdown did not initially separate from the residual assemblage. This is plausible because the permeability of the mantle would be very low for small-degree melt produced when phlogopite breaks down (McKenzie, 1989; Tainton and McKenzie, 1994). A scenario is therefore envisaged where heating of the lower cratonic lithosphere occurs due to rising temperatures in the underlying asthenosphere, perhaps due to the proximity of a mantle plume. Phlogopite breaks down (~ 1300 °C) as temperatures rise at the base of the lithosphere but compaction and segregation of the kimberlite melt occurs at higher temperatures (~ 1400 °C). The argument for the melt equilibrating at normal adiabatic temperatures is well founded as long as the original source of K₂O and H₂O is phlogopite. If melting temperatures were lower, then melt H₂O contents have to be higher (Fig. 6). To achieve the required melt H₂O content from a GPP rock at 1300 °C, the melt fraction would have to be even lower and the resulting K₂O concentration of the melt would be much higher than group II kimberlites. Alternatively the H₂O content of the source might be increased by adding more phlogopite but this would again result in melt K₂O contents that were too high. From an analysis of the required H₂O and K₂O concentrations of the group II melts, the temperatures and phlogopite content of the rock are quite narrowly constrained. The model breaks down if we assume H₂O and K₂O were added to the rock in some other fashion i.e. their ratio is not coupled by phlogopite stoichiometry. Previous geochemical studies have also recognized, however, that the K₂O/H₂O ratio proposed for enriched magma components corresponds closely to that found in phlogopite (Michael, 1988). One potential origin for this ratio and for the formation of phlogopite, would be as a result of metasomatism by K-rich fluids rising from a subducting slab as a result of the breakdown of the mineral phengite (Schmidt, 1996). $K(AlMg)_2(OH)_2(SiAl)_4O_{10}$ phengite preserves the same K₂O/H₂O ratio as phlogopite.

The presence of some CO₂ would act to lower the temperature required to reproduce the melt H₂O and K₂O contents in two ways. First it would lower the amount of H₂O required to sustain a melt at lower temperatures and secondly it would lower the activity of H₂O in the melt, forcing more H₂O out of the solid phases. In fact an influx of small amounts of carbonate melt might be a potential trigger mechanism for the formation of the kimberlite because it would lower the stability field of phlogopite (Ulmer and Sweeney, 2002; Yamashita et al., 1995). The amount of CO₂ permissible in the H₂O-rich melts for them still to be in the group II compositional range cannot be accurately determined from existing

studies, however, due to the difficulty in determining melt volatile contents at these conditions.

4. The distribution of H₂O between silicate melt and nominally anhydrous peridotite and the onset of hydrous melting in the deep upper mantle

4.1 Introduction

H₂O is apparently the most abundant volatile component in the Earth's depleted mantle (Marty, 2012) where it is likely present at shallow levels within silicate melts (Asimow and Langmuir, 2003; Kawamoto and Holloway, 1997) and with increasing depth as hydrogen defects inside the nominally anhydrous minerals (NAMs) that comprise mantle peridotite (e.g. Bell and Rossmann, 1992; Kohlstedt et al., 1996; Bofan-Casanova et al., 2000). Only in the lithospheric mantle or in subduction zones are temperatures likely to be low enough for H₂O to be present within a fluid phase or hosted in nominally hydrous minerals such as pargasitic amphibole or phlogopite (Frost, 2006). Although estimates for the amount of H₂O in the depleted upper mantle are relatively low, i.e. 50–200 ppm (e.g. Michael, 1988; Saal et al., 2002), even small amounts of H defects in mantle minerals can have significant effects on transport properties such as electrical conductivity (Wang et al. 2006; Poe et al. 2010), rates of solid state diffusion (Costa and Chakraborty, 2008) and rheological properties (Mackwell et al., 1985; Karato et al., 1986; Hirth and Kohlstedt, 1996; Jung and Karato, 2001), although the extent of the last two effects has been recently questioned (Fei et al., 2013). One of the most important influences of H₂O in the mantle, however, is to lower the solidus temperature of mantle rocks (Kushiro et al., 1968; Green, 1973). For adiabatically up welling mantle, this allows the formation of melts at greater depths than would be possible under dry conditions (Asimow and Langmuir, 2003). This can increase the depth interval of the melting column beneath mid ocean ridges and affect geochemical and geophysical properties, principally through the redistribution of H₂O and other incompatible trace elements (Bercovici and Karato, 2003; Takei and Holtzman, 2009). The viscosity of mantle melts is also strongly influenced by the presence of H₂O (Lange, 1994; Giordano et al., 2008). Given the key roles that H₂O plays in the mantle it is important to be able to predict conditions where it might induce melting below the dry solidus and its distribution between mineral and melt phases.

As described in detail by Hirschmann et al. (2009) the presence and proportion of hydrous melt formed in the mantle at conditions below the dry peridotite solidus will be a function of

the H₂O mineral-melt partition coefficients, $D_{H_2O}^{\min/melt}$, and the melt H₂O content. With decreasing temperature below the dry solidus, melt H₂O contents must increase, leading to an increase in the H₂O concentration in the coexisting NAMs. For a given pressure and bulk composition the maximum storage level of H₂O in NAMs can be determined from the mineral $D_{H_2O}^{\min/melt}$ and the melt H₂O content at the particular temperature. Once there is sufficient H₂O available to surpass this storage level a hydrous partial melt can form, with the melt fraction at any temperature below the dry solidus being essentially proportional to the amount of H₂O in the system.

Many previous studies have focused on determining the solubility of H₂O in NAMs in fluid saturated experiments, where the low density fluid has an H₂O activity that is near unity (e.g. Kohlstedt et al., 1996; Bolfan-Casanova et al., 2000; Smyth et al., 2006). Due to the low H₂O contents in the bulk of the mantle, however, hydrous melting likely occurs at fluid under-saturated conditions. In this case NAM H₂O contents will be a function of the melt H₂O activity. Experiments performed in simplified chemical systems (e.g. Smyth et al., 2006; Grant et al., 2006; Litasov et al., 2007; Bali et al., 2008) will likely have melt H₂O activities that differ to those in the mantle, particularly if the system excludes elements that behave incompatibly or that influence melt H₂O activity. As mantle bulk H₂O concentrations are small, the composition of the solid mantle assemblage will remain mainly unaltered by the formation of small degree hydrous melts, except in the most incompatible elements. The most relevant values of $D_{H_2O}^{\min/melt}$ for the upper mantle will consequently be for small degree melts in equilibrium with peridotite assemblages. This is particularly important because $D_{H_2O}^{\min/melt}$ will also depend on mineral compositions, which will change at higher degrees of melting.

Experimental measurements of $D_{H_2O}^{\min/melt}$ between melts produced in equilibrium with a peridotite assemblage (olivine, clinopyroxene [cpx], orthopyroxene [opx] and garnet) exist to pressures of 2 GPa (Koga et al., 2003; Aubaud et al., 2004; Hauri et al., 2006). A limited number of $D_{H_2O}^{\min/melt}$ values have also been reported for pyroxenes and garnet between 3 and 5 GPa (Hauri et al., 2006; Aubaud et al., 2008; Tenner et al., 2009) produced from mid ocean ridge basalt (MORB) or alkali-basalt bulk compositions, sometimes mixed with additional olivine and opx. However, such melts are generally too Si-rich to crystallise olivine above 2

GPa and melt CaO and Al₂O₃ contents are generally higher than peridotite melts at the same conditions.

Direct $D_{H_2O}^{\text{min/melt}}$ measurements at pressures >2 GPa for natural peridotite systems are very challenging, however, because peridotite partial melts at these conditions do not quench to form glasses but rather crystallize on quenching and thereby lose most of the H₂O. This results from a decreasing SiO₂ content of melts in equilibrium with olivine with pressure, which decreases melt polymerisation and the propensity to form glasses. Such crystallised melts cannot be meaningfully analyzed to provide melt H₂O contents, although some investigators have tried (e.g. Ohtani et al., 2000). One way to overcome this is to determine the proportion of melt in a charge by performing a mass balance based on analyses of other elements, and determine the H₂O content by assuming all H₂O from the starting material enters the melt i.e. negligible H₂O enters solid phases. This mass balance approach relies crucially on the assumption that H₂O is not lost from the experimental charge during the experiment. The accuracy in H₂O contents determined in this way increases with the fraction of melt. If only interstitial melts are formed, as expected for more typical mantle H₂O contents, mass balanced melt H₂O contents are highly uncertain (Tenner et al., 2011). Moreover, the determination of H₂O contents in mineral phases also requires the production of crystals that are sufficiently large for the necessary analysis techniques to be employed, which can also be challenging at high pressures.

In Chapter 3, compositions of hydrous low degree melts in equilibrium with a natural mantle peridotite assemblage at 6 GPa and 1400 °C were determined. These conditions equate to those of an adiabat with a potential temperature of 1327 °C at ~180 km (Stixrude and Linthgow-Bertelloni, 2007). Iterative crystallization experiments were performed whereby large melt fractions were equilibrated with a typical peridotite assemblage. The mineral-melt partition coefficients for all elements in the recovered melt were used to adjust the melt composition in successive experiments until equilibrium with a complete peridotite assemblage was achieved (Dasgupta and Hirschmann, 2007). Melt proportions in most experiments were > 80 wt % such that accurate mass balance could be used to determine melt H₂O contents. In order to minimize the loss of H₂O from the capsules relatively short run durations were employed but because mineral phases were completely recrystallized from the melt, positive indicators for inter phase chemical equilibrium could be demonstrated. The

results indicate that in the absence of other volatiles, a near solidus mantle peridotite melt has an H₂O concentration of ~11 wt %, at conditions equivalent to a ridge adiabat at ~180 km depth (Chapter 3).

Here the H₂O contents of the peridotite minerals olivine+cpx±opx+garnet in equilibrium with this hydrous melt at 6 GPa and 1400 °C have been determined by means of secondary ion mass spectrometry (SIMS) and elastic recoil detection analysis (ERDA). Using these data $D_{H_2O}^{\text{min/melt}}$ for all minerals in the assemblage are calculated, and the results are used to quantitatively examine the onset and extent of melting as a function of bulk H₂O content at depths beneath mid ocean ridges. These data are also used to construct a model for the distribution of H₂O between peridotite minerals as a function of depth in the upper mantle. The results of this model have implications for changes in the dominant slip system in olivine with depth that may explain changes in observed seismic anisotropy in the mantle (e.g. Montagner and Kennet, 1996).

4.2 Methods

4.2.1 Sample synthesis and selection

In previously described experiments (Chapter 3) garnet-lherzolite and garnet-wehrlite mineral assemblages were produced in equilibrium with large pools of hydrous melt (Fig. 4.1) at 1400 °C and 6 GPa through a series of iterative crystallization experiments. A peridotite composition (Jagoutz et al., 1979) and an initial hydrous silicate melt composition were prepared from oxides and hydroxides. Approximately 10-20 % peridotite was mixed with the melt composition and equilibrated in a multianvil apparatus. In order to minimize H₂O loss an inner Fe soaked Au/Pd capsule, containing peridotite and hydrous melt, was enclosed by an outer Pt/Rh capsule containing just hydrous melt (Balta et al., 2011). After each experiment the melt and mineral compositions were analyzed and using the determined mineral-melt partition coefficients a new hydrous melt composition was fabricated based on mineral compositions of a sub solidus peridotite assemblage. In order to aid the formation of large crystals the run temperature of 1400 °C was initially overstepped by 50 °C in the first 5 minutes of the experiment then cooled to 1400 °C for run time of 30 minutes. On piercing recovered experimental capsules H₂O was observed to bubble out, however, this was almost certainly H₂O expelled from the melt as it crystallized. The H₂O concentrations employed

were far below fluid saturated conditions (see Dixon et al., 1995), which would preclude the existence of a solid assemblage at these temperatures.

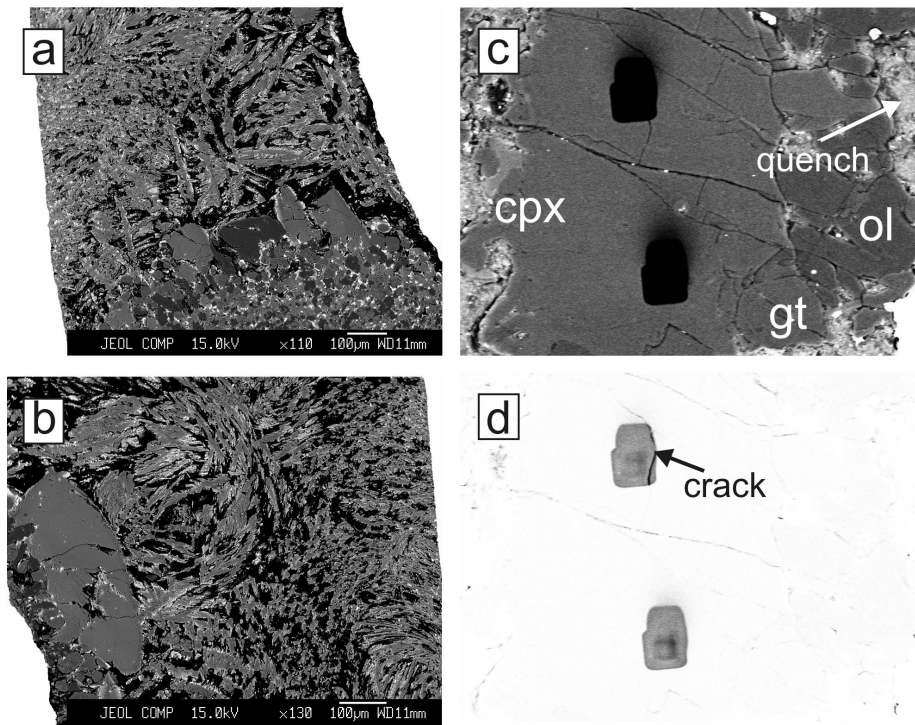


Fig. 4.1: Backscattered electron images of typical experimental charges investigated in this study (run S5581). In this experiment, crystals of olivine (dark), garnet (medium gray with round shape) and large cpx (light grey) are in equilibrium with pools of melt. The dark rectangles in (c) are pits produced by the nanoSIMS analyses (see later). In (d), the same backscattered electron image shown in (c) is displayed with a different setting of contrast, brightness and noise reduction to enhance the details at the bottom of the pit formed by the nanoSIMS analyses. A crack is observed on the right side of the upper pit, and this particular analyses was discarded. Images in panels (c) and (d) are approximately 200 µm in width.

The resulting assemblages contain large fractions of melt for which a mass balance can be performed to determine the H₂O content. The equilibrium mineral compositions are close to those produced from a subsolidus dry mantle peridotite composition (Jagoutz et al., 1979) at the same conditions, which crystallizes a garnet-wehrlite assemblage of olivine, cpx and garnet. Loss of Fe to the capsule walls resulted in mineral FeO contents slightly below those expected for the athenospheric mantle (Fo₈₉₋₉₁) but in good agreement with lithospheric samples from similar conditions (Fo₉₂₋₉₃). In some hydrous melt experiments opx was also formed. NanoSIMS and ERDA H₂O analyses were performed on 6 experimental charges (Table 4.1). Chemical compositions of the mineral phases in these charges are reported in Chapter 3 (Table 3.3) and Table 4.2.

4. The distribution of H₂O between silicate melt and nominally anhydrous peridotite

Table 4.1: water contents of minerals in the experimental charges and partitioning coefficients of H₂O between NAMs and melts

Experiment	n (SIMS)	H ₂ O SIMS (ppm wt)	σ	H ₂ O ERDA (ppm wt)	σ	$D_{H_2O}^{ol/melt}$	$D_{H_2O}^{cpx/melt}$	$D_{H_2O}^{gt/melt}$
<u>S5270-I</u>								
opx	2	681	30			0.0062 (3)		
gt	5	297	103				0.0027 (9)	
<u>S5270</u>								
cpx	5	1097	110			0.0062 (1)		
opx	5	681	11				0.0100 (10)	
gt	8	406	83					0.0037 (8)
<u>S5278</u>								
cpx	5	1132	148			0.0068 (4)		
opx	3	749	45				0.0103 (13)	
<u>S5281</u>								
ol	4	376	25			0.0034 (2)*		
cpx	6	1241	101				0.0113 (9)	
opx	5	676	35				0.0062 (3)	
gt	5	310	34					0.0028 (3)
<u>S5291-I</u>								
ol	1	370				0.0034		
opx	2	753	78				0.0068 (7)	
gt	1	353						0.0032
<u>S5291</u>								
ol	4	399	28			0.0036 (3)		
cpx	1	1316					0.0120	
gt	4	296	16					0.0027 (1)
<u>S5577</u>								
ol	3	411	6			0.0037 (1)		
gt	6	305	52				0.0028 (5)	
<u>S5581</u>								
ol	10	485	52			0.0044 (5)		
cpx	9	1451	41				0.0132 (4)	
gt	7	410	75					0.0037 (7)
Average								
n (SIMS): number of nanoSIMS analyses on different crystals; σ : 1 standard deviation of the SIMS and ERDA analyses								
*: analyses from the inner capsule of the experimental charge (see text); *: 1 standard deviation in reference to the last digit.								

Table 4.2: chemical composition (in wt %) of mineral phases in experiments S5270-I and S5291-I and in the subsolidus peridotite at same P-T conditions

Experiment	SiO ₂	Al ₂ O ₃	CaO	FeO	NiO	MgO	Na ₂ O	Cr ₂ O ₃	TiO ₂	MnO	K ₂ O	Total
S5270-I												
opx (11) ¹	57.09(56) ²	1.25(25)	1.28(17)	5.75(1.05)	0.07(4)	34.44(46)	0.15(2)	0.23(5)	0.07(5)	0.12(2)	0.007(9)	100.46(32)
gt (10)	43.19(11)	21.19(15)	3.76(19)	6.32(14)	0.02(2)	23.67(29)	0.03(2)	2.22(6)	0.24(3)	0.22(6)	0.003(4)	100.85(20)
S5291-I												
ol (2)	41.32(11)	0.05(1)	0.10(1)	7.70(45)	0.05(5)	51.56(52)	0.02(1)	0.06(1)	0.05(2)	0.12(3)	0.005(7)	101.03(23)
opx (6)	57.90(29)	1.44(19)	1.27(18)	4.56(39)	0.04(3)	35.10(31)	0.27(2)	0.17(3)	0.02(1)	0.10(5)	0.007(5)	100.87(22)
gt (10)	43.78(23)	21.86(14)	3.42(27)	5.31(25)	0.02(2)	24.65(37)	0.04(1)	1.33(6)	0.17(2)	0.16(4)	0.007(8)	100.75(29)
subsolidus												
ol	40.48(33)	0.12(5)	0.17(2)	9.60(15)	0.37(6)	48.84(24)	0.03(2)	0.10(2)	0.05(3)	0.13(4)	0.004(3)	99.99(48)
cpx	54.24(93)	2.68(65)	9.63(48)	5.18(11)	0.16(7)	24.80(63)	1.03(7)	0.44(3)	0.31(4)	0.19(5)	0.08(2)	99.33(100)
gt	42.91(75)	21.33(1.05)	4.77(37)	6.56(15)	0.02(2)	22.19(24)	0.06(4)	1.53(10)	0.90(5)	0.26(4)	0.001(1)	100.59(23)

¹ number of microprobe analyses performed on the mineral; ² one standard deviation of the components in reference to the last digit. For the subsolidus run (chapter 3) approximately 20 crystals for each phase were employed in the calculations of average and standard deviation.

4.2.2 nanoSIMS

Analyses were performed using a Cameca NanoSIMS 50L ion microprobe installed at the Department of Terrestrial Magnetism, Washington D.C. To avoid the release of volatiles from epoxy resin, resins were removed and polished capsules were pressed into indium contained inside a hole produced in an aluminium disk (Koga et al., 2003). Samples were then cleaned with ethanol, coated with gold and dried in a vacuum furnace at ~100 °C for approximately 1 day. Prepared charges were mounted in a sample holder and kept overnight under vacuum (~5 x 10⁻¹⁰ Torr). Procedures described by Koga et al. (2003) were followed to maintain a low-H background and improve the H detection limit. The NanoSIMS chamber was baked for more than 1 day before the analyses, to further reduce the contamination of H₂O in the vacuum. Analyses were performed with a vacuum of ~2 x 10⁻¹⁰ Torr. A primary Cs⁺ beam with a current of ~14 nA was used with a raster area for each measurement of 25x25 μm. To avoid surface contamination, pre-sputtering was conducted for 3 minutes and ions were then counted for a further 3 minutes from an area of 6x6 μm. In addition to ¹⁶OH⁻, species ¹²C⁻, ¹⁹F⁻ and ³⁰Si⁻ were measured simultaneously. The concentrations of C and F were found to be sensitive indicators of surface contamination as neither of these elements were intentionally added to the sample. High C and F analyses in the range 10-100 ppm wt were found to correspond to voids or cracks in the crystal surface or the overlap of the ion beam with the edge of a crystal. Such measurements, which were then discarded, were observed particularly when the grain size of the crystals was <30 μm.

Each pit formed in the crystals by NanoSIMS analysis was subsequently examined by secondary electron or backscattered electron imaging using a scanning electron microscope. Through this procedure the exact location of each analysis was obtained and the absence of cracks or inclusions in the analyzed portion of the crystal was confirmed (Fig. 4.1). If such features were present the H₂O analysis was discarded. The ¹⁶OH⁻ signal was standardized using natural and synthetic olivine, garnet, clinopyroxene and orthopyroxene standards with varying H₂O contents (Koga et al., 2003). The detection limit was determined to be between 6 and 8 ppm wt H₂O using synthetic anhydrous crystals of olivine.

4.2.3 ERDA

The concentration of H in some crystals was additionally investigated using ERDA (Table 4.1). Recently, the detection limit for H in NAMs was reduced to ~54 ppm wt H₂O with this technique (Withers et al., 2012), an improvement by a factor of 9 compared to previous analyses (Sweeney et al., 1997). Details of the technique can be found in Khodja et al. (2001), Raepsaet et al. (2008), Bureau et al. (2009), Aubaud et al. (2009) and Withers et al. (2012). Withers et al. (2012) recently calibrated Fourier transform infra red (FTIR) measurements of H₂O in large (300-1000 µm) olivine crystals using ERDA and in addition found good agreement with SIMS analyses.

ERDA measurements were carried out at the Laboratoire d'Etudes des Eléments Légers, SIS2M, CEA, Saclay, using a Van de Graff accelerator producing a 3 MeV ⁴He⁺ micro-beam. Measurements were performed with a grazing angle in order to enhance the ejection of H atoms by the incident ⁴He particles, allowing a final size of the incident beam of approximately 4x16 µm². The geometry of the analysis was determined by examining a series of well-known standards (see e.g. Raepsaet et al., 2008). A series of simultaneous analyses of secondary emissions were performed: an X-ray detector collects particle induced X-ray emissions (PIXE), an annular detector records Rutherford backscattered (RBS) particles and an ERDA detector collects H atoms expelled from the samples. PIXE and RBS analyses were used to map the major elements and therefore identify the correct crystals. RBS was used to determine the total number of incident particles on the target during acquisition. To measure H contents the beam was scanned over an area of approximately 150x150 µm during ~ 2 hours. Using the resulting H-maps a region was selected from which H data were processed. The H content of the crystals was calculated by processing both RBS and ERDA data with the SIMRA software (Mayer, 1999). An example of an ERDA H-map and an energy spectrum are shown in Fig. 4.2.

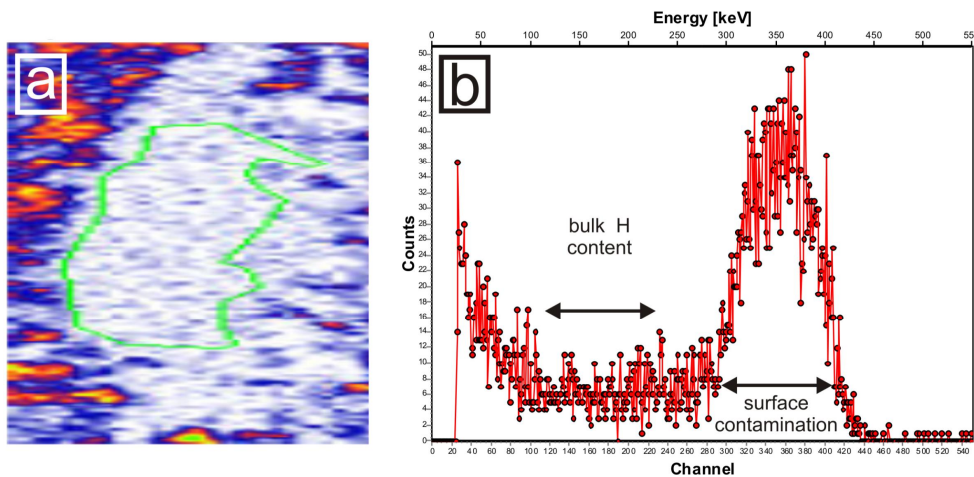


Fig. 4.2: (a) ERDA map of hydrogen from experiment S5581-O. The concentration of H is indicated by the different colours starting from white (lowest) and increasing through blue, red, yellow and green (highest). The white-blue region delimits a clinopyroxene crystal while the strong signal (yellow-red) in the surroundings comes from interstitial voids in the quenched melt that were filled with superglue during the sample preparation. The area of interest within the crystal, delimited by the green line, is employed in the calculation of the H₂O content. If cracks or inclusions of significant dimensions can be identified in such maps, they can be excluded from the H determination. The entire image is 270 x 270 µm. (b) ERDA spectrum of the cpx crystal shown in (a). In this image the number of counts accumulated is displayed versus the energy of the H atoms arriving at the detector. The high energy signal corresponds to contamination by surface H atoms, which can be distinguished from bulk H atoms that are ejected with lower energy since the incident beam must penetrate the sample. Simulations of the ERDA spectrum performed to calculating the H content only consider the flat region of the spectrum.

4.3 Results

4.3.1 H₂O concentrations in NAMs

In most charges crystals ranged in size up to 50 µm, however, in a few cases crystals >150 µm were grown (Fig. 4.1). NanoSIMS analyses were performed on crystals with diameters down to ~20 µm. Up to 10 NanoSIMS analyses could be performed on many crystals with approximately 6 analyses for each mineral in each charge providing suitable statistics. In the majority of experiments the H₂O content determined for each phase varied very little. Olivines displayed maximum H₂O variations within charges of between 2 and 11 %. Only in one experiment (S5270) did the garnet H₂O concentrations vary by 35%. Although variations in mineral H₂O contents between experiments are also small they do correlate with small changes in mineral compositions as discussed below. Average mineral H₂O contents for each phase in each experiment are reported in Table 4.1.

ERDA measurements were carried out on 4 crystals of ol, cpx and gt (Table 4.1), which were previously measured by NanoSIMS, allowing a direct comparison between techniques (Table 4.1, Fig. 4.3).

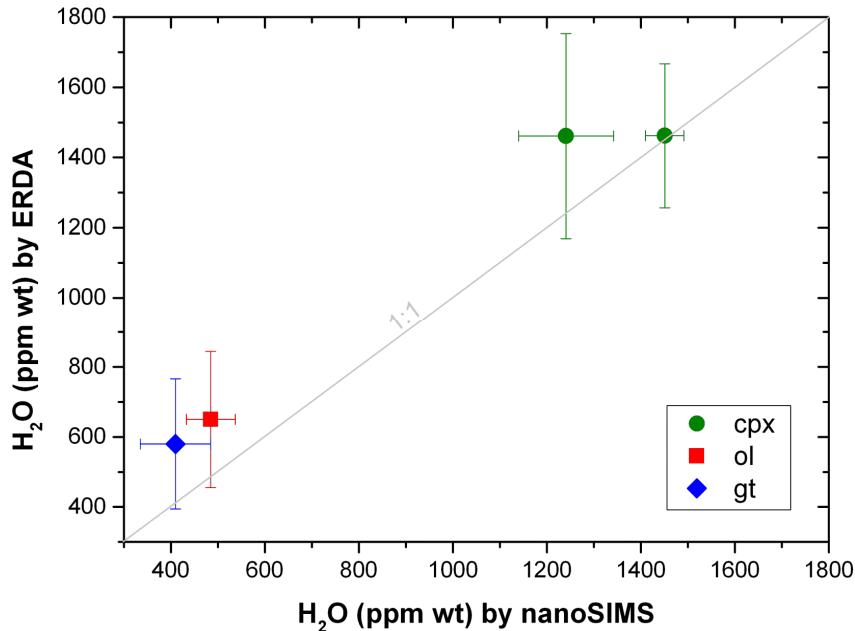


Fig. 4.3: H₂O contents of olivine, cpx and garnet determined by nanoSIMS and ERDA (values and errors are reported in Table 4.1). 1:1 correlation between the two techniques is displayed by the gray line.

Within the analytical error there is agreement in the H₂O concentration of all crystals determined by ERDA and nanoSIMS. ERDA values are higher than NanoSIMS measurements, however, with the agreement between the techniques increasing with H₂O content from 40 % to better than 1 %. Rather than being due to the H₂O contents, however, this is likely related to the size of the crystal analysed because the smallest deviation corresponds to a crystal >150 µm in diameter, whereas the other crystals were in the range 50-100 µm. As shown in Fig. 4.2a for crystals smaller than 150x150 µm ERDA H data must be selected from a region (outlined in green) of the H map, with the analysis statistics improving with the size of the region. Bright H-rich regions exist around the crystal due to quenched melt or remnants of glue used to embed and polish the crystal. Due to the quality of the imaging the potential for H contamination increases for smaller crystals but for larger crystals the entire mapped area can be within the grain. For the largest cpx crystal the correspondence between the techniques is 11 ppm wt, which given that ERDA is an absolute technique requiring no standards confirms the accuracy of the NanoSIMS measurements.

4.3.1.1 Olivine

Average olivine H₂O concentrations are 434 ± 61 ppm wt for crystals measured in 5 different charges. In general, previous studies indicate olivine concentrations increase with pressure but decrease with temperature once hydrous melting commences due to a decrease in the H₂O activity in the melt (Smyth et al., 2006; Bali et al., 2008). All mineral H₂O contents are expected to follow this temperature trend. As shown in Fig. 4.4a there is reasonable agreement with measurements of 489 ppm H₂O made by Bali et al. (2008) on forsterite produced in the MgO-SiO₂-H₂O system at identical conditions.

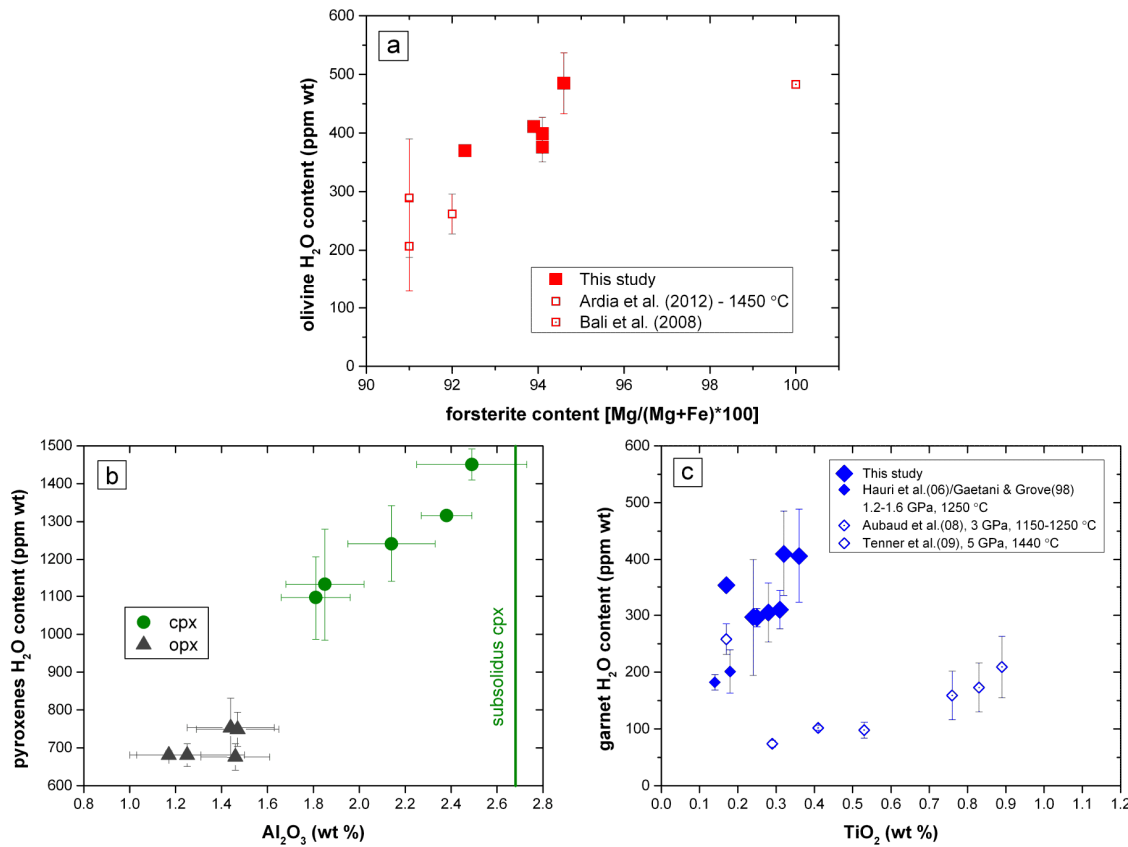


Fig. 4.4: The H₂O contents of NAMs compared to mineral chemical compositions. (a) The H₂O content of olivine synthesised at 6 GPa versus the olivine forsterite content i.e. [Mg/(Mg+Fe)*100]. Results are shown from this study at 1400 °C (large, filled squares), Ardia et al. (2012) at 1450 °C (small, empty squares) and from Bali et al. (2008) at 1400 °C (small, empty square with dot). (b) The H₂O content of pyroxenes synthesised in this study as a function of mineral Al₂O₃ content (wt %). The subsolidus concentration of cpx is from Chapter 3. (c) Garnet H₂O concentration as a function of TiO₂ content (wt %). Filled diamonds indicate experiments saturated with a peridotite phase assemblage. Large, filled diamonds are experiments from this study while small, filled diamonds are from experiments of Gaetani and Grove (1998) reported by Hauri et al. (2006). Experimental data from Tenner et al. (2009) and Aubaud et al. (2008) are from basaltic bulk compositions which were not in equilibrium with olivine.

The measurements of Ardia et al. (2012) were also performed on olivines produced in natural hydrous peridotite assemblages at these pressures, although the experiments were performed at 1450 °C. When plotted as a function of the olivine forsterite content there appears to be a trend of decreasing H₂O with olivine Mg-content. Mg contents vary due to loss of Fe alloyed with the capsule during the experiments from this study. If we assume, however, that H₂O contents decrease approximately linearly with increasing temperature to negligible values at the dry melting temperature, then the 50 °C temperature difference between this study and that of Ardia et al. (2012) can reasonably explain the difference in average H₂O contents. In addition, a trend of decreasing H₂O content with Mg would be the exact opposite to trends demonstrated previously by Withers et al. (2011) and Zhao et al. (2004) for olivine.

4.3.1.2 Clinopyroxene

The average cpx H₂O content from 5 experiments is 1268± 173 ppm, however, as shown in Fig. 4.4b the variation in H₂O between samples is a clear function of the cpx Al₂O₃ content, as observed in previous studies (Aubaud et al., 2004; Hauri et al., 2006; Hirschmann et al., 2009; Ø Leary et al., 2010). The H₂O content increases by 350 ppm upon an increase in Al₂O₃ content of 0.7 % between 1.85 to 2.49 wt %. Per 6 oxygen formula units the amount of H in cpx increases from 0.02 to 0.03 formula units, which means that the amount of H is similar to the amount of Al that resides in the tetrahedral Si site. Similarly the amount of Na in the larger M2 cpx cation site is sufficient to charge balance the remaining Al that resides on the smaller M1 site as a jadeite component, i.e. NaAlSi₂O₆. This implies that tetrahedral Al cannot be charge balanced by M1 Al as a Ca-Tschermak component, i.e. CaAl[AlSi]O₆. Although there is some uncertainty due to the unknown Fe³⁺ content, the cation proportions are consistent with tetrahedral Al being entirely charge balanced by H via the Si substitution mechanism Si⁴⁺ – Al³⁺ + H⁺, as proposed by Rauch and Keppler, (2002) for opx. This is a departure from dry cpx synthesised in a peridotite composition at the same conditions, where tetrahedral Al substitutes as a Tschermak component. Dry peridotite cpxs contain ~2.7 wt % Al₂O₃ at the experimental conditions (Table 4.2) and although H could potentially influence the equilibrium Al content in wet systems, wet peridotite cpxs of Ardia et al. (2012) have comparable 2-3 wt % Al₂O₃ contents at similar conditions.

4.3.1.3 Orthopyroxene

Average opx H₂O concentrations from 6 charges are 700± 46 ppm wt. This small variation in H₂O content does not correlate with any other component as shown for Al, for example, in

Fig. 4.4b, although the chemical composition of opx in the experiments varies very little. Tenner et al. (2009) reported opx H₂O contents of 819 and 996 ppm at 4 GPa and 1400 °C but the solid assemblage was crystallised from a MORB composition and opx Al₂O₃ contents were higher, 3-6 wt %. By comparison this is consistent with a dependence of the opx H₂O content on Al, as recognized in previous studies (Rauch and Keppler, 2002; Yamada et al., 2004; Mierdel et al., 2007; Withers and Hirschmann, 2007; Férot and Bolfan-Casanova, 2012). However at 12 GPa and 1400 °C Tenner et al. (2011) report 1040 ppm H₂O in opx containing only ~0.2 % Al₂O₃, implying also a pressure effect on the equilibrium H₂O content.

4.3.1.4 Garnet

For 6 experiments average garnet H₂O contents are 347± 83 ppm wt. Water solubility in garnet has been determined at temperatures ~1000 °C in simplified systems (Ackermann et al., 1983; Geiger et al., 1991; Withers et al., 1998) up to 13 GPa and in natural pyrope up to 10 GPa (Lu and Keppler, 1997). Mookherjee and Karato (2010) investigated the H₂O solubility of garnet crystals in equilibrium with olivine at 5-9 GPa and 1100-1200 °C by FTIR and measured 578-863 ppm at 6 GPa and 1100 °C. Previous literature data for garnets in peridotitic compositions are limited to analyses by Hauri et al. (2006) from the experiments of Gaetani and Grove (1998) at 1.6 and 2 GPa and ~1250 °C. Aubaud et al. (2008) and Tenner et al. (2009) report garnet H₂O concentrations crystallised from MORB compositions between 3 and 5 GPa. In Fig. 4.4c these garnet H₂O concentrations are plotted as a function of garnet TiO₂ concentration for both peridotite and MORB experiments. A correlation exists, as pointed out previously by Aubaud et al. (2008) for MORB samples, but the trend for peridotitic samples appears to be higher and steeper. Given the uncertainties and the narrow range of TiO₂ content examined it is hard to accurately determine the significance or slope of this trend and the main conclusions are that peridotite garnets contain more H₂O compared to MORB samples and there appears to be very little pressure effect on peridotite garnet H₂O contents.

4.3.2 Distribution of H₂O

Using the experimental data H₂O mineral-melt partition coefficients, $D_{H_2O}^{\text{min/melt}}$, can be calculated between melts in equilibrium with a peridotite assemblage at 6 GPa and 1400 °C (Table 4.1) and olivine, cpx, opx and garnet. Mineral H₂O contents determined with

NanoSIMS (Table 4.1) are used to calculate $D_{H_2O}^{\text{min/melt}}$, while the concentration of H₂O in the melt at these conditions was determined to be 10.91 ± 0.61 wt % (Chapter 3), which is an average determined from 6 experiments. Average values of $D_{H_2O}^{\text{min/melt}}$ across all experiments for cpx, opx, olivine, and garnet are 0.0115 ± 0.0016, 0.0064 ± 0.0004, 0.0040 ± 0.0006, and 0.0032 ± 0.0008 respectively.

The partitioning of H₂O between mineral phases can also be calculated. Pyroxenes $D_{H_2O}^{px/ol}$ values are 3.20 and 1.92 for clinopyroxene and orthopyroxene, respectively. Ardia et al. (2012) proposed a general relationship for both pyroxenes of $D_{H_2O}^{px/ol} = 2.63 \cdot C_{Al_2O_3}^{Px} + 0.78$, where $C_{Al_2O_3}^{Px}$ is the pyroxene Al₂O₃ concentration. Cpx and opx produced in this study contain approximately 3 and 1.5 wt % Al₂O₃ respectively, which, using this relationship, gives $D_{H_2O}^{px/ol}$ of 8.7 and 4.7 respectively, which are twice as high as the values determined in this study. Between the pyroxene phases $D_{H_2O}^{cpx/oxp}$ is 1.65. The calculated $D_{H_2O}^{\text{min/min}}$ have relative errors of 6-13 %. $D_{H_2O}^{gt/ol}$ is close to unity with an average value of 0.8.

4.4 Discussion

4.4.1 The pressure dependence of $D_{H_2O}^{\text{min/melt}}$ for peridotite assemblages

H₂O mineral-melt partition coefficients from this study are compared with data from the literature collected at lower pressures (Fig. 4.5). The majority of previous partitioning studies were performed on mineral phases crystallised from MORB melt compositions because, as stated previously, peridotite melts do not quench to form glasses above ~2 GPa. Only partition coefficients measured by Hauri et al. (2006) on phases produced in experiments by Gaetani and Grove (1998) performed between 1.2-2 GPa and 1200-1370 °C involved peridotite assemblages. Studies by Koga et al. (2003), Aubaud et al. (2004) and (2008), Tenner et al. (2009) and ØLeary et al. (2010) examined MORB compositions where olivine did not generally form and mineral and melt compositions differ from those expected for small degree peridotitic hydrous melts particularly at pressures above 2 GPa.

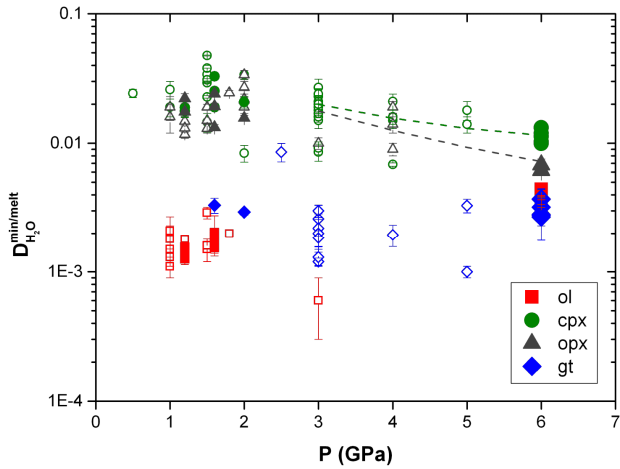


Fig. 4.5: Partitioning of water between NAMs and hydrous melt ($D_{H_2O}^{\text{min/melt}}$) as a function of pressure. Large symbols are data determined in this study at 6 GPa while small symbols are data from the literature up to 5 GPa (Koga et al., 2003; Aubaud et al., 2004, 2008; Hauri et al., 2006; Tenner et al., 2009 and OøLeary et al., 2010). Small, filled symbols are data reported by Hauri et al. (2006) from the experiments of Gaetani and Grove (1998) where minerals coexisted within a complete peridotite phase assemblage. Unfilled symbols are values reported for minerals within other phase assemblages, which generally did not include olivine. Green and dark grey dashed lines indicate parameterizations between 3 and 6 GPa describing the variation of $D_{H_2O}^{\text{min/melt}}$ for cpx and opx as a function of the mineral Al₂O₃ content, which is then parameterised as a function of pressure. Details regarding the parameterizations are described in the text and later in Fig. 4.7.

As shown in Fig. 4.5 significant variation exists for some determinations of $D_{H_2O}^{\text{min/melt}}$ at particular pressures from previous studies, which can be mainly attributed to variations in mineral composition due to different starting materials, rather than differences in temperature. Partitioning data from Grant et al. (2007) however show appreciably lower values compared to other from the literature at similar P-T conditions. Grant et al. (2007) report mineral H₂O contents that are 2-3 times lower than data from the literature at similar pressure and temperature (e.g. Bali et al., 2008). If we recalculate these $D_{H_2O}^{\text{min/melt}}$ with mineral H₂O content from Bali et al. (2008), however, their values increase and become similar to the literature values plotted on Fig. 4.5. Important to notice is that Grant et al. (2007) determined mineral H₂O contents with wavenumber-dependant calibration of Libowitzky and Rossman (1997) while Bali et al. (2008) employed the more recent mineral specific absorption coefficient of Bell et al. (2003). This cause differences in the calculated mineral H₂O content. Also, the cooling approach of the experiments of Grant et al. (2007) for enhancing the crystal growth might have potentially influenced the generation of vacancies in the crystal and therefore the incorporation of H.

By comparison, $D_{H_2O}^{\min/melt}$ variations determined in this study are relatively narrow although as shown in Fig. 4.4b even the very small changes in cpx Al₂O₃ contents coexisting with peridotite assemblages cause variations in the corresponding H₂O content that are responsible for the small range in $D_{H_2O}^{cpx/melt}$ values. This underlines the importance of determining $D_{H_2O}^{\min/melt}$ for peridotite saturated melts where mineral compositions are buffered at the most appropriate values due to partitioning between the coexisting minerals.

Between 1 and 6 GPa there is an increase in $D_{H_2O}^{ol/melt}$ by a factor of 2-3, apart from a single outlier to this trend at 3 GPa from data by Tenner et al. (2009). The evolution of $D_{H_2O}^{ol/melt}$ as a function of pressure in the upper mantle, employing data determined in this study and from the literature is shown in Fig. 4.6. Due to large uncertainties on data determined at 12 GPa (Tenner et al. 2011), which employ a mass balance to determine the melt H₂O contents of relatively small degree melts, the results are fitted only linearly using data on peridotite assemblages between 1.2 and 6 GPa.

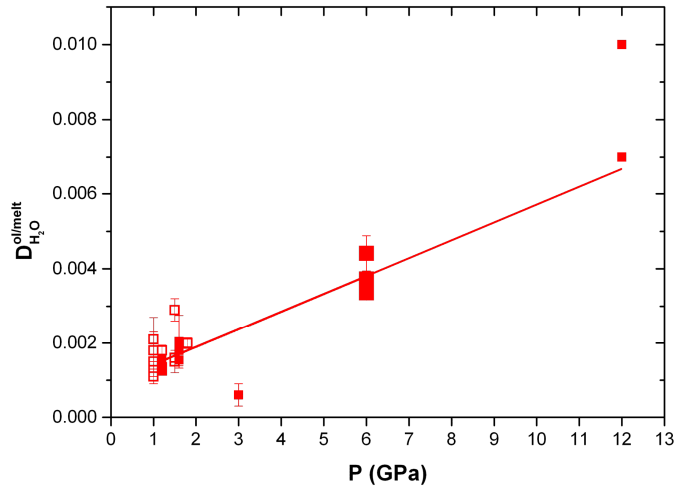


Fig. 4.6: Variation of $D_{H_2O}^{ol/melt}$ as a function of pressure in the upper mantle. Small symbols indicate data from the literature. Up to 3 GPa values are taken from the studies of Koga et al. (2003), Aubaud et al. (2004), Hauri et al. (2006), Tenner et al. (2009) and those at 12 GPa are from Tenner et al. (2011). Filled symbols indicate experiments with peridotitic phase assemblages. Large symbols show data determined in the present study at 6 GPa while the small filled symbols at lower pressure are reported by Hauri et al. (2006). A linear parameterization for the change of $D_{H_2O}^{ol/melt}$ as a function of pressure based on the peridotite saturated data up to 6 GPa is shown by the red line and is described by $D_{H_2O}^{ol/melt} = 4.77E-4 * P + 0.00094$ with $R^2 = 0.93$.

$D_{H_2O}^{px/melt}$ for both cpx and opx decrease with pressure, between 2 and 6 GPa. The decrease for opx is slightly greater and more discernable than for cpx. As demonstrated in many previous

studies $D_{H_2O}^{px/melt}$ for cpx and opx are both correlated with the mineral Al content (Hauri et al., 2006; Aubaud et al., 2004, 2008; Tenner et al., 2009; ØLeary et al., 2010). Above 2 GPa, where garnet becomes stable, the Al₂O₃ contents of both cpx and opx decrease with pressure causing a decrease in $D_{H_2O}^{px/melt}$. In Fig. 4.7 $D_{H_2O}^{cpx/melt}$ and $D_{H_2O}^{oxp/melt}$ are each parameterized as a function of Al₂O₃ content. Additionally, the Al₂O₃ concentration of pyroxenes in dry and hydrous peridotite experiments are plotted and parameterised as a function of pressure (Fig. 4.7a, b). With the parameterizations presented in Fig. 4.7, the $D_{H_2O}^{px/melt}$ can be estimated at different depths in the mantle based on the Al content of pyroxenes in a peridotite composition, which is then shown as the dashed curves in Fig. 4.5.

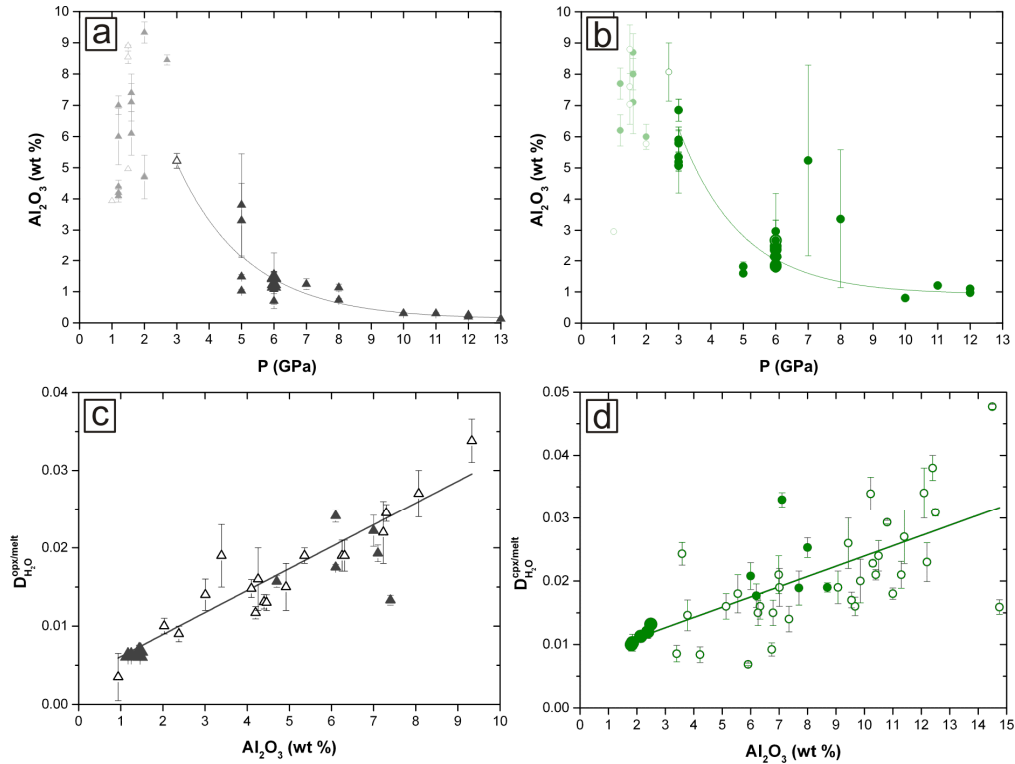


Fig. 4.7: In (a) and (b), Al₂O₃ contents (wt %) of opx and cpx measured in various studies are plotted as a function of pressure. Pale symbols indicate literature data from below 2.7 GPa where garnet was not present in the assemblage. Empty pale symbols are from anhydrous peridotite experiments (Takahashi and Kushiro 1983; Robinson et al., 1998; Robinson and Wood 1998), and filled pale symbols are from hydrous peridotite experiments (Hauri et al. 2006). Above 3 GPa small symbols indicate data from hydrous, peridotite saturated experiments (Ardia et al. 2012; Tenner et al. 2011) while large symbols are from this study. Open symbols, at 3 GPa are from anhydrous experiments of Davis et al. (2011) and Balta et al. (2011). Parameterizations to describe the Al-dependence above 3 GPa are shown by solid, thick lines, which correspond to the equations, wt%Al₂O₃= 0.11423 + 19.61901 * exp(-0.45381 * P) for opx (a) and wt%Al₂O₃= 0.92153 + 25.27449 * exp(-0.51786 * P) for cpx (b). Panels (c) and (d): the variation of $D_{H_2O}^{oxp/melt}$ and $D_{H_2O}^{cpx/melt}$ as a function of mineral Al₂O₃ content, where large symbols are from this study and small symbols are from the literature (Dobson et al. 1995; Koga et al. 2003; Aubaud et al. 2004, 2008; Hauri et al. 2006; Tenner et al. 2009; ØLeary et al., 2010). Filled symbols indicate experiments in equilibrium with a complete peridotite phase assemblage, whereas open

symbols are for experiments generally in basaltic bulk compositions where olivine was normally absent. The parameterisations are described by the equations $D_{H_2O}^{opx/melt} = 0.00281 * \text{wt\%Al}_2\text{O}_3 + 0.00328$ with R²= 0.81 in (c) and $D_{H_2O}^{cpx/melt} = 0.00162 * \text{wt\%Al}_2\text{O}_3 + 0.00777$ with R²= 0.62 in (d).

The variation in $D_{H_2O}^{gt/melt}$ between previous studies is relatively large particularly at 3 and 5 GPa (Fig. 4.5), however, as shown in Fig. 4.4c garnets produced in peridotite and MORB compositions have apparently different H₂O dependencies and there may in addition be a dependence on TiO₂. The latter could introduce significant variation into $D_{H_2O}^{gt/melt}$ in the mantle because TiO₂ is incompatible during melting and large variations could potentially exist in mantle rocks. $D_{H_2O}^{gt/melt}$ for peridotite samples, however, appears to be independent of pressure.

4.4.2 The production of low degree hydrous melts in the upper mantle

Using the measured H₂O partition coefficients for each peridotite mineral, the partitioning of H₂O between a mantle peridotite assemblage and a low degree melt ($D_{H_2O}^{pdt/melt}$) can be determined. $D_{H_2O}^{pdt/melt}$ is calculated as the sum of the individual mineral-melt partition coefficients multiplied by the mineral abundance in the assemblage i.e.:

$$D_{H_2O}^{pdt/melt} = x_{ol} \cdot D_{H_2O}^{ol/melt} + x_{px} \cdot D_{H_2O}^{px/melt} + x_{gt} \cdot D_{H_2O}^{gt/melt} \quad (4.1)$$

where x_{ol} is, for example, the modal proportion of olivine in the assemblage. In Chapter 3, a sub solidus experiment to determine the mineral compositions and proportions for the Jagoutz et al. (1979) primitive mantle (PM) composition at 6 GPa and 1400 °C produced an olivine, cpx and garnet assemblage i.e. a garnet wehrlite, with the respective modal abundances of 54 %, 32 % and 14 %. The abundances are in good agreement with estimates made by Tenner et al. (2009) at 6 GPa based on the dry peridotite melting data of Walter (1998). The corresponding $D_{H_2O}^{pdt/melt}$ at these conditions is 0.0063. Using this value and knowledge of the H₂O content of hydrous melt, the amount of H₂O required to produce hydrous melts in the upper mantle and the melt fraction as a function of bulk H₂O can be determined. The melt fraction (F) can be calculated as a function of the bulk H₂O concentration of the mantle (C_{bulk}) using a rearrangement of the batch melting equation (Shaw, 1970),

$$F = \frac{(C_{\text{bulk}} / C_{\text{melt}}) - D_{H_2O}^{\text{pdt/melt}}}{1 - D_{H_2O}^{\text{pdt/melt}}} \quad (4.2)$$

where C_{melt} is the concentration of H₂O in the melt, and $D_{H_2O}^{\text{pdt/melt}}$ is the partition coefficient of H₂O as described in equation 4.1. The melt H₂O concentration is that derived for melts in equilibrium with peridotite at 6 GPa and adiabatic conditions i.e. 10.91 ± 0.61 wt % (Chapter 3). It is assumed that this does not change significantly for small melting intervals. In reality it will change due to the dilution of incompatible elements K and Ti as F increases but this is likely to be a relatively small effect. The uncertainty bounds are propagated from the partitioning measurements. For a similar garnet wehrlite bulk composition the same calculation can be performed at lower pressure adiabatic conditions using low degree melt H₂O contents determined by Balta et al. (2011) at 3 GPa and 1375 °C, which are ~5 wt % H₂O. In order to calculate $D_{H_2O}^{\text{pdt/melt}}$ at 3 GPa values are taken from the trends given in Fig. 4.5 and Fig. 4.6 determined from the peridotite data of this study and the measurements of Hauri et al. (2006) from experiments of Gaetani and Grove (1998).

Modal abundances of olivine, cpx and garnet (56 %, 34 % and 9 % respectively) were calculated using mineral compositions from the study of Balta et al. (2011) but assuming the Jagoutz et al. (1979) PM composition at 3 GPa. Using equation 4.1 a value of 0.0082 is determined for the $D_{H_2O}^{\text{pdt/melt}}$ at 3 GPa and adiabatic temperature, which is only a slight increase from 6 GPa and in good agreement with the estimate of Tenner et al. (2009). As shown in Fig. 4.8a at 6 GPa, i.e. ~180 km depth, melting would commence only if the mantle contained ~690 ppm H₂O and at 3 GPa, i.e. 90 km, if it contained ~400 ppm H₂O. At 180 km a mantle H₂O content of 1800 ppm would be required for the production of 1 % melt with this reducing to 900 ppm at 90 km. These H₂O contents are much higher than estimates for the depleted mantle, which are in the range 50–200 ppm (e.g. Dixon et al., 1988, 2002; Saal et al., 2002; Workmann and Hart, 2005), implying that for such fertile mantle compositions H₂O alone would not extend the MORB melting column significantly deeper than 50 km from the surface.

Based on analyses of ocean island basalts (OIB) it has been proposed that their source rocks are richer in volatiles, with H₂O contents possibly up to 900 ppm (e.g. Dixon et al., 1997;

Aubaud et al., 2005, 2006). The plume sources of OIBs are also proposed to have adiabatic temperatures up to 200°C higher than normal mantle (e.g. Courtney and White, 1986). By assuming that values of $D_{H_2O}^{pdt/melt}$ change little with temperature, in accordance with Hauri et al. (2006) and results reported later in Chapter 6, and using melt H₂O contents estimated from Tenner et al. (2012), the proportion of melt for +100 °C and +200 °C adiabatic temperatures at 180 km have been calculated as a function of bulk mantle H₂O content (Fig. 4.8a).

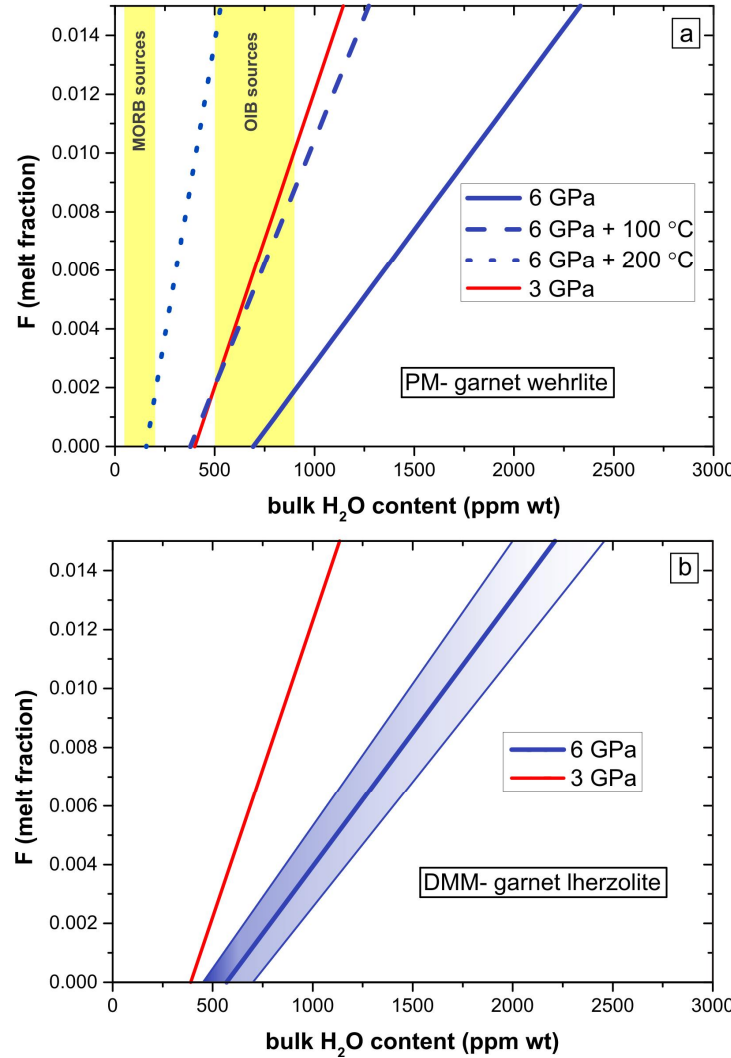


Fig. 4.8: Silicate melt fraction (F) as a function of bulk mantle H₂O content determined at 3 and 6 GPa (~90 and ~180 km) and adiabatic temperatures. The curve at 6 GPa is calculated based on data experimentally determined in this study, while the curve at 3 GPa is determined based on literature data (see text). Panel (a) shows calculations based on a primitive mantle (PM) composition (Jagoutz et al. 1979) which corresponds to a garnet wehrlite assemblage. In panel (b) the same calculation is performed for a depleted MORB mantle (DMM; Workman and Hart, 2005) which corresponds to a garnet lherzolitic assemblage. In panel (a) data at 6 GPa are also calculated for temperatures 100 and 200 °C higher than the adiabat, to indicate the plausible effect on melting relations of a mantle plume. Yellow areas indicate proposed H₂O contents for the MORB source and the range of maximum H₂O contents proposed for OIB source regions (references in the text). In panel (b), the shaded area indicates the propagated uncertainty, which would be similar for all curves.

For H₂O contents at the maximum end of the estimated OIB range ~1 % melt could be produced at 180 km for +100 °C, whereas for +200 °C, 1 % melt could be formed with a plume mantle H₂O content of only 400 ppm. The PM bulk composition of Jagoutz et al., (1979) is relatively fertile in comparison to estimates for the depleted MORB mantle, DMM, (Workman and Hart, 2005). Mineral proportions for DMM determined by Stixrude and Linthgow-Bertelloni (2007) predict a garnet Iherzolite assemblage at upper mantle pressures containing ~60 % olivine, 23 % opx, 12 % cpx and 5 % gt at 3 GPa. With increasing pressure at 6 GPa the proportion of pyroxenes decrease to approximately 10 % opx and 14 % cpx and garnet increases to 16 %. The corresponding values for $D_{H_2O}^{pdt/melt}$ are 0.0078 and 0.0052 at 3 and 6 GPa respectively, which is a relatively small change compared to the PM composition although the difference is higher at 6 GPa. Changes in the fertility of the bulk composition are mainly reflected by the replacement of opx for cpx but as $D_{H_2O}^{opx/melt}$ is only slightly lower than $D_{H_2O}^{cpx/melt}$ the over all effect is very small. At 3 GPa the onset of melting is still determined to be for ~390 ppm bulk mantle H₂O, while at 6 GPa melts are first produced for ~570 ppm H₂O, a drop of ~100 ppm compared to the PM composition (Fig. 4.8b). This decrease is due to the slightly greater decrease in $D_{H_2O}^{opx/melt}$ compared to $D_{H_2O}^{cpx/melt}$ with pressure.

Recently Ardia et al. (2012) made estimates for the H₂O concentration of mantle peridotite required for the onset of melting at adiabatic temperatures. However, due to a lack of data for garnet they assumed 3 possible values for $D_{H_2O}^{gt/olivine}$, being 0.9, 4.2 and 9. Compared to the current study the first value is quite precise. Using this value Ardia et al. (2012) estimate that H₂O contents of ~350±100 ppm are required to instigate melting at 6 GPa, which is lower than in the current study, i.e. 570 ±80 ppm for DMM. This difference mainly arises from the parameterisation used for the olivine H₂O concentration by Ardia et al., (2012) i.e. $C_{H_2O}^{olivine} = 39.1 \cdot P^{0.66}$ (ppm). At 6 GPa this relationship predicts 170 ppm, compared to 434±61 ppm in this study, which is ~100 ppm lower than their own data at these conditions. The conclusions of this and the current study remain the same, however, in that there will be no melting for typical mantle H₂O concentrations at pressures > 2 GPa.

4.4.3 The variation in inter-mineral partitioning of H₂O with depth and the effect on seismic anisotropy in the upper mantle

Although changes in $D_{H_2O}^{olivine/melt}$ and $D_{H_2O}^{px/melt}$ with pressure for mantle peridotite are relatively small, the changes are in opposite directions, with negative pyroxene slopes caused by decreasing Al₂O₃ contents (Fig. 4.7). The opposing slopes means, however, that changes in $D_{H_2O}^{px/olivine}$ will be much larger with pressure, with the parameterisations used in this study implying $D_{H_2O}^{cpx/olivine}$ changing from ~10 to 3 between 3 and 6 GPa and $D_{H_2O}^{opx/olivine}$ from ~9 to 1.8. Therefore, even if the H₂O concentration of the mantle is constant with depth, there will be a shift in mineral H₂O concentrations with pressure, with more H₂O partitioning into the pyroxenes with decreasing pressure, as proposed by Mierdel et al. (2005). This will be compounded at higher pressures as the modal proportions of opx and cpx decrease, particularly as majoritic garnet forms. The result will be that at higher pressure H₂O will be partitioned strongly into olivine. As H defects in olivine apparently control many important transport properties, describing this shift in olivine H₂O content with depth is quite relevant.

H₂O concentrations of individual minerals in a DMM assemblage are calculated as a function of depth in Fig. 4.9, assuming a constant bulk mantle H₂O concentration of 200 ppm, which is at the upper end of DMM estimates (e.g. Michael, 1988; Saal et al., 2002). The calculation is performed using the adiabatic DMM modal proportions of Stixrude and Lithgow-Bertelloni (2007) and the $D_{H_2O}^{\min/melt}$ of peridotitic pyroxene Al₂O₃ concentrations parameterised in Fig. 4.7. At each condition a fictive H₂O melt composition is adjusted until the sum of the corresponding mineral H₂O contents multiplied by their modal proportions equals 200 ppm wt. The model decreases in precision above 180 km due to uncertainties in partition coefficients, however as modal proportions of pyroxenes are decreasing the uncertainties in these partition coefficients become less important and the main uncertainty comes from the implied value of $D_{H_2O}^{gt/olivine}$ which does not take into account the increasing majorite component of garnet. Bolfan-Casanova et al. (2000) reported 677 ppm H₂O in Mg₄Si₄O₁₂ majorite produced at 17.5 GPa and 1500 °C, however, which implies a relatively small influence of the majorite component on garnet H₂O contents.

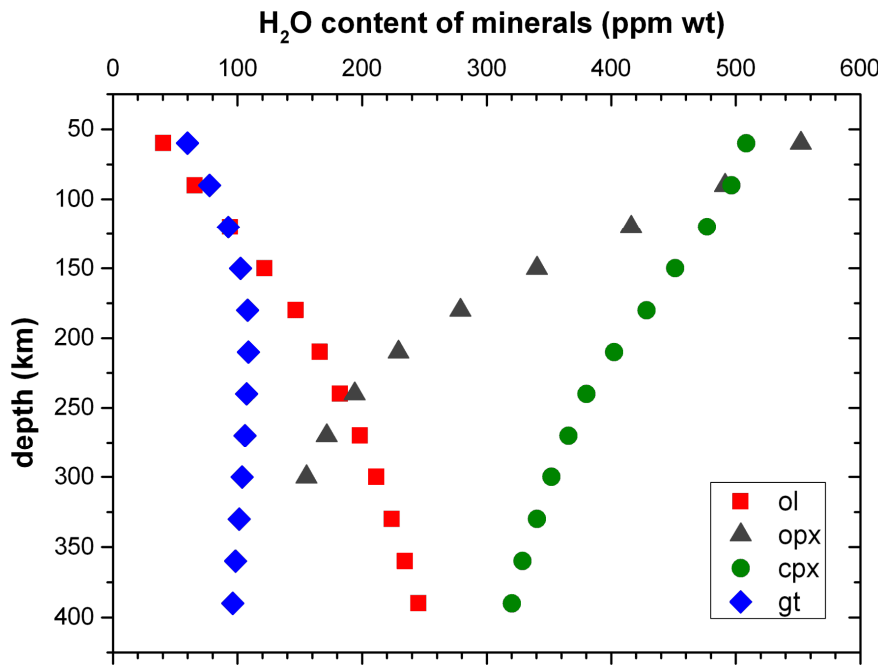


Fig. 4.9: Variation of mineral H₂O contents as a function of depth for a garnet lherzolite assemblage (DMM; Workman and Hart 2005) assuming a constant bulk mantle H₂O content of 200 ppm wt. At a given pressure (depth), the water contents of olivine, cpx, opx and garnet are calculated based on the $D_{H_2O}^{\text{min/melt}}$ modelled in this study (see text) and modal proportions of phases from Stixrude and Linthgow-Bertelloni (2007).

Fig. 4.9 indicates a steady decrease in the H₂O content of olivine with decreasing pressure even when the bulk mantle H₂O content remains constant. This is due to the increasing proportion of pyroxenes as they exsolve from garnet and the increase in $D_{H_2O}^{\text{px/olivine}}$ with decreasing pressure. This might potentially influence rheological properties of the mantle as suggested by Mierdel et al. (2007).

One particular property that has been proposed to depend on the H defect concentration in olivine is the nature of the dominant olivine slip system during deformation by dislocation glide (Jung and Karato, 2001; Jung et al., 2006). Lattice preferred orientation (LPO) occurs through the accommodation of strain by dislocations acting along a dominant slip system. In fabrics developed in natural and experimentally deformed olivine crystals the [100] axes and (010) planes rotate to become parallel to the shear direction, with this dominant [100](010) slip system generally referred to as A-type. As olivine is elastically anisotropic the olivine LPO fabric developed due to A-type slip as a result of horizontal mantle flow will produce seismic anisotropy, causing the velocity of S-waves polarised in the horizontal direction to be greater than that of vertically polarised S-waves, i.e. V_{SH}>V_{SV}. This is consistent with global anisotropy models which show V_{SH}>V_{SV} down to 250 km. These models, however, also show

weaker anisotropy below this depth and in some instances $V_{SV} > V_{SH}$ towards the base of the upper mantle. This could be interpreted as a reduction in fabric development with depth but the observations including those on corresponding P-wave anisotropy are more consistent with a change in the type of LPO fabric with depth (Mainprice et al., 2005). The dominant olivine slip system can be influenced by many factors (Karato et al., 2008). The experiments of Jung and Karato (2001) and Jung et al. (2006) for example, indicate that slip along (001)[100], referred to as E-type fabric, may dominate in olivine with moderate H₂O contents and C-type (100)[001] for high olivine H₂O contents. These fabric transitions have also been confirmed in high pressure experiments to 6 GPa (Shekhar, 2011). This is relatively controversial as other studies have proposed that increasing pressure may also favour C-type slip (Couvy et al., 2004; Ratteron et al., 2007; Jung et al., 2009; Ohuchi et al., 2011). Mainprice et al., (2005) demonstrated that a progression from A-type to C-type fabric would cause a decrease in both S and P-wave anisotropy with depth, fitting extremely well to seismic observations. S-wave polarisation anisotropy can be described using the anisotropic parameter $\epsilon = (V_{SH}/V_{SV})^2$ (Montagner and Kennet 1996). For horizontal mantle flow ϵ is >1 for A-type fabric, 1 for E-type fabric and slightly <1 for C-type (Karato et al., 2008). The fabric transitions A to E and E to C occur at olivine H₂O contents of approximately 60 and 240 ppm according to Jung et al. (2006), with the H₂O contents recalculated using the FTIR calibration of Bell et al. (2003) and extrapolated to 0 MPa stress. In Fig. 4.10 the H₂O contents at which these fabrics dominate are compared to the olivine H₂O content as a function of depth from Fig. 4.9. In reality there is unlikely to be a sharp transition between these dominant regimes and olivine textures in the mantle may experience large depth intervals where different slip systems compete. It can be seen that the olivine H₂O content is consistent with the transition to the C-type fabric at a similar depth to where the S-wave polarisation anisotropy of the mantle reverses. This means that if an increasing H₂O content of olivine is responsible for the gradual shift in the dominant olivine slip system with depth, an increase in the H₂O content of the mantle is not implied, it is simply a result of inter-phase partitioning of H₂O. The decrease in anisotropy with depth is also consistent with a reasonable estimate for an average H₂O concentration of the mantle of ~200 ppm.

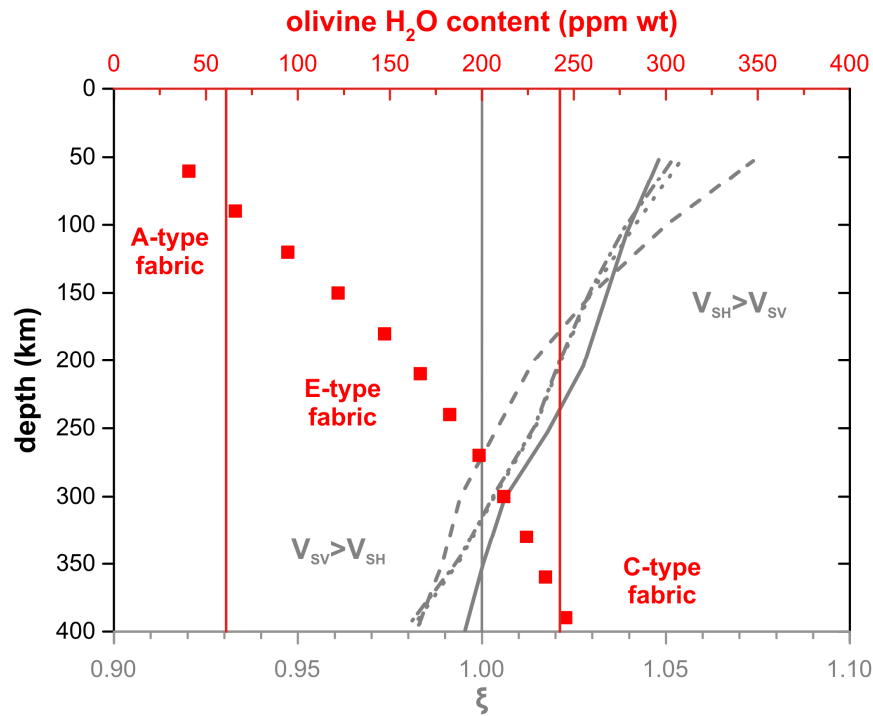


Fig. 4.10: Variation in the olivine H₂O content as a function of depth (red squares) as calculated in Fig. 4.9, compared with the variation in the anisotropic parameter with depth (grey lines). The anisotropic parameter is reported from 4 different, 1-D seismic reference models: *iasp* (dashed line), *sp6* (solid line), *ak303* (dash-dot line) and *ak135* (dotted line) from Montagner and Kennet (1996). A grey, vertical line indicates the absence of S-wave anisotropy i.e. $\xi=1$. Values of >1 indicate $V_{SH}>V_{SV}$ while values of <1 indicate $V_{SH}<V_{SV}$. Olivine fabrics (A-, E- and C-type) regions are delimited by red, horizontal lines based on the crystal water contents determined by the experimental work of Jung et al. (2006).

5. Melting phase relations in the systems Mg_2SiO_4 - H_2O and MgSiO_3 - H_2O at upper mantle conditions

5.1 Introduction

The effect of H_2O on the formation of silicate melts underlies a number of igneous processes taking place within the Earth's mantle. H_2O has an important influence on the production of magmas at subduction zones being integral in both metasomatism of the arc magma source region and responsible for the high degrees of melting that produce arc magmas (e.g. Tatsumi et al., 1986). The lithospheric mantle shows ample evidence for metasomatism by H_2O -bearing melts (Menzies and Hawkesworth, 1987; Erlank et al. 1987) and several exotic magma types such as kimberlites and lamproites are likely formed, at least in part, as a result of H_2O lowering the mantle solidus (e.g. Kushiro et al., 1968; Kawamoto and Holloway, 1997). H_2O induced melting of the deep mantle has also been proposed to explain a number of geophysical observations such as the Earth's seismic low velocity zone (Lambert and Wyllie, 1970) and a possible low velocity layer present on top of the transition zone (Tauzin et al., 2010).

A number of studies have been performed to quantify the effects of H_2O on lowering melting temperatures and increasing melt yields in natural mantle rock systems (Mysen and Boettcher, 1975; Hirose and Kawamoto 1995; Gaetani and Grove, 1998; Balta et al., 2011; Tenner et al. 2012). Determining the effect of H_2O on melting in natural chemical systems is challenging, however, due to the large number of components that are potentially influenced by H_2O . Such determinations are further complicated by a number of factors, such as the necessity to control oxygen fugacity, attainment of equilibrium, H_2O and FeO loss from experimental capsules and the difficulty in determining the H_2O contents of melts.

It has long been appreciated that the effects of H_2O on silicate melts can be more easily quantified by examining melting behaviour in simple systems (Kushiro et al., 1968; Kushiro and Yoder 1969; Kushiro 1972; Hodges 1973). From results of experiments in systems such as Mg_2SiO_4 - SiO_2 - H_2O , Kushiro (1972) proposed for example that hydrous mantle partial melts would be more SiO_2 -rich compared to dry melts. Studies in simple systems can also be used to quantify the effect of H_2O on mineral melting at high pressures and experiments have

been performed up to conditions equivalent to those in the mantle transition zone (Kushiro & Yoder, 1969; Luth, 1993; Inoue, 1994). While relatively detailed melting phase relations on hydrous forsterite (Kushiro & Yoder, 1969; Hodges 1973) and enstatite (Kushiro & Yoder 1969; Kushiro et al. 1968) exist up to 3 GPa, phase relations at higher pressures are more sparse and show less mutual agreement. Luth (1993) and Inoue (1994) investigated the melting behavior of forsterite in equilibrium with 17-20 wt% H_2O , up to 12 and 15.5 GPa respectively, although the studies are in poor agreement. In addition, while Inoue (1994) also studied the phase relations of hydrous enstatite and an intermediate Mg/Si ratio composition to similar pressures, this study has more emphasis on determining the hydrous solidus and provides only sparse data through which to quantify the depression of melting temperatures as a function of melt H_2O content.

Recently several studies performed using natural chemical systems have proposed generalized models for the effects of H_2O on peridotite melting temperatures (Medard and Grove, 2008; Tenner et al., 2012). While such models are quite successful in reproducing the experimental observations, they make assumptions concerning both thermodynamic data and the mechanism by which H_2O dissolves in melts that can be more easily tested using results on simplified systems. In simplified systems additional constraints are also provided by calorimetric measurements such as those performed to determine the entropy of fusion (Bottinga, 1985; Navrotsky et al., 1989; Richet et al., 1993; Tangeman et al., 2001). One advantage of examining experiments in simple systems is that treatment with relatively simple thermodynamic models should provide a firmer basis for understanding hydrous melting on a mechanistic level (Silver and Stolper, 1985) and can be used to examine how the effect of H_2O on melting may be modified purely by pressure.

The goal of this study is to determine the melting phase relations in the systems Mg_2SiO_4 - H_2O and MgSiO_3 - H_2O at upper mantle conditions. In particular, the aim is to determine the H_2O contents of melts in equilibrium with forsterite and/or enstatite as a function of temperature at high pressure by bracketing the location of the hydrated liquidus curves. The experimental data are analysed using thermodynamic models to provide insight into the H_2O dissolution mechanism and its effects at high pressures. Results are presented for both systems at 6 and 13 GPa corresponding to ~180 and ~390 km depth in the mantle, and temperature ranging between 1150 to 1900 °C.

5.2 Experimental and analytical details

Two sets of compositions were prepared for experiments in the systems Mg_2SiO_4 - H_2O and $MgSiO_3$ - H_2O . In the system Mg_2SiO_4 - H_2O starting compositions were mixed from two end-member mixes; Mg_2SiO_4 forsterite synthesized from the high purity oxides, MgO and SiO_2 , and a 2:1 molar mixture of brucite ($Mg(OH)_2$) and SiO_2 . The pure forsterite was synthesized by firing the oxides at 1500 °C for 2 hours and then grinding for 1 hour under ethanol. This firing and grinding process was repeated 4 times. The 2:1 brucite silica mixture corresponds to an Mg_2SiO_4 plus 20.4 wt % H_2O composition. In order to prepare this end member, brucite and SiO_2 were dried overnight at 120 °C and 1000 °C respectively. The calculated amount of each component was weighed, grinded for 1 hour under ethanol and dried under a heat lamp. By varying the weight % proportions of the end member compositions a range of further mixtures were prepared with varying H_2O content but with a constant Mg/Si of 2 (Table 5.1).

Table 5.1: Starting mixtures water contents

	Mg_2SiO_4 - H_2O system		$MgSiO_3$ - H_2O system
Mixture	H_2O (wt %)	Mixture	H_2O (wt %)
Fo A	20.4	En A	4.3
Fo B	15	En B	8.2
Fo C	10	En C	11.9
Fo D	5	En D	15.2
Fo E	18.3	En F	6.3
Fo F	13.8	En G	10.1
Fo G	9.7	En H	13.6
Fo H	7.9		
Fo I	4.1		
Fo J	2.1		

All mixtures with water contents lower than 20.4 wt % were prepared by grinding the weighed proportions of dry forsterite and forsterite plus 20.45 wt % H_2O , for 30 minutes under ethanol and then drying. Before each mixture was weighed out the forsterite composition was dried at 1000 °C for one hour and the water bearing forsterite end member was dried overnight at 120 °C. This approach was also followed for the preparation of starting mixtures in the system $MgSiO_3$ - H_2O . In this case, an end-member 1:1 molar mixture of brucite and SiO_2 , corresponding to an $MgSiO_3$ plus 15.2 wt % H_2O composition, was initially prepared (Table 5.1). The dry end member $MgSiO_3$ was prepared from high purity oxides MgO and SiO_2 and the dry and hydrous end-members were mixed in different weight % proportions to obtain the compositions given in Table 5.1. Before each experiment, all

mixtures were dried overnight at 120 °C to avoid absorption of water. Platinum or platinum/rhodium capsules were fabricated from 2 mm diameter Pt or Pt/Rh (Pt₉₀Rh₁₀) rods cut into 1 mm sections. The obtained discs were spark eroded on one surface, obtaining rows of 4 to 6 chambers per disc with each chamber being 0.25 mm in diameter and approximately 0.66 mm deep. Each chamber was loaded with a different starting powder such that H₂O contents increased across the row of chambers. Sample powders were packed into each chamber using a tungsten-rhenium needle. When packed sufficiently the chambers remained full even when air was blown across the surface. Blowing air removed extraneous sample powders from chambers that had not yet been loaded. Pt capsules were closed by placing a second disk of Pt or 0.25 mm thick on top of the chambers, which was held closed under pressure. When Pt/Rh capsules were employed the open extremities of the chambers were closed by placing on top 6 foils of Pt/Rh with total thickness of ~0.25 mm.

High pressure and high temperature multianvil experiments were carried using a multianvil apparatus installed at the Bayerisches Geoinstitut (BGI). The experiments were performed in an 18/11 assembly, with an 18 mm edge length Cr₂O₃-doped MgO octahedral pressure medium and 11 mm WC anvil truncation. Experiments at 6 GPa were performed using a 500 tonne Walker-type multi anvil press and a 5000 tonne Kawai type multianvil press. The experiments at 13 GPa were carried out with the 5000 tonne multianvil apparatus. The pressure calibration at 6 GPa was performed based on the CaGeO₃ garnet to perovskite phase transition (Ross et al, 1986) for the 500 tonne multianvil apparatus, while the pressure calibration described by Frost et al. (2004) was employed for the experiments performed with the 5000 tonne press. A stepped graphite heater was used in the experiments at 6 GPa, while for those performed at 13 GPa a LaCrO₃ heater was employed. Temperatures during the experiments were monitored using a W₉₇Re₃W₇₅Re₂₅ (D type) thermocouple inserted within an alumina sleeve. The thermocouple junction was in contact with the base of the spark eroded capsules, ~0.5 mm from the sample chambers, with an estimated temperature uncertainty of ~50 °C. A 25 µm thick foil of rhenium was placed on the top of the capsule in order to avoid direct contact between the capsule and the thermocouple junction. The maximum temperature fluctuation during the experiments was ± 5 °C. The capsule was surrounded by MgO spacers and sleeves. Each experiment was first pressurised over 4 hours then heated in ~15 minutes to target temperature where it remained for up to 30 minutes depending on target temperature. Once heated, the experiment was quenched by turning off

the power supply to the graphite/LaCrO₃ heater, and decompression was carried out over approximately 15 hours.

After each experiment, the Pt or Pt/Rh sample disk was recovered, mounted in epoxy and polished in the absence of water. Due to the high porosity of the charges, impregnation with either epoxy resin or superglue was often required in order to fill up the void spaces of the charges and avoid loss of material during the polishing. Once the samples were polished, phase identification and chemical analyses were carried out using a JEOL-JXA-8200 electron microprobe (EMPA). Conditions of 15kV and 15 nA for the beam voltage and current were adopted in all the chemical analyses, using a beam diameter of ~1 μm. Standards for SiO₂ and MgO were forsterite and enstatite and ZAF corrections were adopted for all analyses.

Raman spectroscopy was conducted on all experimental charges to confirm the nature of the mineral phases produced. The analyses were performed by means of a LABRAM Raman spectrometer operating with a He-Ne laser with 632 nm red line wavelength. Analyses were performed with 3 collections and accumulation time of 15 seconds each.

5.3 Results

Typical experimental run sections are shown in Fig. 5.1. At both pressures of 6 and 13 GPa melts quenched to produce a fine intergrowth of quench crystals. However crystals that were solid during heating in the experimental charges were easily distinguished from such quenched crystals based on their euhedral character and grain size. In some experiments quenched areas with different grain sizes and crystallite shapes could be observed that might be interpreted as separate coexisting liquids, or vapour. Fig. 5.1a, for example, shows two quench textures in the same charge with different fibrous grain sizes. Given that the H₂O contents of the charges are relatively low for fluid saturated conditions to be encountered, it seems more likely that these differences in texture result from differences in nucleation and growth during quenching of the experiments. All quench textures are consistent with an origin as H₂O-bearing melts rather than fluids. This distinction is made based on the quench crystal density compared to previous studies performed at lower temperatures where sub solidus fluid phases were encountered (Mibe et al. 2002).

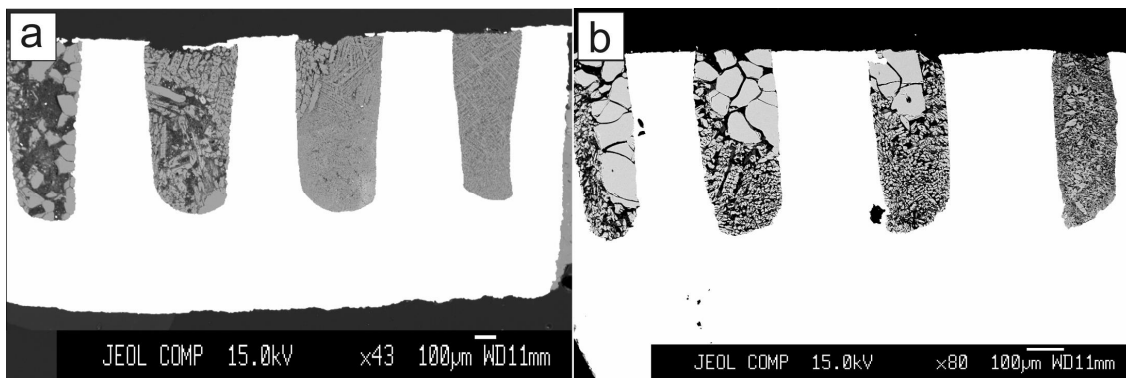


Fig. 5.1: Backscattered electron (BSE) images of experiments performed at 6 GPa in the Mg_2SiO_4 - H_2O system. The bright material is the Pt capsule. Grey crystals (50 to 100 μm across) of forsterite can be easily distinguished from the fine grain quenched melt. (a): figure corresponds to experiment V649 (Table 5.2, see later) where in order from left to right are sample chambers containing starting mixtures of Mg_2SiO_4 plus 5, 10, 15 and 20.4 wt % H_2O . (b): BSE image of experiment V660 (Table 5.2, see later) where, from left to right, starting mixtures of Mg_2SiO_4 with 7.9, 9.7, 13.8 and 18.3 wt % H_2O were employed.

Sections were ground by hand to over half way through the sample chamber to ensure the absence of crystals in super liquidus experiments. Continual checks were made during grinding to examine for crystals that might not otherwise appear in the final section. Some samples were ground more than 80% through to ensure that no crystals were present in further sections. The small size of the sample chambers should ensure that thermal gradients across the samples are minimal. The large relative size of the metal capsule should also help to relax thermal gradients. Based on measurements performed in similar assemblies using two pyroxene thermometry the thermal gradients within each chamber are estimated to be <20 °C.

Several experiments were performed at the same conditions but with different heating durations in order to assess H_2O loss from the Pt capsules during the experiments. Two experiments bearing the same starting mixtures were performed at 6 GPa and 1400 °C for 5 and 30 minutes, and in both cases the resulting assemblages in each sample chamber were identical. At 13 GPa an identical result was obtained by following the same approach at 1450 °C. These observations imply that significant loss of H_2O does not occur in experiments with run times up to 30 min and at temperatures up to 1450 °C. However, it was observed that in some experiments performed at high temperatures (>1650 °C), experimental time periods > 30 min led to substantial crystallisation, likely due to H_2O loss from the Pt capsule. Therefore, experiments performed above 1650 °C were held at temperature for 5-20 minutes.

With increasing temperature the H_2O content of the liquidus in both systems decreases rapidly. The sensitivity of the liquidus to temperature creates a challenge for multianvil experiments where very small changes in the position of the sample can lead to large differences in the sample temperature due to thermal gradients along the length of the furnace. Due to very small differences in the placement of the capsule it was possible to obtain very different assemblages in experiments which showed the same thermocouple temperature. Great efforts were required in the reproducible assembly of the multianvil octahedra in order to obtain reproducible phase assemblages. Few multianvil studies in the past have been performed on such temperature sensitive systems.

5.3.1 Results of experiments performed at 6 GPa

Experimental conditions and phase assemblages of the experiments performed at 6 GPa for both $\text{Mg}_2\text{SiO}_4\text{-H}_2\text{O}$ and $\text{MgSiO}_3\text{-H}_2\text{O}$ systems are summarized in Table 5.2. In the forsterite- H_2O system, experiments were performed starting from 1250 °C up to 1650 °C. In experiments performed at 1250 °C crystals of enstatite were also observed in some chambers, and forsterite was interpreted to melt incongruently at these conditions. This observation is not in agreement with the experimental results of Inoue (1994), which indicate the transition from congruent to incongruent melting of forsterite in system $\text{Mg}_2\text{SiO}_4\text{-H}_2\text{O}$ to occur between 7.7 and 12 GPa. In experiments conducted at temperature >1250 °C chambers contained either forsterite plus melt or just melt, implying congruent melting. At 1250 °C it was not possible to reach liquidus conditions i.e. crystals in equilibrium with quenched melt were found for the highest H_2O content sample, 20.4 wt % (Table 5.2). However, at temperatures higher than 1250 °C, most experiments produced a super liquidus melt chamber containing only quenched melt. At 1400 °C for example (Fig. 1b, Table 2) forsterite crystals coexisting with melt were produced by bulk compositions with H_2O contents of 7.9, 9.7, 13.8 wt %, but the chamber containing 18.3 wt % H_2O contained only melt. The proportion of crystals in each chamber decreases in line with the lever rule as the crystal melt region is crossed as a function of H_2O content. No interpretation of these proportions is made, however, as it may be unreliably biased due the particular sample section obtained during polishing.

Table 5.2: Experimental conditions and phase assemblages of the experiments at 6 GPa

Run	T (°C)	time (min)	starting mix.	phase assemblage
<i>Mg_2SiO_4-H_2O system</i>				
V678	1250	30	Fo A; E; B; F	Fo+L; Fo+L; Fo+L; Fo+En+L
V702	1250	30	Fo A; E; B; F	Fo+En+L; Fo+En+L; Fo+L; Fo+L
V731	1250	30	Fo A; E; B; C	Fo+En+L; Fo+L; Fo+L; Fo+L
V675	1300	30	Fo A; E; B; F	L; Fo+L; Fo+L; Fo+L
V704	1300*	30	Fo C; F; B; E	Fo+L; Fo+L; Fo+L; Fo+L
Z1021&	1350	30	Fo A; E; B	Fo+L; Fo+L; Fo+L
V656	1400	30	Fo E; F; G; H	L; Fo+L; Fo+L; Fo+L
V660	1400	45	Fo E; F; G; H	L; Fo+L; Fo+L; Fo+L
V674	1450*	30	Fo A; E; B; F	L; L; L; Fo+L
V740	1450*	30	Fo I, D, H, G, C	Fo+L; Fo+L; Fo+L; Fo+L; Fo+L
V663	1500*	30	Fo J; I; D; H	Fo+L; Fo+L; Fo+L; Fo+L
V666	1500*	30	Fo E; F; G; H	L; L; Fo+L; Fo+L
V672	1500	30	Fo J; I; D; H	Fo+L; Fo+L; Fo+L; Fo+L
V738A	1500	30	Fo H	Fo+L
Z1023A&	1500	30	Fo A; E; B; C	L; L; L; L
Z1020A&	1550	10	Fo G; C; F	Fo+L; Fo+L; Fo+L
V703A	1600	30	Fo I; D; H; G	Fo+L; Fo+L; Fo+L; Fo+L
V730A	1600*	30	Fo J; D; H	Fo+L; Fo+L; Fo+L
V709A	1600	30	Fo I; D; H; G	Fo+L; Fo+L; Fo+L; Fo+L
V649	1650*	30	Fo A; B; C; D	fl; fl+L; L; Fo+L
V737A	1650	30	Fo J, D, H	Fo+L; Fo+L#; Fo+L
V661	1650*	30	Fo E; F; G; H	L; L; L; L
<i>$MgSiO_3$-H_2O system</i>				
V732	1050*	30	En D; C; B; A	En+L; En+L; En+L; En+L
V702	1250	30	En C; H	En+L; En+L
V731	1250	30	En D	En+L
V704	1300*	30	En F; G; H; D	En%+L; En+L; En+L; En+L
V738B	1500	30	EnA, EnB, EnC	En-L, En+L, En-L
Z1023B&	1500	30	En G; C; H; D	En+L; En+L; En+L; En+L
Z1020B&	1550	10	En C; H; D	En+L; En+L; L
V703B	1600	30	En G; C; H; D	En+L; L; L; L
V730B	1600*	30	En F; G; H;	En+L; En+L; L
V709B	1600	30	En G; C; H; D	En+L; L; L; L
V737B	1650	30	En F, G, C	En+L; L; L

Fo: forsterite; En: enstatite; L: quenched melt; #: presence of enstatite crystals; %: presence of forsterite;

* temperatures estimated based on the power (Watts) utilized during heating; &: experiment performed using the 5000t multianvil apparatus.

In the $MgSiO_3$ - H_2O system, experiments were carried out from 1050 °C to 1650 °C, with starting mixtures containing up to 15.2 wt % H_2O . All sample chambers contained enstatite and melt or just melt, indicating that melting occurred congruently over the entire temperature range. In one experiment (V704, Table 2) a tiny crystal of forsterite was found as an inclusion in a large enstatite crystal, but this was most likely a consequence of inhomogeneity of the starting mixture. At temperatures of 1500 °C and lower the highest

H_2O bearing sample yielded enstatite plus melt but between 1550 °C and 1650 °C it was possible to determine the liquidus at approximately 14.5 and 10.5 wt % H_2O respectively (Fig. 5.2).

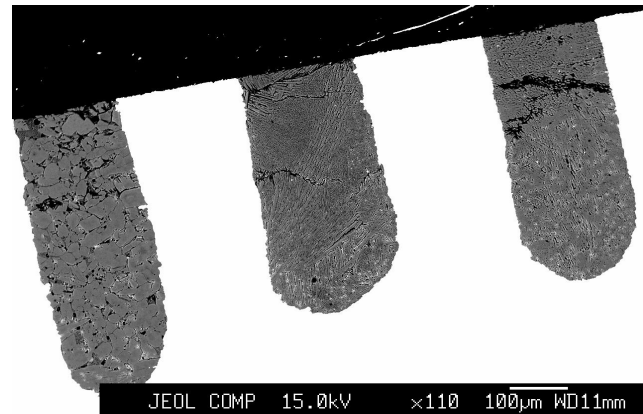


Fig. 5.2: BSE image of experiment V737B carried out in the $\text{MgSiO}_3\text{-H}_2\text{O}$ system at 6 GPa and 1650 °C (Table 5.2). The bright material is the Pt capsule. The water content of the starting mixture used in each chamber increases from left to right. Crystals of enstatite, in equilibrium with interstitial quenched melt can be recognized in the chamber on the left which contained MgSiO_3 plus 6.3 wt % H_2O . Middle and right chambers, bearing mixtures of enstatite plus 10.1 and 11.9 wt % H_2O respectively, produced both quenched melt.

5.3.2 Results of experiments performed at 13 GPa

Experimental conditions and phase assemblages of the experiments performed at 13 GPa for both systems $\text{Mg}_2\text{SiO}_4\text{-H}_2\text{O}$ and $\text{MgSiO}_3\text{-H}_2\text{O}$ are summarized in Table 5.3.

Table 5.3: Experimental conditions and phase assemblages of the experiments at 13 GPa

Run	T (°C)	time (min)	starting mix.	phase assemblage
<i>Mg₂SiO₄-H₂O system</i>				
Z825A	1300	30	Fo A; F; D	Fo+L, Fo+En+L, Fo+En+L
Z824A	1500	30	Fo A; F; D	Fo+En+L, Fo+L, Fo+L
Z837A	1600	5	Fo A; F; D	Fo+En+L, Fo+En+L, Fo+L
Z826B	1700	20	Fo A; F; D	L, Fo+L, Fo+L
Z836A	1900	3	Fo A; F; D	L, L, Fo+L
<i>MgSiO₃-H₂O system</i>				
Z825B	1300	30	En D; G; F;	En+L, En+St+L, En+St+L
Z824B	1500	30	En D; C; B;	En+L, En+L, En+L
Z837B	1600	5	En D, G, F	En+L, En+St+L, En+L
Z826A	1700	20	En C; F	L, En+St+L
Z836B	1900	3	En D, G, A	L, L, En+L

Fo: forsterite, En: enstatite, St: stishovite, L: quenched melt

Experiments were performed between 1300 and 1900 °C. In the Mg_2SiO_4 - H_2O system, forsterite was found to melt incongruently to an assemblage containing enstatite at temperatures below 1600 °C. As shown in Table 5.3, forsterite was found to coexist with enstatite and melt at temperatures between 1300 and 1600 °C. However, the congruent forsterite liquidus could be bracketed at 1700 °C between 13.8 and 20.4 wt % H_2O (Fig. 5.3) and at 1900 °C between 5 and 13.8 wt % H_2O .

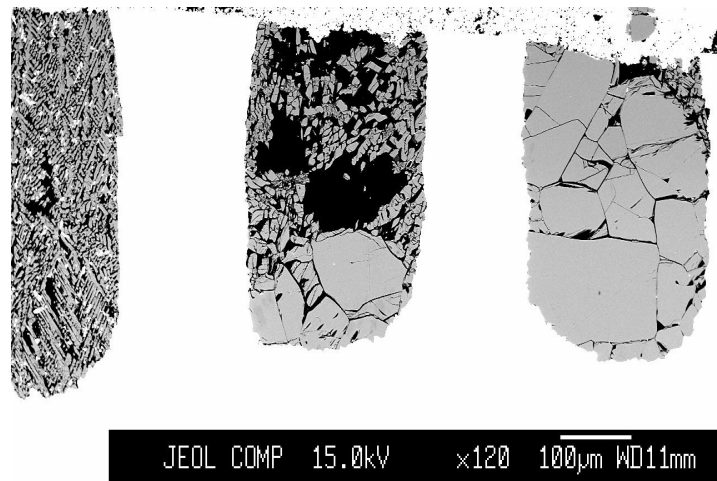


Fig. 5.3: BSE image of experiment Z826 performed in the Mg_2SiO_4 - H_2O system at 13 GPa and 1700 °C. The bright material is the Pt capsule, that contained 3 chambers where starting mixtures Fo A (left, 20.4 wt % H_2O), F (middle, 13.8 wt % H_2O) and D (right, 6 wt % H_2O) were employed. Dark cavities are voids formed during polishing preparation. Large crystals of forsterite (up to ~150 μm across), in equilibrium with quenched melt were produced in the chambers where 13.8 and 6 wt % H_2O was present in the starting material. Composition Fo A, containing forsterite plus 20.4 wt % H_2O , produced only quenched crystals resembling melt.

At 1500 °C, the experiment with starting mixture containing Mg_2SiO_4 with 5 wt% H_2O produced forsterite and melt along with a tiny crystals of MgO (estimated to be <1 vol %). The formation of such crystals in this experiment was interpreted to be a consequence of a slight deviation from stoichiometric Mg_2SiO_4 of the starting mixture.

In the system MgSiO_3 - H_2O enstatite was found to melt congruently at 1900 °C and the liquidus curve was bracketed at this temperature between 4.3 and 10 wt % H_2O . However, in some of the experiments performed between 1700 and 1300 °C, the formation of tiny crystals of stishovite was observed along with enstatite and melt, in agreement with observations of Yamada et al. (2004) at 13.5 GPa. This phase however was observed only as a minor component, ~2 vol %, and therefore it is not expect to cause significant effects on the determined phase relations. Additionally, the liquidus curve was bracketed at 1700 °C between 6.2 and 11.8 wt % H_2O respectively. At 1600 °C the highest H_2O -bearing charge

containing 15.2 wt % H₂O produced enstatite plus liquid, which constrains the minimum H₂O content on the liquidus.

5.4 Discussion

5.4.1 Models for the effect of H₂O on the melting of Mg₂SiO₄ and MgSiO₃

A number of studies have examined the melting point depression of silicate minerals as a function of melt H₂O content using a cryoscopic equation (e.g. Silver and Stolper 1985; Medard and Grove, 2008; Hirschmann et al., 2009). For Mg₂SiO₄, for example, at equilibrium,

$$\ln(a_{Mg_2SiO_4}^{melt}) = \ln(1 - a_{H_2O}^{melt}) = \frac{-\Delta G_{fusion}^o}{RT} \quad (5.1)$$

where ΔG_{fusion}^o is the standard state Gibbs free energy change of pure forsterite melting (see appendix) and $a_{Mg_2SiO_4}^{melt}$ is the activity of Mg₂SiO₄ in the Mg₂SiO₄-H₂O melt. At temperatures below the dry Mg₂SiO₄ melting point ΔG_{fusion}^o can be determined by integrating $\Delta \bar{S}_f$, the entropy of fusion of pure Mg₂SiO₄, between T and the anhydrous melting point Tm. Making the assumption that $\Delta \bar{S}_f$ is constant with temperature this becomes:

$$\ln a_{Mg_2SiO_4}^{melt} = \left[\frac{1}{RT} \Delta \bar{S}_f (T - Tm) \right] \quad (5.2).$$

Determinations of $\Delta \bar{S}_f$ for Mg₂SiO₄ and MgSiO₃ have been made using calorimetric data at 1 bar (e.g. Navrotsky et al. 1989; Richet et al., 1993) and expressions for $\Delta \bar{S}_f$ at higher pressures can be determined from data on dry melting curves combined with an equation of state for solid Mg₂SiO₄ or MgSiO₃. The complexity in deriving a melting model using such a cryoscopic equation, however, comes in determining the correct relationship between $a_{Mg_2SiO_4}^{melt}$ and $X_{Mg_2SiO_4}^{melt}$, which influences how $a_{Mg_2SiO_4}^{melt}$ relates to the weight % H₂O in the melt. Mixing of molecules of Mg₂SiO₄ and H₂O does not produce sufficient depression in the

liquidus to explain the experimental data and it is well recognized that H₂O dissociates as it dissolves in silicate melts to produce hydroxyl groups bonded to silicate molecules i.e.,



Spectroscopic analyses also indicate that both molecular H₂O and OH⁻ groups can be present in silicate melts (Stolper, 1982). Silver and Stolper (1985) proposed a thermodynamic model to describe the effects of H₂O speciation on the activity of silicate melt components. They assumed that all 3 species mix ideally forming a homogeneous melt equilibrium for which they defined an equilibrium constant $K_{5.3}$,

$$K_{5.3} = \frac{(X_{\text{OH}^-}^{\text{melt}})^2}{(X_{\text{H}_2\text{O}}^{\text{melt}})(X_{\text{O}^{2-}}^{\text{melt}})} \quad (5.4).$$

The activity of the silicate component, $a_{\text{Mg}_2\text{SiO}_4}^{\text{melt}}$, is related to the mole fraction of available oxygens in the melt $X_{\text{O}^{2-}}^{\text{melt}}$ through the expression,

$$a_{\text{Mg}_2\text{SiO}_4}^{\text{melt}} = (X_{\text{O}^{2-}}^{\text{melt}})^r \quad (5.5)$$

where r is the number of oxygens per mole of silicate, i.e. 4 for Mg₂SiO₄. The factor r can be set to 1 and therefore neglected by employing a single oxygen formula unit, i.e. Mg_{0.5}Si_{0.25}O for forsterite. This implies that H is mixing on all possible oxygens of the silicate molecule.

The total initial mole fraction of H₂O, $X_{\Sigma\text{H}_2\text{O}}^{\text{melt}}$, is therefore:

$$X_{\Sigma\text{H}_2\text{O}}^{\text{melt}} = X_{\text{H}_2\text{O}}^{\text{melt}} + 0.5X_{\text{OH}^-}^{\text{melt}} \quad (5.6).$$

$X_{\Sigma\text{H}_2\text{O}}^{\text{melt}}$ can then be related through the equilibrium constant $K_{5.3}$ to the mole fraction of any of the other melt species e.g.:

$$X_{\Sigma\text{H}_2\text{O}}^{\text{melt}} = 1 - X_{\text{O}^{2-}}^{\text{melt}} + \frac{1}{4} \left\{ K_{5.3} X_{\text{O}^{2-}}^{\text{melt}} - \left[\left(K_{5.3} X_{\text{O}^{2-}}^{\text{melt}} \right)^2 + 4K_{5.3} X_{\text{O}^{2-}}^{\text{melt}} - 4K_{5.3} \left(X_{\text{O}^{2-}}^{\text{melt}} \right)^2 \right]^{\frac{1}{2}} \right\} \quad (5.7).$$

If the activity of forsterite is determined using equation 5.1 on a single oxygen basis, then $X_{\Sigma\text{H}_2\text{O}}^{\text{melt}}$ can be determined using equations 5.5 and 5.7 for a given value of $K_{5.3}$ and $r=1$, and the H_2O content of the melt can then be determined from

$$\text{wt \% H}_2\text{O} = \frac{(X_{\Sigma\text{H}_2\text{O}}^{\text{melt}})(18.015)}{(X_{\Sigma\text{H}_2\text{O}}^{\text{melt}})(18.015) + (1 - X_{\Sigma\text{H}_2\text{O}}^{\text{melt}})(35.17)} \quad (5.8)$$

where 18.015 and 35.17 are, for example, the molecular weights of water and forsterite on a single oxygen basis respectively.

5.4.1.1 Results at 6 GPa

Fig. 5.4 shows the experimental data at 6 GPa for the liquidus of Mg_2SiO_4 as a function of melt H_2O content compared to calculations of the liquidus made using the model of Silver and Stolper (1985). To determine $\Delta G_{\text{fusion}}^{\circ}$ at high pressure the equation of state of Stixrude and Lithgow-Bertelloni (2011) was used for solid Mg_2SiO_4 along with the model of de Koker and Stixrude (2009) for Mg_2SiO_4 liquid (see appendix). In order to arrive at a model that is close to the experimental data, the thermodynamic data of de Koker and Stixrude (2009) had to be modified such that the value of $\Delta \bar{S}_f$ for Mg_2SiO_4 at 1 bar was consistent with that proposed by Navrotsky et al. (1989) of 52.7 J/K.mol. This is at the lower end of the range of values reported in the literature, which vary from 70 to 47.5 J/K.mol (Bottinga, 1985; Navrotsky et al., 1989; Richet et al., 1993; Tangeman et al., 2001). Values for the heat capacity and volume of Mg_2SiO_4 liquid were then also adjusted to bring the model into agreement with experimental data on the melting curve of Mg_2SiO_4 (Davis & England, 1964; Kato and Kumazawa, 1985; Presnall and Walter, 1993). The values employed in the model are given in Table a1 in the appendix.

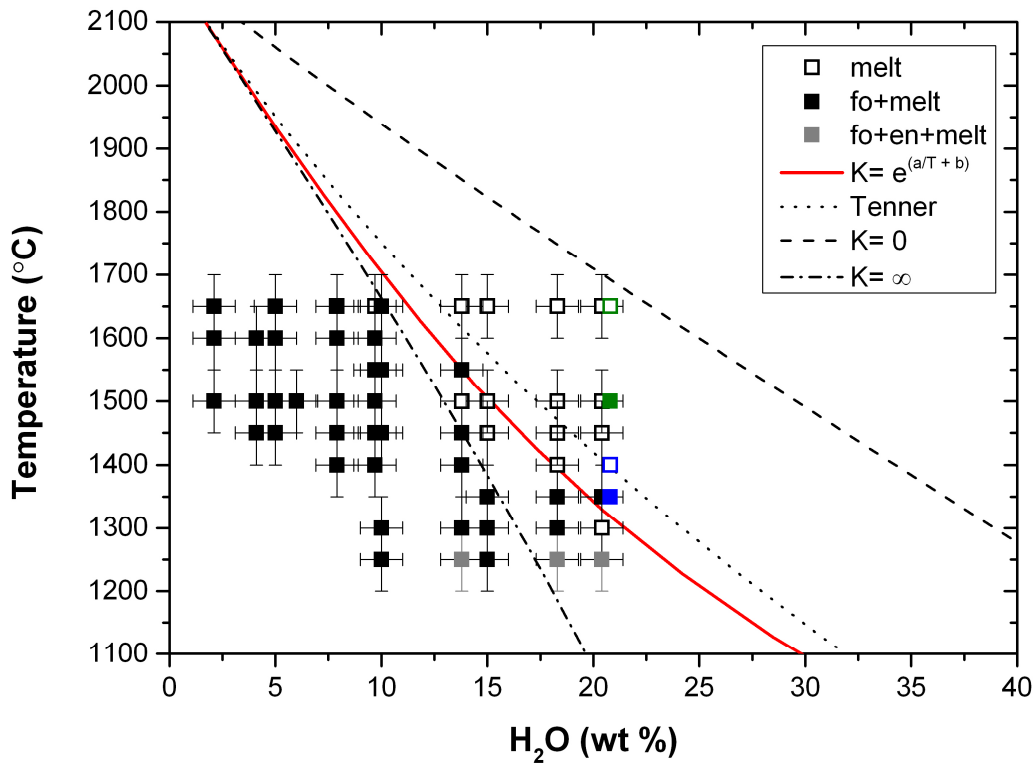


Fig. 5.4: Phase diagram in the Mg_2SiO_4 - H_2O system at 6 GPa showing experimental data and models for the liquidus curves (described in the text). Data points determined in this study (Table 5.2) are displayed by black and gray symbols while data from Luth (1993) at 6 GPa and Inoue (1994) at 5.5 GPa are shown by blue and green symbols, respectively. Data from Luth (1993) and Inoue (1994) were determined for bulk compositions of Mg_2SiO_4 plus 20.4 wt % H_2O but are plotted at slightly higher H_2O content (20.8 wt % H_2O) for comparison with data determined in this study. The liquidus at approximately 20 wt % H_2O is $\sim 200^\circ$ lower than reported by Inoue et al. (1994) at 5.5 GPa and in agreement, within uncertainty, with data of Luth (1993) at 6 GPa. The liquidus curves are all constrained by the dry melting temperature of forsterite at 6 GPa reported by Kato and Kumazawa (1985). Details regarding the different curves are reported in the text. Uncertainties of 1 wt% in the melt composition and 50 °C for the temperature of the experiments are displayed by the error bars.

Three curves for the Mg_2SiO_4 liquidus are plotted in Fig. 5.4 based on different values of $K_{5.3}$. If equilibrium in equation 5.3 is assumed to proceed completely to the right and all H_2O becomes dissociated to OH^- then $K_{5.3}$ becomes infinity and the straight liquidus curve labelled $K = \infty$ is determined. However, the experimental data at the lowest temperatures are in poor agreement with this curve as the liquidus becomes flatter at high H_2O contents. On the other hand by assuming no dissociation to produce OH^- occurs and molecular H_2O remains the only melt water species, then $K_{5.3} = 0$ and the liquidus curve does not at all account for the extent of the depression of melting observed. The flattening out of the experimental liquidus implies that $K_{5.3}$ does not assume a constant value over the range of temperatures but must change with temperature from a value >50 , (which is indiscernible from infinity), above 1400 °C to <10 below 1300 °C. Variations in $K_{5.3}$ with temperature can be described using an expression of the form,

$$\ln K_{5.3} = \frac{a}{T} + b \quad (5.9).$$

The experimental data do not provide sufficient constraints to determine the a and b terms in equation 5.9, which are highly correlated. Values of a and b of approximately -22000 and 16, respectively, are in reasonable agreement with the data, although only once the uncertainties on the experimental data are considered. Values of approximately -8000 and 8 proposed recently for alkaline basalt by Lesne et al. (2011) based on spectroscopic measurements would equally well fit within the uncertainties of the data. The experimental data can only be used to imply a qualitative strong dependence of $K_{5.3}$ on temperature but independent in situ spectroscopic data could potentially make an extremely accurate estimate of this dependence.

Although the model is relatively simple it is difficult to find improvements that provide a significantly better fit to the experimental data, without it becoming completely empirical. The liquidus curve, for example, would be in slightly better agreement with the experimental data if it predicted slightly lower H₂O contents at ~1450 °C, however the only way to do this would be to lower the value of $\Delta \bar{S}_f$ at 1 bar for Mg₂SiO₄, and the value employed is already at the lower end of the range proposed in calorimetric studies. Non ideal mixing could also be included in the model, however, a simple symmetric mixing parameter between the two components produces no improvement in the fit. In addition such terms have been shown to be unnecessary to describe the effect of H₂O on melting in systems at even lower temperatures where non ideal effects should be more important (Silver and Stolper, 1985). A model could also be considered where not all of the silicate oxygens are protonated but only, for example, 1 or 2 per 4 oxygen formula units. This raises 2 issues. Firstly it would imply limited solubility of H₂O in the melt, which appears not to be the case. Secondly if the number of sites on which protons are mixing became an adjustable parameter in the model, being allowed to change, for example, with total H₂O content, the resulting fit parameters would be highly correlated with $K_{5.3}$ and impossible to meaningfully determine without an independent determination of $K_{5.3}$. Therefore the Silver and Stolper (1985) model supported by current estimates for $\Delta \bar{S}_f$ and the melting curve of Mg₂SiO₄ appears to provide an adequate and well constrained approximation of the experimental data.

In addition, plotted in Fig. 5.4 is a curve determined from the model of Tenner et al. (2012). This model employs the same expression as equation 5.1 but assumes that all H₂O dissolves as OH⁻ i.e.:

$$X_{O^{2-}}^{melt} = (1 - X_{OH^-}^{melt}) \quad (5.10).$$

Tenner et al. (2012) determine $X_{OH^-}^{melt}$ from the expression:

$$X_{OH^-}^{melt} = \frac{(2H_2O\text{wt\%}/18.015)}{(2H_2O\text{wt\%}/18.015) + (100 - H_2O\text{wt\%})/\text{mol.wt}_{(\text{Silicate})}} \quad (5.11).$$

In Fig. 5.4 a curve for the Tenner et al. (2012) model is calculated using the same thermodynamic data employed for the Silver and Stolper (1985) models and assuming a single oxygen formula unit. Equation 5.10 is used instead of equation 5.7 in these calculations and the H₂O content of the melt is then determined from a rearrangement of equation 5.11. The resulting curve is quite different from that predicted from the Silver and Solper (1985) model when $K_{5.3}$ is equal to 0, although both models should be equivalent in describing the effect when H₂O dissolves completely as OH⁻. The difference arises in the way that the melt wt % H₂O is converted into $X_{OH^-}^{melt}$. Tenner et al. (2012) multiply the mass of H₂O directly by 2 in the numerator and denominator of equation 5.11, whereas as to be equivalent to the Silver and Solper (1985) model the expression would have to be,

$$X_{OH^-}^{melt} = 2 \cdot \frac{(H_2O\text{wt\%}/18.015)}{(H_2O\text{wt\%}/18.015) + (100 - H_2O\text{wt\%})/\text{mol.wt}_{(\text{Silicate})}} \quad (5.12).$$

Although the model of Tenner et al. (2012) has been found to quite accurately reproduce the liquidus from experiments on natural systems when silicates are mixed on a 3 oxygen formula basis, the model is not able to reproduce the data on Mg₂SiO₄ at 6 GPa, regardless of the silicate molecular unit considered, and appears to be only semi empirical due to the unclear implications of equation 5.11.

In Fig. 5.5 data bracketing the MgSiO_3 - H_2O liquidus at 6 GPa are compared with the same models described above. Equation of state data for MgSiO_3 solid are from Stixrude and Lithgow-Bertelloni (2011) while those for MgSiO_3 liquid are from de Koker and Stixrude (2009).

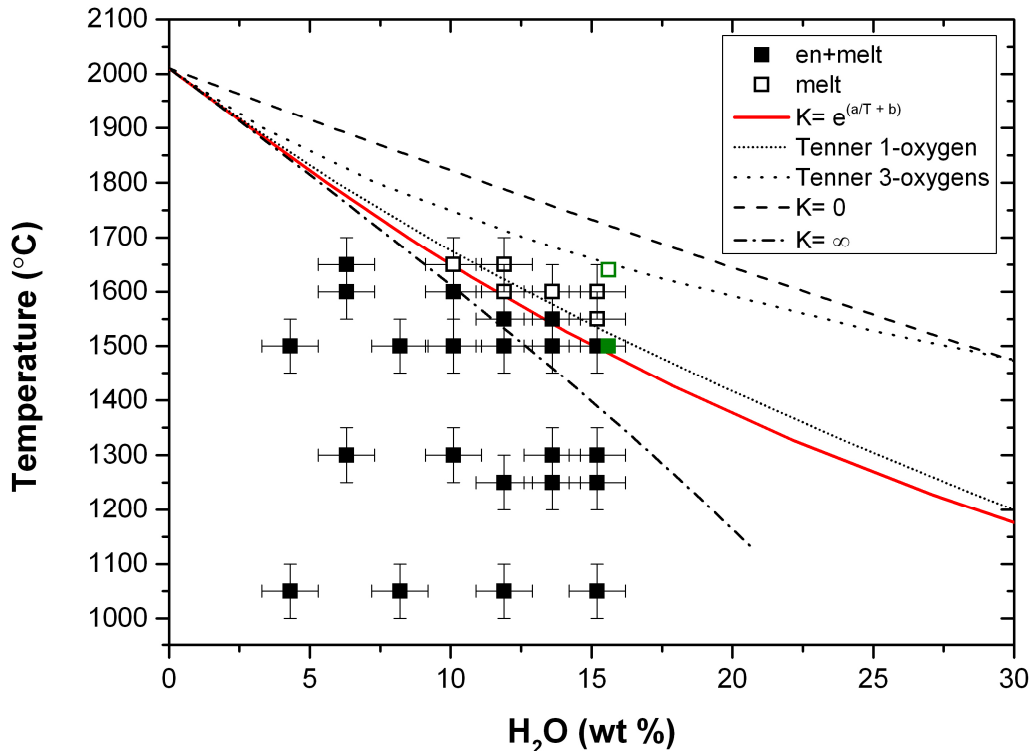


Fig. 5.5: The depression of the MgSiO_3 melting temperature at 6 GPa as a function of melt H_2O content. Data points determined in this study (Table 5.2) are displayed by black symbols while green symbols are from Inoue (1994), which show good agreement. Data of Inoue (1994) are from experiments performed in the MgSiO_3 system with 15.2 wt % H_2O but are plotted at slightly higher H_2O content (15.6 wt % H_2O) so as not to overlap with data determined in this study. Uncertainties of 1 wt% in the melt composition and 50 °C for the temperature of the experiments are displayed by the error bars. Curves describing the liquidus by different models as described in the text are also shown. The liquidus curves are all constrained by the dry melting temperature of enstatite at 6 GPa reported by Kato and Kumazawa (1985).

The equivalent $\Delta \overline{S}_f$ at 1 bar for MgSiO_3 is $40 \text{ J} \cdot \text{K}^{-1} \text{mol}^{-1}$ which is in perfect agreement with calorimetric determinations of Richet and Bottinga (1986). The thermodynamic data are reported in Table a1 (appendix) and provide good agreement with the experimentally determined melting curve (Kato and Kumazawa 1985). The Silver and Stolper (1985) models assume mixing of $\text{Mg}_{1/3}\text{Si}_{1/3}\text{O}$ molecules.

The model that considers complete dissociation to OH^- ($K_{5.3} = \hat{0}$), as for the case of the forsterite- H_2O system, agrees with experimental data only at the highest temperatures investigated (down to 1600 °C). At lower temperatures, in fact, the experimental data imply a flattening of the liquidus that is not followed by the straight line corresponding to the $K_{5.3} = \hat{0}$ model. Also, mixing only of molecular H_2O ($K_{5.3} = 0$) results in a liquidus curve far outside of the experimental uncertainties. As H_2O is added as $\text{Mg}(\text{OH})_2$ in the experiments, the total H_2O examined cannot exceed 15 wt %. For this reason the liquidus can only be bracketed at higher temperatures (Table 5.2) where H_2O apparently remains dissociated. A model considering a variation of $K_{5.3}$ with temperature as described by equation 5.9 fulfils the constraints imposed by the experiments, although a large range of parameters for this equation can provide an adequate fit to the data. The curve in Fig. 5.5 was calculated with values of a and b of -6000 and 4.5 with $K_{5.3}$ varying from ~7 at 2100 °C to ~2 at 1300 °C. In addition, two models from Tenner et al. (2012) that assume mixing of silicate molecules with 1- and 3-oxygens per formula unit are shown in Fig. 5.5. The model of Tenner et al. (2012) based on 1-oxygen per formula unit predicts values within the experimental uncertainties. Tenner et al. (2012), however, find the best agreement with natural melting data when a 3 oxygen silicate molecule is assumed but as shown in Fig. 5.5 this is in poor agreement with the data in this simpler system.

Both enstatite and forsterite melting experiments at 6 GPa can be described by Silver and Stolper (1985) models that assume mixing of 1-oxygen silicate molecules i.e. mixing of H on all silicate oxygens, and temperature dependent dissociation of H_2O which goes towards complete OH^- formation above ~1400 °C. An interesting observation is that the wt % H_2O in the liquidus melt at a given temperature is nearly identical at 6 GPa for both MgSiO_3 and Mg_2SiO_4 over the range of temperature at which the experiments are performed.

5.4.1.2 Results at 13 GPa

In Fig. 5.6 experiments to bracket the Mg_2SiO_4 - H_2O liquidus at 13 GPa are shown and compared to the same models for the depression of melting as described above for the results at 6 GPa.

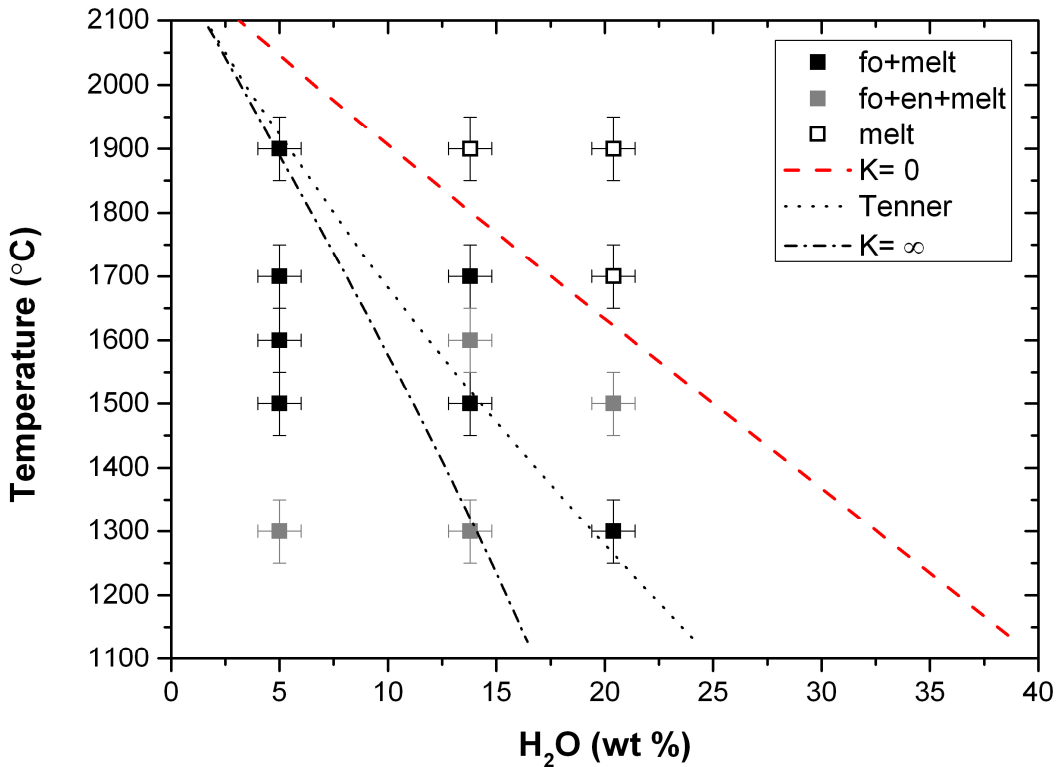


Fig. 5.6: The melting phase relations in the Mg_2SiO_4 - H_2O system at 13 GPa and the depression of the melting temperature as a function of melt H_2O content (details reported in the text). Uncertainties of 1 wt % in the melt composition and 50 °C for the temperature of the experiments are displayed. The incongruent melting of forsterite is consistent with the results of Inoue (1994), even though the onset of incongruent melting was determined to be 200 °C lower compared to the current study. Dry melting temperature of forsterite at 13 GPa was calculated to be 2200 °C by extrapolations of de Koker and Stixrude (2009).

The melting of pure Mg_2SiO_4 becomes incongruent above 10 GPa, with Mg_2SiO_4 reacting to produce MgO plus melt at the solidus (Presnall and Walter, 1993). However, in Fig. 5.6 thermodynamic data for congruent Mg_2SiO_4 melting are extrapolated using the melt model of de Koker and Stixrude (2009) to 13 GPa, which none the less creates some uncertainty due to the lack of comparable experimental observations. Although on the addition of H_2O melting becomes congruent at least between 1700-1900 °C (Table 5.3), it becomes incongruent again, this time to produce enstatite plus forsterite, at lower temperatures. Models from Tenner et al. (2012) and Silver and Stolper (1985) with $K_{5.3} = \hat{0}$ do not reproduce the experimental data presented here (Table 5.3, Fig. 5.6). The best fit with the experimental liquidus is for the Silver and Stolper (1985) model that assumes mixing of molecular H_2O ($K_3 = 0$), i.e. no dissociation to OH^- groups. A model where $K_{5.3} = 0.2$ also just agrees with the experimental uncertainties.

There are larger inherent uncertainties in this evaluation at 13 GPa arising from the melting temperature assumed for dry Mg_2SiO_4 . Because Mg_2SiO_4 melting becomes incongruent the only way to assess the dry melting temperature experimentally is to extrapolate melting temperatures determined at lower pressures. Here the thermodynamic model of de Koker and Stixrude (2009) is used to provide justification to this extrapolation because it is based on computer simulations, however the resulting dramatic change which is implied in the H_2O speciation most probably arises from uncertainties in this temperature. By assuming an anhydrous melting temperature that is 250 °C higher, the best fitting temperature dependent model for $K_{5.3}$ determined at 6 GPa for Mg_2SiO_4 fits well to the experimental liquidus. Therefore rather than concluding that there is a dramatic shift in H_2O speciation at high pressure, which seems unlikely, the most plausible explanation for the weak depression of melting for Mg_2SiO_4 at 13 GPa most likely arises from uncertainties in the dry melting temperature. This highlights the problems of examining melting point depression in incongruent systems, which are likely to be even more problematic for natural complex systems such as mantle peridotite melts.

Fig. 5.7 shows the depression of melting results for MgSiO_3 determined from the experimental data at 13 GPa. In complete contrast to Mg_2SiO_4 at these conditions, the best fit Silver and Stolper (1985) model for MgSiO_3 is for almost complete dissociation to OH in the melt. Only a very slight improvement to the fit can be obtained by imposing a temperature dependence to $K_{5.3}$ causing the liquidus to pass to the right of one sub liquidus experimental point at 1600 °C. This is, however, not justified by the experimental uncertainties. A molecular H_2O model is far outside of the experimental constraints, as is the model corresponding to that of Tennen et al. (2012).

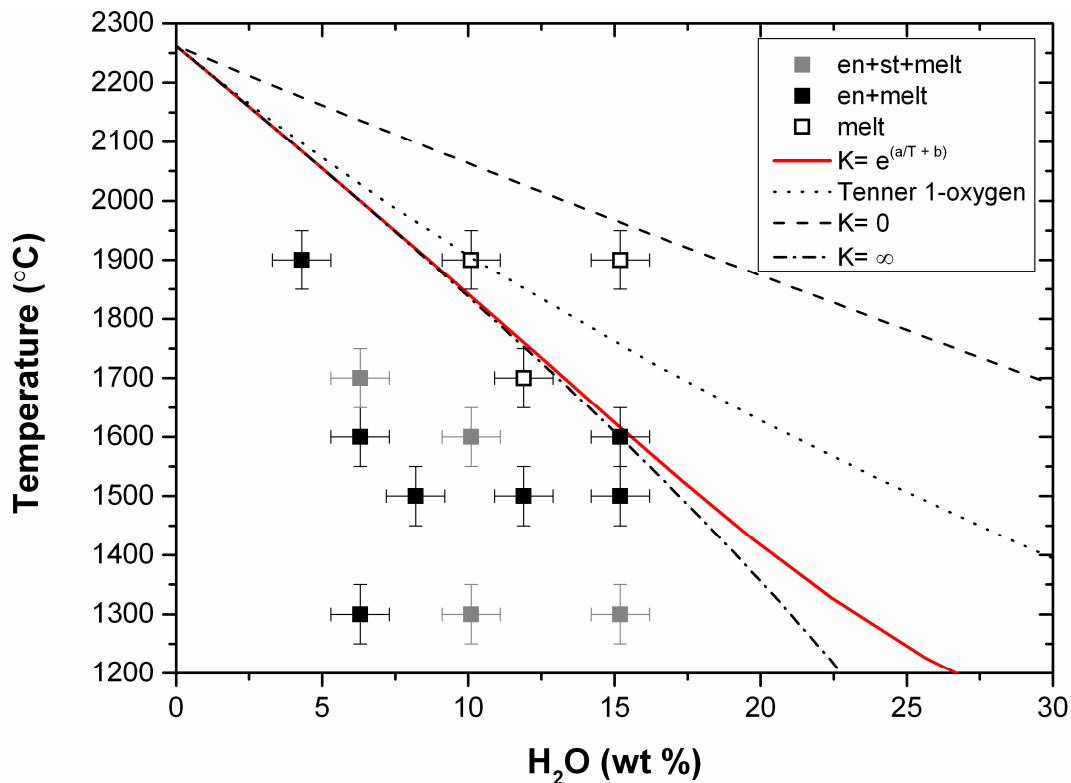


Fig. 5.7: The melting phase relations in the $\text{MgSiO}_3\text{-H}_2\text{O}$ system at 13 GPa and the depression of the melting temperature as a function of melt H_2O content (details reported in the text). Uncertainties of 1 wt% in the melt composition and 50 °C for the temperature of the experiments are displayed. Dry melting temperature of enstatite at 13 GPa was calculated to be 2250 °C by extrapolations of de Koker and Stixrude (2009).

5.4.2 The effect of pressure on melting point depression due to H_2O in simple and complex silicate systems

The depression in the hydrous melting temperature compared to the anhydrous melting point is shown for both the $\text{MgSiO}_3\text{-H}_2\text{O}$ and $\text{Mg}_2\text{SiO}_4\text{-H}_2\text{O}$ systems at 6 and 13 GPa in Fig. 5.8. In addition, data from Kushiro et al. (1968) for $\text{MgSiO}_3\text{-H}_2\text{O}$ are used to construct a further curve at 1 GPa. A value of $K_{5.3} = 0.5$ provides a good fit to these data, which bracket the liquidus between 1375 and 1525 °C. For MgSiO_3 , pressure enhances the influence of H_2O in depressing the melting temperature in line with thermodynamic estimates for the entropy of fusion and the anhydrous melting curve of MgSiO_3 . Although different H_2O speciation models are used at 1 and 6 GPa, for 6 and 13 GPa identical models assuming almost no molecular H_2O above 1400 °C can explain the experimental observations. Using the model of Silver and Stolper (1985), this implies an increase in the degree of H_2O dissociation with pressure mainly between 1 and 6 GPa for MgSiO_3 .

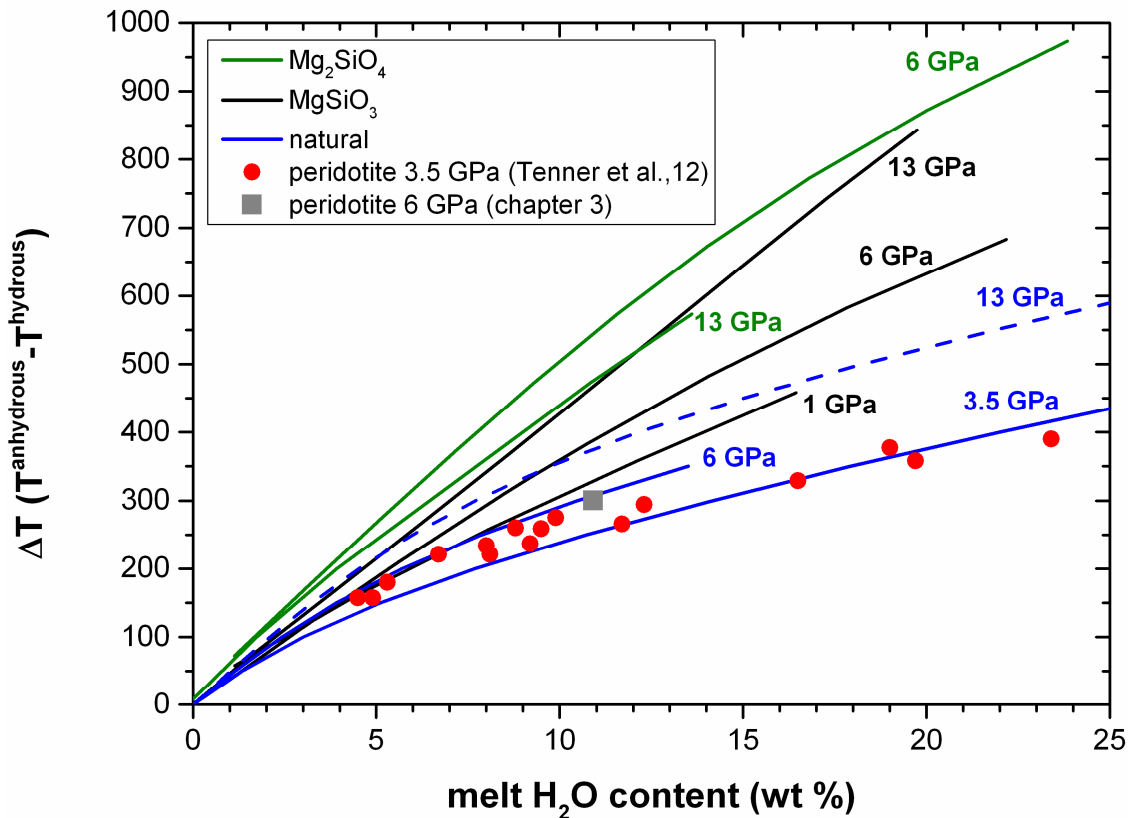


Fig. 5.8: The depression in the hydrous melting temperature as a function of H_2O for MgSiO_3 - H_2O (black lines), Mg_2SiO_4 - H_2O (green lines) and natural melt compositions between 1 and 13 GPa. Hydrous garnet peridotite melt compositions are from Tenner et al. (2012) at 3.5 GPa (red dots) and Chapter 3 at 6 GPa (grey square). Blue lines are models for the H_2O effect on melting temperature depression for melts in natural compositions (details regarding the modeling are explained in the text).

For Mg_2SiO_4 - H_2O however, there is a decrease in the effect of H_2O on melting between 6 and 13 GPa. As described previously this observation is most likely caused by the uncertainty in the dry melting temperature of pure Mg_2SiO_4 , which melts incongruently above 10 GPa. If anhydrous melting temperatures are inferred to be 250° higher, then this trend is reversed. This implies that the extrapolated flat melting curve for pure anhydrous Mg_2SiO_4 predicted by the model of de Koker and Stixrude (2009) based on computer simulations is incorrect.

In Fig. 5.8, data for the depression of melting due to H_2O for melts of natural peridotite compositions are shown from Tenner et al. (2012) at 3.5 GPa and this study at 6 GPa (Chapter 3). The depression of melting due to H_2O is much smaller for these complex melts compared to either of the simple systems at the same pressures. Some proportion of this difference is expected as a result of the lower anhydrous melting points of the natural compositions. As indicated by equation 5.2 the magnitude of the depression of melting

should increase with the anhydrous melting temperature, as observed in all experiments. In Fig. 5.8 these data are fitted using a Silver and Stolper (1985) model assuming an average single oxygen molecular mass of 37 g·mol⁻¹ and a $\Delta \overline{S}_f$ of 0.4 J·K⁻¹g⁻¹ (Tenner et al. 2012; Kojitani and Akaogi, 1997). A constant value of $\Delta \overline{S}_f$ is assumed at all pressures and temperatures (i.e. using equation 5.2) and anhydrous melting points are taken from Walter (1998). The best fit models at 3.5 GPa requires a temperature dependent value of $K_{5,3}$ which starts at ~1 close to the dry melting temperature but decreases to effectively 0 below 1200 °C. Although there is only one data point available at 6 GPa the depression of melting is consistent with a similar model as for 3.5 GPa with the only difference in the model being the temperature of the dry melting point. The Silver and Stolper (1985) model therefore implies a much greater proportion of molecular H₂O in natural melt compositions at these conditions compared to simple systems. This difference may have several origins, however. Firstly, the value of $\Delta \overline{S}_f$ employed for peridotite melt may well be incorrect as it is derived from calorimetric data from 1 bar measurements on CMAS melts (Kojitani and Akaogi, 1997) and may not suitably account for the effects of pressure and composition. Secondly, it is possible that certain components present in the natural peridotite melt compositions, such as Al₂O₃, cause a reduction in the effect of H₂O on the configurational entropy of the melt. As a result of this difference in behaviour, however, melting in simple systems seems to be of little relevance for determining melt H₂O contents in mantle chemical systems.

It is interesting to note that although the model of Tenner et al. (2012), which is based on equations 5.10 and 5.11, appears to lack theoretical justification, due to the way in which the mole fraction of OH⁻ is calculated (eq. 5.11), it does predict almost perfectly the depression of melting for the melt compositions from peridotite experiments at both 3.5 and 6 GPa, based on a 3 oxygen melt model. The Tenner et al. (2012) model predicts curves identical to those shown in Fig. 5.8 fitted to the peridotite melt data using the Silver and Stolper (1985) model at 3.5 and 6 GPa. Although only empirical it achieves as good a fit to the natural data with fewer adjustable parameters. As there seems to be no clear justification to the way in which the OH⁻ mole fraction is derived in this model, the predictive capacity is probably just a coincidence.

In Fig. 5.8 the Silver and Stolper (1985) models fitted to the peridotite melt data at 3.5 and 6 GPa are extrapolated to 13 GPa by assuming a dry melting temperature of 1900 °C (Takahashi, 1986). The $K_{5.3}$ speciation model is held the same as that at 3.5 and 6 GPa, with a temperature dependent $K_{5.3}$ varying between ~1 and 0. The Tenner et al. (2012) model would predict an identical curve. The implications of this extrapolation are more clearly indicated in Fig. 5.9, which shows the melt H_2O content determined along an adiabatic gradient for MgSiO_3 and Mg_2SiO_4 melts, in addition to melts derived from natural peridotite.

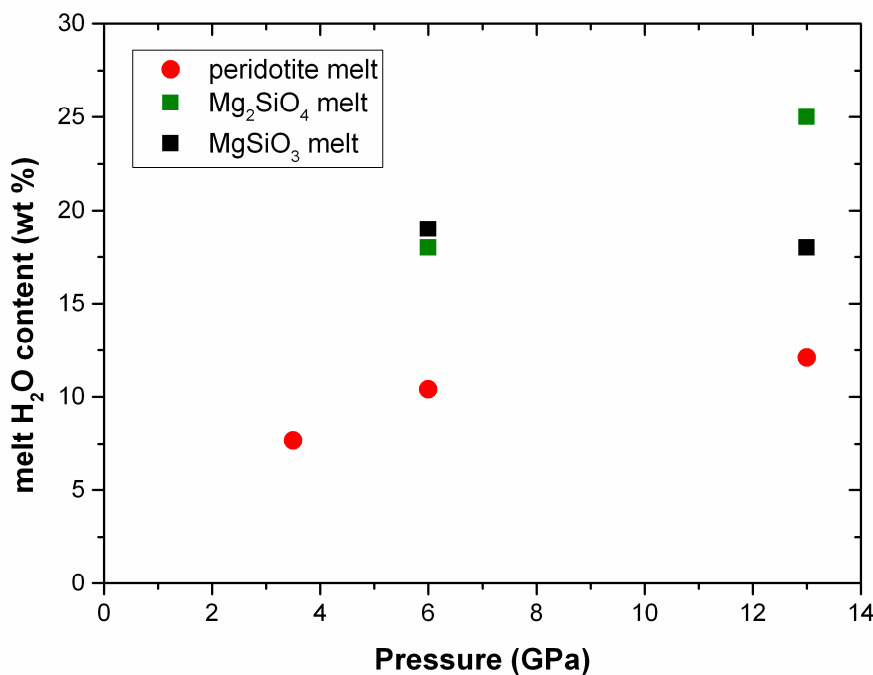


Fig. 5.9: Melt H_2O contents as a function of pressure determined at 3.5, 6 and 13 GPa and at temperatures corresponding to a mantle adiabat (1350 °C, 1400 °C and 1500 °C, respectively). Data at 3.5 GPa are from Tenner et al. (2012) while melt H_2O contents in a natural peridotite system at 6 GPa are from experimental data presented in Chapter 4. The values for the peridotite system at 13 GPa are extrapolated from the model described in the text.

With decreasing pressure a smaller amount of H_2O is required to stabilize an Mg_2SiO_4 melt along a mantle adiabat. This would favour an increase in the proportion of melt produced as pressure decreases if the bulk H_2O contents of the mantle were constant. For MgSiO_3 the melt H_2O content actually increases very slightly between 13 and 6 GPa, which would favour the production of more melt at higher pressures for a constant mantle H_2O content. However, this increase is extremely small and the tendency for a larger melt degree would be counteracted by the increase in mineral melt H_2O partition coefficients with increasing pressure. Peridotite melts are also predicted to require more H_2O to be stable at higher pressures, although the

H_2O melt contents are predicted to vary very little towards the base of the mantle, as observed for MgSiO_3 . Based on this analysis there seems to be no grounds to argue that increasing pressure towards the base of the upper mantle would favour an increase in the extent of hydrous melt formation.

Numerous seismic observations have argued for low seismic velocities above the 410 km discontinuity at the base of the upper mantle (e.g. Tauzin et al., 2010). The existence of small degree volatile bearing melts has been the main argument to explain these observations (Bercovici and Karato, 2003). Given the results in Fig. 5.9 and a constant mantle H_2O content, there is no reason why melting should commence or be seismically more visible at ~410 km depth compared to any other pressures in the upper mantle, as more H_2O is required to stabilize melts at these conditions.

In order for hydrous melts to form at the base of the upper mantle the average mantle would need to be significantly enriched in H_2O compared to most estimates, because mineral-melt H_2O partition coefficients also increase with pressure (see Chapter 4). For the mantle to be enriched in H_2O at this depth would require a fractionation process to operate. Bercovici and Karato (2003) proposed that hydrous melts formed at these conditions may be neutrally buoyant and therefore separate from the up welling mantle, and concentrate at these depths. Whether this is possible or not is mainly dependent on the H_2O content of the melt. Melt density experiments by Matsukage et al. (2005) seem to indicate that this may be possible, however, they considered a melt H_2O content of 6 wt %, which is half that estimated in Fig. 5.9 for natural peridotite derived melts. Following the density systematics of Jing and Karato (2009), melts in equilibrium with peridotite at 13 GPa should be much less dense than the surrounding mantle if melt H_2O contents are close to those predicted in Fig. 5.9. In conclusion, if large scale low seismic velocities observed on top of the 410 km discontinuity result from the presence of small degree melts, these melts are unlikely to exist as a result of the presence of H_2O alone.

6. Effect of temperature and CO₂ on mineral-melt H₂O partitioning in the upper mantle and the production of volatile-bearing melts atop the transition zone

6.1 Introduction

The subduction of oceanic crust results in the recycling of volatiles (e.g. H₂O and CO₂) from surface reservoirs into the deep Earth (e.g. Schmidt and Poli, 1998; Kawamoto, 2006). On the other hand, at mid-ocean ridges volatiles are out-gassed from the mantle during the process of melting and the formation of basaltic oceanic crust. Both subduction and outgassing are extremely important in terms of the global cycle of H₂O and CO₂ and the reservoirs of these volatiles in the bulk Earth (Hirschmann, 2006). The transport of H₂O within the deep Earth has enormous consequences for the geophysical and geochemical properties of mantle materials (e.g. Bolfan-Casanova, 2005). Melting processes in particular are affected by the presence of volatiles (e.g. Wyllie, 1977; Abe et al., 2000; Asimow and Langmuir, 2003). Low degree, volatile-bearing melts forming within the deep mantle have been proposed to cause detectable seismic anomalies (e.g. Tauzin et al., 2010). In addition, the water filter model proposed by Bercovici and Karato (2003) invokes the formation of melt at the upper mantle-transition zone boundary, which in turn causes trace element depletion of material advecting into the overlying mantle. In order to understand the transport of volatiles in the mantle it is crucial to understand the effects of major volatiles such as H₂O and CO₂ on mineral melting processes.

Like H₂O, the addition of CO₂ to a volatile-free mantle peridotite decreases its melting temperature (e.g. Dalton and Presnall, 1998). Quantitative constraints on the formation of hydrous melts at depth can be obtained by assessing the distribution of H₂O between peridotite minerals and low degree melts at upper mantle conditions (see Hirschmann et al., 2009 for a review). However, a more rigorous description of volatile-induced melting processes in the mantle should also consider the inevitable influence of CO₂ in addition to H₂O. Compared to a hydrous system, the presence of CO₂ will lower the H₂O activity of melts while still allowing the melts to remain stable below the volatile-free solidus. As a consequence, the concentrations of H₂O in the minerals coexisting with such melt are expected to decrease. Non-ideality might also potentially lead to an influence of CO₂ on melt

H₂O activity that would then affect the mineral/melt H₂O partition coefficient ($D_{H_2O}^{\text{min/melt}}$). As detailed in Chapter 3, determining the mineral-melt H₂O partition coefficient for high pressure melts is challenging due to the difficulty in measuring melt H₂O contents. However, as shown in Chapter 5 the H₂O content of melts can be bracketed in a straightforward manner for simple congruent melting systems.

In this study we report measurements of forsterite and enstatite H₂O contents that were synthesized at 6 and 13 GPa and 1150-1900 °C. Some of the experiments investigated here were conducted in the simplified system MgO-SiO₂-H₂O (MSH) and are presented in a complementary study (Chapter 5). Additionally, experiments were performed in the system MgO-SiO₂-H₂O-CO₂ (MSCH) at 13 GPa and 1400-1800 °C and the H₂O content in the produced forsterite and enstatite crystals was addressed. The experiments in the MSCH system employed starting materials with H₂O/(H₂O+CO₂) weight ratios of 0.69 and 0.80. The estimated liquidus volatile contents are then used to calculate mineral-melt H₂O partition coefficients in H₂O and H₂O+CO₂-bearing systems. The variation of $D_{H_2O}^{\text{min/melt}}$ with temperature at different depths in the mantle, as well as the effect of CO₂ on the distribution of H₂O atop the transition zone, is then examined and the conditions for melt formation at such extreme conditions are evaluated.

6.2 Experimental and analytical methods

Olivine and enstatite crystals produced in the MSH system were selected from experiments reported in Chapter 5. These experiments were conducted in the forsterite-H₂O and enstatite-H₂O binary systems at 6 and 13 GPa. In addition experiments in the MSCH system at 13 GPa were performed, with an experimental approach similar to that described in Chapter 5. Two sets of starting compositions were prepared for the experiments in the MSCH system (Table 6.1).

Table 6.1: starting mixtures in the systems MSCH

<i>Fo₉₅En₅-CH5</i>	<i>CH5-EM</i>	<i>CH5-A</i>	<i>CH5-B</i>	<i>CH5-C</i>
MgO	38.30	44.25	47.51	50.77
SiO ₂	29.64	33.73	35.97	38.22
H ₂ O	22.01	15.12	11.34	7.56
CO ₂	10.06	6.91	5.18	3.45
Total	100.00	100.00	100.00	100.00
H ₂ O/(H ₂ O+CO ₂)	0.69	0.69	0.69	0.69
Mg/Si [#]	1.93	1.96	1.97	1.98
<i>Fo₉₇En₃-CH7</i>	<i>CH7-EM</i>	<i>CH7-A</i>	<i>CH7-B</i>	<i>CH7-C</i>
MgO	41.70	44.99	48.06	51.14
SiO ₂	31.67	33.99	36.17	38.35
H ₂ O	21.25	16.78	12.58	8.39
CO ₂	5.37	4.24	3.18	2.12
Total	100.00	100.00	100.00	100.00
H ₂ O/(H ₂ O+CO ₂)	0.80	0.80	0.80	0.80
Mg/Si [#]	1.96	1.97	1.98	1.99

values given in weight percent of oxides. #: atomic ratio.

Starting mixtures were obtained by mixing dry forsterite with volatile-bearing end member mixtures (CH5-EM and CH7-EM). The volatile-bearing end members were produced by grinding under ethanol different proportions of brucite [Mg(OH)₂], magnesium carbonate hydrate [Mg(OH)₂ · MgCO₃ · 2.2 H₂O] and SiO₂ for 1 hour. Before weighing, SiO₂ was dried at 1000 °C for at least 6 hours while the other reagents were stored at 120 °C to limit the adsorption of H₂O from air. CH5-EM and CH7-EM mixtures consisted of forsterite plus minor amounts, 5 and 3 wt %, of enstatite respectively. The end-member mixtures had H₂O/(H₂O+CO₂) wt fractions of 0.69 (CH5-EM) and 0.80 (CH7-EM), and total volatile contents of 32.1 and 26.7 wt %, respectively (Table 6.1). The other starting mixtures listed in Table 6.1 were obtained by mixing for 30 minutes under ethanol different proportions of CH5-EM and CH7-EM with dry forsterite powder that was previously prepared. The dry forsterite was obtained by mixing the right proportions of MgO and SiO₂, grinding for 2 hours under ethanol and then drying. The mixture was placed in a Pt crucible and heated overnight at 1400 °C in a 1 atm furnace, quenched and ground to a powder. This procedure was repeated 2-3 times.

The high pressure (HP) and high temperature (HT) experiments in the MSCH system were performed using a 5000 tonne multianvil apparatus at the Bayerisches Geoinstitut (BGI). An 18/11 (octahedron edge length/truncated edge length) assembly was used in all the

experiments and pressure calibration of the press is reported by Frost et al. (2004). The pressure media was a Cr₂O₃-doped, MgO octahedron and a stepped LaCrO₃ heater was employed. Temperatures were monitored by means of a W₉₇Re₃-W₇₅Re₂₅ (Type D) thermocouple which was separated from the capsule by a Re foil. The effect of pressure on the thermocouple emf was ignored. The capsule was fabricated from a Pt disk that was spark-eroded in order to produce up to 8 chambers with 250 µm diameter and ~700 µm depth on a single disk, where different starting mixtures were loaded, following the same procedure described in Chapter 5. The chambers were held closed at HP-HT by placing a Pt disk of 0.25 mm thickness on top of the open side. In order to limit the potential loss of H₂O, the experiments were heated for a short period especially at the higher temperatures investigated. Experiments containing the same starting compositions were performed with different run durations (3 and 30 minutes) and produced the same phase assemblages. This implies that substantial amounts of H₂O loss at high temperature in the experiment did not occur over the duration of heating adopted in this study.

The capsules recovered from the HP-HT experiments were at first mounted in epoxy resin and polished. During the polishing procedure charges were impregnated with superglue to avoid significant loss of the quenched material. Scanning electron microscopy (SEM) analyses were initially performed at the BGI for the determination of the phase assemblage of the experiments. Electron microprobe analysis was also conducted at the BGI employing a 5 spectrometers JEOL JXA-8200 electron probe in order to precisely check the mineral compositions. Analyses were performed with 15 kV and 15 nA and counting time of 20 s on the pick position and 10 for the background. Raman spectroscopy was also performed at the BGI in order to confirm the presence of forsterite and rule out the formation of the HP polymorph wadsleyite at 13 GPa. Spot analyses (~5 µm diameter) were performed in air using a LABRAM Raman spectrometer with 632 nm red line wavelength laser and a resolution of 1-2 cm⁻¹.

In order to determine the H₂O contents of forsterite and enstatite produced in the experiments performed in the MSH (Chapter 5) and MSCH systems some of the capsules were prepared for mineral H₂O determination using secondary ion mass spectrometry (SIMS). Analyses were conducted by means of a CAMECA NanoSIMS 50 L ion probe installed at the Department of Terrestrial Magnetism. Measurements were performed following the procedure described by Koga et al., (2003) in order to perform low-blank analyses. After the

sample characterization, the selected capsules were removed from the epoxy resin, cleaned to remove small portions of epoxy attached to the Pt disk, and pressed into indium metal contained within a hole drilled in an aluminium disk. This procedure was necessary to obtain a low background signal from other potential hydrogen sources. NanoSIMS analyses were performed using a Cs⁺ primary beam which ejected ¹⁶OH⁻ secondary ions. Mineral H₂O contents were characterized by reference to mineral standards with known H₂O contents described in Koga et al. (2003). The limit of detection during the analyses was ~10 ppm H₂O based on measurements performed on dry silicates (Koga et al., 2003). NanoSIMS analyses were conducted on crystals as small as ~30 µm across. Samples were dried overnight before measurements and analyses were performed under a vacuum of ~ 2 x 10⁻¹⁰ Torr. A pre-sputter time of 3 minutes was employed in order to avoid surface contamination, followed by a counting time of 3 minutes. Along with ¹⁶OH anions the species ¹²C, ¹⁹F, ³⁰Si were also measured simultaneously and used as indicators of contamination (see e.g. Chapter 4). Pits produced during the analyses were subsequently examined using an SEM in order to discard analyses biased by the presence of cracks or visible inclusions, which would affect the measured signal and the calculated mineral H₂O contents.

In addition to SIMS analyses, elastic recoil detection analyses (ERDA) were also carried out on some of the polished samples at the Laboratoire d'Etudes des Éléments Légers, CEA in France. ERDA is a powerful absolute technique for the determination of H₂O in solids which is independent of calibrant materials (Raepsaet et al., 2008). H atoms that are ejected from the sample after elastic collisions with an incident ⁴He⁺ beam are collected by an ERDA detector. In addition, particle-induced X-ray emissions (PIXE) and Rutherford backscattered (RBS) particles ejected from the sample are also collected by an X-ray detector and an annular detector, respectively, and are used to determine the composition and location of the sample. During the analyses the beam is scanned over an area of approximately 150x200 µm over a period of 1 to 2 hours depending on the H₂O content of the measured mineral. The signal collected by the ERDA and RBS detectors generated from the sample is processed with the SIMRA software package (Mayer, 1999). The analyses were conducted on crystals of at least 50 µm. Further details concerning the ERDA procedure can be found in Raepsaet et al. (2008) and Bureau et al. (2009).

6.3 Results

Run conditions and phase assemblages for the experiments in the MSH system are reported in Chapter 5 while those for the MSCH experiments are listed in Table 6.2.

Table 6.2: Experimental conditions and phase assemblages in the system MSCH at 13 GPa

Run (system)	T (°C)	T (min)	Start. mix.	Phase assemblage
Z951 (CH7)	1400	20	EM, A, B, C	en+L,en+L, fo+en+L, fo+en+L
Z951 (CH5)	1400	20	EM, A, B, C	en+L,fo+en+L,fo+en+L,fo+en+L
Z959 (CH7)	1500	20	EM, A, B, C	en+L,en+L,fo+en+L,fo+en+L
Z959 (CH5)	1500	20	EM, A, B, C	en+L,fo+en+L,fo+en+L,fo+en+L
Z938 (CH7)	1600	10	A, B	L,fo+en+L
Z938 (CH5)	1600	10	A, B	L,fo+en+L
Z965 (CH7)	1700	10	EM, A, B, C	L,L,fo+en+L,fo+en+L
Z965 (CH5)	1700	10	A, B, C	L,fo+L,fo+en+L
Z952 (CH7)	1800	5	EM, A, B, C	L, L, L, fo+L
Z952 (CH5)	1800	5	EM, A, B, C	L, L, L, fo+L

Fo: forsterite, En: enstatite, L: quenched liquid.

Volatile-bearing melts produced fibrous crystals upon quenching, similar to the MSH system (Chapter 5). Sub-liquidus phases could be easily distinguished from the quenched crystal matrix by their euhedral habits. Typical examples of experimental products and mineral textures in the MSCH system are illustrated in the backscattered electron (BSE) images in Fig. 6.1.

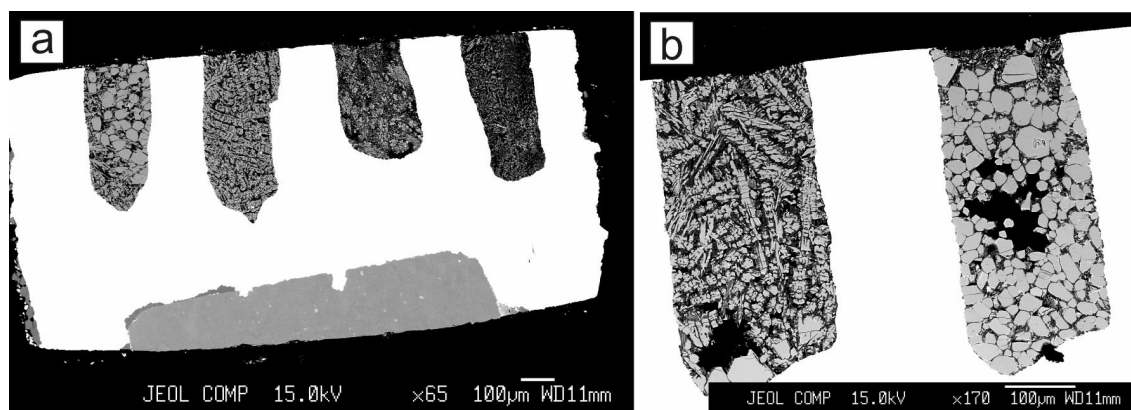


Fig. 6.1: (a) BSE image showing experiment Z952 (CH5) with the shiny Pt disc containing four chambers with different starting mixtures as reported in Table 6.2. Equilibrium crystals are present in the chamber on the left while only quenched crystals resembling the melt at HP-HT are recognized in the other 3 chambers. (b) Two chambers from experiment Z965 (CH5) containing starting mixtures B (left) and C (right) (Table 6.1). It can be seen that the amount of equilibrium crystals diminishes from right to left as a consequence of the higher volatiles budget in the chamber.

In the experiments performed in the MSCH system assemblages of forsterite, forsterite plus enstatite and enstatite were produced in equilibrium with volatile-bearing melt. Small (generally 5 µm across) MgCO₃ crystals were observed in the interstitial space among the herringbone-like crystals resembling the melt phases at HP-HT. Due to their fine grain size and texture they were interpreted to form from the melt phases upon quenching a particular experiment. At 1600, 1700 and 1800 °C chambers where only quenched melt was present were observed (Table 6.2) and this permitted the location of the liquidus to be determined. Melting in the CO₂ bearing system is incongruent up to 1700 °C (Table 6.2) which is apparently 100 °C higher than in the H₂O system (Chapter 5). In the MgO-SiO₂-H₂O ternary system the cotectic liquid composition between forsterite and enstatite liquidus fields must cross the tie line between Mg₂SiO₄ and H₂O at approximately 1650 °C, as shown in Fig. 6.2.

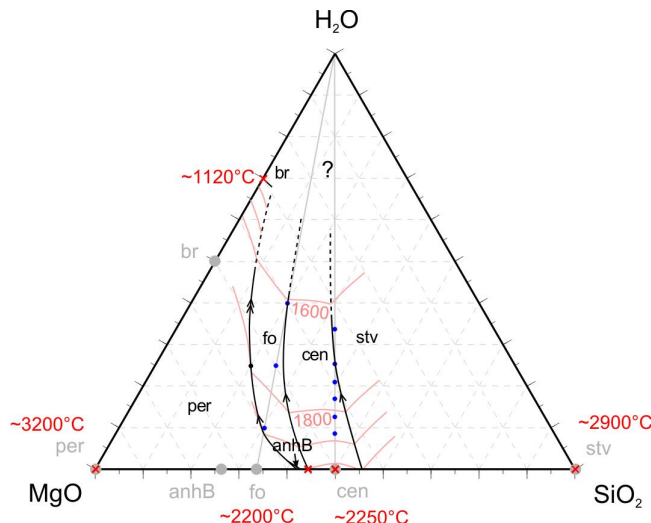


Fig. 6.2: Ternary diagram in the MSH space showing the liquidus at 13 GPa based on the experimental constrains presented in Chapter 5. Br: brucite, per: periclase, anhB: anhydrous B, fo: forsterite, cen: clino-enstatite, stv: stishovite. Blue dots indicate starting mixtures employed in the experiments. In red are shown estimated melting temperatures for brucite (Fukui et al., 2005; Johnson and Walker, 1993), periclase (Zerr and Boehler, 1994), forsterite and clinoenstatite (Liebske and Frost, 2012) and stishovite (Zhang et al., 1993).

Based on the experimental data presented here, the cotectic between forsterite and enstatite in the pseudoternary MgO-SiO₂-[H₂O+CO₂] system must cross the tie line between Mg₂SiO₄ and H₂O+CO₂ at ~1750 °C. At this point assemblages of coexisting forsterite plus enstatite have equilibrium liquid compositions that actually lie along the cotectic, whereas the all liquid assemblages bracket a liquidus curve within the enstatite plus melt field. However, because the cotectic line must be relatively parallel to the Mg₂SiO₄-H₂O tie line, bracketed liquidus compositions will remain very close to those that are in equilibrium with the forsterite plus enstatite assemblage. Given the similarity observed in the melting phase

relations between the MSH (Chapter 5) and MSCH (Table 6.2) systems, the same behaviour is also expected in the presence of CO₂.

The hydrogen concentrations of the minerals determined by NanoSIMs and ERDA in the MSH and MSCH systems are reported in Table 6.3.

Table 6.3: H₂O contents of forsterite and enstatite in the MSH and MSCH systems

(GPa)	T (°C)	n	phase	run	H ₂ O SIMS (ppm wt)	H ₂ O ERDA (ppm wt)
<u>Fo-H₂O[#]</u>						
6	1250	22	fo	V731	681	147
6	1300	11	fo	V675	790	149
6	1500	3	fo	V738	420	25
6	1600	25	fo	V730A	329	136
6	1650	12	fo	V737A	308	242
13	1300	14	fo	Z825A	6578	631
13	1500	7	fo	Z824A	4317	479
13	1600	2	fo	Z837A	3070	54
13	1700	10	fo	Z826B	1286	311
13	1900	5	fo	Z836A	742	14
<u>En-H₂O[#]</u>						
6	1050	1	en	V732	605	
6	1250	6	en	V731	344	98
6	1300	20	en	V704	372	26
6	1500	9	en	V738	353	60
6	1600	11	en	V730B	275	7
6	1650	1	en	V737B	292	
13	1300	13	en	Z825B	1548	348
13	1500	8	en	Z824B	1320	346
13	1600	7	en	Z837B	1183	88
13	1700	5	en	Z826A	439	6
13	1900	3	en	Z836B	336	6
<u>Fo₉₅En₅-CH5 [H₂O/(H₂O+CO₂)=0.69]</u>						
13	1400	13	fo	Z951	2187	235
13	1400	15	en	Z951	1189	377
13	1500	2	fo	Z959		1039
13	1600	5	fo	Z938	934	85
13	1600	10	en	Z938	581	169
13	1700	1	fo	Z965		672
13	1800	5	fo	Z952	474	96
<u>Fo₉₇En₃-CH7 [H₂O/(H₂O+CO₂)=0.80]</u>						
13	1400	8	fo	Z951	2631	61
13	1400	12	en	Z951	1408	222
13	1500	1	fo	Z959		2151
13	1500	1	en	Z959		1315
13	1600	4	fo	Z938	1396	35
13	1600	9	en	Z938	807	93
13	1700	1	fo	Z965		865
13	1800	5	fo	Z952	682	126

fo: forsterite, en: enstatite. n: number of analyses on different crystals. H₂O contents of fo and en at a given temperature are averages from different experiments performed with different H₂O contents in the starting mixture. #: experiments described in Chapter 3.

In both MSH and MSCH systems the H₂O contents of forsterite and enstatite are observed to decrease with increasing temperature at a given pressure, as the activity of H₂O in the melt ($a_{H_2O}^{melt}$) drops as more silicate enters the melt. At 13 GPa, the concentration of H₂O in forsterite and enstatite is also observed to drop as the CO₂ content of the melt increases (CH5, Table 6.1). The difference in the H₂O content of forsterite between the MSH and MSCH systems appears to decrease with increasing temperature.

6.4 Discussion

6.4.1 The distribution of water in the MSH system at upper mantle conditions

The H₂O contents of olivine and enstatite produced in the experiments performed in the MSH system at 6 GPa and reported in Table 6.3 are displayed in Fig. 6.3. In Fig. 6.3 the concentration of H₂O in the melts forming in the systems Mg₂SiO₄-H₂O and MgSiO₃-H₂O and modelled in Chapter 5 are also shown. Mineral H₂O concentrations from the literature determined in the same simplified system (MSH) are displayed for comparison. At 6 GPa forsterite H₂O contents apparently increase between 1000 and 1100 °C and then start to decrease with temperature (Bali et al., 2008). This observation is consistent with the onset of silicate melting occurring between these temperatures, in agreement with the experiments of Stalder et al. (2001). The forsterite H₂O contents determined in this study by NanoSIMS are in very good agreement with values of Bali et al. (2008) determined by Fourier transform infrared spectroscopy (FTIR). Forsterite H₂O contents are observed to decrease with temperature up to 1650 °C, where a value of ~310 ppm wt H₂O is reached (Table 6.3).

The temperature effect on the enstatite H₂O content at 6 GPa was extended up to 1650 °C in this study. As for forsterite, enstatite H₂O contents decrease with increasing temperature from 1100 up to 1650 °C where a value of approximately 290 ppm wt H₂O is reached (Table 6.3). Values at low temperatures, 1150 °C and 1250 °C, determined in this study by NanoSIMS are in agreement with data from Rauch and Keppler (2002) and Withers et al. (2011) determined by FTIR and SIMS, respectively (Fig. 6.3b).

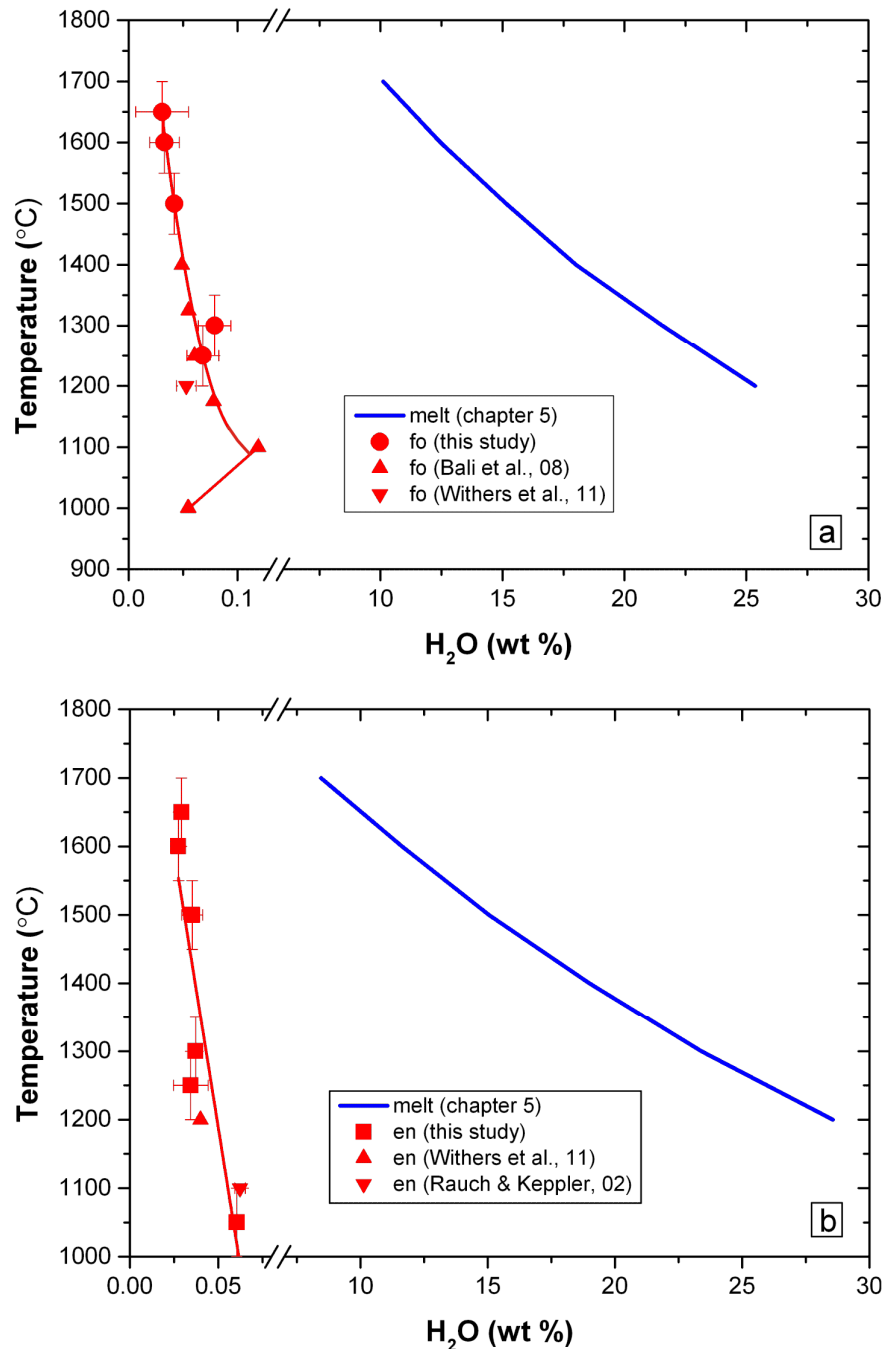


Fig. 6.3: (a) and (b): Phase equilibria in the forsterite-H₂O and enstatite-H₂O binary systems, respectively, at 6 GPa. H₂O contents of forsterite and enstatite determined in this study are plotted along with data from the literature determined at 5-6 GPa (red). Red lines show the variation of minerals H₂O content with temperature, based on this study and literature studies. Liquidus curves in the binary systems forsterite-H₂O and enstatite-H₂O (blue lines) are those described in Chapter 5.

H₂O contents of forsterite and (clino) enstatite determined at 13 GPa in the MSH system are displayed in Fig. 6.4 along with data from previous studies determined in the same chemical system.

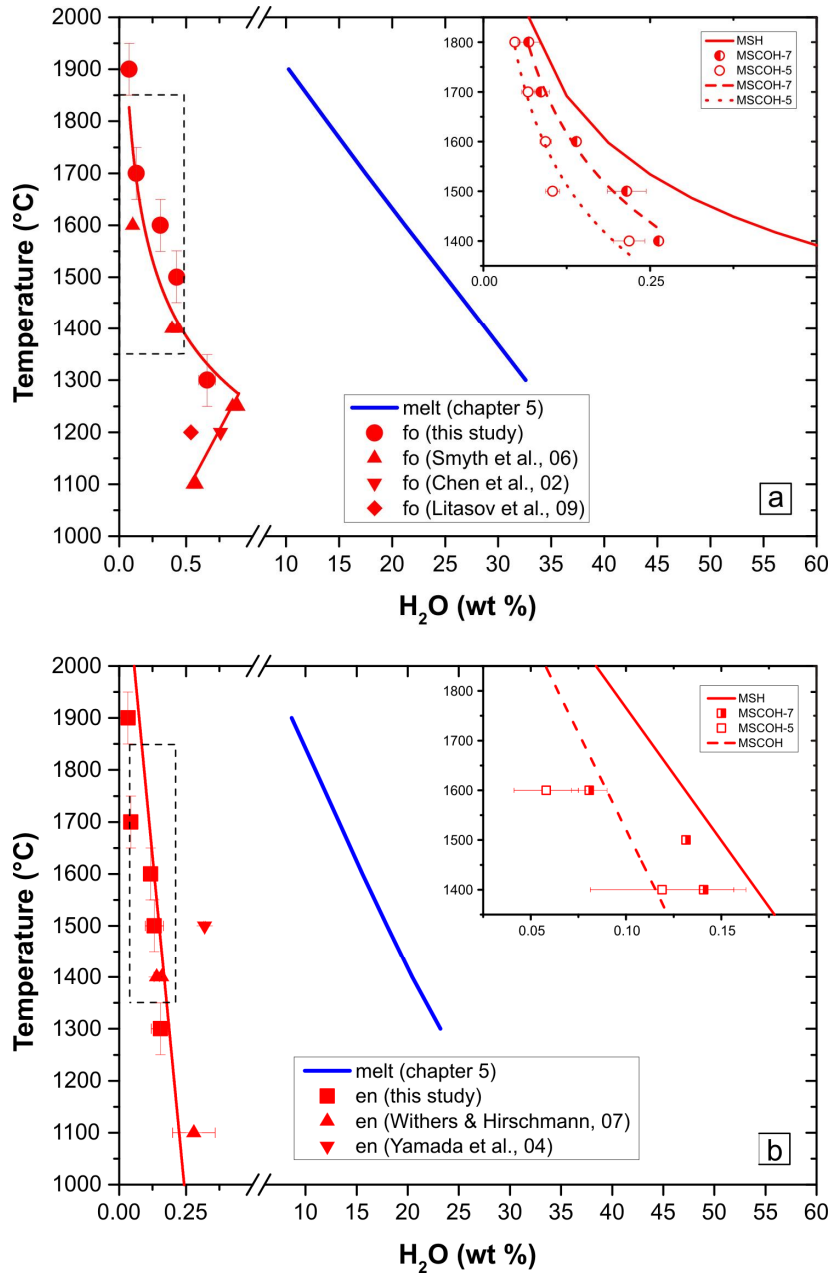


Fig. 6.4: Water contents of minerals (red) in the forsterite-H₂O system (a) and enstatite-H₂O system (b) determined at 13 GPa in this study along with data from the literature. Liquids are shown as blue lines and their determination is described for both systems in Chapter 5. The red lines are regression lines for mineral H₂O contents based on data from this study and the literature. The figures inserts are enlargements of the dashed boxes and show forsterite (a) and enstatite (b) water contents determined in the MSH and MSCOH. The dashed and dotted lines in Fig. 6.4a are regression lines for the H₂O content of forsterite in the CO₂-bearing systems with H₂O/(H₂O+CO₂)=0.80 and 0.69.

Melt H₂O concentrations estimated in Chapter 5 are also shown. Saturated mineral H₂O concentrations are generally observed to increase with pressure (e.g. Mosenfelder et al., 2006) and this is observed for both phases when the experimental data at 6 and 13 GPa are compared (Table 6.3). The results of the measurements in the MSH systems are in agreement

with results from the literature at similar pressure and temperature conditions (Fig. 6.4). The forsterite H₂O content has been reported to increase between 1100 to 1250 °C, and then to decrease with increasing temperature above 1250 °C (Smyth et al., 2006). This, combined with measurements performed in this study, is consistent with an H₂O-saturated melting temperature between 1250 and 1280 °C at 13 GPa. The FTIR measurements of Smyth et al. (2006) made on forsterite synthesised at 12 GPa, are in reasonable agreement with data determined in this study at 13 GPa. The slightly lower general trend in H₂O contents measured by Smyth et al. (2006) likely reflects the 1 GPa difference in pressure between the studies. In Fig 6.3 forsterite H₂O contents determined by SIMS at 13.7 GPa (Chen et al., 2002) and FTIR at 13 GPa (Litasov et al., 2009) at 1200 °C are also shown for comparison. The experimental results determined in this study show that the concentration of H₂O in forsterite drops to ~750 ppm wt by 1900 °C.

At 13 GPa (clino) enstatite H₂O contents decrease with temperature from ~1550 ppm wt H₂O at 1300 °C to ~340 ppm wt H₂O at 1900 °C. The temperature trend is in reasonable agreement with values reported by Withers and Hirschmann (2007) at ~12 GPa and 1100 °C determined by SIMS (Fig. 6.4b). At 1500 °C, however, enstatite H₂O contents determined in this study are significantly lower (by ~1800 ppm wt) than values reported Yamada et al. (2004) at 13 GPa measured using SIMS. The origin of this discrepancy is unclear.

With knowledge of mineral H₂O contents determined here and the location of the liquidus curves modelled in Chapter 5 for the binary systems forsterite-H₂O and enstatite-H₂O (Fig. 6.3 and 6.4), $D_{H_2O}^{\text{min/melt}}$ in the MSH system was determined at 6 and 13 GPa and between 1050 and 1900 °C. This allows the effect of temperature on $D_{H_2O}^{\text{min/melt}}$ to be evaluated, as displayed in Fig. 6.5. $D_{H_2O}^{\text{min/melt}}$ was determined from literature mineral H₂O contents in the MSH systems based on melt H₂O contents determined in Chapter 5 (Fig. 6.4). Values of $D_{H_2O}^{\text{fo/melt}}$ determined at 6 GPa show no significant change with temperature between 1250 and 1650 °C. The olivine/melt H₂O partition coefficients ($D_{H_2O}^{\text{ol/melt}}$) determined for peridotitic systems at 6 GPa and 1400 °C (Chapter 4) and at 1-2 GPa and between 1100-1400 °C (Hauri et al., 2006) are also displayed in Fig. 6.4a. Data from Hauri et al. (2006) imply a weak increment in the $D_{H_2O}^{\text{ol/melt}}$ with increasing temperature from 1200 to 1400 °C at 1.2 GPa and a similar trend would easily fit within the uncertainties of the current study.

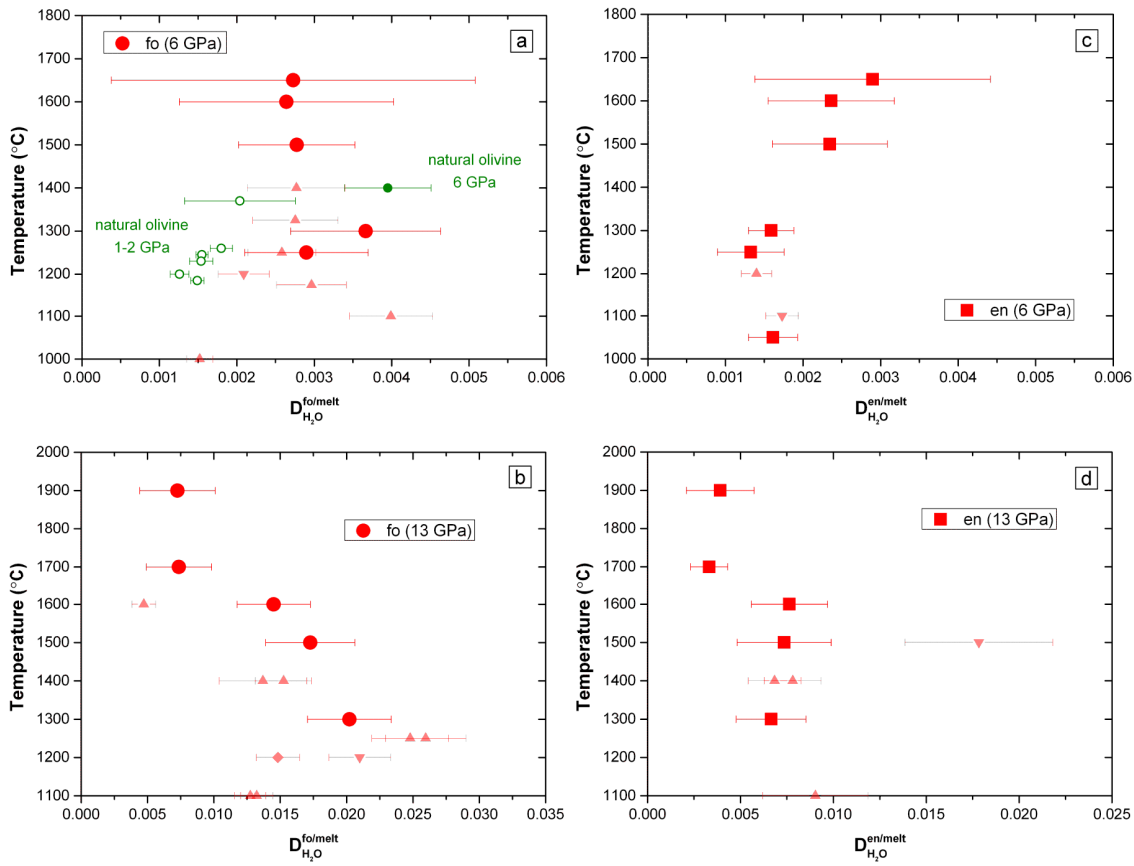


Fig. 6.5: Variation of $D_{H_2O}^{\text{min/melt}}$ with temperature at 6 and 13 GPa. Panels (a) and (b) report data for forsterite at 6 and 13 GPa while panels (c) and (d) are for enstatite at 6 and 13 GPa, respectively. Error bars are 1 standard deviation and are calculated based on the mineral H₂O uncertainties reported in Table 6.3 and an uncertainty of 4 wt % H₂O in the melts. Error for experiments V732 and V737B (only 1 nanoSIMS analyses) were calculated considering an uncertainty of 100 ppm wt H₂O in enstatite. Green symbols in panel (a) are data from experiments in natural compositions reported by Hauri et al. (2006) at 1-2 GPa and in Chapter 4 at 6 GPa. Values calculated from literature mineral H₂O data and melt H₂O contents from Chapter 5 are also displayed and symbols are as in Fig. 6.2 and 6.3 at 6 and 13 GPa, respectively.

At 6 GPa and 1400 °C the peridotitic (natural) olivine partition coefficient is slightly higher than the trend in the MSH system, which is mainly caused by the difference in melt H₂O content in the two systems at these conditions. At 13 GPa, however, $D_{H_2O}^{\text{fo/melt}}$ is observed to decrease with temperature, from ~0.020 at 1300 °C to ~0.007 at 1700-1900 °C (Fig. 6.4b). It must be noted that melt H₂O contents are only bracketed at and above 1700 °C and are extrapolated below this temperature. In addition melting becomes incongruent below this temperature. An underestimate of the melt H₂O content below 1700 °C, however, may contribute to the relatively strong temperature dependence of $D_{H_2O}^{\text{fo/melt}}$ observed at these conditions.

$D_{H_2O}^{en/melt}$ shows a weak, positive trend with temperature at 6 GPa increasing from ~0.0015 to ~0.003 between 1050 and 1650 °C. Values are significantly lower than reported for enstatite produced from peridotitic compositions (~0.007, Chapter 4), most likely due to the absence of aluminium. At 13 GPa, $D_{H_2O}^{en/melt}$ shows no temperature dependence up to 1600 °C but decreases by approximately 50 % once the temperature is >1700 °C, which is due to a similar percentage drop in the enstatite H₂O content over this temperature interval.

6.4.2 The distribution of water at 13 GPa in the MSCH system

In Fig. 6.4 the H₂O content of forsterite and enstatite in the CO₂-bearing experiments (MSCH system) determined by NanoSIMS and ERDA are reported. Using these data the effect of increasing melt CO₂ content on the H₂O contents of minerals in equilibrium with hydrous melt can be examined at conditions corresponding to the base of the upper mantle. It can be seen that the presence of CO₂ in the melt lowers the H₂O contents of coexisting minerals, which is an expected consequence of lowering $a_{H_2O}^{melt}$. This effect is enhanced at lower temperatures, particularly for forsterite, where mineral H₂O contents for CO₂ and CO₂-free systems show a greater divergence. For example, at 13 GPa and 1500 °C (which corresponds to a typical mantle potential temperature of ~1320 °C) forsterite contains ~4300 ppm wt H₂O in the MSH system, while in the CO₂-bearing system with a melt CO₂/(H₂O+CO₂) weight ratio of 0.20 and 0.31 it contains 2150 and 1050 ppm wt H₂O respectively. It should be noted that these melt CO₂ ratios are only 0.06 and 0.16 when calculated on a molar basis. A similar effect is also observed for enstatite at these conditions (Fig. 6.4b), but is not as well constrained by available experimental data.

The volatile content of the melts formed in the MSCH system at 13 GPa were bracketed at 1600, 1700 and 1800 °C by determining the position of the liquidus (Table 6.2). The liquidus curves bracketed in the H₂O+CO₂ bearing systems are displayed in Fig. 6.6. Note that there is great uncertainty in total melt volatile contents below 1700 °C as the compositions melt incongruently and the liquidus must be extrapolated below 1600 °C. However, errors in the determined volatile contents should be similar and in the same direction (i.e. underestimated) for both MSCH and MSH systems at the same conditions.

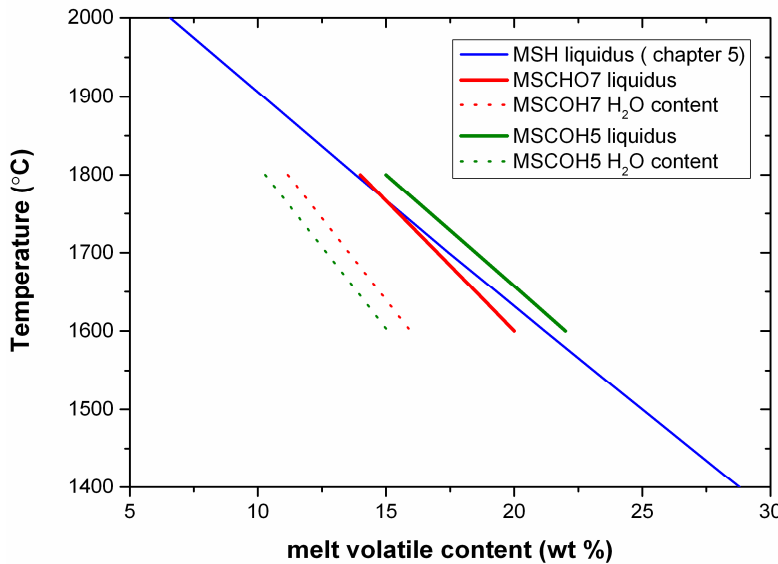


Fig. 6.6: Volatile contents of melts at different temperatures in the MSH and MSCH systems. The blue line is the liquidus curve calculated in the forsterite-H₂O system at 13 GPa from the model described in Chapter 5. Green and red solid lines indicate the volatile content of the melts forming in the CO₂-bearing systems employing starting mixtures MSCH5 [CO₂/(CO₂+H₂O)= 0.2] and MSCH7 [CO₂/(CO₂+H₂O)= 0.3], respectively. The green and red dotted lines indicate the H₂O contents of these melts calculated by the known H₂O/(H₂O+CO₂) ratio of the starting mixtures employed in the experiments.

As the volatile ratio of the starting mixture is known, the H₂O content in the H₂O- and CO₂-bearing melts can be estimated between 1500 and 1800 °C, which allows $D_{H_2O}^{fo/melt}$ being calculated (Table 6.4).

Table 6.4: forsterite/melt water partition coefficients at 13 GPa

T (°C)	Fo-H ₂ O		Fo ₉₇ En ₃ -CH7		Fo ₉₅ En ₅ -CH5	
	$D_{H_2O}^{fo/melt}$	$D_{H_2O}^{melt}$	$D_{H_2O}^{fo/melt}$	$D_{H_2O}^{melt}$	$D_{H_2O}^{fo/melt}$	$D_{H_2O}^{melt}$
1700	0.0074	0.0025	0.0064	0.0021	0.0053	0.0018
1600	0.0145	0.0028	0.0087	0.0022	0.0062	0.0017
1500	0.0173	0.0034	0.0112	0.0028	0.0058	0.0014

The total melt volatile contents in the CO₂-bearing experiments at 1500 °C were estimated to be 24 and 26 wt % for the CH7 and CH5 systems, respectively. Based on the data shown in Fig. 6.6 and the experiments reported in Table 6.2, the uncertainty in the melt volatile content in the CO₂-bearing systems at 1500 °C is expected to be at least 4 wt %, which is propagated into the calculation of $D_{H_2O}^{fo/melt}$. The effects of temperature and CO₂ on forsterite H₂O contents and $D_{H_2O}^{fo/melt}$ at 13 GPa are displayed in Fig. 6.7.

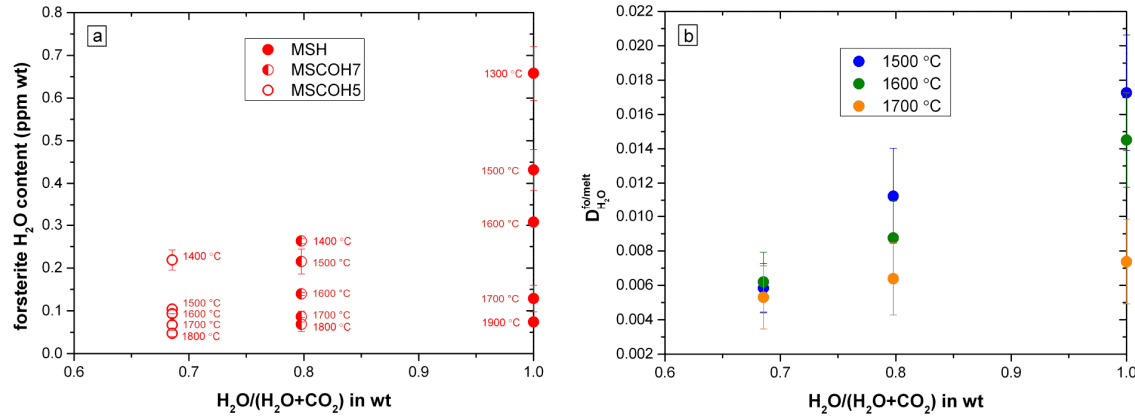


Fig. 6.7: (a): Forsterite H₂O content variation with H₂O/(H₂O+CO₂) at 13 GPa and temperatures investigated in this study. (b): $D_{H_2O}^{fo/melt}$ as a function of H₂O/(H₂O+CO₂) at 13 GPa and 1500, 1600 and 1700 °C. Data presented in both figures are reported in Tables 6.3 and 6.4. Propagation of error corresponds to ± 1 sigma calculated as explained in the text.

At 13 GPa $D_{H_2O}^{fo/melt}$ is lowered by the presence of CO₂ with the effect diminishing with increasing temperature (Fig. 6.5b). Differences are observed among values of $D_{H_2O}^{fo/melt}$ determined in H₂O and H₂O+CO₂ systems at 1700 °C that are within the calculated errors. At 1600 and 1500 °C, however, $D_{H_2O}^{fo/melt}$ drops by over 50% as the weight fraction of CO₂ increases to only ~0.3. Although there are significant uncertainties on the total volatile contents of the melts at 1500 °C, as stated previously, due to the similarity in the melting relations, errors should shift partition coefficients in both MSH and MSCH systems by similar amounts and in the same direction. The calculations of the partition coefficients assumed that all the CO₂ is dissolved in the melt phase. The concentration of CO₂ in the starting mixtures reported in Table 6.1 are considerably below the CO₂ saturation levels of e.g. a basaltic melt extrapolated at 13 GPa (e.g. Ni & Keppler, 2013), with only starting composition CH%-EM being close. These values support our assumption and do not suggest the formation of a CO₂-rich gas phase induced by the saturation of this volatile in the melt. This gas phase would certainly cause some H₂O to dissolve into it with a potentially effect on the $D_{H_2O}^{fo/melt}$. No experimental data, however, support this theory up to date.

The incorporation of H₂O in forsterite at 13 GPa and 1500 °C in the MSH and MSCH systems can be examined by employing H₂O dissolution equilibrium:



The H₂O content of forsterite and melt in the MSH system can be used to calculate the equilibrium constant for equation 6.1. Using this constant it is then possible to calculate the expected forsterite H₂O content and $D_{H_2O}^{fo/melt}$ for any melt H₂O content, assuming ideal mixing. This is calculated for melt H₂O contents encountered in this study at 1500 °C and the results are shown in Fig. 6.8.

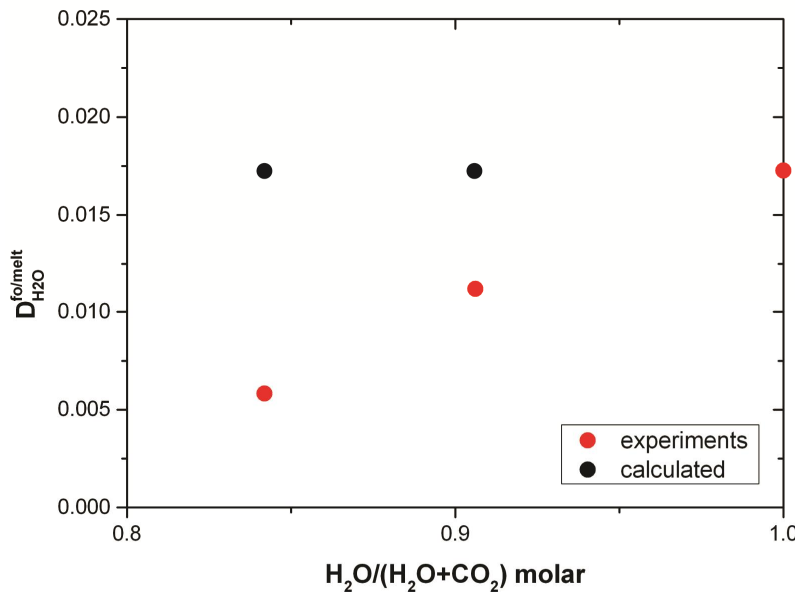


Fig. 6.8: Values of $D_{H_2O}^{fo/melt}$ as a function of H₂O/(H₂O+CO₂) molar ratio at 13 GPa and 1500 °C. Red circles indicate the experimental data determined in the MSH and MSCH systems, while the black circles are the $D_{H_2O}^{fo/melt}$ calculated based on the model as described in the text.

Although the forsterite H₂O content is calculated to go down as the amount of H₂O in the melt decreases, $D_{H_2O}^{fo/melt}$ remains constant. The experimental data indicate, however, that $D_{H_2O}^{fo/melt}$ decreases quite strongly. As C does not significantly dissolve in forsterite (Shcheka et al., 2006) and if a vapor phase does not form, this must result from an interaction between CO₂ and H₂O in the silicate melt, which lowers the activity of H₂O in the melt.

6.4.3 The production of melts atop the transition zone

If $D_{H_2O}^{ol/melt}$ is substantially lowered in the presence of moderate amounts of CO₂ in hydrous melts, then this will lower the amount of H₂O necessary to cause peridotite melting below the volatile-free solidus and influence the proportion of melt that can be produced for a given

mantle H₂O content. As this effect must result from a lowering of the activity of H₂O in the melt it should affect all minerals coexisting with the melt, although the magnitude of the effect may vary if different mineral H₂O substitution mechanisms occur. This may be a particularly relevant phenomenon at the base of the upper mantle where seismic studies have proposed that silicate melts may be present (e.g. Tauzin et al., 2010). Using the obtained partition coefficients the melt fraction produced from a mantle peridotite at the base of the upper mantle (13 GPa, 1500 °C) can be estimated as a function of the bulk H₂O content of the mantle and for a mantle with a CO₂/(H₂O+CO₂) weight ratio of 0.31, which is close to the ratio in the MORB source estimated by Saal et al. (2002).

For this calculation values of $D_{H_2O}^{\min/melt}$ for olivine, clinopyroxene and garnet coexisting with hydrous melts were calculated at 13 GPa using the parameterizations of $D_{H_2O}^{\min/melt}$ as a function of pressure described in Chapter 4 for peridotitic natural systems. Following this approach and based on the modal abundances of olivine, clinopyroxene and garnet in a peridotitic assemblage at 13 GPa proposed by Stixrude and Lithgow-Bertelloni (2007), $D_{H_2O}^{pdt/melt}$ was calculated to be approximately 0.0058 in a hydrous system. $D_{H_2O}^{pdt/melt}$ was then calculated for a melt with a CO₂/(CO₂+H₂O) (weight) ratio of 0.31 by assuming that $D_{H_2O}^{ol/melt}$ drops to 33 % of the value estimated for the CO₂-free system, in line with the observations for forsterite made above. The H₂O content of the melt was then estimated from the depression of melting analysis made in Chapter 5 assuming that 31% CO₂ replaces H₂O in the melt without a significant change in the total volatile content of the melt. This is consistent with the phase equilibria measurements highlighted in Fig. 6.6. This results in a CO₂-bearing melt containing 8.6% H₂O and 3.7% CO₂. Using values of $D_{H_2O}^{pdt/melt}$ and the melt H₂O content, the amount of melt that is produced as a function of the bulk mantle H₂O content can be calculated by using the batch melting equation (Shaw, 1970). The results of this calculation are shown in Fig. 6.9, where the fraction of melt produced as a function of mantle H₂O content is displayed for both solely hydrous melting and melts where CO₂/(CO₂+H₂O)= 0.31.

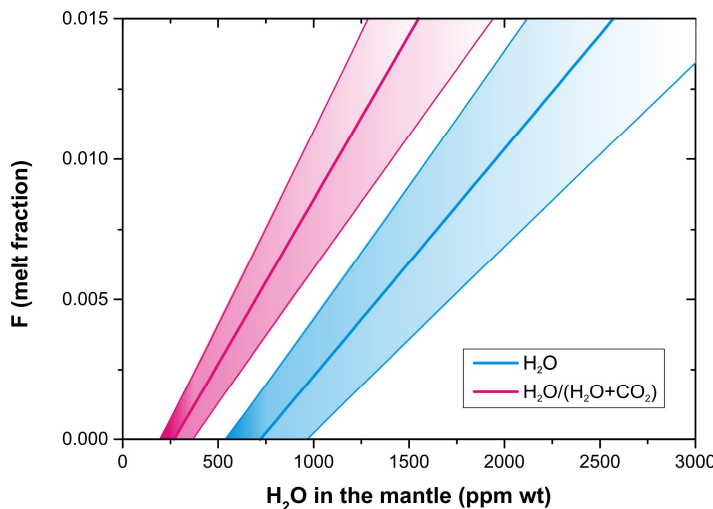


Fig. 6.9: Thick lines show melt fraction (F) calculated as a function of mantle water content at 13 GPa and 1500 °C for a hydrous system (blue) and a hydrous plus CO₂ system (magenta). Error bars, indicated by the shaded areas, correspond to ±1 sigma calculated on the F values considering a 20% relative uncertainty of the melt H₂O content and the partition coefficient of H₂O between the peridotite and the melt.

The main uncertainty in this calculation is caused by the uncertainty in the H₂O content of the melts at 13 GPa, as outlined above. If the melt H₂O content is in error then this would change the relationship between bulk mantle H₂O and melt fraction. On the other hand, this uncertainty is unlikely to affect the magnitude of the difference between values calculated for the H₂O and H₂O+CO₂ systems. Also, it is important to note that the calculation does not account for the effect of CO₂ on lowering the partitioning of H₂O between the other peridotite minerals, clinopyroxene and garnet, which would certainly shift the required bulk H₂O contents in the CO₂-bearing system towards even lower values. Due to uncertainties in the substitution mechanisms there is insufficient data to quantify the effect of CO₂ on other minerals at this stage. However, even given the uncertainties in the calculation the indication is that reasonable proportions of mantle CO₂ would strongly enhance the production of hydrous melts produced at the base of the upper mantle for a given mantle H₂O content. Based on the results displayed in Fig. 6.9, for example, CO₂ would induce the formation of melts at the base of the upper mantle for a bulk H₂O concentration of ~250 ppm, which is close to the top end of some estimates for the MORB source (Dixon et al., 2002; Saal et al., 2002). The formation of 1% melt would still require a mantle H₂O content of 1000 ppm, but this is still close to the range of some values estimated for the plume source (e.g. Dixon et al., 2002; Nichols et al., 2002). Intriguingly, higher temperature plumes may well result in lower degrees of melting as a result of the effect of CO₂ lowering $D_{H_2O}^{ol/melt}$ at high temperatures as shown in Fig 6.7. It seems quite plausible, however, that seismic observations of melts at the

base of the mantle may result from the presence of H₂O-CO₂ bearing melts with volatile ratios in line with those estimated for mantle sources from analyses of basaltic magmas. If this is the case it would also have implications for the oxygen fugacity of the mantle at these conditions, which has been argued to be sufficiently low to reduce CO₂ to either diamond or CH₄ (Frost and McCammon, 2004).

7. General conclusions

Tectonic processes within the Earth result in a continuous exchange of volatiles between surface reservoirs and the mantle, through the processes of subduction and mid ocean ridge melting. Volatiles in the Earth may therefore have either a primordial origin or be recycled from the surface since Earth formed. Most estimates of mantle volatile contents for the MORB source are low, however, and H₂O contents fall into a range where they can be absorbed by nominally anhydrous minerals at depth (e.g. Saal et al., 2002). Enriched mantle sources associated with mantle plumes are generally agreed to source a more volatile rich reservoir, which may contain different proportions of recycled and primordial volatiles compared to surface reservoirs (e.g. Dixon et al., 2002; Nichols et al., 2002). None the less exotic magmas such as kimberlites demonstrate that sufficient concentrations of volatiles such as H₂O and CO₂ can depress the solidus of the mantle at depths greater than 100 km to produce volatile rich magmas. High concentrations of volatiles at depth seem to be one of the few explanations for evidence of low seismic velocities in the mantle which are observed repeatedly with different seismic techniques near the base of the upper mantle (e.g. Nolet and Zielhuis, 1994; Revenaugh and Sipkin, 1994; Pino and Helmberger, 1997; Song et al., 2004; Tauzin et al., 2010).

In this thesis experiments were performed to try to understand if and how deep mantle melting can occur. The two main lines of information critical to this issue are the extent to which H₂O will partition between nominally anhydrous mantle minerals and silicate melt at high pressure, and the extent to which H₂O lowers the melting temperature of peridotite rocks. This latter point is crucial because it controls the H₂O content of hydrous melts, which in turn determines the amount of hydrous melt which can be produced below the anhydrous solidus. However, there is a major experimental barrier to the determination of melt H₂O contents at deep mantle pressures due to the quench crystallization of hydrous melts, which prevents the direct analysis of melt H₂O contents. This is one of the main problems that has been addressed in this thesis mainly by performing experiments where simple mass balance or phase relations can be used to determine melt H₂O contents. In addition, however, the effect of CO₂ on H₂O partitioning relations has also been examined. This is vital as we attempt to apply experimental results to the mantle where H₂O and CO₂ are both major volatile species.

The conclusions based on the four individual studies described in this thesis can be summarized as follows:

1. The composition of hydrous melts in equilibrium with peridotitic (garnet wehrlite and lherzolite) assemblages at 6 GPa and 1400 °C have been determined using iterative crystallization experiments. These melt compositions would be compatible with those produced by low degree hydrous partial melting of the mantle at depths of approximately 180 km. The hydrous melt compositions are found to be very similar to melts produced at the dry peridotite solidus at approximately 1700 °C, when compared on a volatile free basis, and particularly have almost identical (Mg+Fe)/Si and Al/Ca ratios. H₂O therefore has little influence on the composition of small degree peridotitic melts at this pressure. This is in contrast to the effect of H₂O on melt composition at pressures of 3 GPa and lower, where H₂O-bearing melts display a lower (Mg+Fe)/Si ratio compared with anhydrous melts. The H₂O content of the low degree melt compositions has been constrained to be approximately 11 wt % by mass balance calculations based on chemical analyses performed by means of LA-ICP-MS. The melt H₂O contents are found to be in very good agreement with a previous cryoscopic model for determining melting point depression as a function of melt H₂O content (Tenner et al., 2012). If the asthenospheric low velocity zone (LVZ) is caused by the presence of small degree hydrous melts, then at the base of the LVZ at 220 km these melts are predicted to contain 15-16 weight % H₂O.

Garnet- wehrlite and lherzolite saturated hydrous melt compositions are found to closely resemble those estimated for group II kimberlites, when compared on a volatile free basis. Relatively low FeO and Na₂O but enriched K₂O concentrations in group II magmas attest, however, to their derivation from cratonic lithosphere that has been previously melt depleted but then enriched in K₂O and H₂O. A simple model is proposed where both enrichments occur by the addition of phlogopite to the source peridotite, as observed in metasomatic sequences found in cratonic xenoliths. Constraints can be placed on the melting process using K and H₂O partition coefficients determined in this study and by assuming that the ratio of both components in the source is controlled by their ratio in phlogopite. Considering that melts must contain approximately 11 wt % H₂O at these conditions, group II melts are then constrained to be derived from a source rock enriched with 1.7 wt % phlogopite at a melting fraction of 0.2 wt % undergoing melting at near adiabatic temperatures. If melting occurred at lower temperatures then higher H₂O melt contents would be required, which, if provided by

phlogopite would result in melts that were too rich in K. The presence of some CO₂ would likely loosen this constraint, but the amount of CO₂ that could be added to the melt before its composition strayed out of the range of group II melts cannot currently be determined. This is a major outstanding issue in deep mantle melting, the composition of small degree peridotite melts for known CO₂ and H₂O contents.

2. The partitioning of H₂O between mantle peridotite minerals and low degree hydrous melt compositions has been addressed at 6 GPa and adiabatic temperature of 1400 °C. Peridotite mineral phases were analyzed from 6 melting experiments performed in a natural chemical system that were at fluid-undersaturated conditions. The experiments contained ~80 wt % of a low degree hydrous melt composition that was obtained through a series of experiments where the melt composition was iteratively adjusted until saturation with the appropriate peridotite assemblage was achieved. Ion microprobe measurements of the mineral phases from the selected experimental charges indicate olivine H₂O concentrations of 434 ±61 ppm wt and average clinopyroxene (cpx) concentrations of 1268 ±173 ppm wt H₂O. Orthopyroxene (opx) and garnet contain 700 ±46 ppm wt and 347 ±83 ppm wt H₂O respectively. The chemical composition of the peridotite minerals, e.g. Al₂O₃ in pyroxenes, has been observed to significantly influence the mineral H₂O contents. This highlights the fact that peridotite phase assemblages in equilibrium with low degree melts are required in order to provide representative values of the distribution of H₂O at high depths in the mantle. The H₂O content of the hydrous melts was determined by mass balance to be 10.91 ±0.61 wt % H₂O. Calculated H₂O partition coefficients between minerals and melt ($D_{H_2O}^{\min/melt} = X_{H_2O}^{\min} / X_{H_2O}^{melt}$) are 0.0040 ±0.0006 for olivine, 0.0064 ±0.0004 for opx, 0.0115 ±0.0016 for cpx and 0.0032 ±0.0008 for garnet.

By means of the determined H₂O partition coefficients, the formation of low degree hydrous melts at 180 km depth below mid ocean ridges was quantitatively evaluated. A depleted mantle, which is estimated to contain approximately 50-200 ppm H₂O, does not allow the formation of low degree hydrous melts at such depth, where approximately 700 and 1600 ppm wt H₂O are required in order to produce 0.1 and 1 % melting, respectively. Melting processes can potentially take place at such conditions within the mantle source regions attributed to ocean island basalts, which are estimated to contain up to ~1000 ppm wt H₂O. 1% melting can be achieved within plumes if they have adiabatic temperatures 200 °C higher

than normal mantle. Additionally, a model for the distribution of H₂O among minerals in a peridotite phase assemblage at upper mantle depths and undersaturated conditions has been constructed based on new parameterizations of $D_{H_2O}^{\text{min/melt}}$ as a function of pressure. With this model it is highlighted that in a mantle containing 200 ppm wt H₂O, olivine H₂O content increases with depth as a consequence of the variation of mineral/mineral H₂O partitioning and modal abundances. The change in the olivine H₂O concentration with depth corresponds to proposed changes in the dominate olivine slip system for deformation by dislocation creep, that might account for the attenuation of seismic anisotropy observed with increasing depths to the bottom of the upper mantle (~350 km).

3. Phase equilibria in the simplified systems Mg₂SiO₄-H₂O and MgSiO₃-H₂O have been determined at upper mantle conditions. In this regard, experiments were performed at 6 and 13 GPa, corresponding to approximately 180 and 390 km depths respectively, and temperatures ranging from 1150 to 1900 °C. The experimental results determine the location of the liquidus in the forsterite-H₂O and enstatite-H₂O binary systems as a function of temperature and H₂O content, at both investigated pressures. At 6 GPa in the Mg₂SiO₄-H₂O system the liquidus was bracketed at 1300 °C, at approximately 20 wt % H₂O, and at higher temperatures up to 1650 °C. At 6 GPa in the MgSiO₃-H₂O system the liquidus was constrained at 1550 °C and 1650 °C at 12 and 10 wt % H₂O, respectively. At 13 GPa in the Mg₂SiO₄-H₂O system, the liquidus curve was determined to lie between 13.8–20.4 wt % H₂O at 1700 °C and between 5–13.8 wt % H₂O at 1900 °C. At 13 GPa and in the system MgSiO₃-H₂O, the liquidus was constrained between 4.3–10 wt % H₂O and 6.2–11.8 wt % H₂O at 1900 and 1700 °C, respectively.

Thermodynamic calculations were performed in order to describe the effect of H₂O on lowering the melting temperature of the minerals forsterite and enstatite. Models that reproduce, within uncertainty, the experimental results were constructed based on the formation of the melt equilibrium



where water is present as both molecular H₂O dissolved in the melt and hydroxyl groups OH⁻ bonded to silicate molecules. Using a cryoscopic melting equation, the experimental melting

point depression data can be fitted as a function of melt H₂O content by adjusting the equilibrium constant for equilibrium 7.1. Application of this model to the experimental data reveals that equilibrium 7.1 proceeds strongly to the right hand side for MgSiO₃ melts at 6 and 13 GPa and for Mg₂SiO₄ melts at 6 GPa i.e. OH⁻ is the main species in the melt. However, data for forsterite at 13 GPa provide poor constraints on the equilibrium constant due to uncertainties in the anhydrous melting temperature of Mg₂SiO₄ at these conditions. The depression of melting due to the presence of H₂O was modelled also for natural peridotitic systems where application of the same type of model implies dissolution mainly of molecular H₂O. This difference in H₂O speciation between simple and complex melt systems may arise either from a poor knowledge of the enthalpy of fusion for complex melts or may be due to the effect of other melt species such as Al on the H₂O dissolution reaction. Regardless of the explanation, however, it would seem that melting point depression analysis for simple systems provides little insight into the same mechanisms in complex peridotitic melts.

Models calculated for melts produced in a natural peridotite system indicate an increment in melt H₂O content from 8 to 11 wt % H₂O between 3.5 and 6 GPa along the adiabat, while at 13 GPa and 1500 °C it is predicted to become ~12.4 wt %. Based on these observations, it is concluded that an upper mantle with constant H₂O content would not favor the production of low degree hydrous melts at ~410 km depth compared to any other pressures in the upper mantle, as more H₂O is required to stabilize melts at these conditions. Such high melt H₂O contents mean that melts produced at these depths would not be denser or neutrally buoyant compared to the surrounding mantle and would therefore have no reason to concentrate at this depth in the mantle as previously proposed (Bercovici and Karato 2003). Therefore, low seismic velocity layers observed on top of the 410 km discontinuity are unlikely to result from the presence of small degree melts due to the presence of H₂O alone.

4. The incorporation of H₂O, or hydrogen, in nominally anhydrous minerals olivine (forsterite) and pyroxene (enstatite) was also determined at 6 and 13 GPa and between 1150 to 1900 °C. The investigated samples were synthesized in experiments performed in the systems MgO-SiO₂-H₂O (MSH) at 6 and 13 GPa and in the system MgO-SiO₂-H₂O-CO₂ at 13 GPa, where the volatiles weight ratio H₂O/(H₂O+CO₂) was varied from 0.69 (MSCH5) to 0.80 (MSCH7). In both MSH and MSCH systems the H₂O content of forsterite and enstatite is observed to decrease with increasing temperature at a particular pressure and over the

7. General conclusions

investigated temperature range. At 6 GPa and in the MSH system, forsterite is found to contain 700-800 ppm wt H₂O at 1250-1300 °C and about 300 ppm wt H₂O at 1600-1650 °C while enstatite has 600 ppm wt H₂O at 1050 °C and this amount is lowered to 300 ppm wt H₂O when temperature reaches 1650 °C. In the MSH system at 13 GPa and 1300 °C, forsterite contains ~6600 ppm wt H₂O and enstatite ~1550 ppm wt H₂O, while at 1900 °C forsterite average H₂O content is 740 ppm wt and enstatite average H₂O content is 330 ppm wt H₂O. $D_{H_2O}^{\min/melt}$ was calculated in the different systems based on melt water contents determined from the liquidus phase relations. In the hydrous system at 6 GPa $D_{H_2O}^{fo/melt}$ and $D_{H_2O}^{en/melt}$ have averages of 0.0026± 0.0009 and 0.0020± 0.0006 respectively, and do not show significant variation within the investigated temperature range. At 13 GPa in the MSH system, $D_{H_2O}^{fo/melt}$ decreases from 0.0202 at 1300 °C to 0.0073 at 1900 °C while $D_{H_2O}^{en/melt}$ has a average value of 0.0072± 0.0005 between 1300 and 1600 °C and 0.0036± 0.0004 at 1700-1900 °C. At 13 GPa the concentration of H₂O in the minerals is considerably lowered in the CO₂-bearing systems compared to the MSH system. For example, with H₂O/(H₂O+CO₂)= 0.80, forsterite and enstatite have 2600 and 1400 ppm wt H₂O at 1400 °C, while with H₂O/(H₂O+CO₂)= 0.69 these values drop to 2200 and 1190 ppm wt H₂O for forsterite and enstatite respectively. The addition of CO₂ considerably lowers $D_{H_2O}^{fo/melt}$. At 13 GPa and 1500 °C $D_{H_2O}^{fo/melt}$ is 0.017 in the MSH system, which drops to 0.0112 for H₂O/(H₂O+CO₂)= 0.80 and 0.0058 for H₂O/(H₂O+CO₂)= 0.69.

The distribution of H₂O and the production of melt atop the transition zone can therefore be significantly affected by the addition of modest amounts of CO₂ to a hydrous system since $D_{H_2O}^{fo/melt}$ is reduced in comparison to a purely hydrous system. The fraction of melt that is produced upon melting a mantle peridotite at 13 GPa and adiabatic temperature (1500 °C) as a function of mantle H₂O content was estimated for both H₂O and H₂O+CO₂ systems. In the CO₂-bearing model, $D_{H_2O}^{pdt/melt}$ was calculated employing a value of $D_{H_2O}^{ol/melt}$ that was lowered, compared to a purely hydrous system, in relation to the difference observed between $D_{H_2O}^{fo/melt}$ in the MSH system and in the system with H₂O/(H₂O+CO₂)=0.69. It is shown that in order to produced a considerable amount of melt (0.1 wt %) on top of the transition zone, 350 ppm wt H₂O is required in a CO₂ bearing system with H₂O/(H₂O+CO₂)= 0.69 while in a purely hydrous system, the mantle H₂O content would need to be 850 ppm wt. This strongly implies

that the presence of modest amounts of CO₂ facilitates the formation of melts atop the transition zone.

7.1 Further work

The experimental data obtained in this thesis improve our knowledge of the distribution of H₂O and the formation of hydrous melts in the upper mantle. However a number of issues remain outstanding.

Experiments described in Chapter 4 and 5 qualitatively and quantitatively address the formation of hydrous melts at ~180 km depth in the mantle. The knowledge of low degree melt chemical composition and the $D_{H_2O}^{\text{min/melt}}$ for the coexisting minerals provide the most realistic information regarding the genesis of volatile-bearing melts at this depth in the upper mantle. Hydrous melts forming at depths comparable to the top of the transition zone, ~400 km, have been suggested to explain mantle geochemical differentiation and geophysical anomalies (Bercovici and Karato, 2001; Tauzin et al., 2010). However, the formation of purely hydrous melts atop the transition zone is not supported by the thermodynamic calculations presented in Chapter 6. Whether hydrous melting is a possible scenario in the upper mantle can be better constrained by determining the composition of a low degree melts forming and the H₂O concentration in the coexisting peridotite minerals at 13 GPa and adiabatic temperature in a natural system. This would allow precise quantification of the production of low degree hydrous melts atop the transition zone.

Further, it has been observed that the determination of the phase equilibria of mantle minerals in simple systems Mg₂SiO₄-H₂O and MgSiO₃-H₂O provide constraints on the melt H₂O content forming in such systems (Chapter 5). The results from these experiments can be used to construct thermodynamic models that describe the effect of H₂O on lowering melting temperatures of mantle minerals through the use of a cryoscopic equation. While providing a good approximation for simplified mantle minerals, the models resulting from such experiments differs from those determined for melts forming in natural systems. To improve our understanding on the effect of water on lowering melting temperature of mantle materials, further experiments including additional components to MgO and SiO₂, such e.g. Al₂O₃, are required in order to approach the behavior observed for the natural systems. These data would also provide reliable estimates of the H₂O content of peridotite derived melts.

The addition of CO₂ to a hydrous mantle peridotite is suggested to enhance the formation of hydrous melts atop the transition zone based on experiments performed in a simple system in the presence of both H₂O and CO₂ (Chapter 6). This is a consequence of the fact that in the presence of CO₂, $D_{H_2O}^{pdt/melt}$ is notably lowered at 13 GPa compared to hydrous systems. However, in modeling the formation of melts in the presence of H₂O and CO₂, a number of assumptions have been made in order to constrain the melt composition forming at 13 GPa and adiabatic temperature. To provide firmer basis to the hypothesis better constraints on the melt volatile contents are required, particularly in more complex melt systems. Also, it would be important to determine the effect of CO₂ on the distribution of H₂O in the mantle and the formation of volatile-bearing melts at shallower depths in the upper mantle.

It is interesting to note that the effect of CO₂ on H₂O partitioning observed in Chapter 6 decreases with increasing temperature. The effect of varying pressure may also be crucial. If it can be shown that CO₂ effects H₂O partitioning only over certain depth intervals then this might explain seismic observations of deep mantle melts. If CO₂ has a smaller effect on the H₂O partition coefficient at lower pressures then melt fractions may decrease with decreasing pressure. This would provide an explanation for the appearance of deep melts and apparent disappearance at shallower depths.

In addition it is vital to understand how the oxidation state of the mantle may influence CO₂ speciation between diamond and CO₂-bearing melts. Low oxygen fugacities predicted at the base of the upper mantle should preclude the stability of CO₂ rich melts, as CO₂ should be reduced to form diamond (Frost and McCammon 2004; Stagno et al., 2013). However, if CO₂ is dissolved in hydrous silicate melt its stability field with respect to oxygen fugacity should be extended to lower values. There will be a complex interdependence between the activity of CO₂ in the melt, the partitioning of H₂O between minerals and melt and the CO₂ melt activity at which diamond forms. This interplay may control the specification of volatiles and the formation of melts in the mantle and may also be implicated in the formation of kimberlitic magmas.

Acknowledgments

First of all, I extend my deepest gratitude to Prof. Dan Frost for being a great advisor and for his support, energy and patience during the entire course of my PhD. It has been a real pleasure to learn from him and to work together over the last years. I very much appreciate the time he dedicated to me and to this thesis, particularly in the last (intense) months of my PhD. Dr. Tiziana Boffa Ballaran and Prof. Hans Keppler are also kindly acknowledged for their invaluable support, especially received over the last year. I feel immense gratitude toward these 3 persons.

I am grateful to the Elite Network of Bayern (ENB) international graduate school program for supporting my studies, almost in its entirety, and also to the Bayerisches Geoinstitut (BGI) for fundings received in the very last part of my PhD. I am also very thankful to the technical and administration staff at BGI for providing everything I needed to conduct my research, and for making this institute one-of-a-kind.

Many are the persons I had the pleasure to collaborate, and interact with, during my PhD. I would like to offer my thanks to Dr. Erik Hauri and Dr. Yingwei Fei who gave me the privilege to visit Carnegie Institute and conduct some analytical and experimental work in their laboratories. Dr. Helene Bureau, Dr. Caroline Raepsaet and Dr. Mathilde Roberge are also acknowledged for the help during my visits to Commissariat à l'énergie atomique et aux énergies alternatives and to Institut de Minéralogie et de Physique des Milieux Condensés. Many thanks also to Dr. Andreas Audétat for the precious assistance in conducting the numerous laser ablation analyses and to Dr. Bob Myhill and Dr. David Dolejs for discussions. I am very grateful to Dr. Geeth Manthilake for teaching me most of the things I know about Multianvil. Dr. Florian Heidelbach is also acknowledged for translating the summary of this thesis into German.

Many, many thanks go to my family and close friends for always supporting me, and especially to my parents for giving me the great opportunity to study.

Il grazie più grande va in fine a Martha Giovanna. Per dirla in modo semplice e conciso, se non fosse per lei non avrei mai fatto tutto ciò. Per sempre grazie gordis!

References

- Abe, Y., Othani, E., Okuchi, T., Righter, K., Drake, M., 2000. Water in the early Earth. In: Origin of the Earth and the Moon, ed.s R.M. Canup and K. Righter. University of Arizona press, Tucso, pp. 4136433.
- Ackermann, L, Cemi , L. and Langer, K., 1983. Hydrogarnet substitution in pyrope: a possible location for water in the mantle. *Earth Planet. Sci. Lett.* 62, 2086214.
- Allègre, C.J., Staudacher, T., Sarda, P., 1986-87. Rare gas systematics: formation of the atmosphere, evolution and structure of the Earth's mantle, *Earth Planet. Sci. Lett.* 134, 5156526.
- Anderson, A.T., 1975. Some basaltic and andesitic gases. *Rev. Geophys.* 13, 37656.
- Ardia, P., Hirschmann, M.M., Withers, A.C., Tenner, T.J., 2012. H₂O storage capacity of olivine at 5-8 GPa and consequences for dehydration partial melting of the upper mantle. *Earth Planet. Sci. Lett.* 345-348, 1046116.
- Asimow, P.D., Dixon, J.E., Langmuir, C.H., 2004. A hydrous melting and fractionation model for mid-ocean ridge basalts: applications to the mid-atlantic ridge near the Azores. *Geochem. Geophys. Geosyst.* 5(1), doi:10.1029/2003GC000568.
- Asimow, P.D., Langmuir, C.H., 2003. The importance of water to oceanic mantle melting regimes. *Nature* 421, 8156820.
- Aubaud, C., Hauri, E.H., Hirschmann, M.M., 2004. Hydrogen partition coefficients between nominally anhydrous minerals and basaltic melts. *Geophys. Res. Lett.* 31, L20611.
- Aubaud, C., Pineau, F., Hekinian, R., Javoy, M., 2005. Degassing of CO₂ and H₂O in submarine lavas from the Society hotspot. *Earth Planet. Sci. Lett.* 235, 5116527.
- Aubaud, C., Pineau, F., Hekinian, R., Javoy, M., 2006. Carbon and hydrogen isotope constraints on degassing of CO₂ and H₂O in submarine lavas from the Pitcairn hotspot (South Pacific). *Geophys. Res. Lett.* 33, L02308.
- Aubaud, C., Hirschmann, M.M., Withers, A.C., Hervig, R.L., 2008. Hydrogen partitioning between melt, clinopyroxene, and garnet at 3 GPa in a hydrous MORB with 6wt.% H₂O. *Contrib. Mineral. Petrol.* 156, 6076625.
- Aubaud, C., Bureau, H., Raepsaet, C., Khodja, H., Withers, A.C., Hirschmann, M.M., Bell, D.R., 2009. Calibration of the infrared molar absorption coefficients for H in olivine, clinopyroxene and rhyolitic glass by elastic recoil detection analysis. *Chem. Geol.* 262, 78686.
- Bali, E., Bolfan-Casanova, N., Koga, K.T., 2008. Pressure and temperature dependence of H solubility in forsterite: an implication to water activity in the Earth interior. *Earth Planet. Sci. Lett.* 268, 3546363.
- Balta, J.B., Asimow P.D., Mosenfelder, J.L. (2011). Hydrous, low-carbon melting of garnet peridotite. *J. Petrol.* 52(11), 1-27.
- Bagley, B., Revenaugh, J., 2008. Upper mantle seismic shear discontinuities of the Pacific. *J. Geophys. Res.* 113, B12301, doi:10.1029/2008JB005692.
- Becker, M., le Roex, A.P., 2006. Geochemistry of South African On- and Off- craton, Group I and Group II kimberlites: petrogenesis and source region evolution. *J. Petrol.* 47(4), 6736703.
- Bell, D.R., Rossmann, G.R., 1992. Water in Earth's mantle: the role of nominally anhydrous minerals. *Science* 255, 139161397.
- Bell, D.R., Rossman, G.R., Maldener, J., Endisch, D., Rauch, F., 2003. Hydroxide in olivine: a quantitative determination of the absolute amount and calibration of the IR spectrum. *J. Geophys. Res.* 108, 2105.
- Bercovici, D., Karato, S.-I., 2003. Whole-mantle convection and the transition-zone water filter. *Nature* 425, 39644.

- Birch, F., 1947. Finite elastic strain of cubic crystals. *Phys. Rev.* 71, 8096824.
- Bolfan-Casanova, N., 2005. Water in the Earth's mantle. *Min. Mag.* 69(3), 2296257.
- Bolfan-Casanova, N., Keppler, H., Rubie, D.C., 2000. Water partitioning between nominally anhydrous minerals in the MgO-SiO₂-H₂O system up to 24 GPa: implications for the distribution of water in the Earth's mantle. *Earth Planet. Sci. Lett.* 182, 2096221.
- Bose, K., Ganguly, J., 1995. Experimental and theoretical studies of the stabilities of talc, antigorite and phase A at high pressures with applications to subduction processes. *Earth Planet. Sci. Lett.* 136, 1096121.
- Bottinga, Y., 1985. On the isothermal compressibility of silicate liquids at high pressure. *Earth Planet. Sci. Lett.* 74, 3506360.
- Boyd, F.R., 1973. A pyroxene geotherm. *Geochim. Cosmochim. Acta* 37, 2533-2546.
- Boyd, F.R., 1989. Compositional distinction between oceanic and cratonic lithosphere. *Earth Planet. Sci. Lett.* 96, 15-26.
- Brey, G.P., Bulatov, V.K., Girnis, A.V., 2009. Influence of water and fluorine on melting of carbonated peridotite at 6 and 10 GPa. *Lithos* 112S, 249-259.
- Brey, G.P., Bulatov, V.K., Girnis, A.V., Lahaye, Y., 2008. Experimental melting of carbonated peridotite at 6-10 GPa. *J. Petrol.* 49(4), 797-821.
- Brey, G.P., Köhler, T., 1990. Geothermobarometry in four-phase Iherzolites II. New thermobarometers, and practical assessment of existing thermobarometers. *J. Petrol.* 31(6), 1353-1378.
- Brey, G.P., Köhler, T., Nickel, K.G., 1990. Geothermobarometry in four-phase Iherzolites I. Experimental Results from 10 to 60 kb. *J. Petrol.* 31(6), 1313-1352.
- Brooker, R., Holloway, J., Hervig, R., 1998. Reduction in piston cylinder experiments: the detection of carbon infiltration into platinum capsules. *Am. Mineral.* 83, 985-994.
- Bureau, H., Trocellier, P., Shaw, C., Khodja, H., Bolfan-Casanova, N., Demouschy, S., 2003. Determination of the concentration of water dissolved in glasses and minerals using nuclear microprobe. *Nucl. Instrum. Methods Phys. Res., Sect. B* 210, 4496454.
- Bureau, H., Raepsaet, C., Khodja, H., Carraro, A., Aubaud, C., 2009. Determination of hydrogen content in geological samples using elastic recoil detection analysis (ERDA). *Geochim. Cosmochim. Acta* 73, 331163322.
- Canil, D., Scarfe, C.M., 1990. Phase relations in peridotite + CO₂ systems to 12 GPa: implications for the origin of kimberlite and carbonate stability in the Earth's upper mantle. *J. Geophys. Res.* 95, 15805-15816.
- Carswell, D.A., Gibb, F.G.F., 1987. Garnet Iherzolite xenoliths in the kimberlites of northern Lesotho: Revised P-T equilibration conditions and upper mantle Palaeogeotherm. *Contrib. Mineral. Petrol.* 97, 473-487.
- Chamorro, E.M., Brooker, R.A., Wartho, J.-A., Wood, B.J., Kelley, S.P., Blundy, J.D., 2002. Ar and K partitioning between clinopyroxene and silicate melt to 8 GPa. *Geochim. Cosmochim. Acta* 66, 5076519.
- Chen, J., Inoue, T., Yurimoto, H., Weidner, D.J., 2002. Effect of water on olivine-wadsleyite phase boundary in the (Mg,Fe)₂SiO₄ system. *Geophys. Res. Lett.* 29(18), doi:10.1029/2001GL014429.
- Costa, F., Chakraborty, S., 2008. The effect of water on Si and O diffusion rates in mantle olivine and implications for transport properties and processes in the upper mantle. *Phys. Earth Planet. Int.* 166, 11629.
- Courtney, R.C., White, R.S., 1986. Anomalous heat flow and geoid across the Cape Verde Rise: evidence for dynamic support from a thermal plume in the mantle. *Geophys. J. R. Astr. Soc.* 87, 815-867 and Microfiche GJ 87/1.

- Couvy, H., Frost, D.J., Heidelbach, F., Nyilas, K., Ungár, T., Mackwell, S., Cordier, P., 2004. Shear deformation experiments of forsterite at 11 GPa - 1400°C in the multianvil apparatus. *Eur. J. Mineral.* 16(6): 877-889.
- Daudin, L., Khodja, H., Gallien, J. P., 2003. Development of $\ddot{\text{o}}$ position-charge-time $\ddot{\text{o}}$ tagged spectrometry for ion beam microanalysis. *Nucl. Instrum. Methods Phys. Res. B* 210, 153-158. doi: 10.1016/S0168-583X(03)01008-5.
- Davis, B.T.C., England, J.L., 1964. The melting of forsterite up to 50 kilobars. *J. Geophys. Res.* 69(6), 1113-1116.
- Davis, F.A., Hirschmann, M.M., Humayun M., 2011. The composition of the incipient partial melt of garnet peridotite at 3 GPa and the origin of OIB. *Earth Planet. Sci. Lett.* 308, 380-390.
- Dalton, J.A., Presnall, D.C., 1998. The continuum of primary carbonatitic-kimberlitic melt compositions in equilibrium with lherzolite: data from the system CaO-MgO-Al₂O₃-SiO₂-CO₂ at 6 GPa. *J. Petrol.* 39, 1953-1964.
- Dasgupta, R., Hirschmann, M.M., 2007. A modified iterative sandwich method for determination of near-solidus partial melt compositions. II. Application to determination of near-solidus melt compositions of carbonated peridotite. *Contrib. Mineral. Petrol.* 154(6), 647-661.
- Dawson, J.B., Smith, J.V., 1977. The MARID (mica-amphibole-rutile-ilmenite-diopsid) suite of xenoliths in kimberlite: *Geochim. Cosmochim. Acta*, 41, 309-323.
- de Koker, N., Stixrude, L., 2009. Self-consistent thermodynamic description of silicate liquids, with application to the shock melting of MgO periclase and MgSiO₃ perovskite. *Geophys. J. Internat.*, 178, 162-179, doi: 10.1111/j.1365-246X.2009.04142.x.
- Dixon, J.E., Stolper, E.M., Delaney, J.R., 1988. Infrared spectroscopic measurements of CO₂ and H₂O in Juan de Fuca Ridge basaltic glasses. *Earth Planet. Sci. Lett.* 90, 87-104.
- Dixon, J.E., Stolper, E.M., Holloway, J.R., 1995. An experimental study of water and carbon dioxide solubilities in mid-ocean ridge basaltic liquids. Part I: calibration and solubility models. *J. Petrol.* 36, 1607-1631.
- Dixon, J.E., Clague, D.A., Wallace, P., Poreda, R., 1997. Volatiles in alkalic basalts from the North Arch Volcanic Field, Hawaii: extensive degassing of deep submarine erupted alkalic series lavas. *J. Petrol.* 38, 911-939.
- Dixon, J.E., Leist, L., Langmuir, C., Schilling, J.-G., 2002. Recycled dehydrated lithosphere observed in plume-influenced mid-ocean-ridge basalt. *Nature* 420, 385-389.
- Dobson, P.F., Skogby, H., Rossman, G.R., 1995. Water in boninite glass and coexisting orthopyroxene: concentration and partitioning. *Contrib. Mineral. Petrol.* 118, 414-419.
- Downs, R.T., 2006. The RRUFF Project: an integrated study of the chemistry, crystallography, Raman and infrared spectroscopy of minerals. Program and abstract of the 19th General Meeting of the International Mineralogical Association in Kobe, Japan.
- Edgar A. D., Arima M., Baldwin D. K., Bell D. R., Shee S. R., Skinner M. W., Walker E. C., 1988. High-pressure-high-temperature melting experiments on a SiO₂-poor aphanitic kimberlite from the Wesselton mine, Kimberley, South Africa. *Am. Mineral.* 73, 524-533.
- Edgar, A. D., Charbonneau, H. E., 1993. Melting experiments on a SiO₂-poor aphanitic kimberlite from 5-10 GPa and their bearing on source of kimberlite magmas. *Am. Mineral.* 78, 132-142.
- Eggler, D.H., 1972. Role of CO₂ in melting processes in the mantle. *Carnegie Inst. Wash. Year Book*, 72, 457-467.

- Eggler, D.H., 1978. The effect of CO₂ upon partial melting of peridotite in the system Na₂O-CaO-Al₂O₃-MgO-SiO₂-CO₂ to 35 kb, with an analysis of melting in a peridotite-H₂O-CO₂ system. Am. J. Sci. 278, 305-343.
- Eggler, D.H., 1989. Kimberlites, how do they form?. In: Kimberlites and related rocks 1, Ross et al. (eds). Blackwell, pp. 489-504.
- Ellis, D.J., Green, D.H., 1979. An experimental study of the effect of Ca upon garnet-clinopyroxene Fe-Mg exchange equilibria. Contrib. Mineral. Petrol. 71, 13-22.
- Ellis, D.E., Wyllie, P.J., 1979. Hydration and melting reactions In the system magnesium oxide - silicon di oxide - water at pressures up to 100 kbar. Am. Mineral., 64, 162, 41648
- Erlank, E.J., Waters, F.G., Hawkesworth, C.J. Haggerty, S.E., Allsopp, H.L., Rickard, R.S., Menzies, M., 1987. Evidence for mantle metasomatism in peridotite nodules from Kimberly pipes, South Africa. In: Mantle Metasomatism. Menzies M.A., Hawkesworth, C.J. (eds). Academic Press, pp. 313-361.
- Evans, R.L., Hirth, G., Baba, K., Forsyth, D., Chave, A., Mackie, R., 2005. Geophysical evidence from the MELT area for compositional controls on oceanic plates. Nature 437, 249-252.
- Falloon, T.J., Green, D.H., 1987. Anhydrous partial melting of MORB pyrolite and other peridotite compositions at 10 kb: implications for the origin of primitive MORB glasses. Contrib. Mineral. Petrol. 37, 181-219.
- Fei, H., Wiedenbeck, M., Yamazaki, D., Katsura, T., 2013. Small effect of water on upper mantle rheology based on silicon self-diffusion coefficients. Nature 498, 213-215.
- Férot, A., Bolfan-Casanova, N., 2012. Water storage capacity in olivine and pyroxene to 14 GPa: Implications for the water content of the Earth's upper mantle and nature of seismic discontinuities. Earth Planet. Sci. Lett. 349-350, 2186230.
- Foley, S.F., Yaxley, G.M., Rosenthal, A., Buhre, S., Kisieva, E.S., Rapp, R.P., Jacob, D.E., 2009. The composition of near-solidus melts of peridotite in the presence of CO₂ and H₂O between 40 and 60 kbar. Lithos 112, 274-283.
- Frost, D.J., 2006. The Stability of Hydrous Mantle Phases, in: Keppler, H.K., Smyth, J.R. (Eds.), Water in nominally anhydrous minerals. Rev. Min. Geochem. 62, 231-241.
- Frost, D.J., McCammon, C.A., 2008. The redox state of Earth's mantle. Ann. Rev. Earth Planet. Sci. 36, 389-420.
- Frost, D.J., Poe, B.T., Tronnes, R.G., Liebske, C., Duba, A., Rubie, D.C., 2004. A new large-volume multianvil system. Phys. Earth Planet. Int. 143-144, 507-514.
- Fukui, H., Inoue, T., Yasui, T., Katsura, T., Funakoshi, K.I., Ohtaka, O., 2005. Decomposition of brucite up to 20 GPa: evidence for high MgO-solubility in the liquid phase. Eur. J. Min. 17, 261-267.
- Gaetani, G.A., Grove, T.L., 1998. The influence of water on melting of mantle peridotite. Contrib. Mineral. Petrol. 131, 323-346.
- Geiger, C.A., Langer, K., Bell, D.R., Rossman, G.R., Winkler, B., 1991. The hydroxide component in synthetic pyrope. Am. Mineral. 76, 496-509.
- Giordano, D., Russel, J.K., Dingwell, D.B., 2008. Viscosity of magmatic liquids: a model. Earth Planet. Sci. Lett. 271, 123-134.
- Girnis A. V., Brey G. P., Ryabchikov I. D., 1995. Origin of Group IA kimberlites: Fluid-saturated melting experiments at 45-55 kbar. Earth Planet. Sci. Lett. 134, 283-296.
- Girnis A. V., Bulatov V. K., Brey G. P., 2011. Formation of primary kimberlite melts - constraints from experiments at 6-12 GPa and variable CO₂/H₂O. Lithos 127, 401-413.

- Grant, K.J., Kohn, S.C., Brooker, R.A., 2006. Solubility and partitioning of water in synthetic forsterite and enstatite in the system MgO-SiO₂-H₂O±Al₂O₃. *Contrib. Mineral. Petrol.* 151, 651664.
- Green, D.H., 1973. Experimental melting studies on a model upper mantle composition at high pressure under water-saturated and water-undersaturated conditions. *Earth Planet. Sci. Lett.* 19, 37653.
- Green, D.H., Wallace, M.E., 1988. Mantle metasomatism by ephemeral carbonatite melts. *Nature* 336, 459-462.
- Grove, T.L., Chatterjee, N., Parman, S.W., Médard, E., 2006. The influence of H₂O on mantle wedge melting. *Earth Planet. Sci. Lett.* 249, 74689.
- Gudfinnsson, G. H., Presnall, D. C., 2005. Continuous gradations among primary carbonatitic, kimberlitic, melilititic, basaltic, picritic, and komatiitic melts in equilibrium with garnet lherzolite at 3-8 GPa. *J. Petrol.* 46, 1645-1659.
- Hacker, B.R., 2008. H₂O subduction beyond arcs. *Geochem. Geophys. Geosyst.* 9(3), doi:10.1029/2007GC001707.
- Hall, L.J., Brodie, J., Wood, B.J., Carroll, M.R., 2004. Iron and water losses from hydrous basalts contained in Au₈₀Pd₂₀ capsules at high pressure and temperature. *Min. Mag.* 68(1), 75-81.
- Harley, S.L., 1984. An experimental study of the partitioning of Fe and Mg between garnet and orthopyroxene. *Contrib. Mineral. Petrol.* 86, 359-373.
- Hauri, E.H., Gaetani, G.A., Green, T.H., 2006. Partitioning of water during melting of the Earth's upper mantle at H₂O-undersaturated conditions. *Earth Planet. Sci. Lett.* 248 (364), 7156734.
- Hauri, E.H., Shimizu, N., Dieu, J.J., Hart, S.R., 1993. Evidence for hotspot-related carbonatite metasomatism in the oceanic upper mantle. *Nature* 365, 221-227.
- Hirose, K., 1997. Melting experiments on lherzolite KLB-1 under hydrous conditions and generation of high-magnesian andesitic melts. *Geology* 25, 42-44.
- Hirose, K., Kawamoto, T., 1995. Hydrous partial melting of lherzolite at 1 GPa: the effect of H₂O on the genesis of basaltic magmas. *Earth and Planetary Science Letters* 133, 463-473.
- Hirose, K., & Kushiro, I. (1993). Partial melting of dry peridotites at high pressures: determination of compositions of melts segregated from peridotite using aggregates of diamond. *Earth Planet. Sci. Lett.* 114, 4776489.
- Hirschmann, M.M., 2006. Water, melting, and deep Earth H₂O cycle. *Ann. Rev. Earth Planet. Sci.* 34, 6296653.
- Hirschmann, M.M., 2010. Partial melt in the oceanic low velocity zone. *Phys. Earth Planet. Int.* 179, 60-71.
- Hirschmann, M.M., Dasgupta, R., 2007. A modified iterative sandwich method for determination of near-solidus partial melt compositions. I. Theoretical considerations. *Contrib. Mineral. Petrol.* 154(6), 635-645.
- Hirschmann, M.M., Tenner, T., Aubaud, C., Withers, A.C., 2009. Dehydration melting of nominally anhydrous mantle: The primacy of partitioning. *Phys. Earth Planet. Int.* 176, 54-68.
- Hirth, G., Kohlstedt, D., 1996. Water in the oceanic upper mantle: implications for rheology, melt extraction and the evolution of the lithosphere. *Earth Planet. Sci. Lett.*, 144, 936-108.
- Hodges, F.N., 1973. Solubility of H₂O in forsterite melt at 20 kbar. *Carnegie Inst. Washington Yearb.*, 72, 4956497.

- Inoue, T., 1994. Effect of water on the melting phase-relations and melt composition in the system Mg_2SiO_4 - $MgSiO_3$ - H_2O up to 15 GPa. *Phys. Earth Planet. Int.*, 85 (3-4): 237-263.
- Ito, E., 2007. Theory and practice of Multianvil cells and high-pressure experimental methods. In: *Treatise on Geophysics Mineral Physics*, vol. 2, Elsevier.
- Jacobsen, S.D., Jiang, F., Mao, Z., Duffy, T.S., Smyth, J.R., Holl, C.M., Frost, D.J., 2008. Effects of hydration on the elastic properties of olivine, *Geophys. Res. Lett.* 35, doi:10.1029/2008GL034398.
- Jagoutz, E., Palme, H., Baddenhausen, H., Blum, K., Cendales, M., Dreibus, G., Spettel, B., Lorenz, V., Waenke, H., 1979. The abundances of major, minor and trace elements in the Earth's mantle as derived from primitive ultramafic nodules. In: *Proceedings of the Tenth Lunar Planetarium Science Conference*, Tucson, Arizona, pp. 2031-2050.
- Javoy, M., Pineau, F., 1991. The volatile record of a spilling rock from the mid-Atlantic ridge at 148° N: Chemical and isotopic composition of gas trapped in the vesicles. *Earth Planet. Sci. Lett.* 107, 598-611.
- Jing, Z., Karato, S.-I., 2009. The density of volatile bearing melts in the Earth's deep mantle: The role of chemical composition. *Chem. Geol.* 262, 100-107.
- Johnson, K.T.M., Kushiro, I., 1992. Segregation of high pressure partial melt from peridotite using aggregates of diamond: a new experimental approach. *Geophys. Res. Lett.* 19, 1703-1706.
- Johnson, M.C., alker, D., 1993. Brucite $[Mg(OH)_2]$ dehydration and the molar volume of H_2O to 15 GPa. *Am. Min.* 78, 271-284.
- Jung, H., Karato, S.I., 2001. Water-induced fabric transitions in olivine. *Science* 293(5534), 1460-1463.
- Jung, H., Katayama, I., Jiang, Z., Hiraga, T., Karato, S.I., 2006. Effect of water and stress on the lattice-preferred orientation of olivine. *Tectonophys.* 421(162), 1622.
- Jung, H., Mo, W., Green, H.R., 2009. Upper mantle seismic anisotropy resulting from pressure-induced slip transition in olivine. *Nature Geosci.* 2(1), 73-77.
- Kagi, R., Muentener, O., Ulmer, P., Ottoloni, L., 2005. Piston-cylinder experiments on H_2O undersaturated Fe-bearing systems: An experimental setup approaching fO_2 conditions of natural calc-alkaline magmas. *Am. Miner.* 90, 708-717.
- Karato, S.-I., Jung, H., 1998. Water, partial melting and the origin of the seismic low velocity and high attenuation zone in the upper mantle. *Earth Planet. Sci. Lett.* 157, 193-207.
- Karato, S.-I., Jung, H., 2003. Effects of pressure on high-temperature dislocation creep in olivine. *Philos. Mag.*, A 83 (3), 401-414.
- Karato, S.I., Jung, H., Katayama, I., Skemer, P., 2008. Geodynamic significance of seismic anisotropy of the upper mantle: New insights from laboratory studies. *Ann. Rev. Earth Planet. Sci.* 36, 59-95.
- Karato, S.I., Paterson, M.S., FitzGerald, J.D., 1986. Rheology of synthetic olivine aggregates: influence of grain size and water. *J. Geophys. Res.* 91(B8), 8151-8176.
- Kato, T., Kumazawa, M., 1985. Melting and phase relations in the system Mg_2SiO_4 - $MgSiO_3$ at 20 GPa under hydrous conditions. *J. Geophys. Res.* 91(B9), 9351-9355.
- Katsura, T., Yoneda, A., Yamazaki, D., Yoshino, T., Ito, E., 2010. Adiabatic temperature profile in the mantle. *Phys. Earth Planet. Int.* 183, 212-218.
- Kawamoto, T., 2006. Hydrous phase and water transport in the subducting slab. In: *Water in nominally anhydrous minerals, Reviews of Mineralogy and Geochemistry* 62, ed.s H. Keppler and J.R. Smyth, pp. 193-230.
- Kawamoto, T., Holloway, J.R., 1997. Melting temperature and partial melt chemistry of H_2O -saturated mantle peridotite to 11 GPa. *Science* 276, 240-243.

- Kelemen, P.B., Dick, H.J.B., Quick, J. E., 1992. Formation of harzburgite by pervasive melt/rock reaction in the upper mantle. *Nature* 358, 635-641.
- Keppler, H., Bolfan-Casanova, N., 2006. Thermodynamics of water solubility and partitioning. In: *Water in nominally anhydrous minerals, Reviews of Mineralogy and Geochemistry* 62, ed.s H. Keppler and J.R. Smyth, pp. 193-6230.
- Keppler, H., Frost, D. J., 2005. Introduction to minerals under extreme conditions. In: *Mineral Behaviour at Extreme Conditions, EMU Notes in Mineralogy*, vol. 7, Eötvös University Press, Budapest: 1-30.
- Keppler, H., Wiedenbeck, M., Shcheka, S., 2003, Carbon solubility in olivine and the mode of carbon storage in the Earth's mantle. *Nature* 424, 414-6416.
- Khodja, H., Berthoumieux, E., Daudin, L., Gallien, J.P., 2001. The Pierre Sue Laboratory nuclear microprobe as a multi-disciplinary analysis tool. *Nucl. Instrum. Methods Phys. Res., Sect. B* 181, 83-686.
- Koga, K., Hauri, E., Hirschmann, M.M., Bell, D., 2003. Hydrogen concentration analyses using SIMS and FTIR: comparison and calibration for nominally anhydrous minerals. *Geochem. Geophys. Geosyst.* 4(2), 1019, DOI: 10.1029/2002GC000378.
- Kojitani, H., Akaogi, M., 1997. Melting enthalpies of mantle peridotite: calorimetric determinations in the system CaO-MgO-Al₂O₃-SiO₂ and application to magma generation. *Earth Planet Sci. Lett.* 153, 209-6222.
- Kohlstedt, D.L., Keppler, H., Rubie, D.C., 1996. Solubility of water in the , and phases of (Mg,Fe)₂SiO₄. *Contrib. Mineral. Petro.* 123, 345-6357.
- Konzett, J., Ulmer, P., 1999. The stability of hydrous potassic phase in Iherzolitic mantle-an experimental study to 9.5 GPa in simplified and natural bulk compositions. *J. Petrol.* 40, 629-652.
- Kopylova, M.G., Caro, G., 2004. Mantle xenoliths from the southeastern slave craton: evidence for chemical zonation in a thick, cold Lithosphere. *J. Petrol.* 45(5), 1045-1067.
- Kopylova, M.G., Russel, J.K., 2000. Chemical stratification of cratonic Lithosphere: constraints from the Northern Slave craton, Canada. *Earth Planet. Sci. Lett.* 181, 71-87.
- Kushiro, I., 1972. Effect of water on the composition of magmas formed at high pressures. *J. Petrol.* 13, 311-6334.
- Kushiro, I., 1987. A petrological model of the mantle wedge and lower crust in the Japanese island arcs. *Spec. Publ.* 1, pp. 165-181. *Geochem. Soc., University Park, Pa.* *Geochem. Soc., University Park, Pa.*, 1987
- Kushiro, I., Erlank, A.J., 1970. Stability of potassic richterite. *Carnegie Inst. Washington Year Book* 68, 231-6233.
- Kushiro, I., Syono, Y., Akimoto, S-I., 1968a. Melting of a peridotite nodule at high pressures and high water pressures. *J. Geophys. Res.* 73(18), 6023-6029.
- Kushiro, I. & Yoder, H.S. (1969) Melting of forsterite and enstatite at high pressures and hydrous conditions. *Carnegie Int. Washington Yearb.*, 67, 153-6158.
- Kushiro, I., Yoder, H.S.Jr., Nishikawa, M., 1968b. Efefct of water on the melting of enstatite. *Geol. Soc. Am. Bull.* 79, 1685-61692.
- Konzett, J., Sweeney, R.J., Thompson, A.B., Ulmer, P., 1997. Potassium amphibole stability in the upper mantle: an experimental study in a peralkaline KNCMASH System to 8.5 GPa. *J. Petrol.* 38 (5), 537-6568.
- Kopylova, M.G., Russel, J.K., 2000. Chemical strati¢cation of cratonic lithosphere: constraints from the Northern Slave craton, Canada. *Earth Planet. Sci. Lett.* 181, 71-87.

- Lambert, I. B., Wyllie, P. J., 1968. Stability of hornblende and a model for the low velocity zone. *Nature* 219, 1240-1241.
- Lambert, I. B., Wyllie, P. J., 1970. Low-velocity zone of the Earth's mantle; incipient melting caused by water. *Science*, 169, 764-766.
- Lange, R.A., 1994. The effect of H₂O, CO₂ and F on the density and viscosity of silicate melts, in: Carroll, M.R., Holloway, J.R. (Eds.), *Volatiles in magmas*. Rev. Min. Geochem. 30, 3316369.
- Lesher, C.E., Walker, D., 1988. Cumulate maturation and melt migration in a temperature gradient. *J. Geophys. Res.* 93, doi: 10.1029/88JB00056.
- Lesne, P., Scaillet, B., Pichavant, M., Iacono-Marziano, G., Beny, J.M., 2011. The H₂O solubility of alkali basaltic melts: an experimental study. *Contrib. Mineral. Petrol.* 162, 1336151.
- Lewis JS, 2004. Physics and chemistry of the solar system. *International Geophysics*, Academic Press, 87, 16652.
- Libowitzky, E., Rossman, G.R., 1997. An IR absorption calibration for water in minerals. *Am. Mineral.* 82, 111161115.
- Liebske, C. Frost, D.J., 2012. Melting phase relations in the MgO-MgSiO₃ system between 16 and 26 GPa: Implications for melting in Earth's deep interior. *Earth Planet. Sci. Lett.* 3456348, 1596170.
- Litasov, K. D., Ohtani, E., Kagi, H., Jacobsen, S.D., Gosh, S., 2007. Temperature dependence and mechanism of hydrogen incorporation in olivine at 12.5-14 GPa. *Geophys. Res. Lett.* 34, L16314.
- Litasov, K.D., Shatskiy, A.F., Katsura, T., Othani, E., 2009. Water solubility in forsterite at 8-14 GPa. *Doklady Earth Sci.* 425A, 4326435.
- Liu, X., Oø Neill, H.St.C., Berry, A.J., 2006. The effects of small amounts of H₂O, CO₂ and Na₂O on the partial melting of spinel lherzolite in the system CaO-MgO-Al₂O₃-SiO₂±H₂O±CO₂±Na₂O at 1.1 GPa. *J. Petrol.* 47(2), 409-434.
- Lu, R., Keppler, H., 1997. Water solubility in pyrope to 100 kbar. *Contrib. Mineral. Petrol.* 129, 35642.
- Luth, R.W. (1993) Melting in the Mg₂SiO₄-H₂O system at 3 to 12 GPa. *Geophys. Res. Lett.*, 20, 2336235.
- Mackwell, S.J., Kohlstedt, D.L., Paterson, M.S., 1985. Role of water in the deformation of olivine single crystals. *J. Geophys. Res.* 90, 11319611333.
- Mainprice, D., Tommasi, A., Couvy, H., Cordier, P., Frost, D.J., 2005. Pressure sensitivity of olivine slip systems and seismic anisotropy of Earth's upper mantle. *Nature* 433(7027), 7316733.
- Marty, B., 2012. The origins and concentrations of water, carbon, nitrogen and noble gases on Earth. *Earth Planet. Sci. Lett.* 3136314, 56666.
- Matsukage, K.N., Jing, Z., Karato, S-I., 2005. Density of hydrous silicate melt at the conditions of Earth's deep upper mantle. *Nature* 438, 4886491.
- Mayer, M., 1999. SIMNRA a simulation program for the analysis of NRA, RBS, and ERDA, in: Duggan, J.L., Morgan, I.L. (Eds), *Proceedings of the 15th International Conference on the Application of Accelerators in Research and Industry*, American Institute of Physics Conference Proceedings, 475, p. 541.
- McDonough, W.F., 2001. The composition of the Earth. In: *Earthquake thermodynamics and phase transformations in the Earth's interior*, International geophysics series 76. Ed.s R. Teisseyre and E. Majewski, pp. 5624.
- McKenzie, D., 1989. Some remarks on the movement of small melt fractions in the mantle. *Earth Planet. Sci. Lett.* 95, 53-72.

- Médard, E., Grove, T.L., 2008. The effect of H₂O on the olivine liquidus of basaltic melts: experiments and thermodynamic models. *Contrib. Mineral. Petrol.* 155, 417-6432.
- Menzies, M.A., Hawkesworth, C.J., 1987. *Mantle Metasomatism*. xix+472 pp. London, Orlando, San Diego, New York, Austin, Boston, Sydney, Tokyo, Toronto: Academic Press.
- Mibe, K., Fujii, T., Yasuda, M., 2002. Composition of aqueous fluid coexisting with mantle minerals at high pressure and its bearing on the differentiation of the Earth's mantle. *Geochim. Cosmochim. Acta* 66(12), 2273-62285.
- Michael, P.J., 1988. The concentration, behavior and storage of H₂O in the suboceanic upper mantle- implications for mantle metasomatism. *Geochim. Cosmochim. Acta* 52, 555-566.
- Mierdel, K., Keppler, H., Smyth, J.R., Langenhorst, F., 2007. Water solubility in aluminous orthopyroxene and the origin of Earth's asthenosphere. *Science* 315(5810), 364-368.
- Mitchell, R.H., 1986. *Kimberlites: Mineralogy, Geochemistry, and Petrology*. Plenum Press, New York, 442 p.
- Mitchell, R. H., 1995. Kimberlites, orangeites, and related rocks. New York: Plenum Press.
- Mitchell, R. H., 2004. Experimental studies at 5612 GPa of the Ondermatjie hypabyssal kimberlite. *Lithos* 76, 551-564.
- Montagner, J.P., Kennett, B. L. N., 1996. How to reconcile body-wave and normal-mode reference earth models. *Geophys. J. Int.* 125(1), 229-6248.
- Mookherjee, M., Karato, S.I., 2010. Solubility of water in pyrope-rich garnet at high pressures and temperature. *Geophys. Res. Lett.* 37 (3), DOI: 10.1029/2009GL041289.
- Moore, R.O., Gurney, J.J., 1989. Mineral inclusions in diamond from the Monastery kimberlite, South Africa. In: *Kimberlites and related rocks 2*, Ross et al. (eds). Blackwell, pp. 1029-1041.
- Moore, R.O., Gurney, J.J., Griffin, W.L., Shimizu, N., 1991. Ultra-high pressure garnet inclusions in Monastery diamonds: trace element abundance patterns and conditions of origin. *Europ. J. Mineral.* 4, 213-230.
- Mosenfelder, J.L., Deligne, N.I., Asimow, P.D., Rossman, G.R., 2006. Hydration incorporation in olivine from 2612 GPa. *Am. Mineral.* 91, 285-6294.
- Mumma, M. J., Disanti, M. A., Dello Russo, N., Magee-Sauer, K., Gibb, E., Novak, R., 2003. Remote infrared observations of parent volatiles in comets: A window on the early solar system. *Advances Space Res.* 31 (12): 2563.
- Mysen, B.O., and Boettcher, A.L., 1975. Melting of hydrous mantle I. Phase relations of natural peridotite at high pressures and temperatures with controlled activities of water, carbon dioxide, and hydrogen. *J. Petrol.*, 16(3), 520-6548.
- Navrotsky, A., Ziegler, D., Oestrike, R., Maniar, P., 1989. Calorimetry of silicate melts at 1773 K - measurement of enthalpies of fusion and of mixing in the systems diopside-anorthite-albite and anorthite-forsterite. *Contrib. Mineral. Petrol.* 101, 122-6130.
- Ni, H., Keppler, H., 2013. Carbon in silicate melts. *Rev. Mineral. Geochem.* 75, 251-6287.
- Ni, H., Keppler, H., Behrens, H., 2011. Electrical conductivity of hydrous basaltic melts: Implications for partial melting in the upper mantle. *Contrib. Mineral. Petrol.* 162, 637-650.
- Nichols, A.R.L., Carroll, M.R., Höskuldsson, A., 2002. Is the Iceland hot spot also wet? Evidence from the water contents of undegassed submarine and subglacial pillow basalts. *Earth Planet. Sci. Lett.* 202, 77-687.
- Nimis, P., Taylor, W.R., 2000. Single clinopyroxene thermobarometry for garnet peridotites. Part I. Calibration and testing of a Cr-in-Cpx barometer and an enstatite-in-Cpx thermometer. *Contrib. Mineral. Petrol.* 139(5), 541-554.

- Nolet, G., Zielhuis, A., 1994. Low S velocities under the Tornquist-Tesseyre zone: evidence for water injection into the transition zone by subduction. *J. Geophys. Res.* 99, 15813615820.
- Ohtani, E., Mizobata, H., Yurimoto, H., 2000. Stability of dense hydrous magnesium silicate phases in the system Mg_2SiO_4 - H_2O and $MgSiO_3$ - H_2O at pressures up to 27 GPa. *Phys. Chem. Min.* 27, 533-544.
- Ohtani, E., 2005. Water in the mantle. *Elements* 1, 25630.
- Ohuchi, T., Kawazoe, T., Nishihara, Y., Nishiyama, N., Irifune, T., 2011. High pressure and temperature fabric transitions in olivine and variations in upper mantle seismic anisotropy. *Earth Planet. Sci. Lett.* 304(162), 55663.
- O'Leary, J.A., Gaetani, G.A., Hauri, E.H., 2010. The effect of tetrahedral Al^{3+} on the partitioning of water between clinopyroxene and silicate melt. *Earth Planet. Sci. Lett.* 297, 1116120.
- O'Neill, H.St.C., Wood, B.J., 1979. An experimental study of Fe-Mg partitioning between garnet and olivine and its calibration as a geothermometer. *Contrib. Mineral. Petrol.* 70(1), 59-70.
- Palme, H., O'Neill, H.St.C., 2003. Cosmochemical estimates of mantle composition. *Treatise on Geochemistry* 2. Elsevier, Amsterdam, pp. 1-38.
- Peacock, S.M., 1990. Fluid processes in subduction zones. *Science* 248, 3296337.
- Peslier A.H., Woodland A., Bell D.R., Lazarov M., 2010. Olivine Water Contents of the Continental Lithosphere and the Longevity of Cratons. *Nature* 467, 78680.
- Pino, N.A., Helmberger, D.V., 1997. Upper mantle compressional velocity structure beneath the West Mediterranean Basin. *J. Geophys. Res.* 102: doi: 10.1029/96JB03461.
- Plank, T., Langmuir, C. H., 1992. Effects of the melting regime on the composition of oceanic crust. *J. Geophys. Res.* 97, 19749-19770.
- Poe, B.T., Romano, C., Nestola, F., Smyth, J.R., 2010. Electrical conductivity anisotropy of dry and hydrous olivine at 8 GPa. *Phys. Earth Planet. Int.* 181, 1036111.
- Poirier, J.P., 2000. Introduction to the physics of the Earth interior. 2nd ed, Cambridge University Press, Cambridge.
- Presnall, D.C., Gasparik, T., 1990. Melting of enstatite ($MgSiO_3$) from 10 to 16.5 GPa and the forsterite (Mg_2SiO_4)-majorite ($MgSiO_3$) eutectic at 16.5 GPa: implications for the origin of the mantle. *J. Geophys. Res.* 95, doi: 10.1029/90JB00306.
- Presnall, D.C., Walter, M.J., 1993. Melting of forsterite, Mg_2SiO_4 , from 9.7 to 16.5 GPa. *J. Geophys. Res.* 98, pp. 19777619783.
- Raepsaet C., Bureau H., Khodja H., Aubaud C., Carraro A., 2008. μ -ERDA developments in order to improve the water content determination in hydrous and nominally anhydrous mantle phases. *Nucl. Instrum. Methods Phys. Res., Sect. B* 266, 133361337.
- Raterron, P., Chen, J., Li, L., Weidner, D., Cordier, P., 2007. Pressure-induced slip-system transition in forsterite: Single-crystal rheological properties at mantle pressure and temperature. *Am. Mineral.* 92(869), 143661445.
- Rauch, M., Keppler, H., 2002. Water solubility in orthopyroxene. *Contrib. Mineral. Petrol.* 143 (5), 5256536.
- Revenaugh, J., Sipkin, S.A., 1994. Seismic evidence for silicate melt atop the 410-km mantle discontinuity. *Nature* 369, 4746476.
- Reed, S.J.B., 2005. Electron Microprobe analyses and Scanning Electron Microscopy in Geology. Cambridge University press, 189 pp.
- Richet, P., Robie, R.A., Hemingway, B.S., 1993; (1993) Entropy and structure of silicate glasses and melts. *Geochim. Cosmochim. Acta* 57, 275162766.
- Ringwood, A.E., 1966. The chemical composition and origin of the Earth. In: Advances in Earth Sciences, Hurley, P.M. ed., MIT Press, Cambridge, MA, pp.287-356.

- Ringwood, A.E., 1979. Origin of the Earth and Moon, Springer-Verlang, New York, 295 pp.
- Ringwood A. E., Kesson S. E., Hibberson W., Ware N. 1992. Origin of kimberlites and related magmas. *Earth Planet. Sci. Lett.* 113, 521-538.
- Robinson, J.A.C., Wood, B.J., 1998. The depth of the spinel to garnet transition at the peridotite solidus, *Earth Planet. Sci. Lett.* 164, 277-284.
- Robinson, J.A.C., Wood, B.J., Blundy, J.D., 1998. The beginning of melting of fertile and depleted peridotite at 1.5 GPa. *Earth Planet. Sci. Lett.* 155, 97-111.
- Ross, N.L., Akaogi, M., Navrotsky, A., Susaki, J., and McMillan, P., 1986. Phase transformations among CaGeO₃ polymorphs (wollastonite, garnet, and perovskite structures): studies by high-pressure synthesis, high-temperature calorimetry and vibrational spectroscopy and calculation. *J. Geophys. Res.* 91, 460161696.
- Rubey, W.W., 1951. Geologic history of sea water. An attempt to state the problem. *Bull. Geol. Soc. Am.* 62, 111161148.
- Rubie, D.C., Frost, D.J., Mann, U., Asahara, Y., Nimmo, F., Tsuno, K., Kegler, P., Holzheid, A., Palme, H., 2010. Heterogeneous accretion, composition and coremantle differentiation of the Earth. *Earth Planet. Sci. Lett.* 301, 31642.
- Rüpke, L., Morgan, J.P., Dixon, J.E., 2006. Implications of subduction rehydration for Earth's deep water cycle. In: Earth's deep water cycle, Geophysical Monograph 168 AGU. Ed.s S.D. Jacobsen and S. van der Lee, pp. 2636276.
- Saal, A.E., Hauri, E.H., Langmuir, C.H., Perfit, M.R., 2002. Vapour undersaturation in primitive mid-ocean-ridge basalt and the volatile content of Earth's upper mantle. *Nature* 419, 4516455.
- Schmidt M. W., 1996. Experimental constraints on recycling of potassium from subducted oceanic crust. *Science* 272, 1927-1930.
- Schmidt, M. W., Poli, S., 1998. Experimentally based water budgets for dehydrating slabs and consequences for arc magma generation, *Earth Planet. Sci. Lett.*, 163, 3616379.
- Shaw, D.M., 1970. Trace element fractionation during anatexis. *Geochim. Cosmochim. Acta* 34, 2376242.
- Shcheka, S.S., Wiedenbeck, M., Frost, D.J., Keppler, H., 2006. Carbon solubility in mantle minerals. *Earth Planet. Sci. Lett.* 245, 7306742.
- Shekhar, S., 2011. Origins of olivine fabric transitions and their effects on seismic anisotropy in the upper mantle (PhD thesis, University of Bayreuth, Germany).
- Shen, A., Keppler, H., 1995. Infrared spectroscopy of hydrous silicate melts to 1000 °C and 10 kbar: Direct observation of H₂O speciation in a diamond-anvil cell. *Am. Mineral.* 80, 133561338.
- Shlkomanov, I.A., 1993. World fresh water resources. In: Water in Crisis, A guide to the World's fresh water resources. Ed. P.H. Gleick. Oxford University press, pp.13624.
- Silver, L.A., Stolper, E.M., 1985. A thermodynamic model for hydrous silicate melts. *J. Geol.* 93, 1616178.
- Simons, K., Dixon, J., Schilling, J.G., Kingsley, R., Poreda, R., 2002. Volatiles in basaltic glasses from the Easter-Salas y Gomez Seamount Chain and Easter Microplate: Implications for geochemical cycling of volatile elements. *Geochem. Geophys. Geosys.* 3(7), doi:10.1029/2001GC000173.
- Skogby, H., Bell, D.R., Rossmann, G.R., 1990. Hydroxide in pyroxene: variations in the natural environment. *Am. Minral.* 75, 7646774.
- Smith, C. B., 1983. Pb, Sr and Nd isotopic evidence for sources of southern African Cretaceous kimberlites. *Nature* 304, 51-54.
- Smith C. B., Gurney J. J., Barton E. S., Bristow J. W., 1985. Geochemical character of southern African kimberlites: A new approach based on isotopic constraints. *Trans. Geol. Soc. South Africa* 88, 267-280.

- Smyth, J.R., Frost, D.J., Nestola, F., Holl, C. M., Beomiley, G., 2006. Olivine hydration in the deep upper mantle: effects of temperature and silica activity. *Geophys. Res. Lett.* 33, L15301.
- Sokol, A.G., Kupriyanov, I.N., Palyanov, Y.N., Krunk, A.N., Sobolev, N.V., 2013. Melting experiments on the Udachnaya kimberlite at 6.3-7.5 GPa: Implications for the role of H₂O in magma generation and formation of hydrous olivine. *Geochim. Cosmochim. Acta* 101, 133-155.
- Song, T.R.A., Helmberger, D.V., Grand, S.P., 2004. Low-velocity zone atop the 410-km seismic discontinuity in the northwestern United States. *Nature* 427(6974): 530-533.
- Spandler C., Pettke, T., Rubatto, D., 2011. Internal and external fluid sources for eclogite-facies veins in the Monviso Metaophiolite, Western Alps; implications for fluid flow in subduction zones. *J. Petrol.* 52, 1207-1236.
- Sparks, R.S.J., Brooker, R.A., Field, M., Kavanagh J., Schumacher, J.C., Walter, M.J., White, J., 2009. The nature of erupting kimberlite melts. *Lithos* 112, 4296438.
- Stalder, R., Ulmer, P., Thompson, A.B., Günther, D., 2001. High pressure fluids in the system MgO-SiO₂-H₂O under up-epr mantle conditions. *Contrib. Mineral. Petrol.* 140, 607-618.
- Stagno, V., Frost, D.J., 2010. Carbon speciation in the asthenosphere: experimental measurements of the redox conditions at which carbonate-bearing melts coexist with graphite or diamond peridotite assemblages. *Earth Planet. Sci. Lett.* 300, 72-84.
- Stagno, V., Ojwang, D.O., McCammon, C.A., Frost, D.J., 2013. The oxidation state of the mantle and the extraction of carbon from Earth's interior. *Nature* 493, 84-88.
- Stixrude, L., Linthgow-Bertelloni, C., 2007. Influence of phase transformations on later heterogeneity and dynamics in Earth's mantle. *Earth Planet. Sci. Lett.* 263, 45-55.
- Stixrude, L., Lithgow-Bertelloni, C., 2011. Thermodynamics of mantle minerals Ⅱ. Phase equilibria. *Geophys. J. Int.* 184, 1180-1213.
- Stolper, E., 1980. A phase diagram for mid-ocean ridge basalts: Preliminary results and implications for petrogenesis. *Contrib. Mineral. Petrol.* 74, 13-27.
- Stolper, E., 1982. Water in silicate glasses: an infrared spectroscopy study. *Contrib. Mineral. Petrol.* 81, 1617.
- Stolper, E., Newman, S., 1994. The role of water in the petrogenesis of Mariana trough magmas. *Earth Planet. Sci. Lett.*, 121, p. 293-326.
- Suzuki, T., Hirata, T., Yokoyama, T.D., Imai, T., Takahashi, E., 2012. Pressure effect on element partitioning between minerals and silicate melt: melting experiments on basalt up to 20 GPa. *Phys. Earth Planet. Int.* 208-209, 59-73.
- Sweeney, R.J., Prozesky, V.M., Springhorn, K.A., 1997. Use of the elastic recoil detection analysis (ERDA) microbeam technique for the quantitative determination of hydrogen in materials and hydrogen partitioning between olivine and melt at high pressures. *Geochim. Cosmochim. Acta* 61, 101-113.
- Sylvester, P., 2008. Laser Ablation ICP-MS in the Earth Sciences: Current practices and outstanding issues. *Mineralogical Association of Canada, Short Course*, 40, 356 pp.
- Symonds, R.B., Rose, W.I., Bluth, G.J.S., Gerlach, T.M., 1994. Volcanic-gas studies: methods, results, and applications. In: *Reviews of Mineralogy and Geochemistry* 30, ed.s M.R. Carroll and J.R. Holloway, pp. 1666.
- Tainton, K.M., McKenzie, D., 1994. The generation of kimberlites, lamproites and their source rocks. *J. Petrol.*, 35, 787-817.
- Takahashi, E., 1986. Melting of dry peridotite KLB-1 up to 14 GPa: implications on the origin of peridotitic upper mantle. *J. Geophys. Res.* 91(B9) 9367-9382.
- Takahashi, E., Kushiro, I., 1983. Melting of a dry peridotite at high pressure and basalt magma genesis. *Am. Mineral.* 68, 859-879.

- Takei, Y., Holtzman, B.K., 2009. Viscous constitutive relations of solid-liquid composites in terms of grain boundary contiguity: 1. Grain boundary diffusion control model. *J. Geophys. Res.* 114, doi:10.1029/2008JB005850.
- Tangeman, J.A., Lange, R., and Forman, L., 2001. Ferric-ferrous equilibria in K_2O - FeO - Fe_2O_3 - SiO_2 melts. *Geochim. Cosmochim. Acta* 65 180961819.
- Raepsaet C., Bureau H., Khodja H., Aubaud C., Carraro A., 2008. μ -ERDA developments in order to improve the water content determination in hydrous and nominally anhydrous mantle phases. *Nucl. Instrum. Methods Phys. Res., Sect. B* 266, 133361337.
- Tatsumi, Y., Hamilton, D.L., and Nesbitt, R.W., 1986. Chemical characteristics of fluid phase released from a subducted lithosphere and origin of arc magmas: Evidence from high-pressure experiments and natural rocks. *J. Volcan. Geotherm. Res.* 29, 2936309.
- Tauzin, B., Debaille, E., Wittlinger, G., 2010. Seismic evidence for a global low-velocity layer within the Earth's upper mantle. *Nature Geosciences* 3, 7186721.
- Tenner, T.J., Hirschmann, M.M., Humayun, M., 2012. The effect of H_2O on partial melting of garnet peridotite at 3.5 Gpa. *Geochem. Geophys. Geosys.* 13(3), doi:10.1029/2011GC003942.
- Tenner, T.J., Hirschmann, M.M., Withers, A.C., Ardia, P., 2011. H_2O storage capacity of olivine and low-Ca pyroxene from 10 to 13 GPa: consequences for dehydration melting above the transition zone. *Contrib. Mineral. Petrol.* 163, 297-316.
- Tenner, T.J., Hirschmann, M.M., Withers, A.C., Hervig, R.L., 2009. Hydrogen partitioning between nominally anhydrous upper mantle minerals and melt between 3 and 5 GPa and implications to hydrous peridotite partial melting. *Chem. Geol.* 262(1-2), 42-56.
- Toplis, M.J., 2004. The thermodynamics of iron and magnesium partitioning between olivine and liquid: criteria for assessing and predicting equilibrium in natural and experimental systems. *Contrib. Mineral. Petrol.* 149, 22-39.
- Ulmer, P., Sweeney, R. J., 2002. Generation and differentiation of group II kimberlites: constraints from a high-pressure experimental study to 10 GPa. *Geochim. Cosmochim. Acta* 66, 2139-2153.
- Umemoto, K., Wentzcovitch, R.M., Hirschmann, M.M., Kohlstedt, D.L., Withers, A.C., 2011. A first-principle investigation of hydrous defects and Ir frequencies in forsterite: the case of Si vacancies. *Am. Mineral.* 96, 147561479.
- van Achterbergh, E., Griffin, W.L., Stienhofer, J., 2001. Metasomatism in mantle xenoliths from the Letlhakane kimberlites: estimation of element fluxes. *Contrib. Mineral. Petrol.* 141, 397-414.
- Walter, M.J., 1998. Melting of garnet peridotite and the origin of komatiite and depleted Lithosphere. *J. Petrol.* 39, 29-60.
- Walter, M.J., Bulanova, G.P., Armstrong, L.S., Keshav, S., Blundy, J.D., Gudfinnsson, G., Lord, O.T., Lennie, A.R., Clark, S.M., Smith, C.B., Gobbo, L., 2008. Primary carbonatite melt from deeply subducted oceanic crust. *Nature* 454 (7204): 622-626.
- Wang, D., Mookherjee, M., Xu, Y., Karato, S., 2006. The effect of water on electrical conductivity of olivine. *Nature* 443, 9776979.
- Withers, A.C., Hirschmann, M.M., 2007. H_2O storage capacity of $MgSiO_3$ clinoenstatite at 8613 GPa, 110061400 °C. *Contrib. Mineral. Petrol.* 154, 6636674.
- Withers, A.C., Bureau, H., Raepsaet, C., Hirschmann, M.M., 2012. Calibration of infrared spectroscopy by elastic recoil detection analysis of H in synthetic olivine. *Chem. Geol.* 334, 92698.
- Withers, A., Hirschmann, M.M., Tenner, T., 2011. The effect of Fe on olivine H_2O storage capacity: consequences for H_2O in the Martian mantle. *Am. Mineral.* 96, 103961053.
- Withers, A.C., Wood, B.J., Carroll, M.R., 1998. The OH content of pyrope at high pressure. *Chem. Geol.* 149, 1616171.

- Woodland, A.B., O'Neill, H.S.C., 1997. Thermodynamic data for Fe-bearing phases obtained using noble metal alloys as redox sensors. *Geochim. Cosmochim. Acta* 61, 4359-4366.
- Workman, R.K., Hart, S.R., 2005. Major and trace element composition of the depleted MORB mantle (DMM). *Earth Planet. Sci. Lett.* 231: 53-72.
- Wyllie, P.J., 1977. Experimental studies on the influence of CO₂ and H₂O in the upper mantle. In: *High Pressure Research: Applications to Geophysics*, ed.s M. H. Manghnani and S. Akimoto, Academic Press, New York, pp776106.
- Wyllie, P.J., 1980. The origin of kimberlite. *J. Geophys. Res.* 85, 6902-6910.
- Wyllie, P. J. and Ryabchikov, D., 2000. Volatile components, magmas, and critical fluids in upwelling mantle. *J. Petrol.* 41, 119561206.
- Yamada, A., Inoue, T., Irifune, T., 2004. Melting of enstatite from 13 to 18 GPa under hydrous conditions, *Phys. Earth Planet. Int.* 147, 45656.
- Yamashita, H., Arima, M., Ohtani, E., 1995. High pressure melting experiments on Group II kimberlite up to 8 GPa; implications for mantle metasomatism. *Proceedings of the international Kimberlite conference* 6, 669-671.
- Yaxley, G. M., Berry, A. J., Kamenetsky, V. S., Woodland, A. B., Golovin, A. V., 2012. An oxygen fugacity profile through the Siberian Craton & Fe K-edge XANES determinations of Fe³⁺/ Fe in garnets in peridotite xenoliths from the Udachnaya East kimberlite. *Lithos* 140, 142-151.
- Yoshino, T., Katsura, T., 2013. Electrical conductivity of mantle minerals: role of water in conductivity anomalies. *Ann. Rev. Earth Planet. Sci.* 41, 6056628.
- Zerr, A., Boehler, R., 1994. Constraints on the melting temperature of the lower mantle from high-pressure experiments on MgO and magnesiowüstite. *Nature* 371, 5066508.
- Zhang, J., Liebermann, R.C., Gasparik, T., Herzberg, C.T., 1993. Melting and subsolidus relations of SiO₂ at 9614 GPa. *J. Geophys. Res.* 98(B11), 19785619793.
- Zhao, Y-H., Ginsberg, S.B., Kohlstedt, D.L., 2004. Solubility of hydrogen in olivine: dependence on temperature and iron content. *Contrib. Mineral. Petrol.* 147, 1556161.
- Zotov, N., Keppler, H., 1998. The influence of water on the structure of hydrous sodium tetrasilicate glasses. *Am. Mineral.* 83, 8236834.

Appendix: Thermodynamic relations and parameters

Mie-Grüneisen type equations of state (EoS) were employed in order to determine the Gibbs free energy of fusion (ΔG_{fusion}^o) of forsterite and enstatite required for calculating the effect of H₂O on lowering melting temperature in the binary systems Mg₂SiO₄-H₂O and MgSiO₃-H₂O. Expressions to describe the Gibbs free energy changes for Mg₂SiO₄ and MgSiO₃ were taken from Stixrude and Lithgow-Bertelloni (2011) for solids and from de Koker and Stixrude (2009) for liquids and are based on the fundamental thermodynamic relation between the Helmholtz free energy (F) and the Gibbs free energy

$$G(P,T) = F(V,T) + PV \quad (a1)$$

where V is the volume, P is the pressure and T is the temperature. For liquids, the fundamental thermodynamic relation describing the Helmholtz free energy is

$$F(V,T) = F_0(0,T_0) + F_c(V,T_0) + F_{th}(V,T) \quad (a2)$$

where 0 indicates the reference state where $P= 101325$ Pa at a reference temperature T_0 . In equation a2, F_0 is the Helmholtz free energy at the reference state while F_c and F_{th} are the Helmholtz free energies produced from cold compression at ambient temperature and the thermal vibrations, respectively. F_c was calculated based on a Birch-Murnaghan EoS of the form

$$F_{c(V,T_0)} = 9K_0V_0 \left[\frac{1}{2}f^2 + \frac{1}{3}a \cdot f^3 \right] \quad (a3).$$

The Birch-Murnaghan EoS is based on the finite strain theory and its derivation can be found in e.g. Birch (1947) and Poirier (2000). In equation a3, the finite strain (f) is described as

$$f = \left[\left(\frac{V_0}{V} \right)^{2/3} - 1 \right] / 2 \quad \text{while the factor } a \text{ is described as } a = \frac{3}{2}(K' - 4). \quad \text{In this}$$

formulation, K_0 and V_0 correspond to the bulk modulus and the volume at the reference pressure and K' is the first pressure derivative of the bulk modulus. The volume (V) of the liquid was calculated at pressure and temperature of interest by solving the equation

$$P = P_{BM} + P_{th,liq} \quad (a4)$$

where the two components are defined as $P_{BM} = 3K_0 \cdot f \cdot (2f+1)^{5/2} \cdot (1-f \cdot a)$ and $P_{th,liq} = \frac{\gamma}{V} \cdot C_v(T - T_0)$. In the equation determining the thermal pressure of the liquid, C_v is the heat capacity at constant volume, and the Grüneisen parameter (γ) is calculated by the formula $\gamma = \gamma_0 + \gamma' \left(\frac{V}{V_0} - 1 \right)$ where γ_0 is the Grüneisen parameter at the reference state and γ' is its first derivative with respect to the volume. F_{th} was calculated by the equation

$$F_{th(V,T)} = -S_0(T - T_0) - C_v \left[T \ln \left(\frac{T}{T_0} \right) - (T - T_0) \right] - C_v(T - T_0) \left[(\gamma_0 - \gamma') \ln \left(\frac{V}{V_0} \right) + (\gamma - \gamma_0) \right] \quad (a5)$$

where S_0 is the entropy.

For the solids, the Helmholtz free energy relation is the same as the liquid i.e.

$$F(V,T) = F_0(\rho_0, T_0) + F_c(V, T_0) + (F_{th}(V, T) - F_{th}(V, T_0)) \quad (a6)$$

which combined with equation a1 allows the Gibbs free energy of the solid phase to be calculated.

For solid forsterite and enstatite, F_c was calculated according to equation a3 as described for liquids. In the case of a solid phase, however, a slightly different approach was used in the calculation of the volume (V). The thermal pressure of the solid is determined using an expression for the Debye thermal energy ($E_{th(V,T)}$) i.e.

$$P_{th,s} = \frac{\gamma}{V} [E_{th(V,T)} - E_{th(V,T_0)}] \quad (a7)$$

and in this case the Grüneisen parameter is calculated as $\gamma = \gamma_0 \left(\frac{V}{V_0} \right)^{q_0}$ with q_0 being a constant. $E_{th(V,T)}$ is calculated as

$$E_{th(V,T)} = 9nRT \left(\frac{T}{\theta} \right)^3 \int_0^t t^3 / (e^t - 1) dt \quad (a8)$$

where R is the gas constant, $t = \frac{\theta}{T}$ with the Debye temperature (θ) calculated as

$$\theta = \theta_0 \cdot \exp \left[\frac{\gamma_0 - \gamma}{q_0} \right]. \quad (a9)$$

The Helmholtz free energy thermal contribution ($F_{th(V,T)}$) of the solid end members is determined by the formula

$$F_{th(V,T)} = 9nRT \left(\frac{T}{\theta} \right)^3 \int_0^t \ln(1 - e^{-t}) t' dt \quad (a10)$$

and ($F_{th(V,T0)}$) was calculated at T_0 accordingly.

The thermodynamic parameters employed in the calculations of the Gibbs free energy for solid and liquid end members Mg_2SiO_4 and $MgSiO_3$ using the approach described above are reported in Table a1.

Table a1: Thermodynamic parameters of end member solid and liquid Mg_2SiO_4 and $MgSiO_3$

Liquids	Mg_2SiO_4	$MgSiO_3$	Solids	Mg_2SiO_4	$MgSiO_3$
T_0 (K)	1773	1773	T_0 (K)	300	300
V_0 (cm ³ /mol)	49.6 ^a -51.0 ^b	38.5	V_0 (cm ³ /mol)	43.6	62.7
K_{T0} (GPa)	32.1	27.3	K_{T0} (GPa)	128	107
K'_{T0}	5.84	5.70	K'_{T0}	4.2	7.0
α	0.63	0.21	α	0.99	0.78
'	-1.2	-1.8	q_0	2.1	3.4
C_v (J/K/mol)	232.8	179	α (K)	809	812
S_0 (J/K/mol)	430	312	F_0 (kJ/mol)	-220.1	-312.9
F_0 (kJ/mol)	-256.9	-184.2			

^a: value employed at 6 GPa; ^b: value employed at 13 GPa

Thermodynamic data summarized in Table a1 were previously compiled from the literature by de Koker and Stixrude (2009) and Stixrude and Lintgow-Bertelloni (2011) for liquids and solids, respectively. F_0 for liquids were empirically calculated from the room pressure melting temperatures as in Liebske and Frost (2012). Parameters V_0 and S_0 for the liquid were slightly altered compared to those reported by de Koker and Stixrude (2009) in order to obtain better agreement with the experimental melting temperatures and to be consistent with calorimetric data for the enthalpy of fusion of MgSiO_3 and Mg_2SiO_4 (Navrotsky et al., 1989; Richet et al., 1993).

Erklärung

Hiermit erkläre ich, dass ich die vorliegende Dissertation selbständig verfasst und keine anderen als die angegebenen Quellen und Hilfsmittel benutzt habe.

Weiterhin erkläre ich, dass ich niemals ohne Erfolg versucht habe, eine Dissertation einzureichen oder mich der Doktorprüfung zu unterziehen.

Bayreuth, den 25. November 2014

Davide Novella

